CO-ADAPTIVE MULTIMODAL INTERFACE GUIDED BY REAL-TIME MULTISENSORY STOCHASTIC FEEDBACK

By

VILELMINI KALAMPRATSIDOU

A dissertation submitted to the

School of Graduate Studies

Rutgers, The State University of New Jersey

in partial fulfillment of the requirements

for the degree of

Doctor of Philosophy

Graduate Program in Computer Science

written under the direction of

Elizabeth B. Torres

and approved by

_____

_____

_____

_____

_____

New Brunswick, New Jersey

May, 2018

ABSTRACT OF THE DISSERTATION

Co-adaptive multimodal interface guided by real-time multisensory stochastic feedback

By VILELMINI KALAMPRATSIDOU

Dissertation Director:

Elizabeth B. Torres

In this work, I present new data-types, analytics, and human-computer interfaces as a platform to enable a new type of co-adaptive-behavioral analyses to track neuroplasticity. I exhibit seven different works, all of which are steps in creating an interface that collaborates in a closed-loop formula with the sensory-motor system in order to augment existing or substitute lost sensations. Such interfaces are beneficial as they enable the systems to adapt and evolve based on the participants rate of adaptation and preferences in evolution, ultimately steering the system towards favorable regimes.

I started by trying to address the question: *"how does our novel sensory-motor system learn and adapt to changes?"*. In a pointing task, subjects had to discover and learn the sequence of the points presented on the screen (which was repetitive) and familiarise themselves with a non-predicted event (which occurred occasionally). In this very first study, I examined the learnability of motor system across seven individuals, and I investigated the learning patterns of each individual.

Then, I explored how other bodily signals, such as temperature, are affecting movement.

At this point, I conducted two studies. In the first one, I looked into the impact of the temperature range in the quality of the performed movement. This study was conducted in 40 individuals, 20 Schizophrenia patients, known to have temperature irregularities, and 20 controls. I identified the differences between the two populations in the range of temperature and the stochastic signatures of their kinematic data. To have a better look into the relation of movement and temperature, I conducted a second study utilizing data of a pre-professional ballet student recorded during her 6h training and her follow up sleep. For this study, I designed a new data type that allows us to examine movement as a function of temperature and see how each degree of temperature impacts the fluctuations in movement. This new data structure could be used for the integration of any bodily signal.

Next, I identified the need to build visualization tools that could picture in real-time sensory information extracted from the analysis that would be informative to the participant. Such tools could be used in a vision-driven co-adaptive interface. For this reason, I designed an in-Matlab avatar that enables us to color-code sensory information to the corresponding body parts of the participant.

In our next study, I examined two college-age individuals (a control and an Asperger syndrome) under sensory modalities and preferences. I built methods to extract for each individual the preferred sensory modality from the motor stream, **selectivity**, and preferences of the particular modality that motivate the system to perform at its best, **preferability**. These two parameters were critical to finally close the loop by letting the system decide upon the individual preferences.

Therefore, I moved from the open-loop approach, to which all the so-far described studies belong to, into the closed loop approach. Firstly I study a natural closed-loop interface established by the dyadic interaction of two ballet dancers while rehearsing. In this natural paradigm, the closed-loop coadaptation happens through the touches and the pushes that dancers apply on each other in order to co-ordinate, kinesthetic adaptation. Therefore, I applied network connectivity metrics and extracted information such as underlying

synergies, leading, and lagging body-parts to name a few. Such tools could be used in a vison-driven co-adaptive interfaces to evaluate the interaction between the participant and the displayed avatar. Finally, I built an artificial audio-driven co-adaptive interface which can track the adaptation and progress of the individual and intelligently steer the system towards the preferred and motivational conditions of the participant. For this conducted study, I utilized the heart rate of a salsa dancer to adjust the tempo of the music. The study showed that such a system can steer the stochastic signatures even of the heart (autonomic signal) creating strong evidence that I can guide the human system towards desire regimes.

Acknowledgments

This thesis is part of the ongoing research in Sensory Motor Integration Lab (SMILab). Many of the main presented methods have been designed by my advisor Elizabeth B. Torres and are applied in the general research conducted in the lab.

There are two existing publications that this work relies on: "Body-brain-avatar Interface: a tool to study sensory-motor integration and neuroplasticity [42] and "Outcome Measures of Deliberate and Spontaneous Motions" [41] and 3 more that are currently under review: Extracting sensory and contextual information from the motor stream [44], Dancing to ones heart-beat: A study of physiological signal entrainment through the real-time sonification of heart rate data [43], and Methods to Track Dynamically Coupled Coordinated Bodies in Ballet Partnering [40].

I would also like to acknowledge the PhaseSpace Inc. for sharing with us with the motion capture data collected for Bot & Dolly study directed by Tarik Abdel-Gawad. The analysis and result of this study is presented in Chapter 9. I would also like to credit Tarik Abdel and the dancers participated in the stud, Maria Kochetkova and Joan Boada, for allowing us to use part of *vimeo.com*/96030980 to create video 4, Appendix Chapter 9, as well as for the use of Figures: 6.6 9.3 9.1,

Additionally, I would like to acknowledge photographic material that was used to demonstrate the equipment and software used in various Figures:

- Recording equipment, Figure 2.3 6.4 6.3 8.2 7.1 10.4 10.5:

  Enobio: *www.neuroelectrics.com*

  PhaseSpace Motion Capture: *phasespace.com*

  APDM: https:*www.apdm.com*

Vicon Systems: *www.vicon.com*

Polhemus Sensors: *polhemus.com*

- Software, Figure 7.1 10.5 6.4 6.3 6.5 6.6 6.1:

  Max7: *cycling*74.*com/products/max*

  Motion Monitor: *www.innsport.com*

  Recap, PhaseSpace: *phasespace.com*

  Python: *www.python.org*

  LabStremingLayer: *github.com/sccn/labstreaminglayer*

  Matlab: *www.mathworks.com/products/matlab.html*

- The images presented in Figure 1.3:

  Alexa: *a.co*/5*enAuus*

  Sophia: *www.hansonrobotics.com/robot/sophia/*

  OKgoogle: $store.google.com/us/product/google_home?hl = en - US$

- The avatar demonstrated in Figures 1.1 4.6 5.5 7.1 8.1 8.2 8.3

  Character: *www.mixamo.com*

Finally, all these studies were supported by the scholarships of Gerondelis Foundation Graduate Study and Computer Science Graduate Teaching Assistantship. Additional financial support came from the Nancy Lurie Marks Family Foundation Career Development Award to Elizabeth B. Torres and New Jersey Governors Council for Autism Research and Treatment of Autism.

Dedication

This thesis work is dedicated to my family who let me fly away from home to explore my own path in life, and yet they always are "on the other end of the line" waiting to hear that I overcame my daily difficulties for one more time and I keep going. I would also like to dedicate it to all my friends and relatives, teachers and educators who contribute on their own unique way to be who I am, think and conduct the way I do today.

Moreover, I would like to dedicate this thesis to the beautiful people of my lab who create a joyful environment where work is more fun than fun activities, where communication and support does not happen due to responsibility, and where respect is part of research because everyone can contribute in their own unique way.

Finally, I would like to dedicate it to my advisor who advised, inspired, and supported me on every aspect of this project, and most importantly she motivated me to bring in to my work aspects of my life that I love, such as dance, and give this unique essence to my work that impresses people. She has been a teacher, an advisor, a mother, and a friend all these 5 years that I have been working with her.

Table of Contents

List of Tables

List of Figures

Chapter 1

Introduction

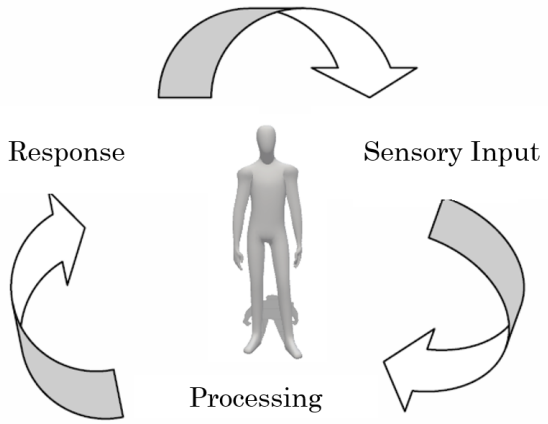

Figure 1.1: **Schematic of the closed-loop interaction of our system with the environment. This loop is a repetitive and continuous process through which we train our system to learn, adapt, and evolve.**

In this chapter, I present an overview of the elementary ideas underlying the core research conducted in Sensory Motor Integration Lab (SMILab).

I begin by introducing how the physiology of the nervous system and the case study of Ian Waterman motivated us on working towards designing closed-loop co-adaptive interfaces. Then, I describe the importance of assessing the variability in different signals in the world: those external to the nervous systems and those which are internally generated by the nervous systems. I study how the evolution of the noise to signal ratio in the signal helps me establish unique patterns of behaviors and how their rates of change contribute to uniquely define features of the nervous systems of a person, i.e. as a fingerprint unique to the individual. I point out the need to assess motions within naturalistic settings that reveal

the spontaneity of self-generated human movements and the relevance of this approach to contemporary AI and robotics, where anthropomorphic artificial agents are becoming ubiquitous. I illustrate four examples that show the utility of assessing variability and its features, along with the detection of significant changes in the continuous signal I harness and manipulate in real time. In what follows I present the outline of the Chapters of this thesis.

1.1 The Closed-loop of Afferent and Efferent Channels

As a computer scientist, one of the most fascinating aspects of my studies in neuroscience has been the realization that this field primarily focuses on the study of the Central Nervous System (CNS), comprising the brain and the spinal cord. To understand these complex systems, researchers rely on animal models and techniques that are for the most part invasive and not appropriate to study humans through direct physical measurements. They have very detailed measurements of rodents and non-human primates, but very little understanding of the activities of the human brain. To study the human brain, the field must rely on non-invasive imaging techniques, or electroencephalography. These techniques often require the person to remain still because covert motions introduce artifacts and distort the signals. As such, we know very little about naturalistic behaviors and their brain signatures. At most, we may theorize about the human brain, the mind and its possible functions. Here I submit to the reader that in fact, the study of the Peripheral Nervous Systems (PNS) offers a new avenue for discovery. The PNS activities may help us compensate for the lack of knowledge on naturalistic behaviors, while offering us a window into the intentions of the brain. By studying the activities at the periphery, I may build a proxy model of the activities of the brain, as the CNS attempts to predict and control its body in motion and produced socially viable behaviors.

In this work, I try to understand the CNS by investigating the PNS. I do not use any invasive methods. Instead, I record bodily signals, such as kinematic signals from limbs,

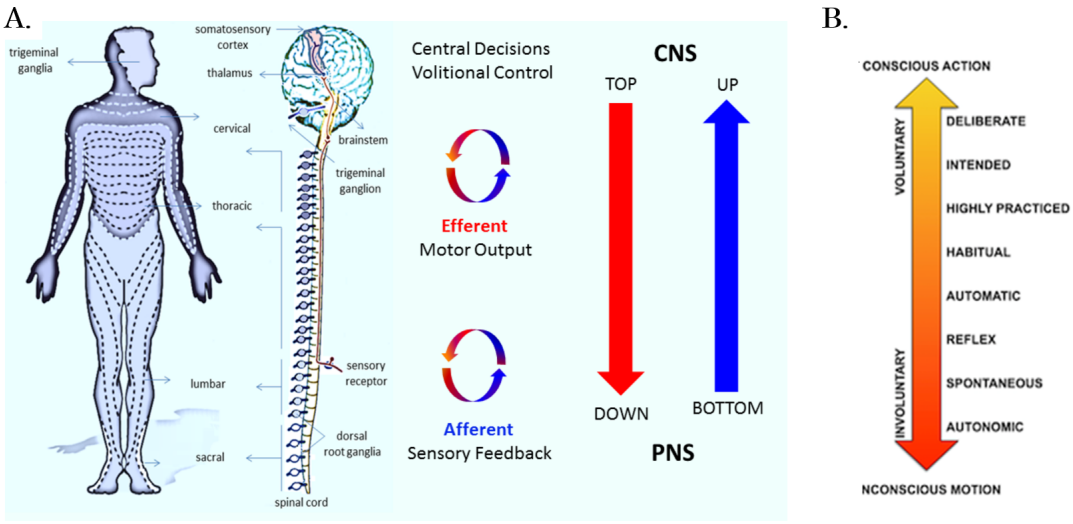

Figure 1.2: **(A) Schematic of the peripheral network divided into the afferent and efferent channels which transfer re-afferent kinesthetic information to the brain and output movement-related information to the periphery. (B) The range of human movement varies from autonomic to deliberate.**

torso, and head, and other physiological signals some examples are temperature, heart rate, and brain waves among others- to extract information that is originated from the CNS trying to control the body in motion. Specifically, I use commercially available technology (wearables and motion capture technology) to record these signals (Section 2.2), methods and techniques to analyze them (Section 2), and reveal what is that the CNS is trying to accomplish and what the intentions lying behind a particular behavior of PNS may be. I essentially use the PNS as a window to access functions of the CNS as it tries to control our actions at will.

In the process of trying to understand these bevaviors and motions at the periphery, we discovered that every complex motion can be decomposed into segments [88] (Figure 1.2.B) that are goal-directed they are happening under conscious control. And others that are spontaneous; they lie beneath our conscious awareness. An example of intentional versus spontaneous motions is the purposeful movement of reaching out to turn ON a light switch versus retracting the hand back to rest right after the light switch was turned ON. However, there is evidence that we can bring movements that we execute spontaneously into

awareness. Teaching techniques to athletes and dancers is a process where a lot of repetition and observation is required, as these two classes of movements coexist. A student repeats the routine, while the teacher points out weaknesses, then the former has to understand the mistakes by observing the routine and correct it bringing awareness to these motions. By maintaining the awareness over these motions, someone can finally adopt the technique, and perform the routine correctly under any circumstances (competitions, performance, and practice, to name a few). This is how the learning of motor tasks tend to take place.

However, it is not possible to exert that level of voluntary control over signals of the autonomic system such as the heart. The heart is an autonomic organ, and even if the person has some awareness of its activity, it is hard to control it at will (you may want an example from yoga people trying to do this and not reaching the level of control they desire). Indeed, signals which play such a vital role in our existence should be that way because it is a matter of survival. However, even in these signals, there are small fluctuations that change and are impacted by our surrounding, as I will discover in Chapter 10.

Previous work, as well as the work presented in this thesis, has shown that the PNS give us the advantage to collect data non-invasively and make inferences about the control of our CNS over our actions, intentions, and thoughts [43] [40] [88]. Based on the physiology of the nervous system, the efferent nerves of the PNS conduct information from the brain out to spinal cord, muscles, and limbs. In contrast, the afferent channels bring information backwards (from the periphery to the brain) and provide feedback that the brain utilizes to control movement [32], Figure 1.2. Research has shown that the efferent information alone cannot produce any controlled movements [69]. When a person loses the afferent nerves conducting the re-entrant signals self-generated by the movement itself (ex. touch, pressure, postures and bodily motions), they lose voluntary control, and they cannot move[16]. A case study that has been well-documented is that of Ian Waterman a deafferented individual, who lost the afferent channels for movement, pressure, and touch and learned to walk by sensory substituting these senses with visual and auditory information and continuously

monitoring his own postures and motor output flow [16] [94].

Ian Waterman was one of the sources of inspiration for developing the ideas, tools, and methods presented in this work. It was the person that made us consider the neuroplasticity of the periphery as a feature of the human system that could be used for creating closed-loop co-adaptive interfaces that bring information from the external world into our system by augmenting existing or substituting lost sensations.

To attain this goal, I identified the needs of studying the various sensory modalities of our system (Chapter 3, 4, 5, and 10) and their integration with our movements (Chapter 4 and 5). I spotted the need for creating full body models and visualization tools as a way to map out activity changing in real time and visually augment sensory modalities with the sources of sensory preference the system showed us through motor variability patterns (Chapter 6). I also created methods that can detect the dominant sensory modality of the studied individual as well as the conditions under which it performs the best (Chapter 7). I applied network connectivity tools derived from weighted directed graphs to explore the patterns of synchronicity and synergies within the person's body in motion and to study as well those patterns as they emerged from very complex interactions in partnering ballet and contemporary pop dances. I studied the social dance between two people interacting within a natural closed-loop co-adaptive interface: that of a dancing dyad (Chapter 9). Finally, I sonified the peripheral bodily biorhythms, including those of the heart, parameterized them and combined them with other sources of sound (musical pieces) to feed it back to the person. I causally altered in real-time the person's heart rate variability and confirmed two modes of autonomy corresponding to the two movement classes previously uncovered in the athletes (Torres 2011) and performing artists (Kalampratsidou and Torres 2016). Namely, deliberate and spontaneous autonomy, with distinct stochastic signatures in their rates of change. To systematically test our model, I built a real-time co-adaptive closed-loop interface and explored many different contexts, sensory conditions, and music types thus building a way to extract preferred sensory information from the motor stream of natural

behaviors unfolding in real time.

To achieve all these step-by-step goals, we build methods that can examine the variability of the bodily signals independently of the type and nature of the signal and investigate them in a personalized manner across large cross-sections of the population, ranging from 5 to 60 years of age, some with pathologies of their nervous systems and inclusive of both sexes. We scaled our data and provided a transform of our waveforms that avoid the possible types of allometric effects that could be emerged in the case of kinematic data when testing people of various ages and anatomical sizes. Finally, by empirically estimating (rather than theoretically assuming) the probability distributions of the fluctuations in such nervous systems signals, we gained additional information on the features of their variabilities, such as levels of randomness, predictability, dispersion and skewness, among others 2.5.

1.2 Variability in the World

When I first started working at the Sensory Motor Integration lab, in Spring Semester of 2013, I was introduced to the idea of noise in our sensory-motor system. In my thesis, I refer to it as noise or noise-to-signal ratio, which is mathematically defined as σ/μ. In real life, the simplest way to describe it is that in our sensory-motor system noise is the reason that we cannot perform exactly the same trajectory twice when, for example, pointing between two targets. But, it is not that simple. Studying the variability of the kinematic parameters, identifying the family of probability distributions that they belong to, extracting the noise, and estimating the stochastic signatures that describe them, was a motivating force that made me start thinking of variability and its noise in the broader context of adaptive processes.

We live in a word that is full of variability, noise, and randomness. Our sensory-motor system continually receives auditory, visual, somatosensory, olfactory, and gustatory sensory signals that we can study as vibrations and convert to sound. When for instance, we take a walk in a park, our spontaneous behavior meets the spontaneity of other people, animals,

events that are in the same park. We might reach a friend that spontaneously decided to take a walk in the same day and time with us. We might experience rain, sun, or wind. We might see tree branches falling. These are all random events that are produced by some stochastic random processes. In reality, we only pay attention to things that we care for and take note of, thus processing the information that we consider valuable while other information serves as supplementary, mostly ignored at a conscious level, but nonetheless playing some role that transpires largely beneath our full awareness. We may care less about a tree branch falling far away in a forest than we do about a tree falling next to the path we are walking on. The latter may demand our attention and more generally, implicitly influence our attitude when walking under trees.

Through my research, I started seeing the world as a collection of stochastic random generators. Everything is random, but the features and their interpretations are what makes them to be different and unique within this chaos. This is how people differ from each other: we all have random behaviors, but they are produced by different random processes. Therefore, some behaviors are very random whereas others are more predictive (Section 2.5 explains the interpretation of the features of the stochastic processes). Haven't you ever have friends that are very reliable and trustworthy when it comes to scheduling meetings whereas others are more random? The possibility of meeting the first ones is high, in contrast, meeting the second category of friends is likely low. In other words, if we were able to correspond your meeting in a numerical parameter, then the distribution that would describe it in the first case would be more Gaussian-like (symmetric and predictive) whereas, in the second case, it will be more exponential like (random).

To respond to all this randomness, we have developed a system that is trained to receive a wide range of randomness from a different kind of stimulus: visual, auditory, olfactory, gustatory, and somatosensory and extract only the critical information. In fact, our system is so well trained that it is hard for me to recognise the existence of all this noise due to the screening of only what we have deemed 'critical' . Our system can collect information

out of all these events and determine if there is a periodicity that characterises a particular random generator and then assesses the degree to which we should believe that an event might come true. This is an on-going process, and the more and better we get to know someone, the more trained our system gets and less unexpected some events look.

Indeed, there might always be 'weak moments' of wondering, what is the critical or true point we should extract from an action, but the more we know a random generator, the less often these will occur. 'Weak moments' are situations where we are not able to extract clear information. It happens when we ask, for instance, from an over-polite person if they would like to share our dinner with us because they don't have food with them and we have plenty. Such a person might reply 'no, thank you!' but we don't know if this was a 'polite no' or a 'real no'. Hence, we repeat the same question rephrased. If the answer is again ambiguous, we might continue that loop until we get some cleared data or tire of trying to clarify. This is happening due to of what I call 'noise of politeness'. Politeness is generally noisy, but, as we are trained in the social rules of our community, we can identify with some accuracy when we get a friendly warning, when we have to respond with an apology, or when we were only given friendly directions. In contrast to 'weak moments', a 'strong moment' is when regardless of the layers of politeness or noise that someone may add on their actions we still can extract the bare intentions.

The more exposed our system is to these random processes, the better training it gets and the more information it learns to extract from the events it perceives. In the community-driven world of dictionaries, intelligence is defined as the ability to acquire and apply knowledge and skills. Similarly, an intelligent artificial system should be the one that can be built by persistent achieving learning and adaptation following exposure to new, unexpected, and unstable environmental parameters.

Figure 1.3: **Technology that aims on imitating human intelligence, natural behavior and language: A. Sophia, social humanoid robot by Hanson Robotics (source:** *www.hansonrobotics.com/robot/sophia/*), **B. Alexa, intelligent personal assistant by Amazon (source:** *a.co/5enAuus*), **C. Google assistant, virtual personal assistant by Google (source:** *store.google.com/us/product/google*$_h$*ome?hl* $= en - US$)

1.3 Variability and Spontaneity in Technology

As individuals, the variability of the tone of our voice, our facial expressions, the phrasing of our sentences, and the unfolding movements during a conversation is what makes us unique and identifies our character. Modern artificial agents such as Alexa [4], Sophia [5], and Google assistant [10] among others are technologies that aim at mimicking the natural behavior of human beings [20] [83] [55] [17]. However, these systems are still significantly lacking features of natural interaction that are characterized by spontaneity and constant adaptation of the human system.

Modern artificial agents require massive improvement to reach a level of self-learning that is similar to that of a human being. Although it is claimed that some systems can be self-taught [5], their interaction still looks like it is a well-scripted presentation [1]. Indeed, they do appear to have some variability in actions, but the spontaneity does not lie within natural range. They are missing unrehearsed wording, the fluctuation of the facial expressions, all the possible colors that our voice reaches to emphasize what we want are only a few of the possible examples. Think of a sentence and try to say with different emotions. Is this something Sophia can do? Then, ask your friend to repeat the same

sentence under the same emotional contexts. Can you find an exact match between your trials and her or his trials? This is the spontaneity that makes us unique, which robots are missing, because there is not much research focusing on the variability of bodily signals; and, the impact of bodily signals on our natural and spontaneous behavior is not widely known.

In this work, I aim at bringing technology a step closer to achieving human-like variability. In this very thesis, I present ways to study natural human behavior and parameterize the noise that human system elides.

1.4 Variability of the Bodily Signals and the Parameterization of Spontaneity

To better understand the variability of the bodily signals, in the section I present four examples that demonstrate how different conditions can affect the stochastic signatures (shape and scale parameters of Gamma distribution) of these signals. More specifically, I review the fluctuations of kinematic signals in the context of the age range, the type of the task performed, the learning progress within a particular task, and the population examined. These are only a few of the conditions that can affect the stochastic signatures of our kinematic parameters, but, yet, enough to illustrate their significance in our life.

Figure 1.4B, 1.5, 1.6C and 1.7A illustrate the Gamma signatures of the studied bodily signal for the four examples. The scale parameter of the Gamma plane (y-axis) is the noise-to-signal ratio or what I simply call as noise. The shape parameter is demonstrated in the x-axis.The corresponding PDF's of these signatures are also shown in these Figures (1.4B, 1.6C and 1.7B).

Figure 1.4B exhibits the effect of age in the stochastic signatures. It is noteworthy that there is an increased shift of signatures to less noisy regimes towards the older ages, with the lowest noise to be noticed on the age at 41 to 60. The shifts of the signatures are more

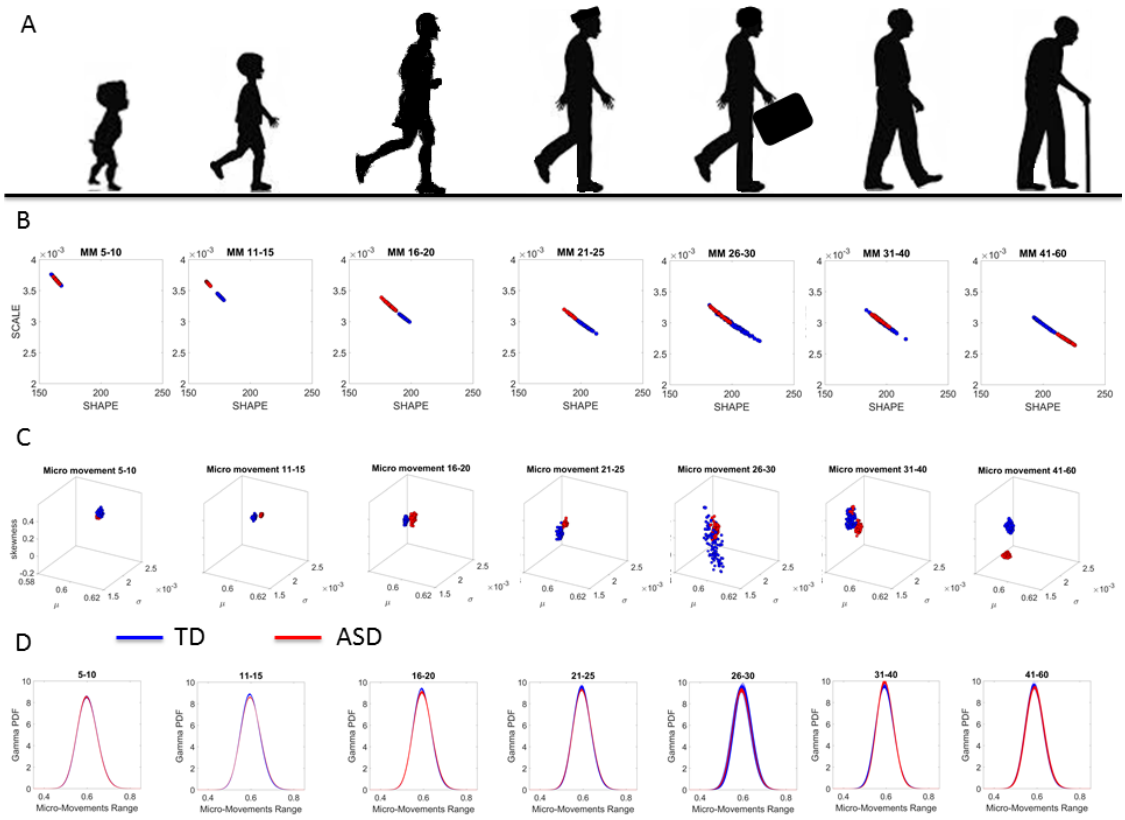

Figure 1.4: **Age-depended evolution of the probability distribution of the micro-movements of the involuntary head motions extracted from resting state fMRI data of the Autism Brain Imaging Data Exchange. The figure demonstrates the landscape of (A) human development from 5 to 60 years of age. (B) Empirically estimated Gamma shape and scale parameters for typically developing controls (blue) and age-matched individuals with autism spectrum disorders (red). (C) The Gamma mean, variance, skewness, and kurtosis (size of markers) of the corresponding signatures and their (D) PDF's. [92].**

prominent on the first three groups (until the age of 20 years old), than in older groups. This is possible due to the quick learning that takes place and the continuous adaptation to a body that is growing. After the age of 18, there is no more development; hence, the signatures shift very little.

In our description of variability so far, I have mainly described it as the fluctuations in the amplitude of the studied signal. However, variability may also be noticed on the temporal dynamics of the performing task. Figure 1.5A shows that based on the type of

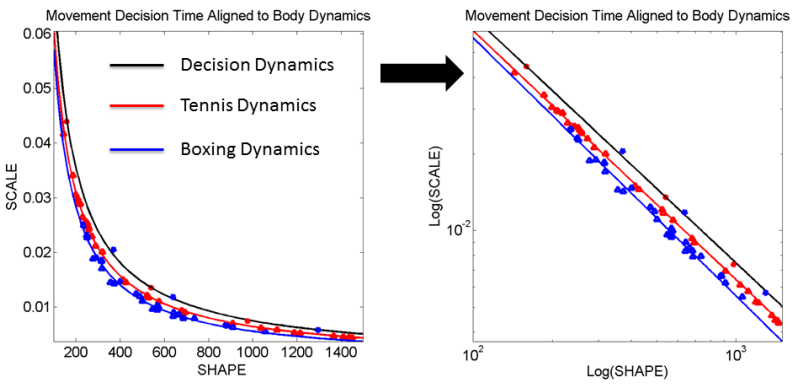

Figure 1.5: **Gamma signatures of mental and physical decision tasks indicating congruent relations between the stochastic signatures of the temporal dynamics [92].**

the task, the stochastic signatures may group on different slopes indicating that the rate of shifts of the signatures varies based on the task. Moreover, this figure reveals the existence of "congruent relations between the stochastic signatures of the temporal dynamics of mental and physical bodily motions" [92].

In a study conducted in the SMILab in 2013 [104], researchers created a very first version of a closed-loop interface by activating media on the display when the participant was holding the hand in a particular region (Fig. 1.6A and B). The study was conducted in non-verbal children with autism, and the use of media was aiming at motivating them to maintain the placement on their hand within that region since no instructions were given. Figure 1.6.C shows the step by step progression of a child during the section. The child started with high noisy stochastic signatures describing the exponential distribution of the kinematic data (unhealthy regimes), and progressively shifted to low noise signatures which correspond to Gaussian-like distributions (healthy regimes) and are similar to the signatures of the controls.

Another outcome of this study is the differences that can be noted across populations, in our example among children with Autism and controls. Figure 1.7A displays the stochastic signatures of the TD(controls) and ASD (Autism spectrum disorder) when inside the volume

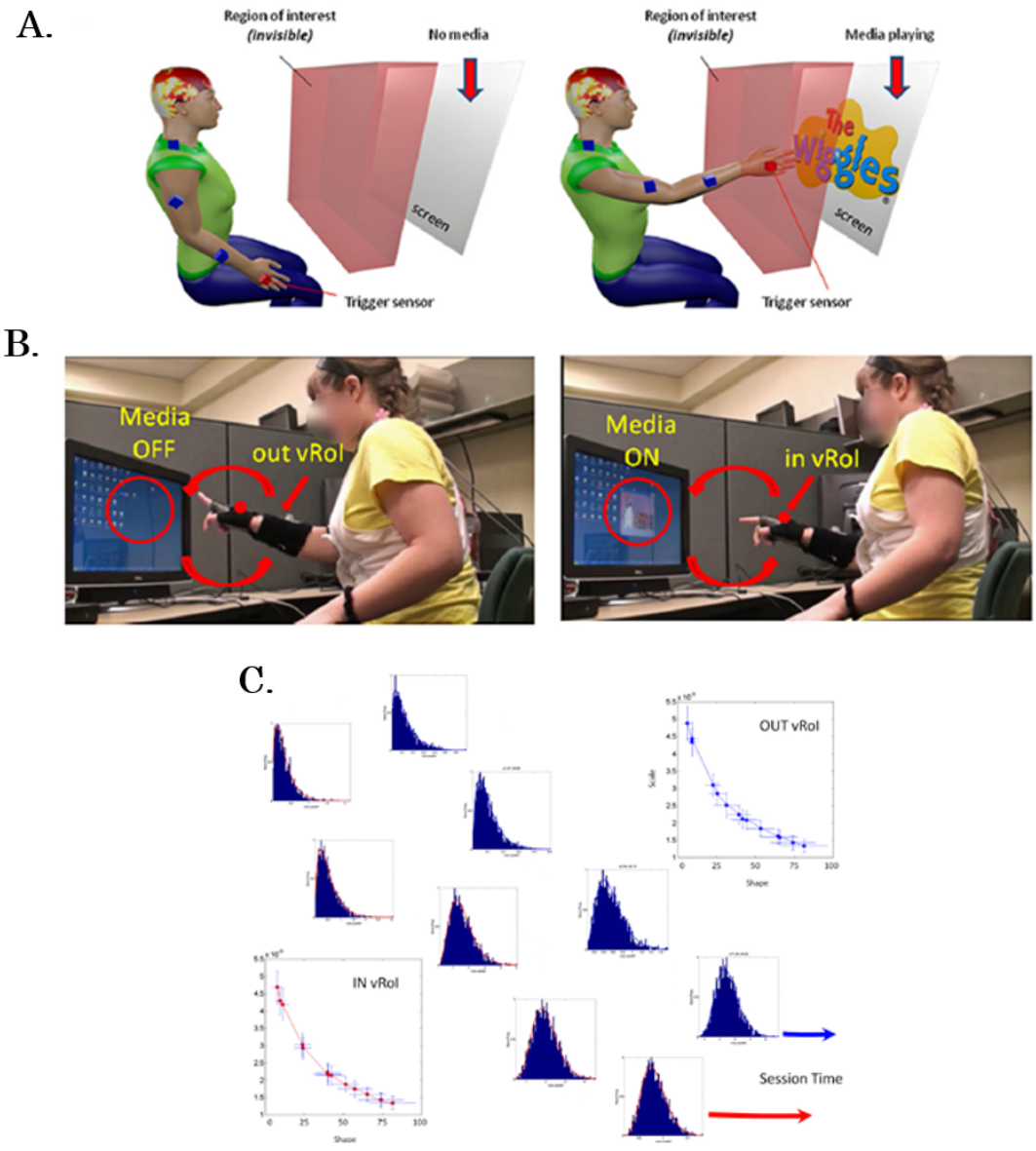

Figure 1.6: **(A)The participant seats in front of the monitor and wears position-recording sensors on the upper body (shoulder, upper arm, forearm and hand). The volume is defined within personal space of the individual (a virtual region of interest, vRoI). (B) When the hand pass from the volume, the media plays on the monitor. The participant should self-discover that the hand must stay inside the vRoI for the media to play continuously (C) Plots demonstrating the progression of the participant during the section. She started from an exponential distribution and shifted towards Gaussian-like distribution similar to those of healthy children [92].**

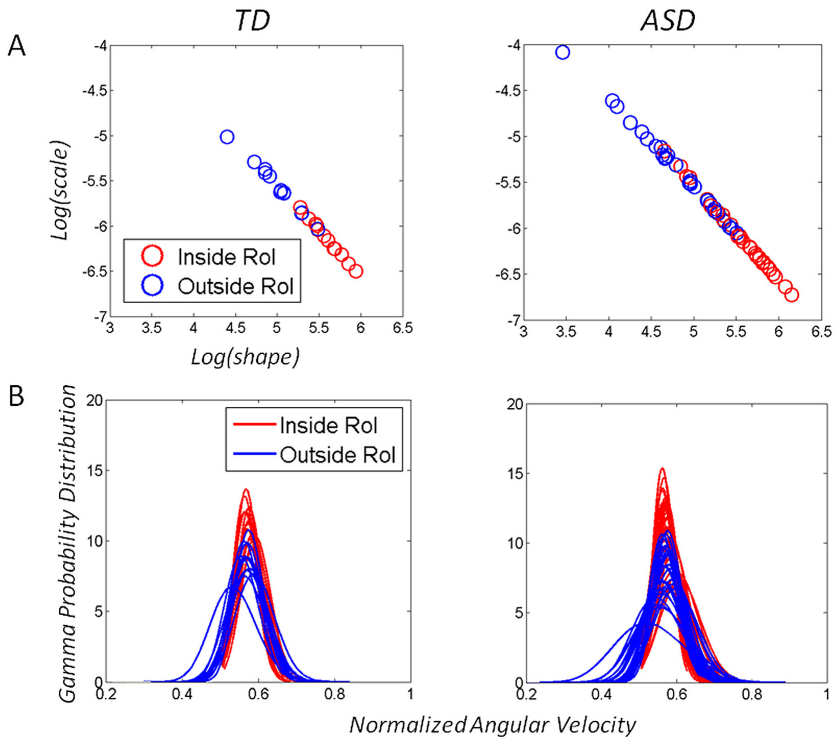

Figure 1.7: **The range of stochastic signatures among different populations (children with Autism and controls). (A) Evolution of the Gamma stochastic signatures and (B) their corresponding PDF's estimated by the hand's fluctuations in the amplitude of the angular speed while moving from the seeking outside the vRoI to the stable motions inside the vRoI. The signatures of both populations shifted towards less noisy and more symmetric regimes while the children were learning the task, indicating the plasticity of the PNS of both populations [92].**

(inside RoI) and outside the volume (outside RoI). It is noticeable that ASD's have a broader range of signatures starting from very noisy unhealthy regimes that are not noticed in the CT's. The results can also be observed on the PDF plots too.

These four examples are only a few of the factor that can affect the variability of the stochastic signatures of our bodily signals. There are numerous other factors that impact them, and may constantly be changing causing new trends on the signatures that reveal new patterns of variability.

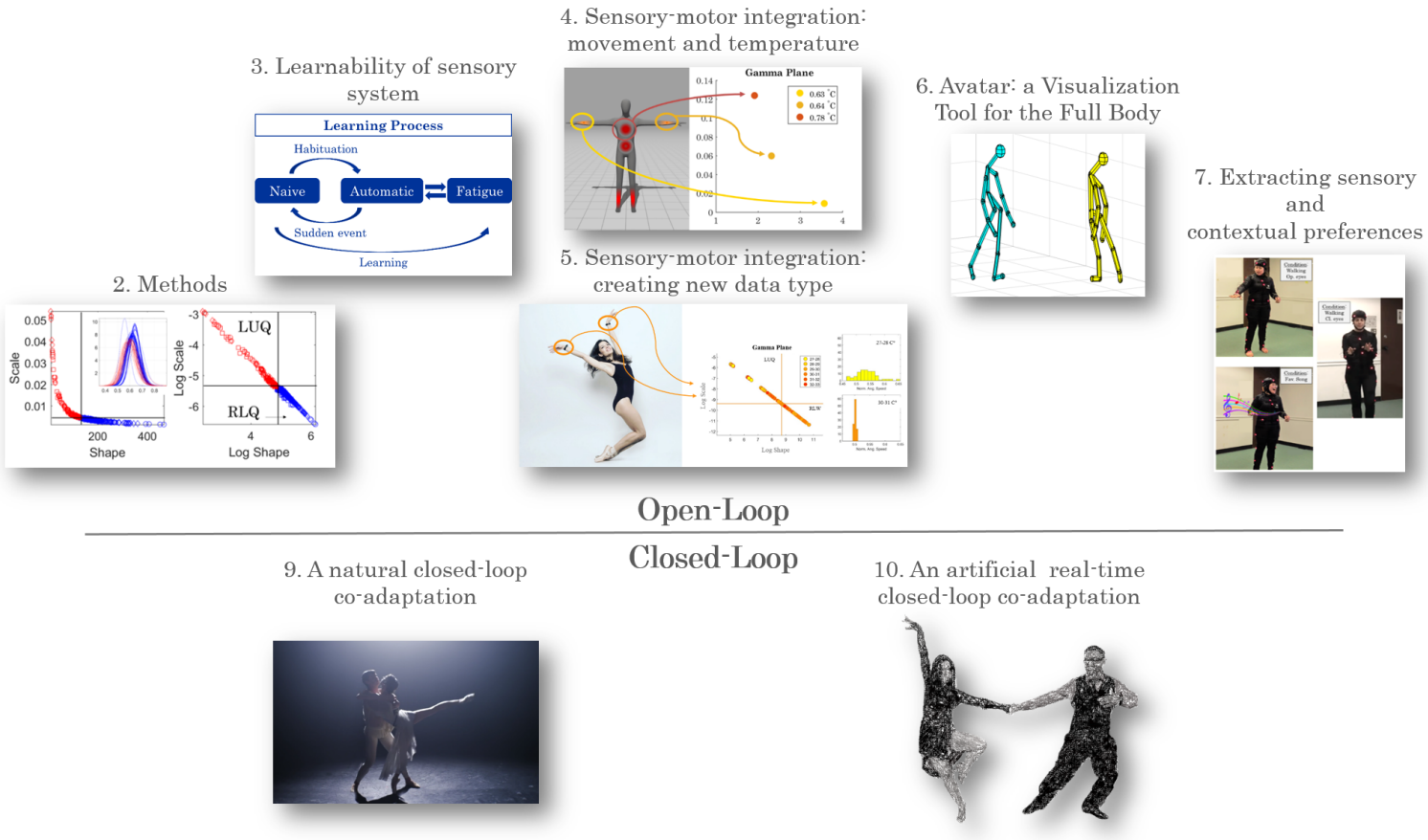

Figure 1.8: **Schematic of the chapters' outline**

1.5 Outline of Chapters

In **Chapter 2**, I present the technology utilized and the various populations studied. We, also, describe the primary data structures used and methods applied in all my studies presented in Chapters 3 - 5, 7, and 9 - 10. Moreover, I compare the methods developed in SMILab with the methods that are currently used in the field outlining advantages and disadvantages. This chapter aims at preparing the reader for the tools that are going to utilize in the following studies.

The first study is presented in **Chapter 3**; it is a baseline study aiming to explore the learnability of human motor system. I investigate the impact of repetition in habituation, how simplicity and complexity affect the learning process, and how an unexpected event can cause negative consequences to this process. I discovered that each individual has different patterns of learning and I managed to characterize fatigue in the process of co-adaptation [38].

Chapter 4 exhibits a study the variability of two kinematic parameters, angular speed and linear acceleration, parameterized by the range of the skin temperature. I studied the paradigm among Schizophrenia patients who are documented for temperature irregularities- and controls. This study revealed differences in the temperature ranges and on stochastic signatures (including noise) of the kinematic parameters studied between the two populations.

Next, **Chapter 5** investigates further the connection between temperature and movement. In this study, I present a new data type which allows me to examine temperature as a function of movement. The analysis takes place in a continuous format to examine variabilities in the stochastic signatures as they unfold every 20 min in 6 hours ballet training of a pre-professional ballet student and her following up sleep. I compared the intended and goal-directed movement performed during the training with the spontaneously generated motion of sleep, and I reveal how different degrees of temperatures can impact the quality

(noise) of our motions. This study opened up new horizons for bodily signals integrations, as well as it uncovered the need for visualization tools that could be informative to the participant to gain awareness over the conditions (temperature and movement performance) obtained in the various body parts [39] [41].

As such, in **Chapter 6**, I demonstrate an in-Matlab developed avatar, which allowed me to color the body parts as a visualization tool that could present the moment-to-moment variability of the studied parameter (ex. noise of a bodily signal) continuously and in real-time for the purpose of building a vision-driven co-adaptive interface [42].

Chapter 7 investigates the extraction of sensory and contextual information from the continuous motor stream. In this study, I examine two individuals (an Asperger Syndrome college student and a control) under various sensory modalities and preferences, and I develop tools to extract selectivity and preferability, which are the critical parameters for closing the co-adaptive interface in real-time [44].

Hence, I use **Chapter 8** to emphasize the completion of the open-loop studies and the beginning of conducting research in a closed-loop approach. In this chapter, I elaborately explain the transition, how this was achieved, and which parameters played an essential role in this.

Chapter 9 describes the study of a natural closed-loop, a dancing dyad (a female and a male professional ballet dancer). I group the data into dancing and non-dancing segments, and I apply network connectivity analysis across the body-parts of the dyad for the two cases. This study uncovers the underlying synergies supporting the network of the two bodies as well as the synchronicity of those. This information could be used in a vision-driven co-adaptive interface to investigate the network connectivity between avatar and participant [40].

Finally, in **Chapter 10**, I present an audio-driven co-adaptive interface where the heart-rate of a female salsa dancer controls the tempo of the music. The study showed that I can steer the stochastic signatures even of the heart which is an autonomic signal creating

strong evidence that I can guide human system towards desired regimes [43].

Lastly, **Chapter 11** has the conclusions, main outcomes and limitations of my research, as well as possible future directions.

Chapter 2

Methods of Studying Peripheral Nervous System as a proxy of Central Nervous System

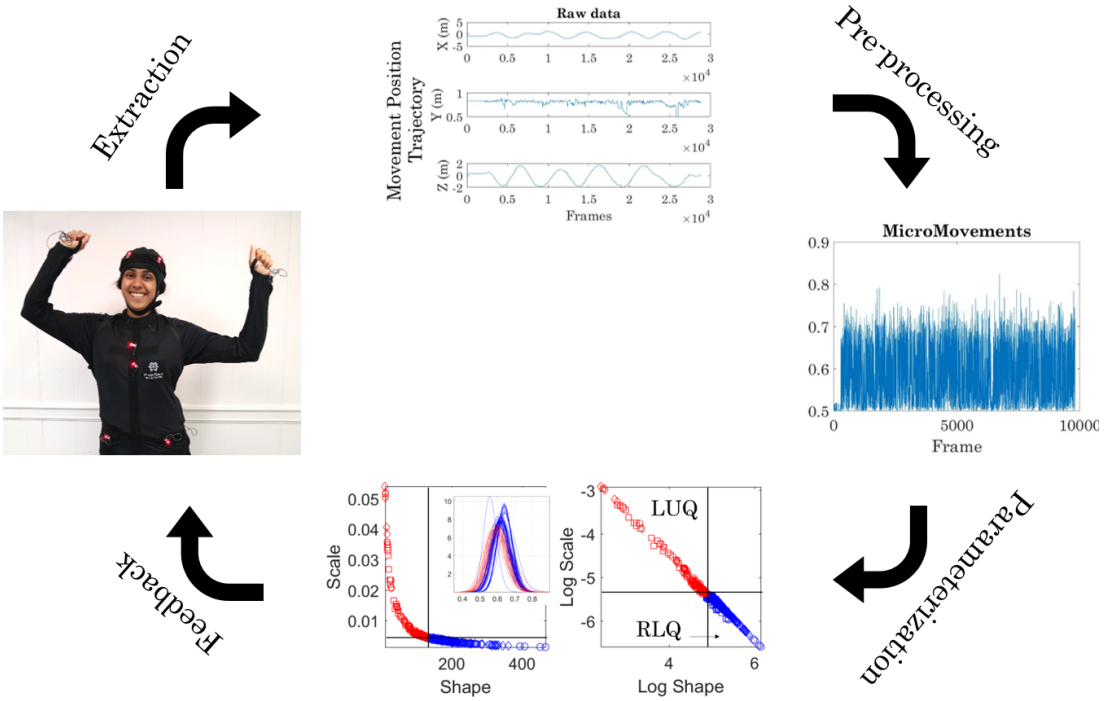

Figure 2.1: **Schematic of the loop of data extraction, pre-processing, parameterization, and feedback generation for the creation of the closed co-adaptive interface.**

Nowadays technology allows us to register a variety of kinematic parameters, such as position, linear and angular velocity and acceleration, as well as other bodily signals, some of which are brain waves, skin temperature, and heart rate. This technology enables the monitoring of physiological data non-invasively and in a high sampling rate. Their accuracy, wireless capability, long-lasting battery, and their lightweight structure that does not

interfere with human movement is ideal for tracking these kinematic signals under any daily performed tasks, from reaching and grasping to dancing. Moreover, it allows us to study a variety of population, from individuals with motor difficulties to professional dancers and athletes. Indeed, all these features have open new horizons to conduct studies that are closer to tasks performed in daily life rather than the "sitting tasks" where subjects have to sit in a chair restricted by wires and other equipment limitations in order to perform a pointing task.

In this chapter, I present the population studied and the technology used for the various studies presented n this thesis. I describe the bodily signals I collected and the basic methods applied for data extraction and signal pre-processing. I explain the step-by-step building of micro-movement spikes, which is a unitless data type developed in Sensory-motor Integration Lab, the main methods, and visualization tools employed in all studies presented in the following chapters. Finally, I demonstrate differences between the traditional and my research approach.

2.1 Populations Studied

A variety of populations were studied for the purpose of the presenting thesis work. Specifically I examined clinical cases such Schizophrenia patients (Chapter 4) and college students with Asperger syndrome (Chapter 7), healthy individuals with no or limited daily exercise (Chapter 3), advanced level Latin dancers (Chapter 10), pre-professional ballet students (Chapter 5) and professional ballet dancers (Chapter 9). My research did not focus on examining a particular group of individuals but instead investigating the features and needs of a wide range populations.The information extracted from each group through my numerous studies contributed towards developing the closed loop interface (Chapter 10) which was the goal of this thesis.

All studies presented in this dissertation were approved by the Institutional Review

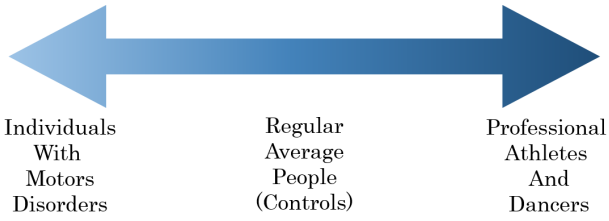

Figure 2.2: **Range of population studied. The was an emphasized interest in studying diverse populations.**

Table 2.1: **Specifications of the motion capture and wearable equipment used to record bodily signal**

Name	Type	Data	Freq.(Hz)	Company
Vicon System T160	Motion Capture	Position	120	Vicon
PhaseSapce	Motion Capture	Position	480	PhaseScape
Liberty	Motion Capture	Position	240	Polhemus
ENOBIO 32 NE006	EEG	EEG Heart Rate	500	Neuroelectronics
OPAL	Inertia Measurement Units	Orientation Ang. Accel. Linear Accel. Temperature	128	APDM

Board of Rutgers University, in compliance with the Helsinki act, and all participants had agreed and signed the related consent forms.

2.2 Motion Recording Technology and Wearables

For this thesis, I experimented with a variety of wearable devices and motion capture systems. The reason being, that we were curious to examine the different features and capabilities of each piece and investigate in real life their advantages and disadvantages.

2.2.1 Movement

Two motion capture systems, Vison and PhaseSpace, and the wearable sensors Opal of APDM (Fig. 2.3) were employed for recording movement.

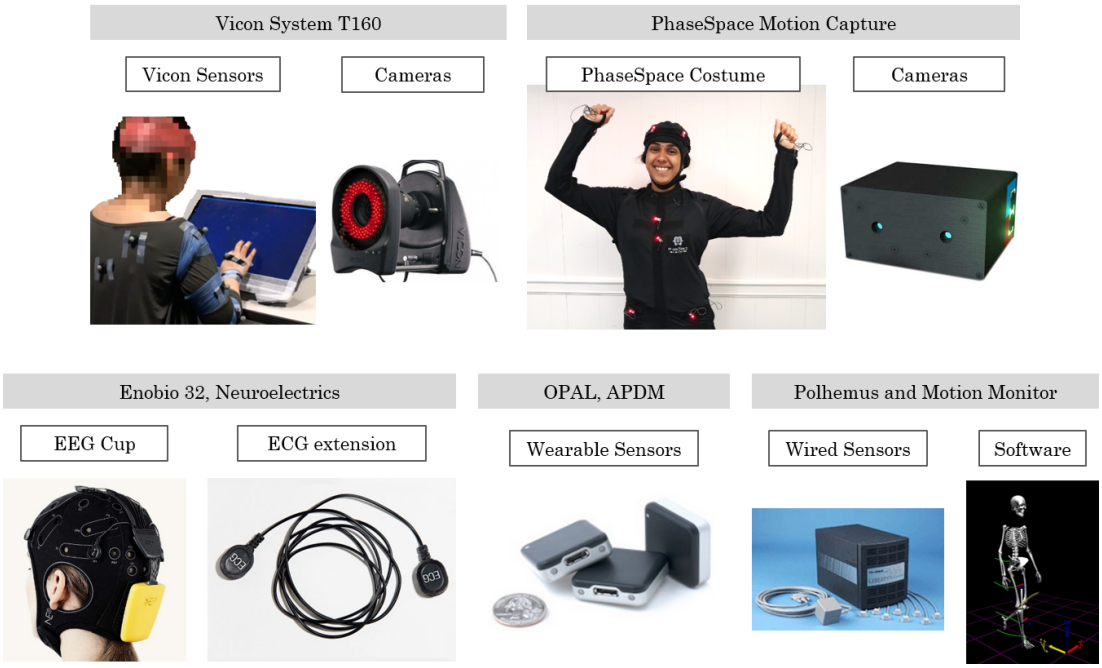

Figure 2.3: **Equipment used for monitoring and registration of the various bodily signals studied. The specifications of the features of these equipments are listed in Table 2.1**

The Phase Space Impulse (San Leandro, CA) was used along with a 38 active LEDs wearable body and head suit. The Vicon system (Denver, CO) is an infrared (IR) based system which is set along with IR reflecting markers. In the single study we utilized this equipment I used a total of 9 markers. Both motion capture systems register 3D position data of each sensor I used. That information could be used to estimate linear speed and acceleration. However, my lab houses a newer version of the PhaseSpace system which has a better sampling rate, 480Hz, compared to the housed Vicon system, 120Hz, and allows the estimation and streaming of the participant's skeleton data in real time. This was done through the Recap Software of PhaseSpace system (Fig. 2.4) and includes the position (not just sensor position) and orientation of 22 human bones in total. From the orientation, I could then estimate the angular fluctuation, velocity, and acceleration.

In contrast, Opal (Portland, OR) sensors were Inertia Measurement Units (IMUs) that

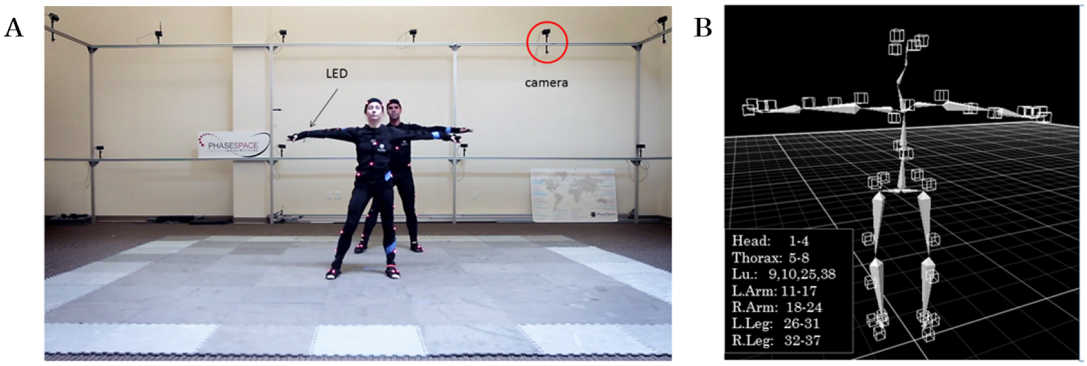

Figure 2.4: **Generating a body skeleton on the Recap software of the PhaseSpace System**

would not record any position data, but angular and linear acceleration, angular velocity, orientation, gyroscope, and temperature among others. These are wearable devices that could be used outdoors without putting the participant into any spatial restrictions. Whereas, the motion capture systems have the restriction that they can only be used in the space where the cameras are set (Fig.2.4.A). The recordings of the IMU's was continuous and synchronous across all sensors (up to 12 sensors could be used at once) and they could record up to 12 hours of battery life. The data is directly saved on the monitor's memory (8 GB) under robust synchronized logging mode with no data loss.

2.2.2 Temperature

Opal sensors have the extra feature that along with the kinematic data can also record skin temperature too. This is a feature that enabled us to study the human movement as a function of temperature and, therefore, build a new data structure that empowers us to see how each degree range affects the quality of movement, Chapter 5 5.

2.2.3 Heart Rate

A 32-channel EEG system, Enobio NeuroElectrics (500Hz, Barcelona, Spain), was used to record brain activity as well as HR using the ECG cable extension (Fig 3B) which was

placed below the participant's left ribcage (Fig 2.3). Due to time restriction, I didn't analyze any brain data for the purpose of my doctorate thesis. Therefore, I only presented ECG data in this work, which have revealed precious information for the co-adaptation of our sensory-motor system as it is going to be shown in Chapter 10.

2.3 Signal Extraction and Pre-Processing

2.3.1 Position Data from Motion Capture Systems

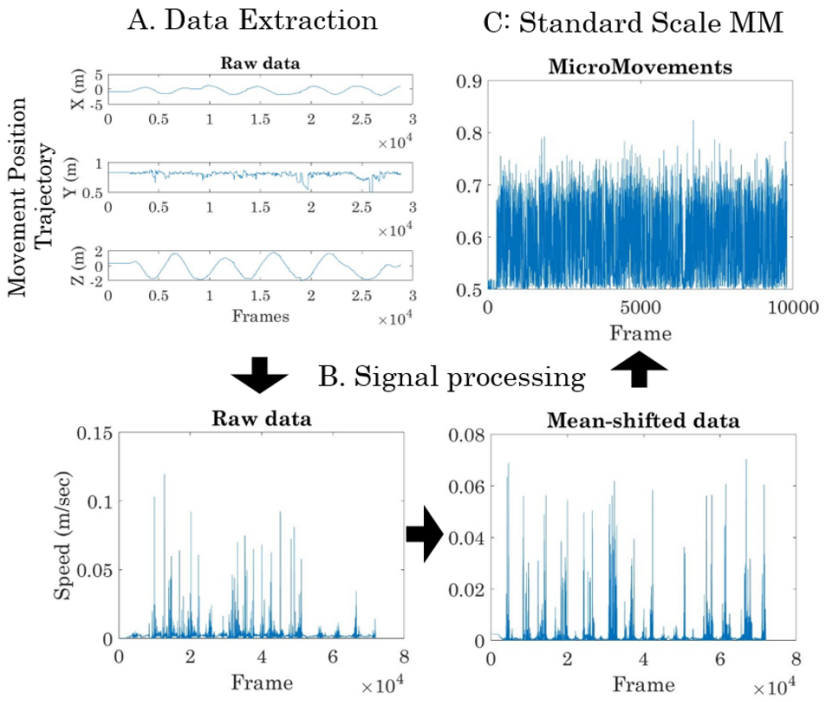

Figure 2.5: **Data extraction, signal processing and design of spike trains as input to a Gamma process for determination of NSR and predictability.**

Both motion capture systems, Vicon and PhaseSpace, were registering the triaxial vector $(x1, x2, x3)$ of the position data (Fig. 2.5.A). The 3D trajectories were already fully constructed when exported for the corresponding software tool of each equipment, hence no interpolation algorithms were applied to the data.

The speed profiles of each trajectory were estimated as the norm of the difference of the position between two continuous frames:

$$\tilde{v} = \sqrt{\sum (x_n - x_{n-1})} \tag{2.1}$$

where n the current frame and x the $3x1$ position vector at the current frame.

Next, the speed profiles were smoothed with a parameter $a = 0.01$. If a was set otherwise, the new value will be stated in the text of the corresponding work presented below.

The linear speed data were then mean-shifted:

$$\tilde{v}_{mean-shifted} = |\tilde{v} - \mu| \tag{2.2}$$

and the maximal deviations from the mean obtained, Fig2.5.B.

2.3.2 Speed and Acceleration from IMU's

Calibrated orientation (quaternions), and acceleration data (m/s^2) were exported from the IMU, using the APDM interface Motion Studio. The time series of angular velocity were extracted from the exported orientation data. The rotation data, parameterized by quaternions, were then converted to Euler angles and used to visualize the traces. The tri-axial velocity field was used to obtain at each point the instantaneous angular speed. Figure 2.6B shows a representative time series of the x-component of a velocity and acceleration trace. The corresponding temporal profile of the angular speed and acceleration for a session is shown in Figure 2.6C.

To convert from the velocity traces (v_x, v_y, v_z) to the scalar speed, we used the Euclidean norm:

$$\tilde{v} = \sqrt{v_x^2 + v_y^2 + v_z^2} \tag{2.3}$$

The time series of angular speed were cropped using the triggers' signals that the IMU sensor's actuator time stamped in the raw data on a third sensor that the experimenter held as the participant initiated and ended each trial (red dots in Figure2.6B).

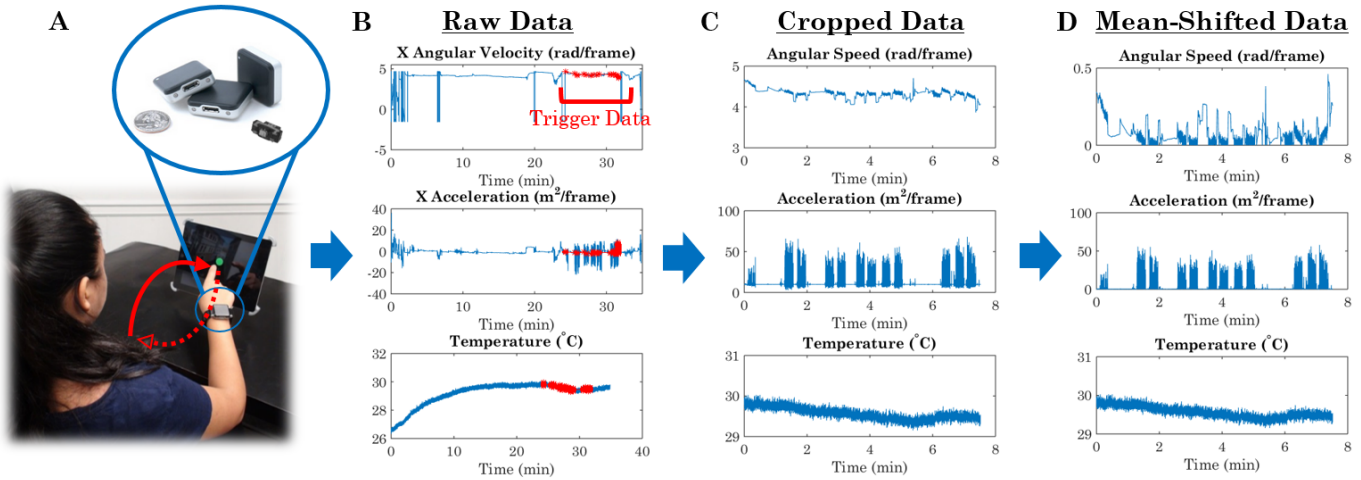

Figure 2.6: Data extraction from the APDM equipment. From the continuous recording of the data (on this figure I demonstrate temperature, angular velocity, and linear acceleration in X axis), I exported only the data labeled by the trigger (red stars on Figure B). Then I estimated the deviation from the mean. (A) Participant is pointing at the dot on the screen and wearing the sensor on the wrist. Arrows mark the flow of hand motions (to and from the green dot target on the touch-screen. The OPAL sensors and button to trigger the epochs of the experiment and time stamp the data are that a shown in the inset. (B) Raw traces from the sensor marked by the trigger from the start to the end of each 15-second block of trials (red). From top to bottom, velocity X-axis, acceleration X-axis, and temperature. (C) Zooming in the cropped data as delineated by the triggered time-stamps. (D) Mean-centered traces (top and middle panels are velocity and acceleration). No centering was applied to the temperature data.

The angular speed and acceleration data were then mean-shifted following Equation 2.2 and the maximal deviations from the mean obtained for the angular speed and acceleration. Samples representing the mean shifted angular speed and acceleration data for a control and patient participants are shown in 2.6D (no mean centering was applied to the temperature data).

2.3.3 Temperature

Calibrated temperature (°C) were exported from the IMU, using the APDM interface Motion Studio.

A sample of temperature data are plotted in Figure 2.6B bottom panel. Note that there is an adaptation period till the trace became stable. This period started from the moment the sensor was attached to the participant's wrist until the start of pointing experiment. During that time period the participant read and signed the consent forms, and the setup of the experiment took place. The button presses to mark the initiation of the pointing experiments also marked the temperature steady-state (Figure 2.6A button).

The temperature data were nor smoothed neither mean-shifted, as I did for the kinematic data.

2.3.4 ECG Data

A typical ECG data includes a set of QRS complexes, and detecting R-peaks (within the QRS complex) is essential, as the HR metrics used in this study focuses on the amplitude of the R peaks. To remove any baseline wandering and to accurately detect the R-peaks, ECG data were preprocessed using the Butterworth IIR band-pass filter for 5-30Hz at 2nd order. The range of the band-pass filter was selected based on the finding that a QRS complex is present in the frequency range of 5-30Hz. Then the signal was mean-shifted, similarly to the kinematic data, see Fig. 2.7.

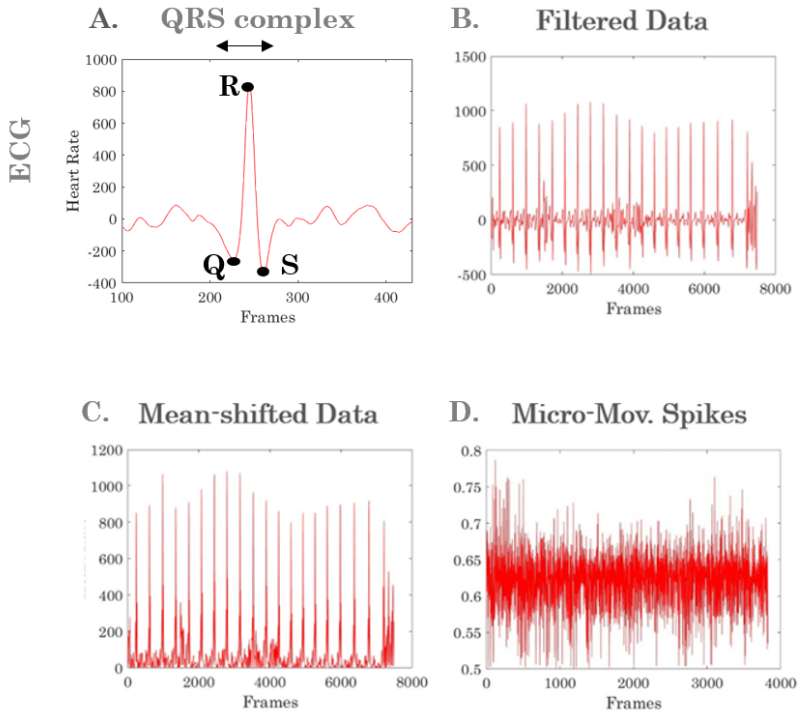

Figure 2.7: **ECG data extraction, pre-processing and micro-movement estimation. The pipeline of analyses to create the micro-movements spike train. Data is filtered and mean shifted to retain fluctuations away from the empirically estimated mean (Gamma mean in this case fitted well the peak distributions).**

2.3.5 Audio Signal

Another signal that I analyzed and processed is the audio signal, music songs, that was played to the participants of my studies presented in Chapters 7 and 10. On these data, I did not apply any filtering, since I did not record them and hence there was no instrumentation noise. As a result, the only pre-processing that was applied to these data was the mean-shifting utilizing Equation 2.2, Fig. 2.8.A and B.

2.4 Micro-Movements Spike Trains

The trajectories of the mean-shifted bodily signals (kinematic data, ECG, and audio, not temperature) were then converted to time-series of bodily parameters (Fig. 2.5.C, 2.7.D, and 2.8.C respectively) and their overall mean was empirically determined using maximum

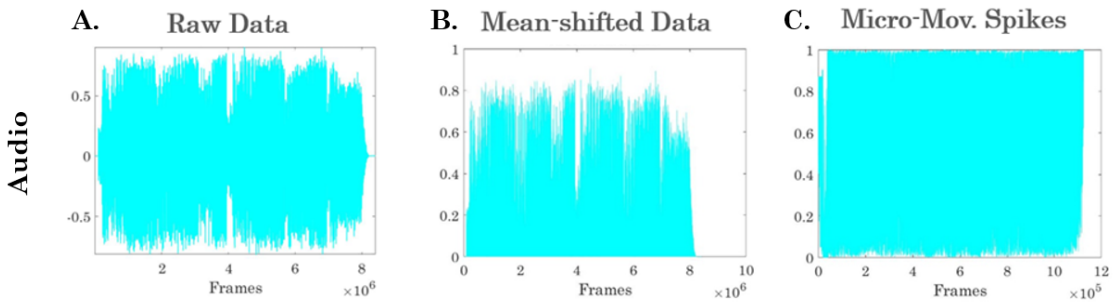

Figure 2.8: **Audio data pre-processing and micro-movement estimation. Data is filtered and mean shifted to retain fluctuations away from the empirically estimated mean (Gamma mean in this case fitted well the peak distributions).**

likelihood estimation (MLE) to select the best continuous family of probability distribution functions (PDF) that fit the frequency histograms of their peaks.

The Gamma family was the best fit (Equation 2.4). A random variable X that is Gamma distributed with shape a and scale b is denoted by $X \tilde{} \Gamma(a,b) = Gamma(a,b)$ with probability density function:

$$f(x,a,b) = \frac{x^{a-1}e^{-x/b}}{b^a \Gamma(a)}, \text{ for } x > 0 \text{ and } a,b > 0 \tag{2.4}$$

The Gamma mean $\mu = ab$ and the variance $\sigma = ab^2$ with the noise to signal ratio $NSR = \frac{\sigma}{\mu} = b$, the scale parameter.

The Gamma mean was then used to mean shift the data (as already explained with Equation 2.2) and focus on the absolute value of the fluctuations away from the mean as the data stream (Fig.2.5.B, 2.7.C, and 2.8.B). The peaks of these fluctuation data stream (Fig. 2.9.B) were converted to spike trains by normalizing the data using Equation 2.5:

$$NormalizedPeak = \frac{LocalPeak}{LocalPeak + LocalAverage_{min-to-min}} \tag{2.5}$$

Unlike cortical spike trains using binary representations, the one introduced here is real-number continuous in the range [0,1]. I have coined this new standardized spike trains (the

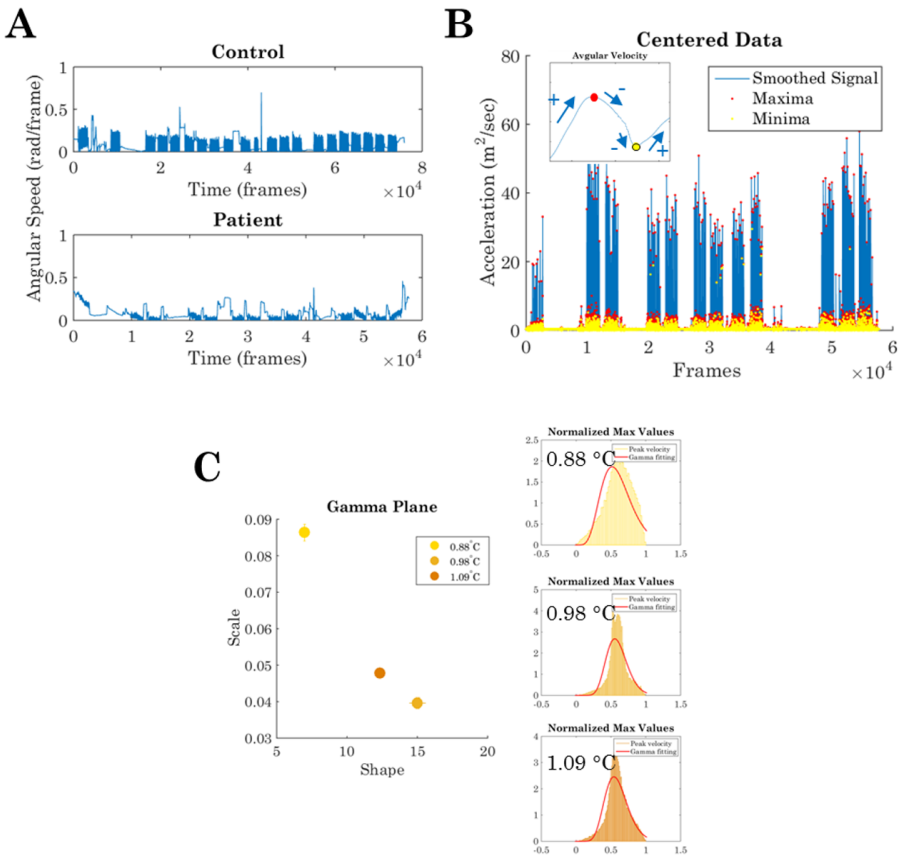

Figure 2.9: **Estimating the micro-movement spikes of an angular speed trajectory. (A) Mean-centered raw angular speed from control and a patient. (B) Mean-centered acceleration data from the patient marking the minima (yellow) and maxima values (red) speed profile as the algorithm detected changes in the slope of the curve (see inset and text). (C) Sample frequency histograms of the acceleration maximal deviations from the mean optimally binned for each sample participant and individual temperature range (i.e. from the minimum to the maximum temperature registered during that participant's session). The Gamma plane and 3 participants localized with 95% confidence intervals using the estimated shape and scale Gamma parameters using maximum likelihood estimation.**

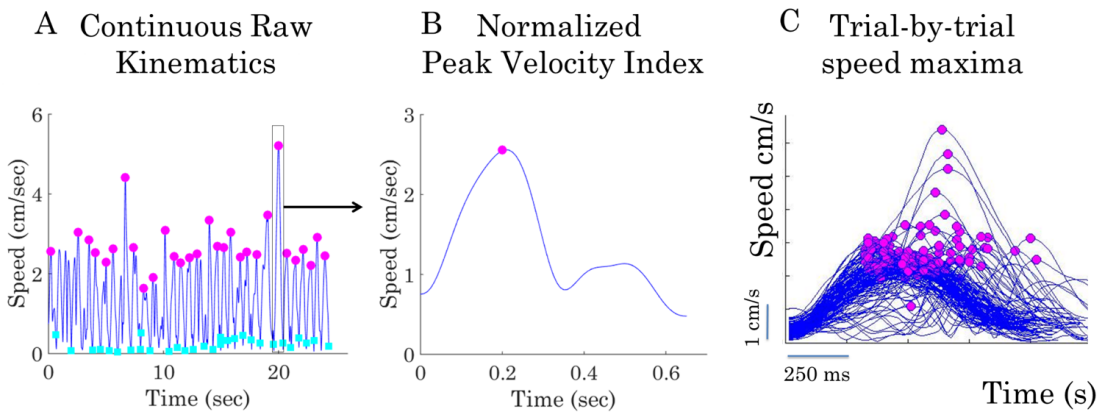

Figure 2.10: **Estimating the micro-movement spikes of an angular speed trajectory from trial-to-trial. The statistical estimation procedure. The raw kinematic data were exported from the interface of Vicon motion tracking system. These data were aligned with the 2D data recorded by the touch monitor and thus, segmentation of the data into trajectories from target to target was feasible. Each trajectory was described by the max velocity value (PV) and the max velocity index (time to PV), image B and C.**

micro-movements [93] [106] [100]) and used them across the various instrumentation signals presented in the previous section.

An exception is the study presented Chapter 3, where I consider peak the maximum value of the speed trajectory between two touches. To do that, I segment the speed trajectories (Fig. 2.10.B and C) from touch-to-touch and I normalize the maximal value of each trial. A further explanation of this analysis will be presented in Chapter 3.

2.5 Micro-Movement Spike Trains Represented by Continuous Gamma Process

The micro-movements spike stream from the real-time motions and audio-visual inputs was represented as a continuous random process under the general rubric of Poisson Random Processes (commonly used in electrophysiology for the analyses of cortical spike trains.). In some studies,

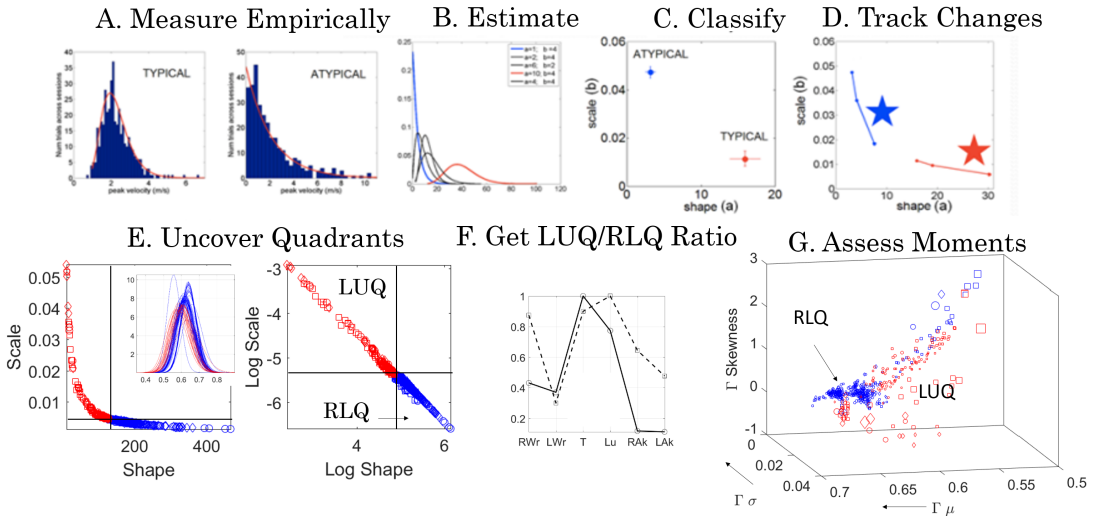

Figure 2.11: **The pipeline of micro-movements spike trains analyses using a Gamma process, tracking the NSR, estimation of the rate of change of stochastic transitions and the four-moments visualization.**

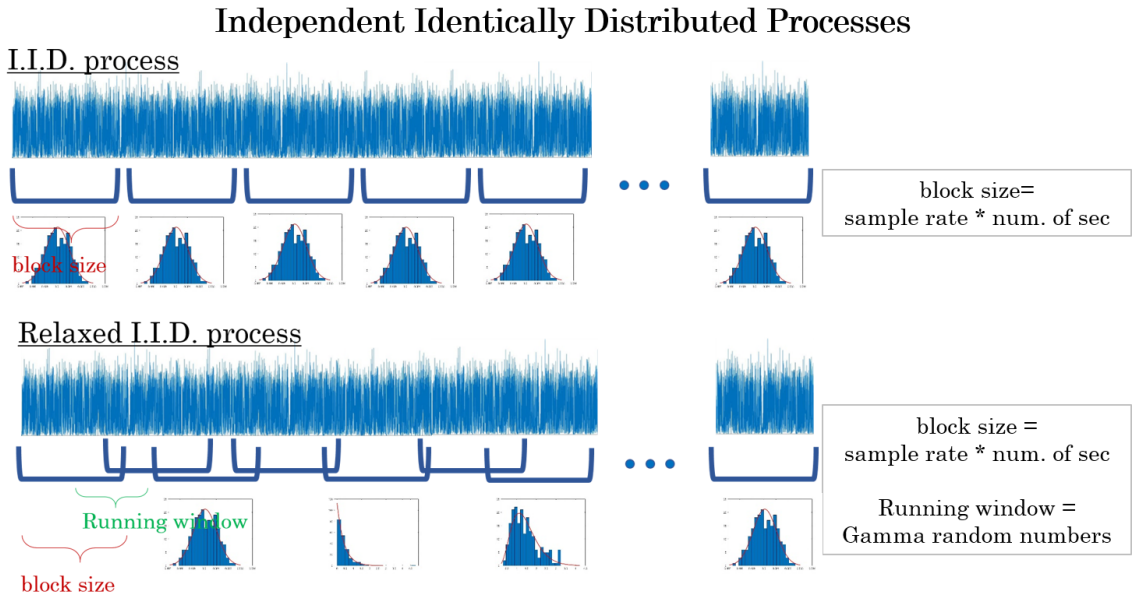

Figure 2.12: **Schematic of the regular Independent Identically Distributed Processes (IID) and the Relaxed Independent Identically Distributed Processes**

In some studies, I adopted a continuous Gamma process to represent continuously processed blocks of these fluctuations using an independent identically distributed (IID), where the size of the block size is equal to $samplingRate * numSeconds$,Fig. 2.12). While in other studies, I adopted a relaxed IID assumption, whereby overlapping running windows of micro-movements were taken with a block size of $samplingRate * numSeconds$ with overlapping sliding window equal to a random Gamma value (generated by the shape and scale values describing the distribution of the data) times the sampling rate of the data,Fig. 2.12). These block sizes ensured enough peaks to perform MLE with tight confidence regions (95%) for each estimated distribution parameter. Figure 2.11.A shows different cases of frequency histograms one may encounter in atypical and typical participants, while Figure 2.11.B shows different PDFs fitting the histograms (colors correspond to Exponential fit with shape parameter 1 (atypical) and typical skewed distribution). Figure 2.11.C shows the corresponding estimated points represented on the Gamma parameter plane with 95% confidence intervals and Figure 2.11.D track changes as the signatures shift with different rates for each participant, across different conditions.

The continuous Gamma family fits the data well and was used to estimate the shape and scale parameters and build stochastic trajectories represented on the Gamma parameter plane (Fig. 2.11.E) with inset showing the estimated PDFs color codes by quadrants in this case. This trajectory included all bodily sensors.

2.5.1 Noise-to-Signal Ration

The next step is to obtain the noise-to-signal ratio (the Fano Factor [21]), which in the case of the continuous Gamma family of probability distributions is given by the b-scale parameter as the ratio of the variance divided by the mean for each window of data

$$FF = \frac{\sigma_s^2}{\mu_w} = \frac{ab^2}{ab} = b \tag{2.6}$$

In the thesis, I mainly refer to this parameter as noise.

2.5.2 Tracking NSR and Predictive Regimes

The median statistic was then used to separate points of the stochastic trajectory with low NSR and high symmetry, tending to the Gaussian limiting range of the Gamma family (located in the right lower quadrant RLQ) from points of high NSR and high skewness tending to the Exponential limiting range of the Gamma family, located in the left upper quadrant (LUQ). The Exponential is the special case where the shape parameter $a = 1$ and the memoryless, most random distribution captures the signature of input micro-movement spikes [73]. Previous empirically informed models have shown that nervous systems with pathologies are well-characterized by this Exponential case [93] [106]; typical populations are well-characterized by intermediate skewed ranges with variable NSR and athletes and performing artists with exquisite timing and coordination are well-characterized by the symmetric and low NSR cases [88] [93] [94] [97].

Larger values across the horizontal axis of the Gamma plane (i.e., shape axis) represents PDFs with more symmetry, with a variety of skewed distributions between the two extremes. We underscore that these statistical features are not theoretical. They have been characterized empirically across large cross-sections of the population involving hundreds [97] and thousands [99] of participants of different ages. Further, longitudinal studies have tracked the participants for weeks [41] [89] or months [98] [97] and provided the means to derive inferential value from these distribution parameter ranges represented on the Gamma parameters' plane.

This body of empirical studies have revealed that when the Gamma parameters representing the PDFs of the person's biorhythms have scale and shape parameters whose range steadily fall in the lower right quadrant (RLQ) of the Gamma parameter plane (low scale and high shape range), the person is healthy. In contrast, when the parameters localize the person steadily on the left upper quadrant LUQ (high scale and low shape), the person is

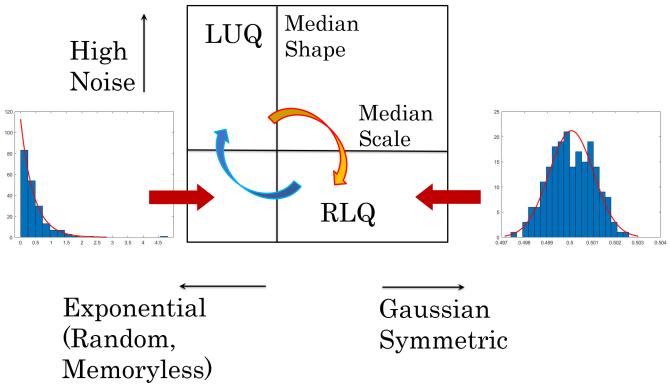

Figure 2.13: **Empirically informed interpretation of the Gamma parameter plane to further help statistical inference of the LUQ/RLQ ratio metric.**

unhealthy. Further, these parameters follow stochastic trajectories that oscillate between these Gamma parameter locations and the frequency and amplitudes of these stochastic shifts also bear information about the development of neuro-motor control (e.g. indexes denoting lack of development in neonates [100] or indexes denoting proper adaptive learning in athletes [104].

The ratio of the number of points in the LUQ/RLQ (defined by the number of points in each quadrant) provides information about the NSR and Predictability. For example, Figure 2.11.F shows differences between two ratios computed for each of 6 body parts. In this hypothetical scenario, all values are below 1 indicating a prevalence of points in the RLQ. If the value of this ratio is above 1 there is higher NSR and lower predictability than if the ratio is below 1.

2.5.3 Four Moments: Mean, Variance, Skewness, and Kurtosis

The four moments of the Gamma family of distributions are the Gamma mean, variance, skewness, and kurtosis.The Gamma means and variances are obtained using the empirically estimated shape and scale parameters. The variance $\sigma^2 = ab^2$ and the mean $\mu = ab$. The

skewness and kurtosis are defined as:

$$skewness = \frac{\sum_{i=1}^{N}(Yi - \tilde{Y})^3/N}{s^3} \tag{2.7}$$

$$kurtosis = \frac{\sum_{i=1}^{N}(Yi - \tilde{Y})^4/N}{s^4} - 3 \tag{2.8}$$

Here 0-skewness identifies symmetric shapes (e.g. the Gaussian distribution) and positive skewness identifies distributions with a leftward density. We use excess kurtosis whereby 3 is subtracted from the kurtosis value to denote Gaussian ranges (the Gaussian kurtosis is 3). Positive kurtosis indicates super-Gaussian (peaked) distributions whereas negative kurtosis identifies sub-Gaussian (flatter distributions).

Figure 2.11.G demonstrates a plot of the four moments points are colored as before but this time they are plotted along the Gamma mean (x-axis); the Gamma variance (y-axis); the Gamma skewness (z-axis) and the Gamma kurtosis (represented in the size of the marker). This visual tool helps us see the changes in variability across conditions and complement the Gamma plane analyses.

2.5.4 Rate of Change in Stochastic Transitions

The log-log representation of the plane is also shown in Fig.2.11E right panel whereby a line fitting $f(x) = nx^m$ captures the rate of change of these transitions (the rate of exponential decay along the linear scale) provides this information in the slope (exponent) which is negative in this case and intercept (scaling factor), along with fitting error (delta) measured by the projection of each point in the scatter to the fitting line of the log-log scale. Slopes with absolute values above 1 indicate a faster rate of change towards the RLQ. As such, desirable states to define preferences according to stochastic signatures are ratio below 1 and slopes above 1. Fig.2.13 shows empirically informed schematics of the

Gamma parameter plane and its quadrants.

2.6 The Traditional Approach of Kinematic Analysis

Up to this point, I presented the steps from data acquisition to micro-movement estimation to maintain the normalized fluctuations, scaled from 0 to 1, of the studied kinematic parameter as a deviation from the mean. Next I utilize Maximum Likelihood Estimation to determine the best family of distribution to characterize the data, Figure 2.14.

In contrast, in the field people average out the fluctuations of the signal, smoothing out the fluctuations of efferent output, which have been a great source of information based on our research [103] [93] [106] [97]. More specifically, currently researchers divide the signal into epochs under the theoretical assumption of Gaussian distribution. Then, they average it based on mean and standard deviation across the epochs smoothing out fluctuations. This way vital information underlying these fluctuations of the motor stream reflecting variations in sensory processing and integration with the motor outflow are thrown away. Moreover, the Gaussian assumption fails since the data are not distributed normally and the assumed Gaussian mean falls outside the ranges of the empirical data, Figure 2.15.

In our research, various studies [103] [93] [106] [60] [38] and [98] among other has shown that bio-signals are well described, based on Maximum Likelihood Estimation (MLE).

2.7 Conclusions

In this Chapter, I presented the populations and technology I employed for the studies presented in the following chapter. I described advantages and disadvantages of the various equipment and their specifications. I demonstrated the main methods applied in the studies that I are going to show in the following chapter. Overall, the purpose of this chapter was to prepare the reader for the tools and methods that are going to be employed in the upcoming studies.

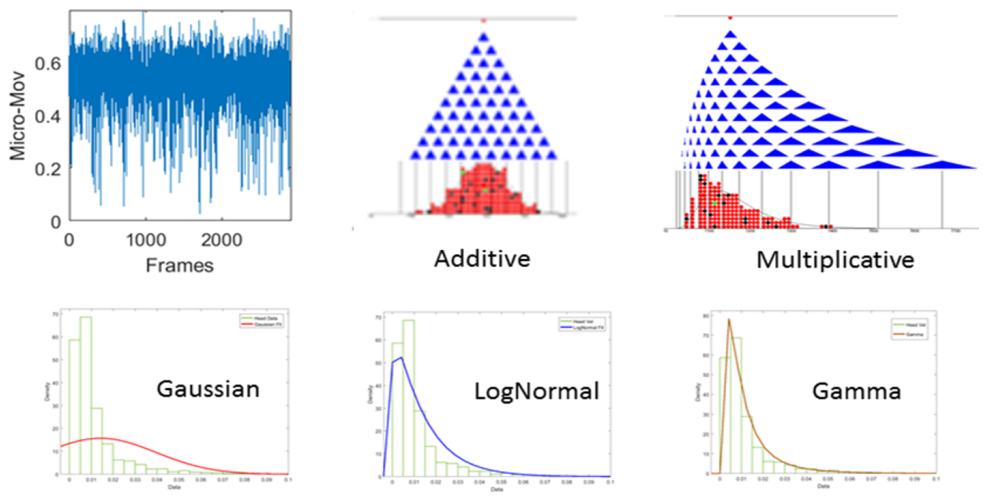

Figure 2.14: **Our approach of kinematic analysis. We built the micro-movements to maintain the normalized fluctuations as a deviation from the mean. Then, we use the MLE to determine what is the best family of distributions to characterize the data.**

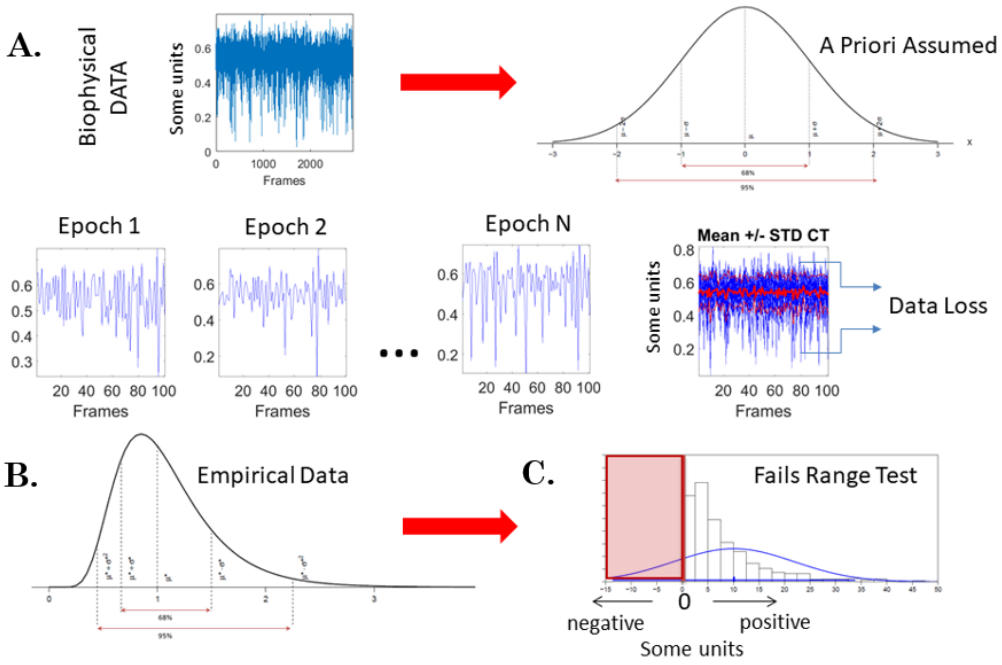

Figure 2.15: **The traditional approach of kinematic analysis. Grand Averaging of biophysical signals smooth out as noise the fluctuations of efferent motor output: a possible source of information about sensory and context preferences. (A) Continuous biophysical data analyzed under the theoretical assumption of Gaussian distribution is divided into epochs. Then parameter averages to summarize mean and standard deviation across these epochs smooth out important fluctuations of the motor stream reflecting variations in sensory processing and integration with the motor outflow. (B) The fluctuations are not normally distributed and (C) fail the range test whereby the assumed Gaussian mean (symmetric distribution) +/- 2 x standard deviation falls outside the ranges of the empirical data.**

Chapter 3

Learnability of Sensory Motor System: Studying Adaptation and Surprise

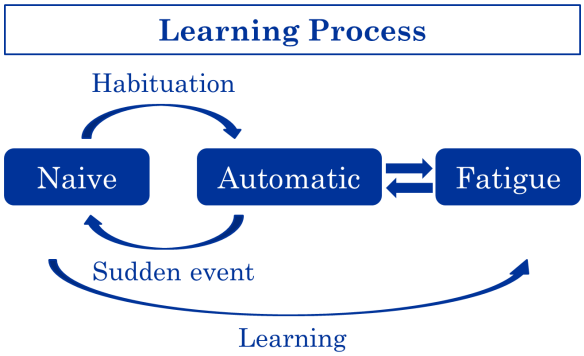

Figure 3.1: **Schematic of the learning process: At the beginning of learning people stand in "Naive" state. While they start learning through "Habituation", they shift to the "Automatic" state, where they are familiar with the environment and can automatically execute movements. Repeating the same task will eventually lead to the "Fatigue" state, as result of mental tiredness or muscular overuse. A negative factor of the learning process is the "Sudden events", which are distractive and cause backward shifts from "Automatic" to "Naive" state.**

The ability of human to learn is a topic that interests diverse fields from numerous points of view. From education to robotics a few of the questions that researchers try to address are how we learn, how repetition affect learning, what are the states of learning, what is the impact of fatigue in learning, among others.

In this chapter, I study the learnability of motor-control. Particularly, I explore the effect of repetition and spontaneity in motor learning. Moreover, I study how these factors can be impacted by the simplicity versus complexity of the routine, and how fatigue can be distinguished in the evolution of the interaction. Finally, in this chapter, I present our

metrics and the formulation of the data in order to achieve the desired study. This chapter presents my first study in SMILab which opened the path on studying the pattern of human motion and started building up the idea towards developing a co-adaptive interface [38].

3.1 Characterizing Habituation, Learning and Fatigue in Interactive 3D Movements

Human movement trajectories contain various information about the quality and purpose of the movement [88] [86] [93]. Particularly, natural behaviors contain small trial-by-trial variations in movement. These variations are fluctuations in amplitude and/or timing of kinematics parameters that include, among others, the minima, the maxima and the time to reach the peaks velocity. Such micro-movements accumulate statistical evidence over the time scale of minutes and such information can be revealing of individualized performance quality. They describe ways in which a person learns, adapts, and fatigues during performance. They are susceptible to changes in the task context and can aid with the classification of movement that ranges from deliberate to highly automatic, as already explained in Chapter 2.

A fundamental advantage of studying human motion for extracting underlying information of interaction is that movements cannot lie. Instead, they hide "honest" information connected with our conscious and subconscious mind activity. Many fields rely on the honesty of body language. An example of this is criminal justice. This gives us the chance to escape from methods and techniques that use oral feedback for as a mean of human behavior evaluation and start relying on metrics that will use patterns and qualities of movement and as a way to study human behavior.

In this work, we utilized motion recording technology to register human kinematic data performed during the interaction with a generalized interface and study the individualized learning performance evolution of each subject. Particularly,we study features of learning such as exploration, repetition, habituation, fatigue and spontaneity. Figure 3.1, illustrates

the schema of the steps of the learning process that we examine in our experiment. We identify three states of motor learning:"Naive", "Automatic" and "Fatigue". Habituation is what helps people to shift from the "Naive" to the "Automatic" state. In contrast, sudden events work as a repressive factor and shift the learning factor back to the "Naive" state. In the presented schema, "sudden event" is used as an umbrella term for anything that can interrupt learning progress -visual stimuli, sudden thoughts, random sounds, unexpected obstacles and others. An extension of "Automatic" is the "Fatigue" state, which is caused only after several repetitions. Examining a general form of learning, we could say that fatigue may emerge after any state even before reaching the "Automatic" state. However, in our approach, motor fatigue occurs after several repetitions of the motor task and once the "Automatic" state has been attained, due to the simplicity of the task we examine.

3.2 Learning of Motor System

An aspect of significant importance in our work was the formulation and modeling of the problem in a way that would allow us to extract the desired information about learning and individualized learnability. In this section we describe the modeling, formulation, and the factors that are considered crucial for the study of the presented problem. Learning is an ability possessed by humans and animals; it is an act that occurs as result of habituation, classical conditioning, or as a result of more complex activities such as play; and it may occur consciously or without conscious awareness. For example, learning an interface, an application, a game, a system, or a virtual environment is a conscious process that is the result of experimentation and habituation. But, looking deep into the learning process we identified a variety of factors that affect it. Some of the factors that we explore in this study are repetition, habituation, simplicity, complexity, spontaneity and fatigue. As it is going to be explained some of them can impact learning in a constructive way and some other in a destructive way.

Repetition is one of the most important factors of learning and "repetition as the

mother of learning" holds true. For instance, the more used to a system people get the faster they interact with it; they feel more confident and their movements are more robust and clear. A very significant consequence of repetition is **habituation**. Specifically in motion tasks, habituation results in automatic movements or movements that tend to lie beneath our conscious awareness. In this work, we associated habituation with the advanced learning state named as automatic, Figure 3.1. **Simplicity** is another factor that works as a catalyst in the transition from naive learning to automatic. Indeed, the simpler the task is the faster the learning process gets, in contrast, **complexity** delays this process. Another factor which impacts negatively on learning is **spontaneity**. Usually during any learning process people are confronted with spontaneous events. By spontaneous events, we could refer to any events that may destruct our mind and/or motion, such as talks, spontaneous thoughts, the appearance of a visual trigger and others. However, in the presented study, by spontaneous events we refer to events that result in a different manner than the expected movement. These events are also called as sudden events in this paper. Finally, **fatigue** is the last factor that was studied. It can be either mental or motor; nevertheless, in the specifics work only the kinetic side of fatigue is examined. Kinetic fatigue emerges after passing the automatic state of learning (Figure 3.1). This is because it can be caused only after numerous repetitions of specific movements -which most likely have firstly led to the automatic state. Of course, some tasks are so complicated that cause fatigue only after few repetitions, which means that the user has not passed from the automatic state; however, we are not examining such complicated cases in this particular study.

Motion-capture technology helps us register the actual motion of the active body-part and analyze such behaviors of it. As it has been already explained, trajectories of the active body-parts could give us valuable information about the way a subject executes the task. Thus, we designed an experimental paradigm to study all aforementioned factors of learning using motion recording system. The design of this task is elaborately explained in the following section.

3.3 Methods and Procedures

3.3.1 Subjects

The experiment included 7 subjects of college level (18-28 years old, 4 females and 3 males). The study was approved by the Institutional Review Board of Rutgers University. All students signed the consent form approved by the IRB of Rutgers University, in compliance with the Helsinki act.

3.3.2 Experimental Paradigm

For the purpose of this experiment, an in-house developed Matlab application (Release 2012b, The MathWorks Inc., Natick, Massachusetts, United States) was utilized in order to enable interaction of the subjects with a touch-screen while performing a visually guided pointing task. The task required adapting to a series of experiments with increasing degree of complexity. Each experiment required touching a target immediately after it was presented on the screen. At the touch of the screen location the target disappeared and was immediately followed by the presentation of another target. The speed of the interaction was depended on the subject's touch, at the subject's comfortable pace, rather than being time-constrained by the experimenter.

The experiment consisted of 3 levels. Level 1 was a line between two points; level 2 was a triangle and level 3 a hexagon, Figures 3.2B, C, and D, respectively. Targets were presented in clockwise order. The level of complexity of the experiment was determined by the number of targets and the shape they formed (target trail), Appendix video 1.

Subjects were asked to sit in front of a 22 inches touch monitor (Dell) placed on a studying desk, Figure 3.2A. Their chair was put far enough from the monitor to execute full arm motion, but close enough to reach it without straightening their elbow. Then, the motion-tracking sensors were stabilized on the head, back, shoulder, upper and forearm, elbow and hand of the subjects. Once this step was complete, they were instructed to interact with

the target constantly until the end of the experimental level. Once the experimental level was over, they were allowed to take a short break, if needed, and then continue to the next level. All subjects started from the simplest level and continued to the more complex ones (Appendix video 1).

At the beginning of the experiment the subject did not know the shape of the target trail but only upon various repetitions of a full target-trail cycle the shape was obvious. As the subject became habituated to the target order along the trail, an unordered surprising target was appeared on a random position on the screen and at a random time. The appearance of this surprising target is called sudden event. Figures 3.2B-D shows samples of the three levels on the 2D touch-screen, including habitual target touches (blue dots), sudden event touches (green dots) and erroneous touches (red dots). By erroneous touches, we defined any touches happening in any area but the currently visible target; for example, they could be on a previous location (i.e. caused by interference from a habituated target).

The number of trail repetitions to be completed before a sudden event was generated using pseudorandom integers from a uniform discrete distribution with 3 and 7 as the minimum and maximum values of repeats. The locations of the sudden events were also generated in the same way, so as to be displayed within the screen size. After the completion of the sudden event, the task was repeated all over from the beginning. The total number of sudden events -task repetitions- was set to 15. The values of the minimum, maximum number of repetitions of the trail and that of the number of sudden events were chosen to be large enough to succeed at habituating the subjects but small enough to maintain the subjects' interest.

For all subjects, the recognition of the target trails was trivial. Only couple of repetition of the trail was enough for them to identify its shape. But, we set the minimum number of repetition equal to 3, so as to have more time to habituate targets' sequence and location, and the maximum number 7, to have a wider variety of numbers of repetition and make the sudden event as unexpected as possible. The total number of sudden events was chosen

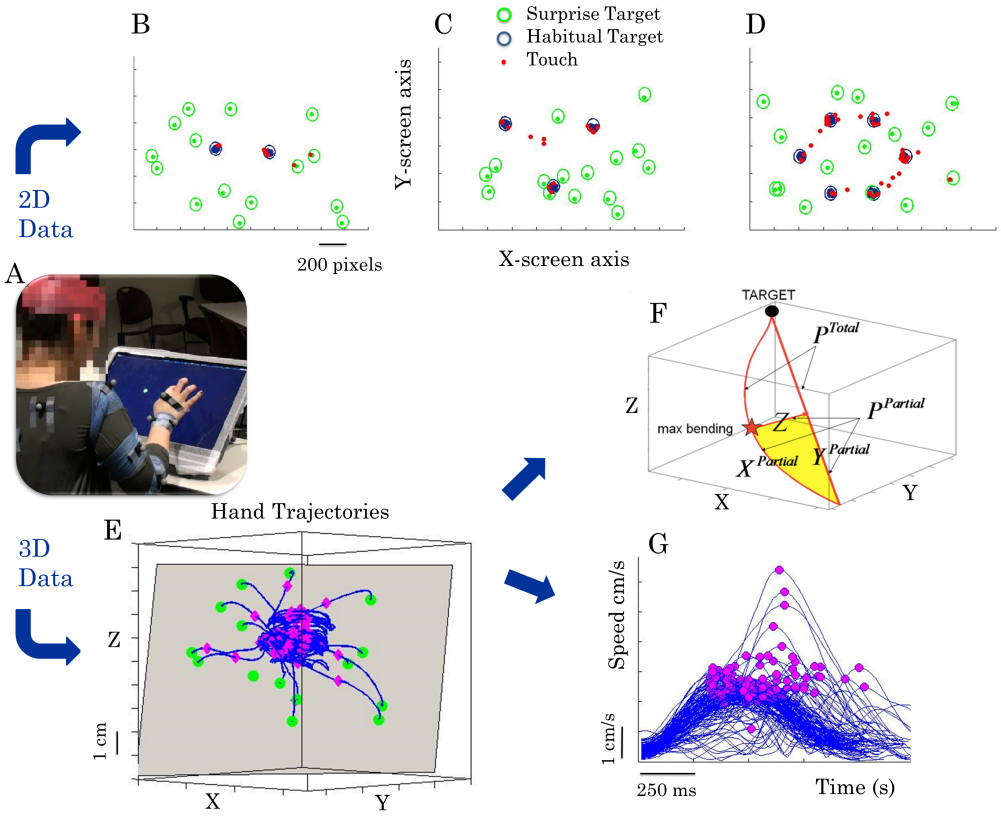

Figure 3.2: **A Vicon motion recording system was utilized for the data collection. Vicon sensors were placed across the right arm (image A). Extra emphasis was given in the area of the hand which data are mainly analyzed in this paper. In addition to the 3D trajectory data of the arm movement, the 2D data of the interaction with the touch monitor were collected. The touches (dots) as well as the target locations, marked as circles, of the three different complexity levels are demonstrated on images B-D, starting from the simplest to more complex level, respectively. The blue color corresponds to the actual regular targets, green color to sudden events, and red color to erroneous touches. Image E illustrates the trajectories -blue lines- of a subject for experimental level 1 (shown on image B) plotted with the actual screen position (grey plane); the green circles represent the regular and sudden-event targets and the magenta diamonds the point that max velocity occurred. On image G, the fluctuations in the velocity of each trajectory (3D hand movement between two targets) are displayed. The magenta dots represent the max velocity of the trajectories shown on image E. Image F demonstrates the graph of the ratio analysis of each trajectory. Each trajectory was re-sampled at equally spaced intervals. The points along the curve were projected on the Euclidean straight line joining the two ends of the trajectory. The max bending point was computed and the area enclosed between the line and the curve and stated as partial area. The partial area ratio is computed by the ratio of the partial area over the whole area enclosed between the line and the curve. The perimeter ratio was computed in a similar way.**

to be 15 for collecting sufficient data for analyses, but also for maintaining the subjects' interest and attention on the experiment.

For collecting data, both the touch monitor, Dell (3ms delay), and the motion recording system, Vicon System T-Series T160 (120Hz) (Oxford, UK) were utilized, Figure 3.2A. We use a total of 9 infrared Vicon marker, places all over the arm, right-upper arm back, and head. However, for the purpose of this study, we only need the hand marker data. More specification for the equipment used can be found in Section 2.2.

Our Matlab application was designed to save the locations and presentation times of the targets, sudden events and corresponding touches on the monitor (including erroneous touches), labeled based on the target they aimed to. Figure 3.2E shows examples of 3D hand trajectories with relevant landmarks of speed maxima.

3.3.3 Analysis

The hand position data recorded during the sessions were exported through the interface of Vicon motion tracking system and they were plotted in Matlab, where all the processing and analysis of the data took place. From the plots of the raw 3D data, we visually located the first touch on the Monitor. Knowing the time of the first touch in Vicon 3D data and in the 2D data registered by the touch monitor, it was then feasible to align them and, as a consequence, to map all the trajectories that connect two continuous touches to the related touches, Figure 3.2E. Each of these trajectories was labeled as erroneous, sudden event or regular target trajectories, based on the type of target they aimed to reach.

The identity of a trajectory (path and label) was very crucial for answering questions that arose through this experimental setup, because it allowed us to group trajectories following different concepts and thus answer questions presented in Section 3.2.

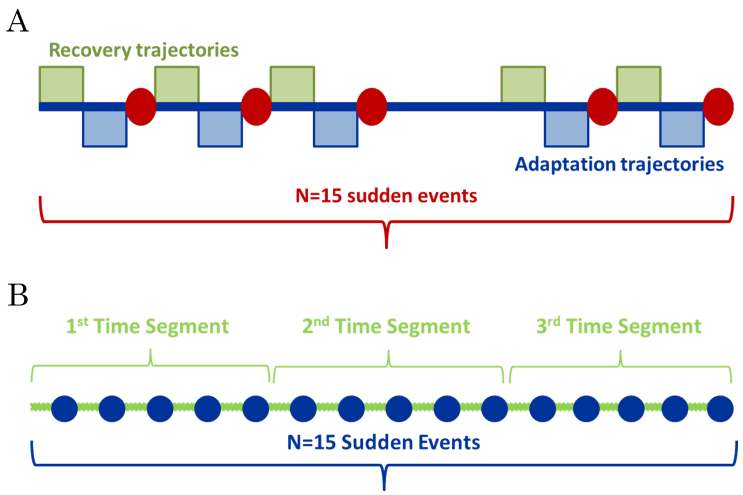

Figure 3.3: **Grouping schematics: Image A exhibits the schematic of the recovery-adaptation analyses. In this case, the trajectories between two sudden events (red dots) are divided into two groups. The first half of the trajectories is named Recovery -they take place right after a sudden event, so the subject tried to recover from it and turn back to habituation- and the second half of trajectories is called Adaptation -the subject has already recovered and is adapted back to the repetition of the regular targets selection. Image B illustrates the segmentation of an experimental level into 3 segments. Each segment included 5 sudden events and all the in-between trajectories. Thus, all the trajectories up to the 5th sudden event belong to the first segment, from 5th to 10th to the second segment and the last 5 as 3rd belong to the last segment. These 3 stages of learning process represent the beginning, intermediate and advanced learning.**

Data Formulation

To address the questions presented in Section 1 Factors of Learning in Interaction, three different concepts of grouping were made that are presented below:

- Complexity-level grouping: This formulation aims at the comparison and study of the differences between the three levels of complexity (Figure 3.2B-D). Complexity-level grouping assists on the examination of how complexity can affect the learning progress. For the Complexity-level Grouping, there were three groups based on the complexity first, second, and third experiment. However, within each group the data of the subjects were studied separately, in order to achieve an individualized examination of the problem. In this grouping, the data of each subject included all three types of trajectories (erroneous,

sudden event, and regular target trajectory), Figure 3.4A-C.

• Recovery-adaptation grouping: In this design, it is assumed that after a sudden event there is a recovery period followed by the adaptation period upon the moment a new sudden event will appear and the process will start all over again. Therefore, the trajectories were split into two groups: "Recovery" and "Adaptation". The recovery group included the first half of them, applying the assumption that they belong to the recovery period right after the first sudden event. The adaptation group included the rest of the trajectories up to the next sudden event. It is important to note that in this analysis the state of learning within each experimental level does not matter. What does matter is the state of recovery between two sudden events, Figure 3.3A. Through this design, it was feasible to examine behavioral differences in motion during the two periods and study the impact of sudden events in the learning process. In contradiction to the other two groupings, in the Recovery-adaptation Grouping the data of each individual at each level were cleaned by erroneous and sudden-event trajectories. Thus, only the regular-target trajectories were studied. In this formulation, there are three distinguished levels of study experimental levels- and within each level the two types of data, recovery and adaptation, of each individual were examined.

• Three-segments grouping: Each experimental level is split into 3 segments. Each of these segments includes equal number of sudden events (5 sudden events per segment) and all their trial repetition between those, Figure 3.3B. The three segments represent the beginning, intermediate, and advanced stage of learning that each subject experienced and thus they facilitated the exploration of the learning progress within each experimental level and differences across each of them. The three-segment grouping assisted on the inspection of the effect of repetition in habituation and the development of fatigue. Similarly to the two other groupings, the Three-segment Grouping also has three experimental levels and within each level three progression segments, beginning, intermediate, and advanced, for every individual. In this case, the segments include all types of trajectories.

Data Processing

In the context of pointing movements with visual guidance, this study explores the trial by trial variability of velocity-dependent parameters as the movement continuously unfolds as well as geometrical characteristics of the actual curve of the trajectory. The parameters that were used in this work are the maximum speed of the trajectories or peak velocity (PV), the time that this value is reached in/en route to the next target, the perimeter ratio and the area ratio, Figure 3.2E-G.

Peak Velocity and Time to Peak Velocity

In goal-directed movements, which in our case are movements from point to point, trajectories tend to have a single peak velocity value. In some cases though, where decision making or ambiguity is involved this may differentiate, Figure 2.10C. The values of the max velocity as well as the time to be reached are still rich in information that lie under patterns of motion variability such as motor learning strategies and adaptation [88] [93] [101].

For each trajectory of the examines group, we smooth our data (Section 2.3) and we estimate the micro-movement spikes from trial-to-trial (Section 2.4), Fig. 2.10. For each peak of the spikes, we also preserve the corresponding time which we name as time to peak velocity.

To normalize the time that the maximum velocity was reached, the percentage of this time out of the duration of the whole trajectory was computed as shown below.

$$t_{maxSpeed}(j) = \frac{t_{maxSpeed}(j)}{t_{total}(j)} \tag{3.1}$$

Perimeter and Area ratio

To assess the effects of task condition and target location on the curvature of the hand trajectory, the deviation of the hand trajectory from the Euclidean straight line was measured, as it was done in [Torres 2010]. For processing the data, a trajectory was re-sampled at

equally spaced intervals, in order to obtain a fine temporal partition. This step was necessary to treat the curve as a geometric object which is independent of its temporal profile. Then, the beginning and the end of the trajectory was connected with a straight line, Figure 3.2E. We obtained the point of maximum bending of the trajectory from the straight line or, in other words, the projection point with the largest distance from the trajectory to the line (star on Figure 3.2). Once this point was identified, the ratio of the partial perimeter over the perimeter of the whole trajectory was computed. In a similar way, the area ratio perimeter was computed, using the area instead of the perimeter. The perimeter ratio is defined as the quotient between the partial perimeter and the total perimeter given by the sum of the lengths of the hand path and the initial hand position to the target line (see Equation 3). The partial perimeter is the summation of the path length and the length of the connecting line of the initial hand position and the target up to the point of the maximum bending.

$$R_{perimeter}(j) = \frac{P_{partial}(j)}{P_{total}(j)} \tag{3.2}$$

where j is the trajectory that is currently examined.

Similarly, the area ratio is defined as a quotient between the partial area under the curve in the first portion of the movement, up to the point of maximum bending, and the total perimeter is given by the total area enclosed between the curve and the line (see Equation 4).

$$R_{area}(j) = \frac{A_{partial}(j)}{A_{total}(j)} \tag{3.3}$$

where j is the trajectory that is currently examined.

Gamma Probability Distribution

We, then, estimate the stochastic signatures of the Gamma distribution as presented in Section 2.5 and is demonstrated in Figure 2.10.

3.4 Results

3.4.1 Complexity Level Grouping

The results of the complexity-level grouping are shown in Figure 3.4. One of the first observations that can be made is that each subject has a different performance rate of normalized PV on each complexity level, see Figure 3.4A-C. For instance, subject 7 reports small improvement across levels. It starts with bad performance in Experiment 1 and shifts towards slight improvement up to Experiment 3. However, other subjects such as 3, 5, and 6 have their worst performance in Experiment 2 but their best one in Experiment 3. Also, a dissimilar case is subject 1, whose worse execution is in Experiment 3, see Figure 3.4A.

It should be noticed, though, that with subject 7 to be an outsider, there is a slip towards improvement (low-right corner of the plane), which is very distinct between Experiment 1 and 3. The mass of the group shifts to the lower right side of the panel. Also, it is significant that in experiment 3 there is not much deviation between subjects' values. Instead, the largest deviation between the subjects appears on Experiment 2.

Regardless of each single subject's shifts and the center of the gathering, it is significant that all normalized PV values are located on the same curve (Figure 3.5A). The fitting line parameters and statistics are presented on Table I and II. It is memorable that the RMSE value of the normalized PV is $3.358 * 10^{-4}$ proving how precisely all the values fit on the same curve. Moreover, based on the Kruskal Wallis results -which are shown on Table III-, the distribution of the mean, μ, values of each experiment come from significantly different distributions.

We obtained similar results with those of normalized PV for the percentage of time to

Table I. Fitting line parameters

	General Model	a	b
Norm. PV	ax^b	0.363 (0.2864, 04396)	-0.8888 (-0.9367, -0.8409)
Time to PV	ax^b	0.4654 (0.4281, 0.5026)	-0.8986 (-0.9911, -0.8061)

Table II. Fitting line statistsics

	SSE	rsquare	DFE	adjsquare	RMSE
Norm. PV	$2.003 * 10^{-6}$	0.9890	18	0.9884	$3.358 * 10^{-4}$
Time to PV	0.0094	0.9663	19	0.9645	0.0222

Table III. Kruskal Wallis

	Source	DF	Chi-sq	Prob. Chi-sq
Norm. PV	Column	2	5.66	0.0589
	Error	18	-	-
Time to PV	Column	2	5.73	0.057
	Error	18	-	-

PV. From the graphs exhibited in Figure 3.4D-F, it is not clear if there is a systematic improvement or worsening from experiment-to-experiment for each subject. However, the values do fit on the same line (the parameters of which are presented on Table I). What is significantly different in this case is that the percentage of time to PV has greater deviation from the fitting line. This is noticeable when on the mapping of μ and σ values (Figure 3.5D); and it can also be explained by the RMSE value, which is 0.0222 (Table II). Moreover and similarly to PV values, based on Kruskal Wallis test, the variance-samples, σ, of each experimental level come from significantly different distributions, Table III.

3.4.2 Recovery-Adaptation Grouping

In the recovery-adaptation grouping, there is a tendency of the adaptation shape-scale values to be placed more on the upper-left of the plane in relation to the respective shape-scale values of the recovery. This is a very distinguished feature of Experiment 1 (Figure 3.6) and it means -based on the characteristics of Gamma plane (Section 2.5)- that adaptation data are more random and than recovery data which tend to be symmetric and predictive. Thus,

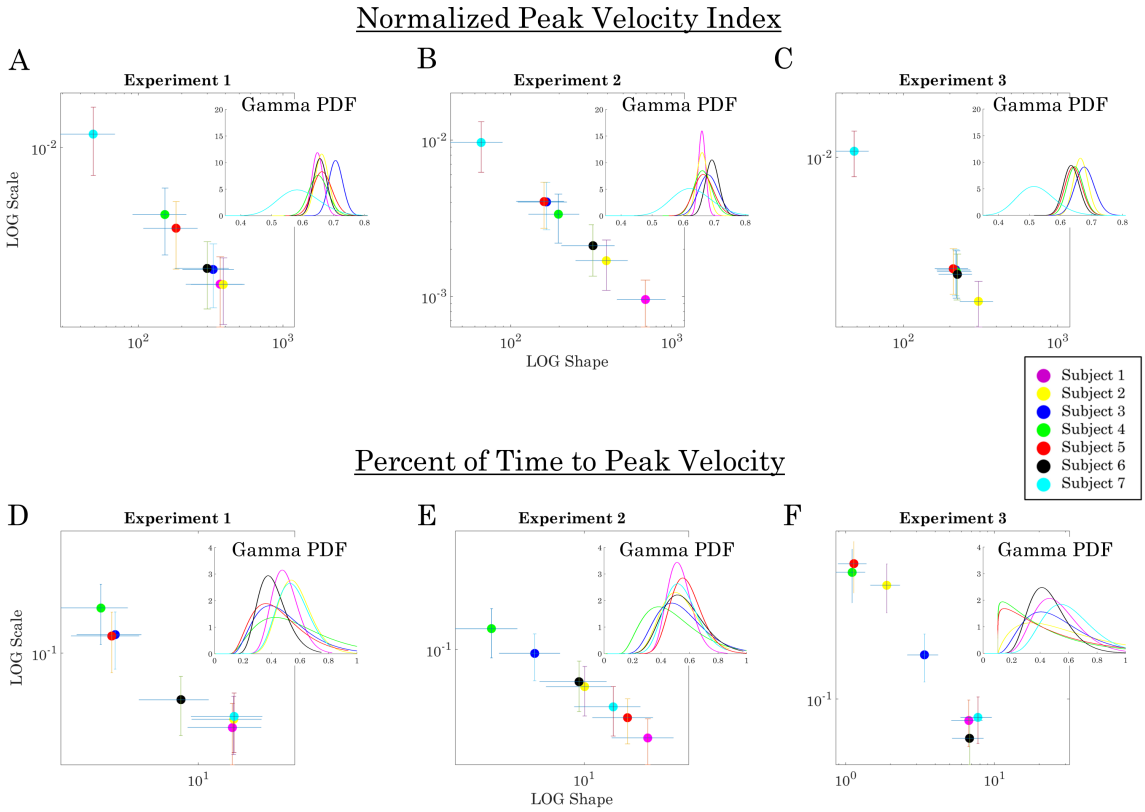

Figure 3.4: **The plane of Gamma distribution applied on complexity-level grouping plotted on log-scaled axes. Each column from left to right represents a different experimental, level from 1 to 3, respectively. The first row includes figures of the Gamma shape and scale parameters that describe the normalized maximum speed distribution of each subject and the second row includes the Gamma shape and scale parameters of the time to PV percentage. Each color denotes a different subject, as shown on the index on the right side of the figure. The color mapping from subject to color is consistent in all figures. Each sub-figure shows the curve of probability distribution function (PDF) of each corresponding case.**

this pattern could have led us to believe that there is not really a recovery and adaptation period, but instead there is a recovery and sudden-event-expectation period, which could explain why the second half of the grouping (currently called adaptation) give us points that are placed more on the upper-left side of the plane (trajectories with higher noise). Unfortunately, there is not enough evidence to support this, since in Experiment 2 and 3 this is not always the pattern that the data follow.

What remains distinguishable on the indexed figure for μ and σ values (Figure 3.6) is

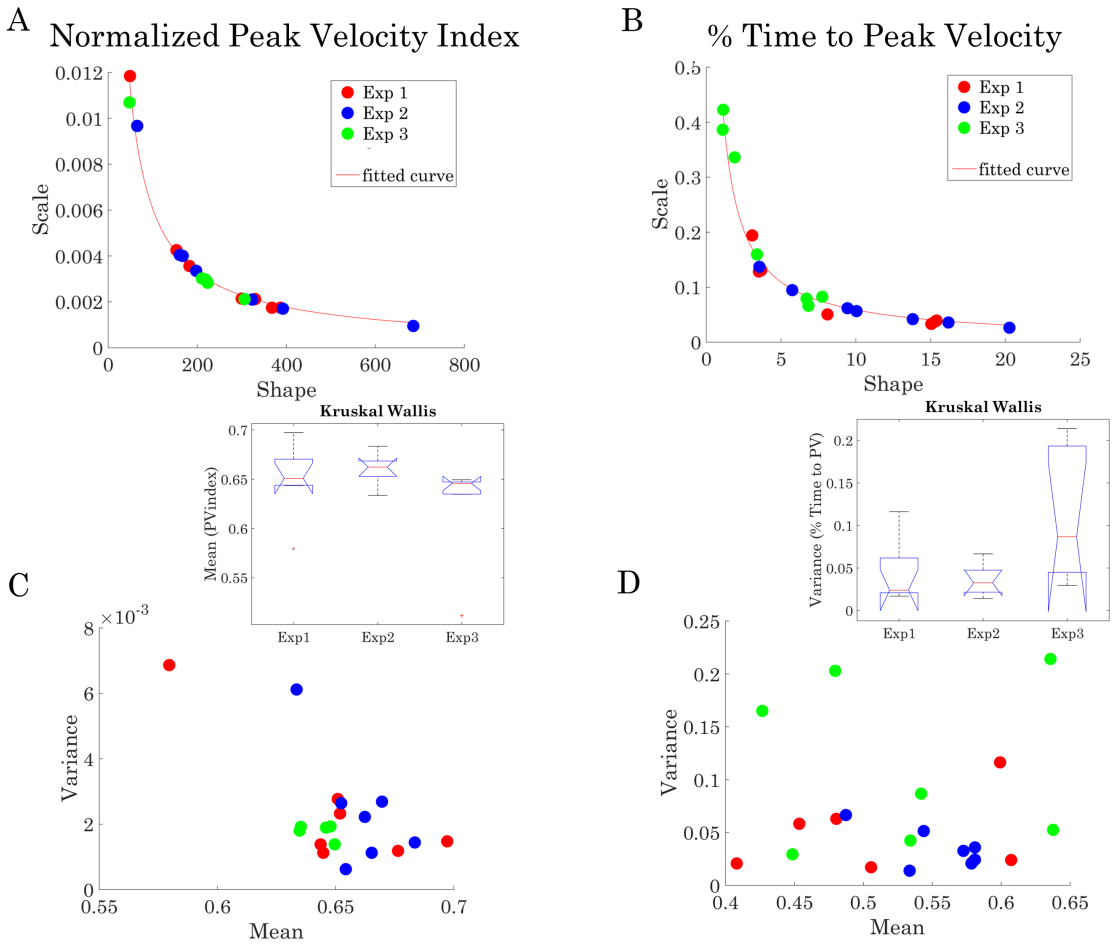

Figure 3.5: **In continuation of Figure 3.4, this figure presents a statistical analysis of PV index and the time to PV graphs across all experimental levels. The left column of graphs corresponds to PV index statistics and the right column corresponds to time to PV statistics. Images A and B illustrate the shape and scale parameters in linear-scaled x and y axes (in contrast on Figure 3.4, they are displayed in log scale) with their actual fitting curve. The parameters of the fitting curve are shown in Table I and II. In this Figure the individualized approach that is mainly presented in all figures has been waived. Thus, the Kruskal Wallis test, exhibited in the middle two figures, grouped the results of all subject based on the experimental level. It is remarkable, that based on this test the samples of (Normalized PV) and (percentage of time to PV) of each experimental level come from different distributions. On C and D images, it can be observed the mean and variance graphs of each column-related case. The numeric results of the test lie in Table III.**

the notable dissimilarity of recovery and adaptation data for each subject. The distance between the two data types -which is represented by a straight line on Figure 3.6- is quite noteworthy. Specifically, the distance is even bigger on the axis of mean values which is in the tens and not in the thousandths (case of variance). Moreover, it can be observed that the variant spreads of μ and σ values across the experiments and that the spread shrinks gradually from Experiment 1 to 3. It can be also noticed that most significant shrink happens in Experiment 3, where the cluster of μ and σ values shrinks and shifts appreciably towards left on the x-axis (mean) and towards the middle on y-axis (variance).

Another analysis that was applied to the recovery-adaptation data was the perimeter versus area ratio, which is shown in Figure 3.7A. On the area-perimeter ratio panel, we can note that the clusters overlap. But, we can get a better and clearer view of the density of each cluster from the histograms, which are located under and on the left of the area-perimeter ratio plane, and correspond to the area ratio and perimeter ratio, respectively. From the histograms, we can observe that each experiment has a very distinguished curvature. Also, within each experimental level the curves of recovery and adaptation data appear in the same form but with some differences on the peaks.

The dissimilarity between the curvatures of each experimental level could be explained by the fact that each level has its own shape of target-trail. Hence, the distances between targets vary, based on the shape, and as a result, the perimeter and area ratio values differentiate from experiment to experiment. However, the differences between the recovery and adaptation curvatures within the same experimental level do not occur due to shape variability. Instead, they revealed different execution patterns of the same target-trail shape that is caused due to the recovery from a sudden event and preparation for it.

To examine in detail what happens within each cluster we obtained, the polynomial $P(x)$ of degree $N = 1$ that fits the area and perimeter ratio data of each subject for each experimental level. Then, we estimate the standard deviation of the error in predicting a future observation of area ratio by $P(x)$. The results of these plots are shown in Figure

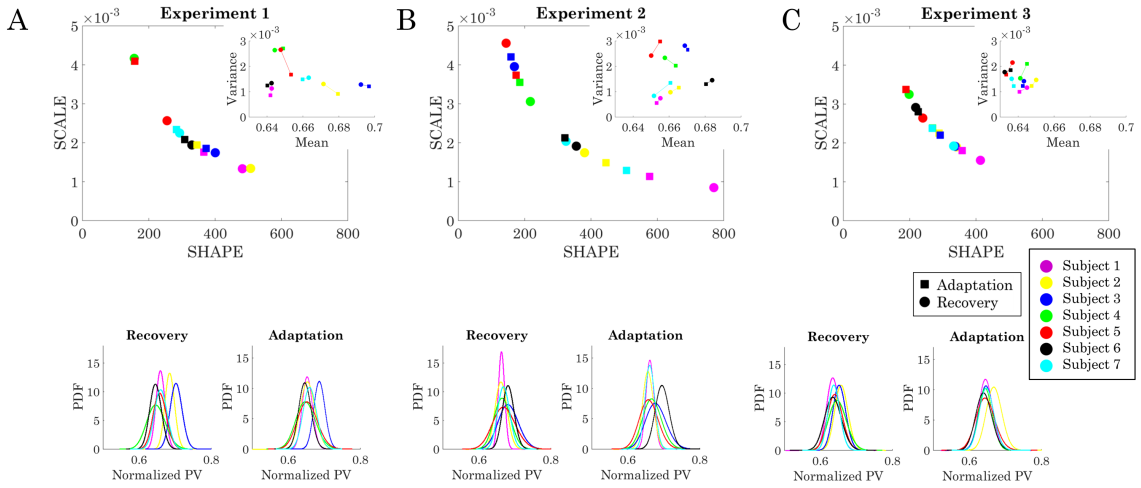

Figure 3.6: **The plane of Gamma distribution applied on recovery-adaptation grouping. The first row shows the Gamma shape and scale parameters that describe the normalized maximum speed distribution of each subject over the experimental case. The sub-figures are plots of the mean and variance of the corresponding cases. In the second row, the PDF of recovery and adaptation of the matched level are exhibited. From left to right each column agrees with an experimental level from 1 to 3, respectively.**

3.7B. It is noticeable, that, regardless the experimental level, we get significantly different results for recovery and adaptation data.

3.4.3 Three Segments Grouping

The last analysis was done on three segments grouping. On the Gama distribution plane, which is shown in Figure 3.3.A-C, we can notice that each subject has its own pattern of learning. Some subjects perform progressively better (Experiment 3 subject 5), others progressively worse (Experiment 3, subjects 1, 2, 4, 6 and 7). The reason for the latter case may be caused because of fatigue. Most of the subjects claim that by the end of the experiment their arm was tired. That can also explain the general case of the experiment 2, where the subjects' improvement from segment 1 to 2 but a worsening in performance in segment 3 was noted. In experiment 1 there was clearly no fatigue. The complexity and the requirements of this level were very low and none of the subjects claimed to get tired. But, since it was the very first experiment and the subjects were learning the idea of sudden

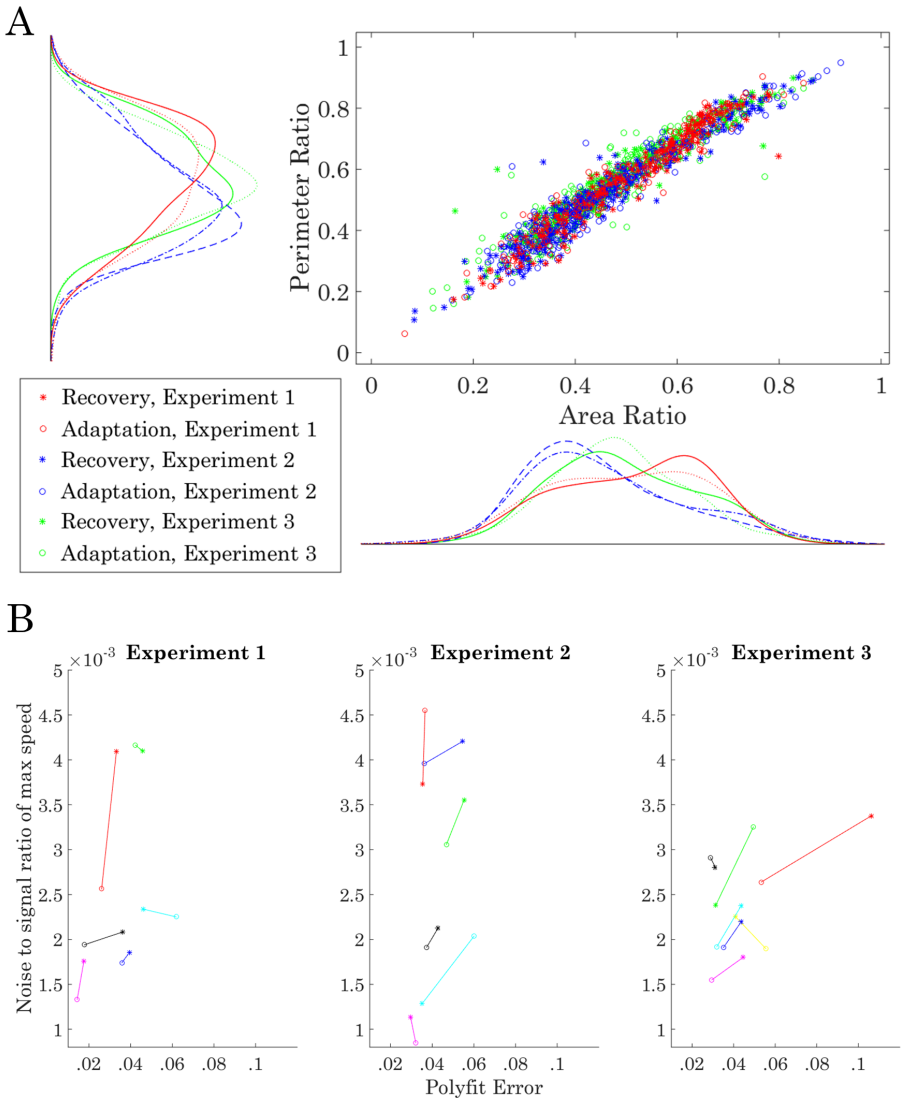

Figure 3.7: **Image A displays the perimeter and area ratio of the recovery-adaptation case. In the parallel of the x and y axes, the histograms of the area and perimeter ratio are displayed, respectively. It is noticeable that there are distinguishable differences in the histogram tendencies between the three experimental levels. Within each experimental level the curvatures have similar characteristics, but still, they differ significantly. For making image B, the polynomial P (x) of degree N = 1 that fits the area and perimeter ratio data of each subject for each experimental level was obtained; and then, the standard deviation of the error in predicting a future observation of area ratio by P (x) was estimated. It is remarkable that regardless the experimental level, each subject has highly differentiated values between recovery and adaptation cases.**

event, there is no obvious pattern of learning.

It is important to note the results of the Kruskal Wallis test were applied to the mean values of each subject and compared to every segment across all experimental levels, Figure 3.8D. Based on the test, the mean values of each experiment come from a significantly different distribution. The actual results of the test are exhibited on Table IV. It should be noted that the most significant shift is between experiment 1 and 3 for any segment.

In order to defend our last statement, we also compared the mean values of segment 1 and 3 across all experiments, see Figure 3.3E. The significant difference between the two outboard segments can be detected. The last result was verified with the Kruskal Wallis and the Friedman test, see Table V. In fact, the Friedman test showed an even more significant difference between the two values.

Table IV. Kruskal Wallis of all segments across experiments

	Source	DF	Chi-sq	Prob. Chi-sq
Segments 1	Column	2	5.11	0.0779
	Error	18	-	-
Segment 2	Column	2	7.37	0.0251
	Error	18	-	-
Segment 3	Column	2	6.06	0.0482
	Error	18	-	-

Table V. Comparison of Segment 1 versus 3 over all experiments

	Source	DF	Chi-sq	Prob. Chi-sq
Kruskal Wallis	Column	1	2.39	0.1218
	Error	40	-	-
Friedman	Column	1	4.96	0.026
	Error	28	-	-

3.5 Conclusions

In this work, we studied human learnability in motor tasks. We designed a pointing paradigm where we examined the effect of repetition, habituation, simplicity, complexity, and surprise in the process of learning a motor task. Our 7 college level participants were

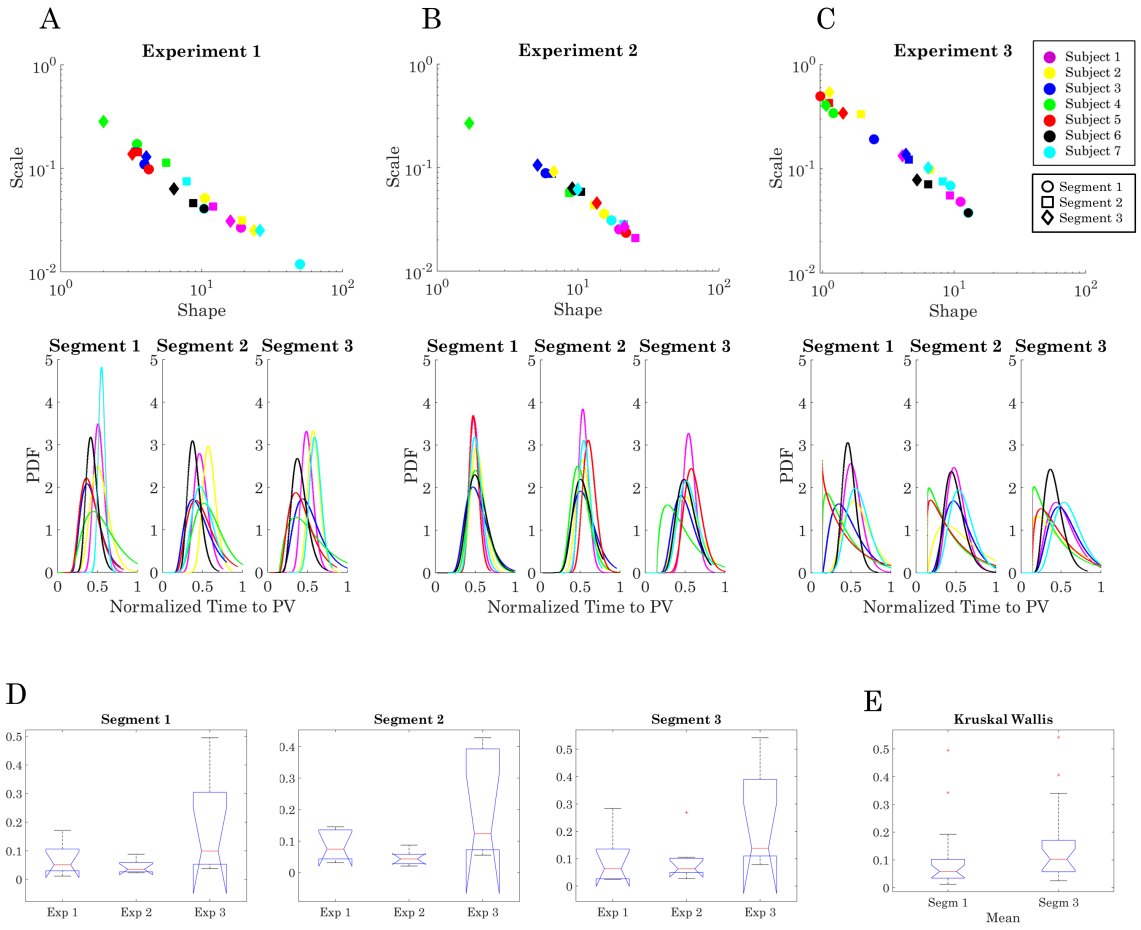

Figure 3.8: **Image A, B, and C demonstrate the shape and scale parameters of segments 1,2, and 3 for each experimental level. Below each graph, the PDFs of the corresponding cases are plotted. Image D shows the plots of the Kruskal Wallis analysis. The Kruskal Wallis test was applied to the mean values that correspond to the shape and scale values of each subject as explained in Section 4.1.4. Each of these graphs represents the in-similarities between each experimental level within the corresponding segment. The exact values of the analysis are printed in Table IV. Image E illustrates the significant difference between segment 1 and 3 overall the experiment. The values of the Kruskal Wallis and the Friedman analysis are shown in Table V.**

asked to interact with 3 different trails of points which differed in schema, complexity, and size. They had to discover, adapt on each trail's regular points as well as on the random sudden points. We grouped and studied our data under 3 points of views: complexity level (compared te tasks), recovery versus adaptation period between sudden events, the three segments of progression during each task.

The complexity level of the task affected each individual differently. Some seemed to be affected by it and performed progressively worse, some other were becoming more familiar with the underlying algorithm of the interface and did not get affected by the complexity. Nevertheless, Kruskal Wallis test showed that the mean values of PV and the variance of the time to PV come from significantly different distributions. The recovery-adaptation analysis showed that our system behaves more like recovery and sudden-event expectation, rather than what it was initially assumed. This was demonstrated through the PV shape and scale values, which had high scale (noise-to-signal ratio) values during the sudden-event expectation period and the perimeter ratio analysis, which indicated that the trajectories tended to have different sizes. The three segment grouping revealed that the mean of PV values come from significantly different distributions with a noticeable difference between first and last segment, indicating the presence of fatigue towards the end of each task.

Overall, each participant had their own patterns of learning and the variability of the individualized learning can be noted in each grouping analysis we investigated. However, the statistics of the stochastic signatures revealed information about the kinematic qualities of the movement during each condition and paved the ground to detect differences in geometry of the trajectory between recovery and adaptation periods and fatigue throughout the execution of a specific task.

Finally, this study opened up the first path on studying human movement in a personalized manner. It created tools and methods that allow us to study the adaptation of the human system and it revealed information about fatigue and how distraction can counter affect the progress of an adaptation. All these are valuables parameters that could

be utilized to evaluate the continuous progress of the interaction unfolding in a closed-loop co-adaptive interface.

3.6 Appendix

1. Experimental set-up for studying sensory-motor system's learnability: adaptation and surprise - https://youtu.be/z65XVbntQ5U

Chapter 4

Sensory-Motor Integration: Movement and Temperature

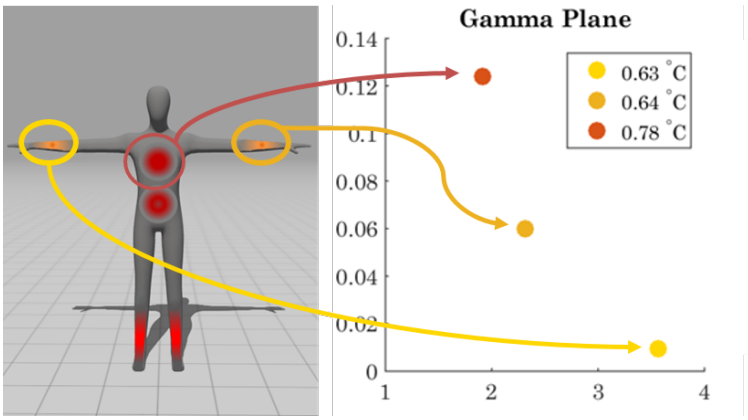

Figure 4.1: **Schematic of the kinematic stochastic signatures corresponding to the range of Celsius degrees of each body-part.**

The question that concerned us next was how to integrate the variability and the stochastic signatures of human movement with those of other bodily signals such as temperature. We found out that there is a paucity of methods that enable personalization of the estimation of statistical signatures of sensory-motor signals. However, such individualized parameterization would help researchers achieve subliminal, real-time manipulation co-adaptation processes between participants and environment.

This chapter introduces methods to achieve individualized profiling of the stochastic signatures of 40 participants. These included 20 normal controls and 20 patients with schizophrenia. Using wearable sensors that register in tandem temperature, linear acceleration and gyroscopic motions, we were able to extract parameter-ranges and estimate with 95% confidence their statistical signatures of their bodily signals. The results are framed in

new proposed ways to potentially help researchers use these parameter estimation methods to boost personalized multimodal sensory-driven interfaces.

4.0.1 Parameter Estimation for Personalized Co-Adaptive Interactions Using Motion and Temperature

In the field of human-computer interaction (HCI), there is growing interest in the use of the senses to aid adaptation within the context of multimodal interactive interfaces [45] (e.g. smell [64] [79], taste [63], sound [61], vision [34]).

Through the manipulation of visual, auditory, olfactory, gustatory, and haptic feedback, one can create immersive environments, which enhance the experience for the end user. The idea of such closed-loop systems for co-adaption is to turn the output from brain or bodily signals into this feedback input to steer the system's performance. Specifically, by taking real-time bodily information (motion, sensory or brain data) from the end user and generating representative real-time feedback in parametric form, one can influence the subsequent state, and interactions with the end user. A problem is how to do so in a personalized manner, away from methods that use average population statistics that assume normality, homogeneity and stationarity of the sensory-motor signal.

Moreover, human-computer interaction has evolved from initial consideration of static interfaces to dynamic brain- and body-computer interfaces. Recent developments within this area have seen the growth of multi-sensory-driven computer interfaces, with new experimental paradigms designed for basic science research [3], crossing boundaries to interactive gaming [25] and sensory-substitution therapies [109] [37] among many others.

In the context of body-computer interfaces, avatars are used to interact with humans via a computer screen, through immersion in a virtual environment. In this instance, the avatars are often endowed with the motions of the person. In turn, during the progression of a session, the person's motions are co-adapted with those of the avatar under a variety of contexts. Some may involve a basic research paradigm to study the brain during

motion observation [3], while others may involve learning a complex task (e.g. driving in a simulator,[36]. A number of these applications aim to facilitate rehabilitation after a stroke [33], to assist individuals adapt to the use of a new prosthetic limb [107], and guide paralyzed patients to exercise muscles, slowing down the degeneration process [59]. Applications may also go as far as helping a person develop better social skills [34]. This type of paradigm may be particularly pertinent to research in rehabilitation but the weakness lies in the use of 'one size fits all' statistical approaches that assume theoretical distributions without empirical estimation of individual statistical differences.

In all these instances, averaged parameters are used from movements co-adapted with visual or auditory input that help enhance afferent sensory input, or sensory-substitute sources of sensory inputs that have been lost or injured due to accident or neurological damage. The averaged values may not reflect subtle minute fluctuations in the sensory-motor signals that evolve as the user and machine co-adapt. This is so because the mere averaging operation smooths out as noise such minute fluctuations in performance that from moment to moment informs the system of the consequences of actions and decisions.

Physiological signals and related biometrics could offer a more reliable outcome measure, while helping automate many of the evaluation processes to assess the quality of the interactions. Such signals could include a range of motions from deliberate to automatic, as well as a mixture of autonomic bodily outputs, such as temperature. Specifically, as the person interacts with the system, self-produced movements and their fluctuations provide a source of continuous kinesthetic sensory input, which is interpreted and transduced by mechano-receptors across the body. This information is then sent back to the brain via afferent sensory nerves [32], that transmit information about touch, pressure and continuous movements (Figure 1A). These are important sensors and channels to help guide motor learning and adaptation [69]. When damaged, the lack of such sensory guidance impedes the sense of proprioception, and along with it the production and voluntary control of movements [16].

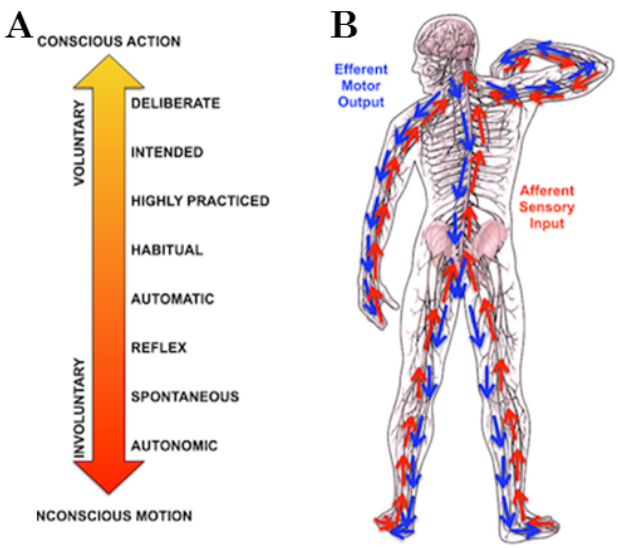

Figure 4.2: **(A) Schematic of movement classes ranging from conscious voluntary actions to involuntary, autonomic motions. (B) Schematic of the afferent and efferent channel that transfer signals to and from the central and the peripheral nervous systems.**

Other afferent sensory channels that are important for sensory guidance and are fundamental for corporeal awareness, are those which carry temperature-related information transduced by thermoreceptors throughout the body [69]. These types of signals are important for internal homeostasis and to track good balance in physiological processes, infections, stress, amongst others. However, these signals are rarely used for co-adaptive interfaces. Indeed, temperature signals remain under-explored within basic scientific research. With the advent of a new generation of wearable sensors that continuously register various forms of temperature in tandem with body motions, there is a new possibility of their use in co-adaptive interfaces as an additional channel to enhance sensory feedback.

This study introduces new biometrics, which extract the range of moment by moment motor fluctuations as a function of fluctuations in temperature during a simple biomechanical task. Its simple structure enables us to use it as a toy-model example to probe various key aspects of the signal statistics.

Motion Signatures

Natural behaviors contain small trial-by-trial variations in performance. These are fluctuations in amplitude and/or timing of kinematics parameters that include, among others, the minima, the maxima and the time to reach the peaks of acceleration and velocity. Such minute changes are imperceptible to the performer at a higher cognitive level but transduced by sensors across the peripheral and central nervous systems. They accumulate statistical evidence over the time scale of minutes and such information can be revealing of individualized performance quality. They describe ways in which a person learns, adapts, and fatigues during performance [38]. They are susceptible to changes in the task context and can aid with the classification of movements that range from deliberate to highly automatic (Figure 4.2A). More information about the importance of motion stochastic signature in our research can be found in Sections 2.4 and 2.5.

The Temperature Channel

The sense of the temperature, known as thermo-reception, is connected with a wide range of physiological functions. For instance, emotions are known to induce fluctuations of temperature across body. Specifically, fear lowers the body temperature, making us feel cold. In contrast, excitement increases the blood flow and thus tends to raise the temperature [2]. Moreover, different emotions affect the temperature of different body parts and may even cause tremor, thus causing significant changes in the quality of motor performance [11].

Temperature is connected with the volume of the physical exercise that is performed. Low-volume exercise may let us maintain a constant temperature value, but this is not the case in high-volume exercise. The latter can lead to rapid fluctuation in body temperature, often resulting in fatigue and changes in muscle patterns that are eventually detrimental to the quality of performance [54].

Haptics are also modulated according to internal and external influences in temperature. If the hands are exposed to low temperatures they lose sensing abilities and if the object to

be manipulated is too hot the hand reacts by rapidly moving away from it. In contrast a cold cup gives us a pleasant feeling on a hot summer day.

Despite the ubiquitous presence of temperature in our bodily interactions with the environment, very little is known about its potential use in HCI and AI. Since we are not really aware of temperature sensation and regulation (unless extreme changes occur), it is possible that using temperature subliminally may aid in the development of realistic environments that at the same time enhance the co-adaptation process with closed loop settings. But to really take advantage of its potential, we must assess this channel in a very personalized manner. Each person experiences temperature slightly different. Because of this we may necessarily register a gradient in the perception of temperature sensations. To go beyond subjective estimations we can use instrumentation that objectively tracks such signals.

One very interesting population in which to study temperature regulation is Schizophrenia (SZ). Schizophrenia is a mental illness primarily defined by psychosis and cognitive function impairments. However, in addition to the psychiatric irregularities, patients experience movement [49] and temperature abnormalities [81]. These abnormalities are documented but most of the time they are based on observation and not on continuous recordings from high resolution instruments. Moreover, very little is known about how this temperature dysregulation is related to their motion.

This work aims to uncover patterns of temperature-dependent motions, which could then be applied within the context of co-adaptive neuro-feedback. Given our understanding of temperature and motion dysregulations in SZ this work will compare the relationship between these two signals between individuals with SZ and a healthy population. Therefore, the purpose of this work is to statistically estimate personalized ranges of temperature and motion so as to visualize them across the human spectrum, from normal to pathological.

4.0.2 Study Methods and Procedure

Subjects

The presented study and protocol were approved by the Rutgers University Institutional Review Board (IRB) in compliance with the Helsinki Act.

In our study of a total of 40 participants, 20 were typical controls (CT), and 20 were diagnosed with schizophrenia (SZ). The CT group was composed of 4 females and 16 males. The SZ group had 5 females and 15 males. The age range was 16-65 (median 46) years old. The SZ group was selected from an outpatient group under treatment; all members of this group can follow instructions and are functionally independent.

Study Set Up and Procedure

In the presented work, inertial measurement units (IMUs) (APDM-OPAL, Portland, OR) were utilized for motion and temperature recording. The watch-size sample sensor is presented in Figure 2.6A. The IMUs register linear and angular acceleration, orientation, temperature, gyroscope and magnetometer data at 128 Hz (for more specification about the equipment, see Section 2.2). The temperature measurements of the sensors include contributions from surface skin, which is one of the parameters that we focus on.

An in-house developed MATLAB program (Release 2014b, The MathWorks, Inc., Natick, Massachusetts, United States) controlled the presentation of targets on an iPad touch display (Apple, Cupertino, CA) and recorded the touches on the screen. The MATLAB program was presented on the tablet using the AirDisplay iOS application (Avatron Software). Each target consisted of a filled green circle, located in the middle of a black background. An IMU was affixed to the wrist of the dominant arm of the participants. Then, the participants were only instructed to touch the target with their dominant hand starting from the edge of the table, but no further instructions were given about the retracting motions. Upon touching the target, the circle disappeared briefly (for 300ms) and then reappeared.

Participants were told to continuously reach for targets once the experimenter instructed them to begin. The experiment was completed after 100 touches were registered by the Matlab program. Data were acquired in 15 second intervals signaled by a beep that indicated resting pauses as well. An extra IMU with a button installation (Figure 2.6A) was used as an actuator to timestamp those 15 sec trials as well as the beginning and the end of the task.

Data Preprocessing

Calibrated temperature (°C), orientation (quaternions), and acceleration data (m/s^2) were exported from the IMU, using the APDM interface Motion Studio. The time series of angular velocity were extracted from the exported orientation data. More details about the data extraction,angular velocity estimation, and data preprocessing can be found in Section 2.3. Figure 2.6B shows a representative time series of the x-component of a velocity and acceleration trace. The corresponding temporal profile of the angular speed and acceleration for a session is shown in Figure 2.6C.

The time series of angular speed were cropped using the triggers' signals that the IMU sensor's actuator time stamped in the raw data on a third sensor that the experimenter held as the participant initiated and ended each trial (red dots in Figure2.6B).

The temperature data were plotted (e.g. Figure 2.6B bottom panel shows a temperature profile). Note that there is an adaptation period till the trace became stable. This period started from the moment the sensor was attached to the participant's wrist until the start of pointing experiment. During that time period the participant read and signed the consent forms, and the setup of the experiment took place. The button presses to mark the initiation of the pointing experiments also marked the temperature steady-state (Figure 2.6A button).

The angular speed and acceleration data were then mean centered (see Section 2.3) ample representative mean centered angular speed and acceleration data for a control and patient participants are shown in 2.6D (no mean centering was applied on the temperature

data).

4.0.3 Analysis

In our movement study approach, we aimed at a moment-by-moment analysis of individuals' motor fluctuations. To achieve this, we applied the analysis explained below to both the linear acceleration and the angular speed time series data. This helped us study the linear and angular aspect of motion as well as confirm the final results extracted by two different instruments, accelerometer (linear accelerometer) and gyroscope (angular speed).

For analysis of the data, we estimate the micro-movement spikes (Section 2.4) and their stochastic signatures (Section 2.5). To incorporate the temperature data in our study we plot the stochastic signatures on the Gamma plane as a function of individualized temperature ranges, Figure 2.9C. In this way, we obtained for each person the range of stochastic parameters for a given range of temperature.

As already explained in Section 2.5, from left to right on the shape axis of the Gamma plane, the stochastic signatures of these parameters vary from Exponential ($a = 1$) to Gaussian-symmetric. The latter is observed in normal controls while the former has been found in pathologies of the nervous system such as autism and Parkinson's disease, but their ranges for SZ have not yet been determined.

We also seek to estimate the summary statistics of these parameters, i.e. the first (mean), second (variance), third (skewness) and fourth (kurtosis) moments of the estimated Gamma probability distribution function (Section 2.5). We then use these to help visualize the interactions of motion and temperature.

Finally, the range of temperature of each subject is obtained as the difference (in degrees $^{\circ}$C) between the maximum and minimum temperature values recorded during the pointing task, and we also look at the rate of adaptation period that takes place when transitioning from the paper-work (signing the consent forms) to the initiation of the pointing task.

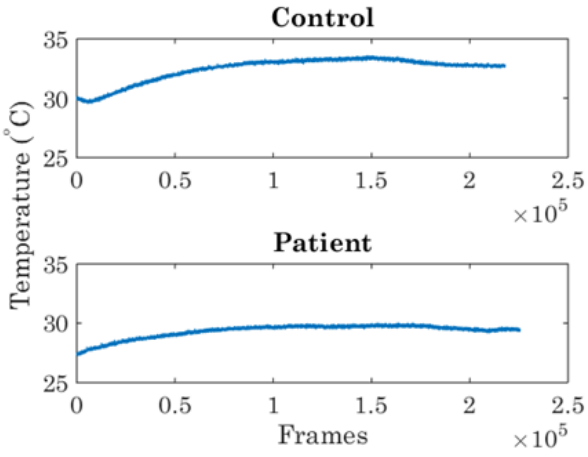

Figure 4.3: **Range of temperature of a sample CT and PT participant registered at 128Hz for ∼ 30 minutes**

4.0.4 Results

Given the evidence for temperature dysregulation in SZ, we expected to see variation in regulation between groups on this variable. As demonstrated in Figure 4.3,we can visually observe a number of dissimilarities between two sample temperature profiles of a patient and a control. The first dissimilarity is that the patient has a lower overall temperature. The second dissimilarity is that the range of temperature is narrower for the patient. This observation can also be made for the whole PT population as illustrated in Figure 4.4A —where the colors of the dots represent the temperature range of each subject. From this figure, it can be noticed that CT participants have a wider range of temperature during the pointing task. Although, such deviations are visible, the Kruskal Wallis test returned a probability value equal to 0.0935 (non-significant), indicating that there is not enough evidence to reject the null hypothesis of median inequality between the two groups. Statistically significant differences between CT and PT participants (P¡0.05) were nonetheless found in the rate of change of temperature during the adaptation period, i.e. between the paper-work completion and the pointing experiment initiation.

Differences in motion across the two populations can be noticed at the very early stages

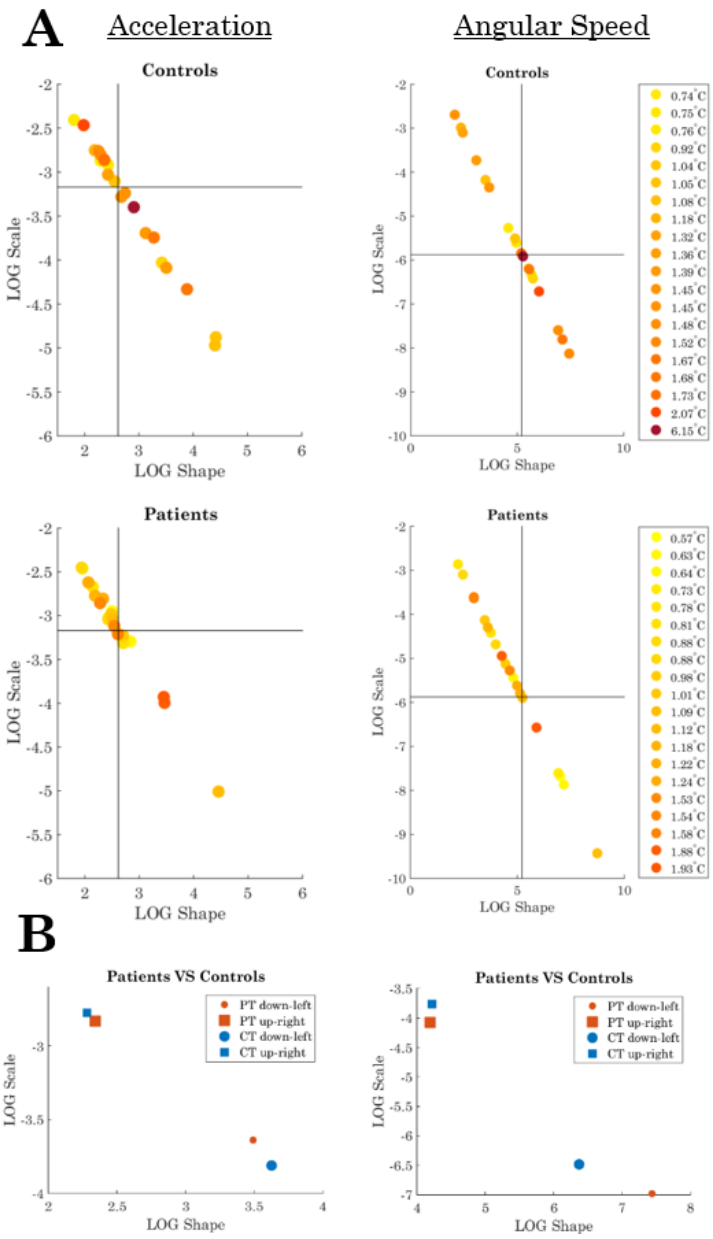

Figure 4.4: **Temperature-dependent motion signatures on the Gamma plane. (A) The representation of participants signatures of the moment-by-moment fluctuations in angular speed and acceleration portrayed on the Gamma (shape, scale) plane according to their unique personalized temperature range as captured by the wearable sensors. The color gradient maps the actual ranges registered by the sensor between the minimum steady-state-value of the temperature at the start of the experiment and the maximum registered value during the session. The line represents the median value of the scale and the shape empirically estimated Gamma parameters. (B) The averaged results of the two populations.**

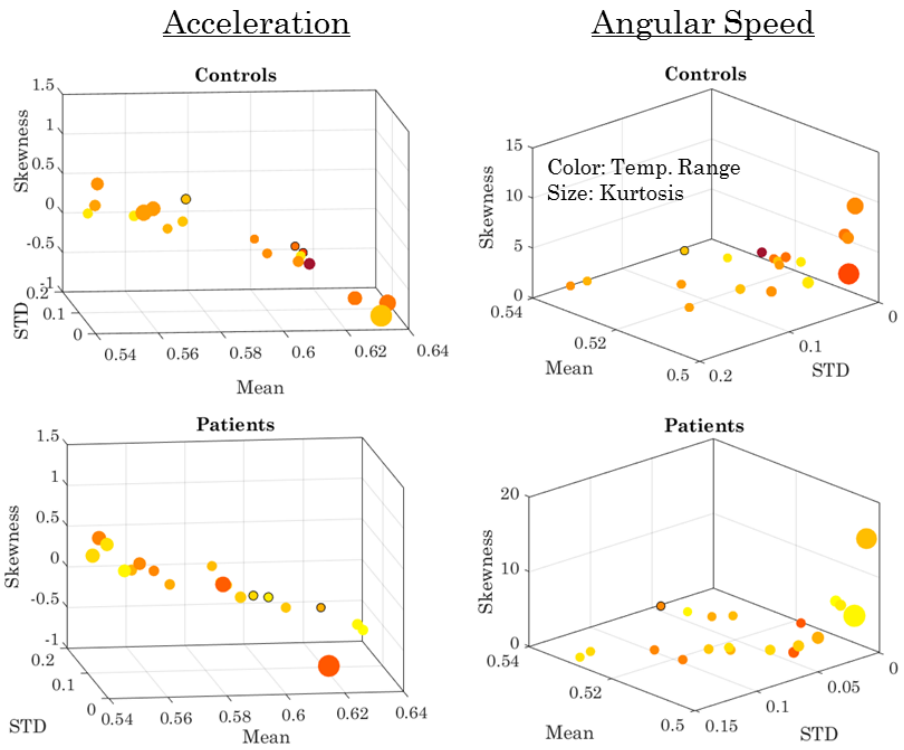

Figure 4.5: **Temperature-dependent multidimensional statistic graph to summarize the statistics of temperature (color) dependent velocity and acceleration by the estimated mean (X), variance (Y), skewness (Z) and kurtosis (size of the circle) of the empirical distributions.**

of data pre-processing. Figure 2.9 provides a sample of angular speed data from a CT (top panel) and PT (bottom panel) participant. The observed pattern of speed data profile for the PT participant indicates that this individual lacks periodic patterns in contrast to the CT participant. His motion patterns tend to be spontaneous and random despite the systematically targeted motions that this pointing experiment demanded.

The Gamma distribution plane, presented in Figure 4.4A, provides further evidence that the above observation extends across the entire population. The results demonstrated in this figure have been systematically registered by two different instruments accelerometer (linear acceleration) and the gyroscope (angular speed). Thus, we can verify our results, as well as examine dissimilarities between linear and angular motion. This figure illustrates the empirically estimated values for the shape and scale Gamma probability distribution

	Angular Speed (rad/s)	Acceleration (m/s^2)
Patients	$P < 0.01$	$P < 0.01$
Controls	$P < 0.01$	$P < 0.01$

Table 4.1: **Wilcoxon rank sum test results between the quadrant sub-groups of the same populations.**

parameters for each subject's acceleration and angular speed data. The lines dividing the plane into 4 quadrants are the median shape and scale values from the controls. These data boundaries have been previously determined in other populations such that professional athletes are likely to fall on the right lower quadrant of the Gamma plane. In contrast, individuals with a neurological condition are likely to fall on the upper left quadrant. Thus the normative median can guide us to establish ranges within the human spectrum.

In this work we find that the majority of PT participants 17/20 (linear acceleration) and 16/20 (angular velocity) fall far from the ranges of the Gamma plane corresponding to the Gaussian distribution. In contrast, the majority of CT participants 10/20 (linear acceleration) and 7/20 (angular velocity) falls towards the Gaussian range. These group differences are summarized in Figure 4.4B and Table 1 shows the statistical differences in the noise-to-signal ratio (the Fano Factor ratio of the estimated variance to the estimated mean, which amounts to the scale Gamma parameter)[73].

In Figure 4.4B, we averaged the individualized results of each group based on the quadrant to which its participants were localized. The size of each symbol indicates the proportion of participants in each quadrant, confirming the paucity of PT participants in the Gaussian range and their prevalence in the Exponential range of the Gamma family.

For each of these averaged dots we applied the Wilcoxon rank sum test for equal medians on scale values. The results of this test were statistically significant and are shown in Table 4.1.

Another aspect of the data that differs between PT and CT participants is the temperature range, which is color-coded in Figure 4.4A (darker indicating the wider range). As it

has been explained, the main finding is that the PT have overall narrower range than CT participants.

Finally, in Figure 4.5,we can examine the four statistic moments of the distribution of each subject across the two populations. The mean, standard deviation, and skewness are on the x, y, and z axis, respectively. Kurtosis is described by the size of the dot —negative kurtosis is identified by a black colored edge. Also, the color of each dot corresponds to the temperature range, as in Figure 4.3A).

Note that both populations follow similar distributions in the 3D space with the trend that higher (positive) skewness is characteristic of lower Gamma mean normalized peak acceleration and lower Gamma mean normalized angular velocity indexes. This signifies that participants with positively skewed distributions of the normalized peak indexes in these two parameters move faster on average. This is so because the denominator of that index carries the average acceleration (angular speed) of each minima-to-minima segment (see methods). Thus the indexes with lower values have higher denominator (i.e. higher linear acceleration or angular velocity on average). Furthermore, in the case of angular speed data, controls, who have low Gamma mean and Gamma standard deviation, but large kurtosis have a wide range of temperature. In contrast PT participants with the same characteristics have narrow range of temperature.

4.0.5 Discussion and Future Directions

This work unveiled stochastic ranges of motion and temperature across participants in a typical control and schizophrenia group. We report differences in temperature and motion patterns that may help us design general multi-sensory co-adaptive interfaces tailored to the person's preferences. The use of temperature as a subliminal parameter to enhance adaptation may be possible when using the parameter ranges found in CT participants. It may be the case that the narrower range found in PT participants is not suitable to guide typical learning. Likewise, perhaps using typical ranges in PT with SZ aids enhance

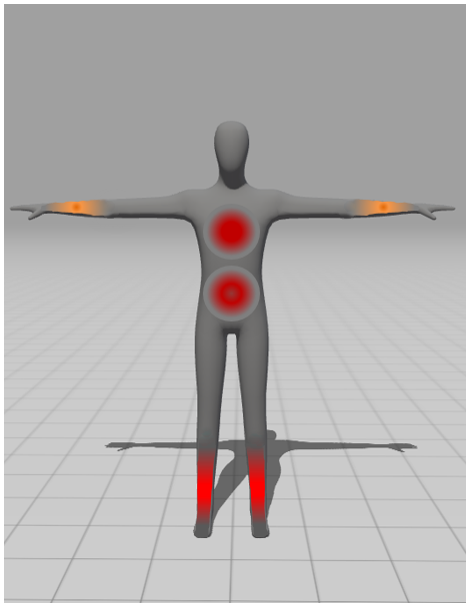

Figure 4.6: **Future directions for HCI designs include endowing an avatar with both motion and body temperature during co-adaptive interactions.**

corporeal awareness and broaden their ranges of motions.

Motion parameters in these groups differed in statistical ranges suggesting that PT participants have a tendency to move in less controllable ways than CT participants as their movements appear to be subject to higher levels of random noise. These results were congruent in both the accelerometer and the gyroscopic data, pointing at diverse forms of motor output patterns and instrumentations that could be systematically used in HCI. It may be possible using these approaches to aid PT with SZ improve their motor control.

Temperature can be used underneath the end user awareness to broaden the bandwidth of the signal to noise ratio in the motor domain

Temperature is an autonomic channel known to be connected with a variety of physiological functions. Since its fluctuations go largely beneath our awareness, it may be possible to use it and alter it in subtle ways to enhance learning and adaptation without disrupting the flow of actions. Some of the issues with adaptation in immersive environments and co-adaptive interfaces are precisely related to the level of awareness that the end user acquires in relation to manipulations that are introduced with the hopes to help the learning process.

For example, a professional baseball player may benefit from practicing with loads placed on his batter so as to increase the speed of his swing during the load-deadaptation period, when the loads are off and aftereffects from the training remain in his muscles for a few seconds. The athlete has no volitional control over that process that takes place when adaptation and deadaptation occur beneath his conscious awareness. Yet these processes impact his performance when he deliberately tries to hit the ball, as he acquires more speed and strength in his motions. Similarly, as it is done with loads, we could use temperature as an unconscious guiding channel and probe the system under various ranges to assess the impact that this autonomous afferent signal has on the acquisition of a motor skill.

Temperature as a possible therapeutic channel

Given the results of a narrower range of temperature in the nervous system affected by SZ, our work in this paper also opens the question as to whether temperature may help broaden the bandwidth of emotions in these participants. Since this is a disorder that impacts emotional states we wonder if the narrower ranges of temperature registered in these PT participants may relate to deficiencies in recognizing the various physiological states at some autonomic level so as to transfer that knowledge within the system towards a conscious deliberate level. Motor may be a channel to explore this question because movements contain both deliberate aspects that we purposefully intend and spontaneous segments that we are unaware of. Thus combining movement and temperature may help us design multimodal sensory-based therapies.

Temperature as an input channel that can be parameterized to steer the system beneath awareness

A critical component to deliver a realistic co-adaptive interface is to maintain a seamless closed loop between motor output and sensory input. One of the challenges of though is to make the co-adaptive process transparent to the end user so as to be able to manipulate the returning (reafferent) sensory input that the end user self-produces in ways that are

well informed and controllable at the programmer's end. The work presented here opens the possibility of doing so in a parametric form using the stochastic signatures of the acting and reacting physiological activity unique to the end user. Since the estimation process is done individually, it is also possible to combine the signatures of the end user with the signatures of other users and expand the user-centered model to dyadic and multi-user settings (Chapters 9 and 10). In this way it may be possible to quantify gains in perceptual awareness of the users thought the enhancement and manipulation of parameters that may drive their corporeal awareness. The present work offers the possibility to tailor the adaptation process to the specific individual(s). This way of tracking performance and adaptation in general is advantageous over methods that use a 'one-size-fits-all' approach and do not necessarily consider subtle individual variations in the parameter ranges and their rates of change unique to each person. In this sense manipulating temperature ranges may help us entrain the users' motions and through this process synchronize their emotions during dyadic plays. Variations of these ideas are presented in Chapters 9 and 10

Using the present methods, we plan to incorporate in our future HCI research new modalities at the intersection of spontaneous motion and autonomic temperature to subliminally steer the person's performance in parametric form (Figure 4.6).

4.0.6 Conclusions

In summary we have presented ways to assess different sensory modalities in an individualized manner. These methods enable the personalized parameterization of various sensory inputs as they are physically registered in real time. Using the methods introduces in this chapter, we could further investigate the crosstalk of the connection of motion fluctuations with temperature and use it to help guide the end user to better adapt to a co-adaptive interface. The advent of wearables that register temperature and motion in tandem can help us integrate these forms of sensory guidance in real-time into a vision-driven co-adaptive interface or other forms of technology that generate variable sensory feedback online.

In the next chapter, we will study movement and temperatures in a "1-1" approach and create a new data type, where the fluctuations of the one signal are studied as a function of the other. Moreover, we will investigate the motor-temperature integration in the full-body and research for visualization methods that could potentially help in developing a vision-driven co-adaptive interface in our future work.

Chapter 5

Sensory-motor Integration: Creating a New Data Type

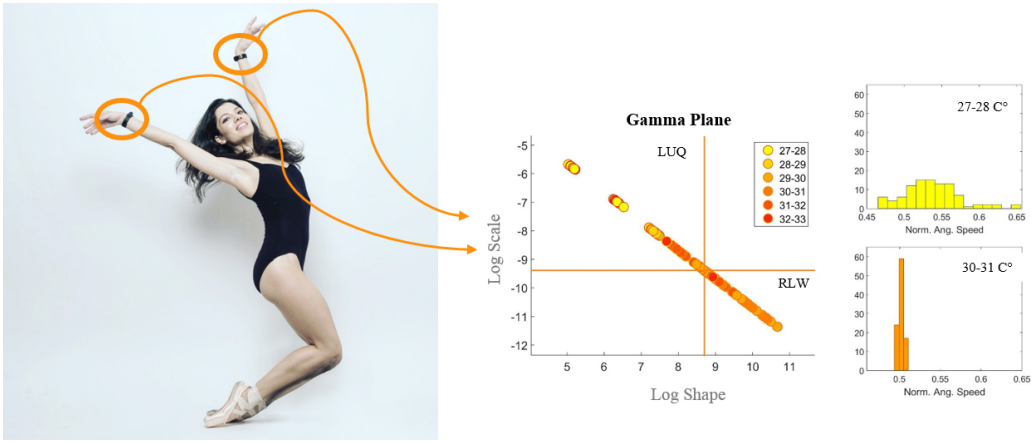

Figure 5.1: **The new data type: studying motion stochastic signatures as fluctuations of the degree-to-degree variability of the body temperature.**

After our first study on temperature-movement integration, we identified the need for developing new methods for studying the moment-to-moment variation of the signals in a continuous and "1-1" manner. A further concern was to develop ways to visualize the extracted information to possibly use in a vision-driven co-adaptive interface.

To that end, in this chapter I present new visualization tools, new data-types, and analytics that enable the automatic identification and tracking of noise-to-signal transitions. The frequency of such transitions differentiate periods of spontaneous random noise (sleep time) from periods of well-structured noise in human motion (performing ballet routines). I study our paradigm through pre-professional ballet student, who recorded 6 hours of exercise and 6 hours of the sleep following her ballet training[41] [39].

5.0.1 Outcome Measures of Deliberate and Spontaneous Motions in Ballet Training

Prior to any important performance, dancers may stress over perfecting their routines and mastering fine choreographic details. During the day they may practice intensely and try to rest during the night, when they sleep. Sleep for dancers and athletes is very important. Research has shown that the quality of sleep can significantly affect dancers' and athletes' performance [23] [72]. Thus, it would be very useful to be able to record the cycles of activity during the dancer's practices as well as the subsequent sleep cycles in order to simultaneously track the dancer's various body parts during active and resting states. Having this ability may help us personalize the routines of a dancer to maximize her resting time so as to provide optimal energy for the daily practices. This ability would also help the trainer monitor the progression of the artist's skill acquisition during rehearsals to selectively focus on body segments requiring more attention to perfect the routine.

The advent of wearable sensors opens new opportunities to study such motion cycles in very naturalistic ways. For example, someone can use wearables that are minimally intrusive and light-weight to facilitate the continuous recordings of the artist's daily practices and the comparison with signals gathered during sleep as the artist rests for the next day of performance. Is the rest adequate or is it not efficient because the body moves in excess during sleep? These are some of the questions that can be addressed nowadays, using current technological advances in wearables.

One challenge, however, has been to extract different motion types and automatically differentiate them as the person changes routines. For example it would be ideal to be able to automatically separate motions that are deliberately performed from motions that happen spontaneously. Examples of the former occur during the practicing of a routine whereas examples of the latter occur during sleep, when the brain is resting and the spontaneous fluctuations in the motions that the body generates are not under explicit volitional control.

Another challenge has been to separate reliable signals in the sensors from random

noise, as the data rapidly accumulates during the hours of recordings. Present algorithms for activity trackers and wellness-fitness sensors have been criticized in the media because of their inaccuracies. This is partly due to the inabilities of such methods to isolate reliable signal from noise and to tailor the signal analyses to the physiological rhythms of the person.

This work characterizes the stochastic signatures of the fluctuations in motor performance from a ballet dancer during her regular workout immediately followed by her sleep. The work presents a new data type combining motion data from IMUs with temperature data simultaneously registered and mapped across the body during her continuous performance and her continuous sleep cycles. Besides automatically separating motion types according to control levels, we present new methods to visualize the continuous output of the IMU's. We also present methods to evaluate the transitions from spontaneous random noise to well-structured noise with statistical regularities and high signal content. We provide a new statistical platform for the personalized analyses of naturalistic behaviors continuously registered as the artist masters a routine during the day and as she rests during her sleep at night.

5.0.2 Subjects and Experimental Set up

This study was approved by the Rutgers University Institutional Review Board (IRB) in compliance with the Helsinki Act.

The subject of the experiment was a 26-year-old dancer attending pre-professional ballet classes. For the study, both her regular ballet workout and her sleep session (immediately following the workout) were recorded. The workout included 1.5 hours of bare- and center-work, 1 hour of pointe class, 0.5 hour lunch break, and 3 hours of intense rehearsals with pointe shoes, for a total of 6 hours. The sleep session was approximately 5.5 to 8 hours long (Appendix video 1). The dance exercise data were a sample of high-activity with deliberately executed motion data registered during highly controlled exercise, while the sleep cycle data represented spontaneous activity that is not under explicit volition.

Apparatus

Six IMUs (APDM-OPAL, Portland, OR) (see Section 2.2 for more specification) were placed on the subject's wrists, ankles, lumbar, and torso(Appendix video 1). More importantly, the technology used by these sensors ensures continuous synchronous registration across all 6 sensors during the 12 hours of battery life. The data is directly saved on the monitor's memory (8 GB) under robust synchronized logging mode with no data loss. Here the orientation data from the gyroscope and the temperature are combined to provide an example of a new data type to study motion patterns and isolate random noise from reliable signal.

A total of 3 days of exercise and sleep were recorded. The results for one day were consistent in other days, namely the differences between active performance during the day and spontaneous motions during the sleep were consistent. Due to space limitation, in this publication we focus on the outcome of one day comprising 6 hours of exercise and 5.5 hours of sleep data to illustrate the signal integration and analytical methods (Appendix video 1).

5.0.3 Methods

Calibrated temperature (°C) and orientation (registered in quaternion format) were exported from the IMUs (Section 2.3). The time series of angular velocity were extracted from the orientation data. Samples of angular speed traces of the exercise session and its corresponding temperature traces (simultaneously recorded) are presented in Figure 5.2.A where we illustrate the methods step by step. These samples correspond to the output of the left ankle activity during exercise in one session but Figure 5.4 later shows the sensor placement across the body along with the matrices displaying the new data type to be next explained.

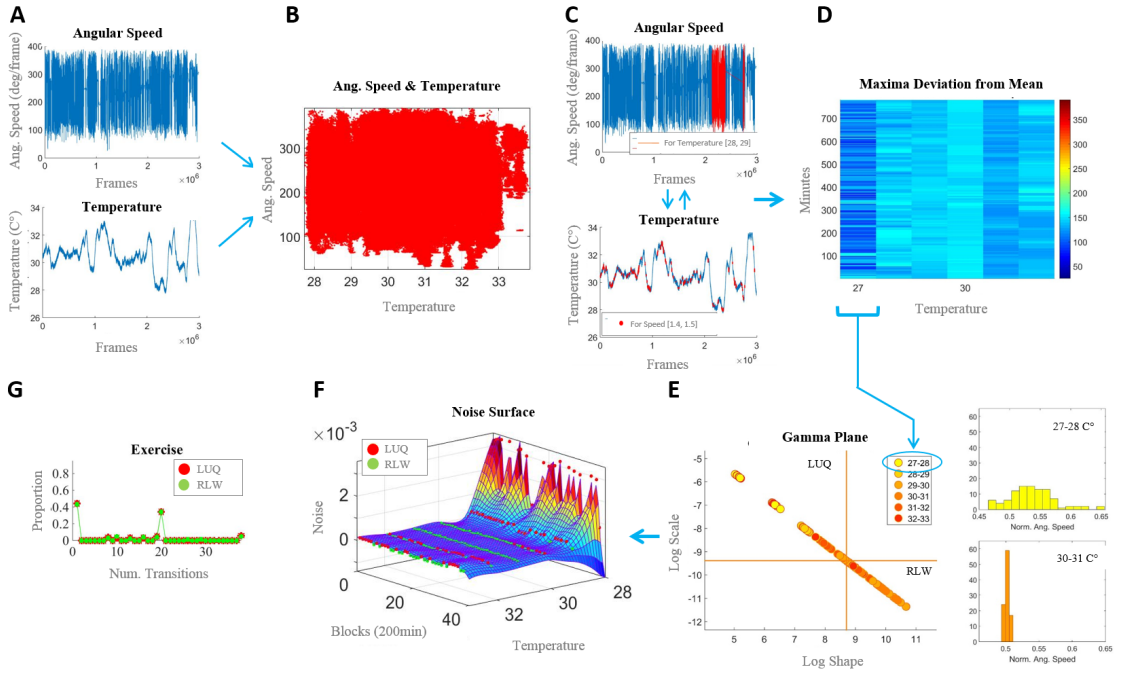

Figure 5.2: **Methods figure (A) Raw angular speed and temperature traces simultaneously recorded at 128Hz by the sensor of the left ankle during the exercise session. (B) Full ranges of angular speed and temperature gathered as all the motion data corresponding to each temperature degree-interval. (C) Example of selectively isolating the motion data for a specific temperature interval e.g. [28 - 29]°Celsius. Likewise, an example is shown, using the same data interval as in the above panel, of isolating the temperature data for specific ranges of angular motion, [1.4-1.5] degrees/frame. (D) Minute-by-minute color map of the maximal deviations from the mean angular velocity registered for each selected temperature interval across the 6 hours of the exercise session. The color-bar represents the range of the motion values (degrees/frame). Each column of the matrix is one temperature interval (°C) and each row is half-minute (128Hz x 30sec) measurements from which the maximal deviation of the angular velocity in that interval and time is selected as the matrix entry. (E) Frequency histograms obtained by gathering the motion data from the matrix entries corresponding to each column (27-28°C)-yellow and (30-31°C)-orange across all the whole session. The frequency histogram was fit with the continuous Gamma family of probability distributions (see text) and the shape and scale Gamma parameters obtained with 95% confidence using MLE. The motion data for each estimated (shape, scale) pair per temperature degree used a block of 200min with a sliding window of 5min sweeping across the total hours. This built a continuous stochastic trajectory along the gradient of temperature. The values thus obtained are plotted on the Gamma parameter plane for each temperature interval (see legend) and the median of each of the shape and scale values computed to plot the lines and divide the plane into quadrants. The left-upper...**

***Figure 5.2:* ... quadrant (LUQ) and right-lower quadrant (RLQ) provide information about the noise-to-signal levels (see text) used in panels F and G to visualize and quantify the noise levels across the recordings. (F) The noise surface is obtained across time and temperature range for each sensor (left ankle here) using the scatter of points continuously generated with the 200min block and 5min sliding window. Regions of the low noise-to-signal ratio (RLQ) are marked in green and red marks regions of high noise (LUQ) (see methods in the text). In this way it is possible to identify the temperature regime for which the data is noisy and separate it from the temperature regimes for which the data has high signal content and is reliable. (G) Distributions of the number of noise-to-signal transitions between the LUQ and RLQ (see text for methods) to track the changes in stochastic signatures during active motions in the performance and spontaneous motions during sleep.**

New Data Type

We combine the angular velocity with the temperature output in order to help identify regimes of motion for various temperature levels where the noise is minimal (i.e. the signal is most reliable). For example we would like to know which temperature levels correspond on average to which motion levels. Further, we are interested to know if during spontaneous motions such as those generated in the sleep cycles, the temperature regimes are similar to those generated during active deliberate motions of comparable magnitude.

To combine these sensors' output parameters, we gather all the angular velocity data and all the temperature data simultaneously recorded across the exercise. Their outputs are contrasted in Figure 5.3.B, where we can see the full range of angular velocity and the full range of temperatures registered by the sensor during different cycles in the day.

Since the sensors simultaneously recorded both signals with a similar sampling resolution and were synchronized throughout the entire recording time, they can selectively isolate temperature recorded within a specific range of angular velocities. Likewise we can also isolate for a given temperature interval, all the corresponding angular velocities. This is further illustrated in Figure 5.2.C, where we color a specific range of motion for a particular temperature range on the top panel, while on the bottom panel we do the opposite. Namely, we plot on the temperature trace the points corresponding to a specific angular velocity

range.

Using these new data type we construct a matrix across the total hours of recordings. Particularly, for each temperature interval (C) we gather all the angular velocity (deg/s) of the motion output and form a color map in Figure 5.2.D using the maximal deviations from the mean angular velocity corresponding to each temperature-degree interval. The rows of this matrix are the minute-by-minute data while the columns are the temperature degrees. The matrix entries contain the motion activity which in this case consists of the maximal deviation from the mean angular velocity (the mean empirically estimated across the entire session). The color-bar on the right provides the range of maximal deviations from the mean angular velocity color coded from the minimum to the maximum of the range.

Personalized Statistics

Using blocks of 200min and a sliding window 5min wide, we continuously sweep through the data and accumulate the peaks of the fluctuations in angular velocity above the mean into an orderly time series to finally estimate the micro-movements (Section 2.4).

The time series of the micro-movement spikes in motor performance corresponding to each temperature interval is our waveform of interest as it reflects the minute fluctuations in motor performance.

The peaks of this waveform are then gathered into a frequency histogram. Examples of frequency histograms are shown in Figure 5.2.E for two different temperature values. Then, the continuous Gamma family of probability distributions is used to estimate the shape and the scale of the probability density function corresponding to the empirical motion data gathered per temperature interval (see Section 2.5).

The next step is to obtain the noise-to-signal ratio (the Fano Factor [21]), which in the case of the continuous Gamma family of probability distributions is given by the b-scale

parameter as the ratio of the variance divided by the mean for each window of data

$$FF = \frac{\sigma_s^2}{\mu_w} = \frac{ab^2}{ab} = b \tag{5.1}$$

The next step aims at helping to visualize two aspects of the data. One aims to help visualize the differences in activity and sleep cycles according to their noise regimes separating deliberate from spontaneous fluctuations in motor performance. The other is to help us differentiate the temperature regimes corresponding to spontaneous random noise *vs.* well-structured noise with statistical regularities conducive of a predictive code denoting deliberate control or volition in the motions. Figure 5.2.F shows the surface used to address both points above. In this figure we fit a surface to the scatter obtained from the temperature measurements across the activity and sleep times (200 minutes in this example) and the noise levels along the z-axis. Further, the median-ranked data from the LUQ and RLQ are used to mark the areas of low noise-to-signal ratio that correspond as well to symmetric distributions *vs.* those corresponding to high noise-to-signal and skewed distributions. In this way we can isolate the regions of times of the day with the highest signal content in the exercises/sleep cycles as well as the temperature regimes for which the noise is maximal.

Noise-to-Signal Transitions

During the various hours of data registration the stochastic signatures of the motion-temperature signals may be at times non-stationary. Thus we track the noise-to-signal transitions between the LUQ and RLQ as well as the time blocks when the signatures turn steadier in one quadrant or the other. To this end, we use the selection criteria of the points that belong to each quadrant. The order of the indexes into these points tells us about the time periods when the stochastic signatures remained within the same quadrant *vs.* the number of times when they jumped from one quadrant to the other. The two arrays containing such indexes for the LUQ and RLQ are differentiated to gather the number of

instances when the change was consecutive within one quadrant (i.e. the difference from one shift to another is 1). In contrast, differences from one shift to another that are greater than 1 denote instances when the shifting is from one quadrant to another. For example if the indexes array for the points in the LUQ has values [1,2,3,4,6,9,10,11], then the difference array will be [1, 1, 1, 2, 3, 1, 1]. This means that the process remained stationary in the LUQ for 3 consecutive times, then jumped to the RLQ, remaining there 1 instance and then came back to the LUQ (2nd instance, a total of 2) and returned to the RLQ for 2 instances before it came back to the LUQ (3rd instance, a total of 3) where it finally stayed for 2 more consecutive times. We gather these instances in a histogram and normalize each bin by the number of occurrences to obtain the distribution of noise-to-signal transitions and the proportion of times spent in each quadrant of high or low noise along with the proportion of shifts. These distributions are shown in Figure 5.2.G for each quadrant.

5.0.4 Results

Regimes of Motion and Temperature in Activity *vs.* Sleep

The characterization of the motion and temperature regimes corresponding to activities and sleep cycles indicate that during active deliberate sessions the body tends to move within higher regimes of angular velocity ranging on average between -14.90 and 29.58 (deg/s) across the body. The temperatures corresponding to these regimes of active motions range between 27.04 and 34.34 (°C). In contrast, the spontaneously generated motions registered during sleep cycles were found to range between -20.83 and 26.17 (deg/s) corresponding to temperature regimes of 29.53 and 37.92 (°C). For example, panels in Figure 5.3 illustrate general differences in range of motions between activity and sleep cycles across the temperature ranges registered by one sensor. Active exercises display rotational motions across all degrees of temperature but sleep cycle isolates the motion to specific temperature regimes in the two extreme intervals registered.

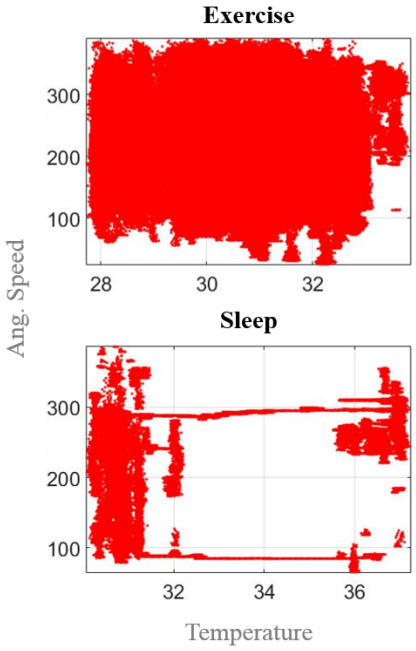

Figure 5.3: **Angular speed as a function of temperature for sleep and exercise session.**

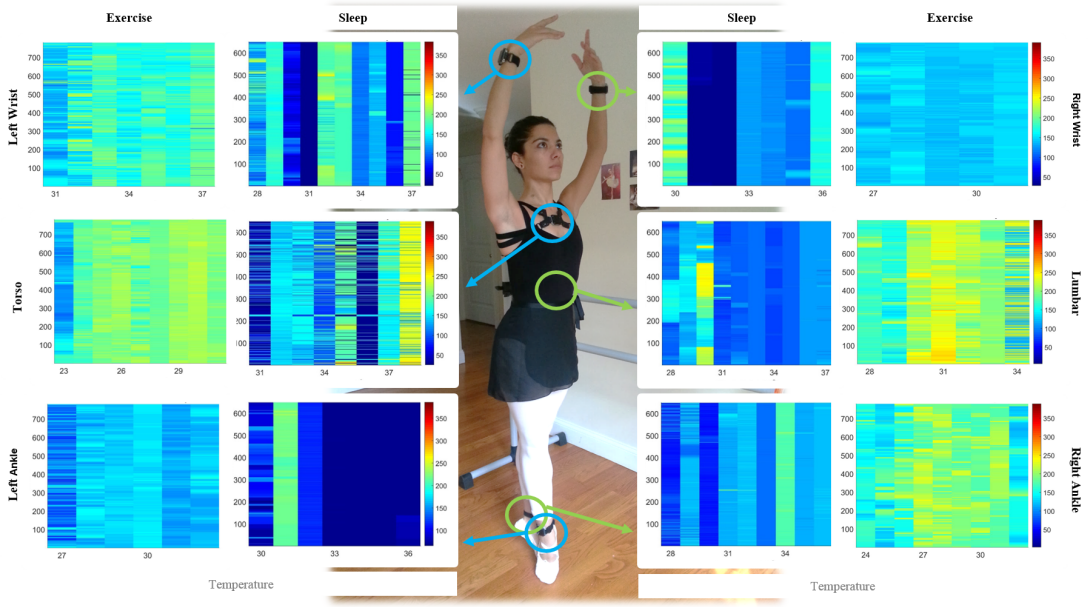

Figure 5.4: **The matrices of maximal deviation from the estimated Gamma mean of angular speed for sleep and exercise sessions. The columns correspond to temperature intervals increased by one and the rows of half-minute segments (30sec).**

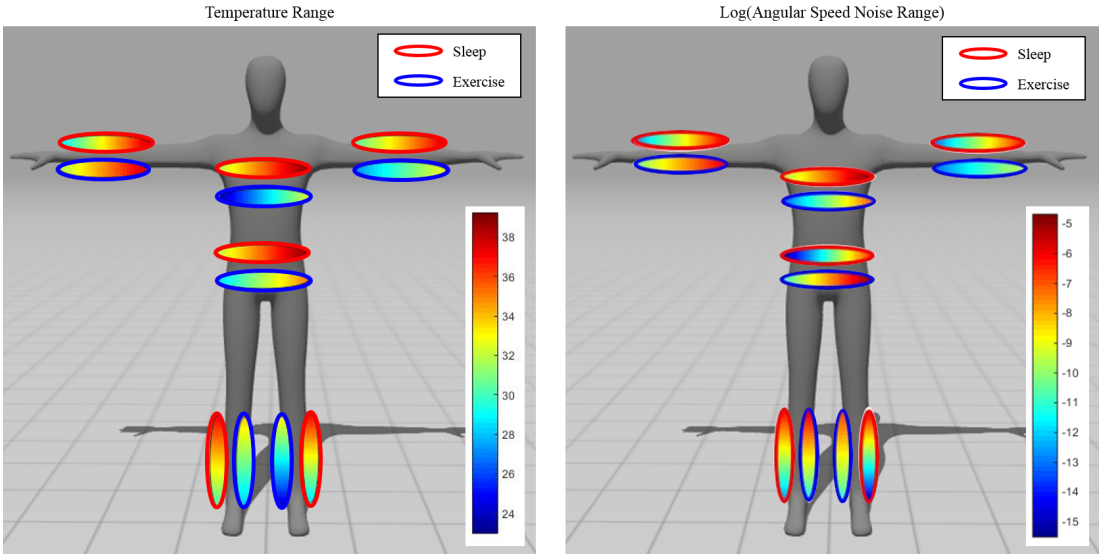

Figure 5.5: **Temperature Range: The range of temperature (C$^\circ$) for sleep and exercise across the different body-parts. Log (Angular Velocity Noise Range): The range of noise of sleep and exercise as extracted by the Gamma distribution analysis of speed-dependent fluctuations.**

Deliberately performed actions have a noise level of $1.8 * 10^{-6}$ to $9.71 * 10^{-5}$and distributions with shape ranging between 60.61 and $1.31 * 10^{4}$ in the symmetric range of the Gamma plane. Spontaneously generated motions during sleep are characterized by noise to signal ratios of $1.62 * 10^{-7}$ to $1.5 * 10^{-3}$ and the shapes tend to 1.88 to $1.07 * 10^{4}$ values.

Mapping Temperature and Noise-to-Signal Regimes Across the Body

The range of temperature values changes across the body with marked differences in the torso and lumbar regions between active practice and sleep. These differences can also be appreciated in the ankle regions, which are highly impacted by pointe exercises during the day, and display marked changes at night. Figure 3 shows the temperature-dependent matrices for all landmarks corresponding to the sensors' locations on the dancer's body. The corresponding summary ranges of temperature and noise-to-signal regimes are displayed in Figure 5.5.A and 5.5.B respectively. These plots show the marked contrast between active motions during the exercises and spontaneously generated motions during sleep. For

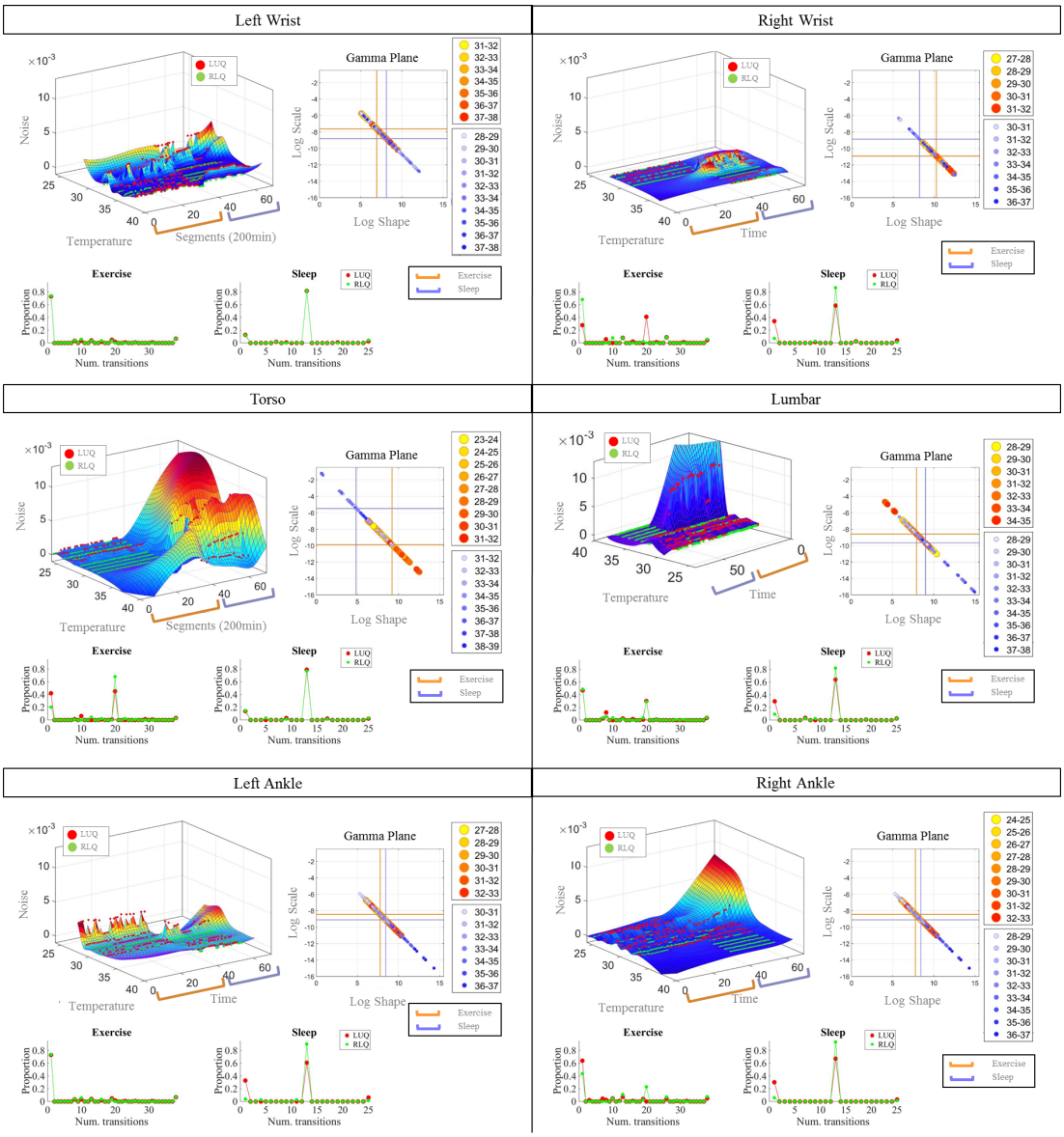

Figure 5.6: **The Gamma plane of sleep (dots with blue shades) and exercise (dots with red shades) data for each of the body-parts. The orange crossed lines correspond to the median values of the exercise data and the blue crossed lines correspond to the median values of sleep data. The 3D surface displays the distribution of noise across time and different degrees of temperature. Each of the time segments is 200min long. The first 38 segments match to the exercise session (orange bracket) whereas the rest of the segments match to the sleep segments (blue bracket). The red dots correspond to the high noise values classified by the median values of the dataset they belong to (sleep or exercise) and the green dots correspond to the low noise values. The lower two figures demonstrate the proportion of transmissions between the two quadrants for the exercise data only.**

	Exercise				Sleep			
	Lowest Noise		Highest Noise		Lowest Noise		Highest Noise	
Body part	Temperature	Blocks (200min)	Temperature	Blocks (200min)	Temperature	Blocks (200min)	Temperature	Blocks (200min)
Right wrist	32	6	29	19	35	41	33	47
Left wrist	36	1	33	20	35	60	31	40
Torso	31	23	28	16	33	42	37	60
Lumbar	34	5	35	7	37	61	32	42
Right ankle	33	4	27	6	37	59	29	63
Left Ankle	30	2	28	6	32	53	31	39

Table 5.1: **This table illustrates the exact temperature degree and time block that the lowest and highest noise was reached for both exercise and sleep.**

example, the torso's temperature range and values during sleep are significantly narrower than during the exercise phase. Likewise the noise levels of the torso during exercise are significantly lower than those during the sleep. The dancer controls the torso's motions during the routine practice but during the sleep cycle the torso spontaneously moves much more and the motions are random and noisy.

Figure 5.5 shows the ranges mapped across the body. During the sleep cycle, the spontaneous motions of the torso reach high levels of noise ranging between $4.732 * 10^{-4}$ and 0.0097 (versus exercise where the noise ranges from $1.833 * 10^{-6}$ to $9.796 * 10^{-4}$) with shapes in the skewed range tending towards the memoryless Exponential. This denotes more random fluctuations during sleep take place in the torso region than those registered in other parts of the body. For example the wrists and ankles move during sleep between -4.12 and 25.74 (deg/s) but those motions in the sleep have high noise content that separate them from their counterparts during deliberate performance times when the rotations are highly structured with minimal noise ranging between $2.13 * 10^{-6}$ and 0.0093.

Automatic Quantifications of Noise-to-Signal Transitions Across the Body

In addition to the summary maps of distributions of temperature and noise levels across the body, the tracking of noise-to-signal transitions over the 11.5 hours of exercise and sleep is possible using these methods. Figure 5.6 provides an example of the visualization of

	Exercise				Sleep			
	Lowest Noise		Highest Noise		Lowest Noise		Highest Noise	
Body part	Raw Speed	Normalized Speed	Raw Speed	Normalized Speed	Raw Speed	Normalized Speed	Raw Speed	Normalized Speed
Right wrist	144.28 - 157.31 (13.03)	0.50 - 0.51 (0.01)	138.23 - 163.61 (25.38)	0.49 - 0.54 (0.05)	100.37 - 111.22 (10.85)	0.50 - 0.50 (0)	0.44 - 1.92 (1.48)	0.47 - 0.75 (0.28)
Left wrist	149.23 - 201.56 (52.33)	0.50 - 0.52 (0.02)	130.45 - 243.26 (112.82)	0.41 - 0.61 (0.2)	101.18 - 110.42 (9.24)	0.50 - 0.51 (0.01)	32.40 - 117.25 (84.85)	0.33 - 0.70 (0.37)
Torso	203.28 - 218.16 (14.88)	0.50 - 0.51 (0.01)	140.80 - 221.14 (80.34)	0.47 - 0.58 (0.11)	130.79 - 167.79 (37)	0.50 - 0.53 (0.03)	3.89 - 178.85 (174.96)	0.04 - 0.90 (0.86)
Lumbar	188.49 - 223.34 (34.85)	0.50 - 0.52 (0.02)	110.86 - 256.65 (145.79)	0.37 - 0.68 (0.31)	108.96 - 110.82 (1.86)	0.50 - 0.50 (0)	64.10 - 183.90 (119.8)	0.37 - 0.68 (0.31)
Right ankle	118.94 - 214.18 (95.24)	0.50 - 0.52 (0.02)	141.33 - 232.38 (91.05)	0.44 - 0.61 (0.17)	119.64 - 123.93 (4.29)	0.50 - 0.52 (0.02)	48.54 - 97.68 (49.14)	0.40 - 0.63 (0.23)
Left Ankle	136.29 - 156.54 (20.25)	0.50 - 0.51 (0.01)	71.00 - 184.88 (113.88)	0.44 - 0.67 (0.23)	201.1 - 224.51 (23.41)	0.50 - 0.51 (0.01)	66.48 - 158.99 (92.51)	0.40 - 0.67 (0.27)

Table 5.2: **Summary of the physical ranges of speed and the normalized scale for the window of time that returned the lowest and highest noise values for the exercise and sleep session.**

the surfaces fit to the scatter of points generated with the 200min block and 5min sliding window. In each sensor it was possible to identify the LUQ and RLQ regions separating hours during the day when the noise was at its highest regimes from hours during the day when the signal was at its highest. The distributions of the noise to signal transitions and their frequency along with the quantification of the proportion of times when the process remained in each of the LUQ and RLQ provided an automatic way to classify the temperature regimes and the time periods of the day when the signal was most reliable and predictable because of statistical regularities. In this sense, we were able to identify the body parts, where the dancer's spontaneous motions during her sleep were maximally noisy and separate within the hours of active exercise when she performed in the most efficient ways. For example, Table 5.1 summarizes the regimes of temperature and the times of the day when the signal from the motions was at its highest and contrasts these with the regimes of temperature and the time of the day when the opposite pattern emerged.

5.1 Discussion

This work introduced a new data type and methods that enable the tracking of the shifts in stochastic signatures of physiological bodily rhythms during different cycles of daily

activities. In particular, we use the active rehearsing of ballet routines and the spontaneous motions during sleep to illustrate the use of these new data type and analytical methods. The study employed light wearables that unobtrusively permitted the recording of natural motions in a dancer while combining signals from rhythms reflecting the ebb and flow of voluntary control (velocity dependent) as well as that reflecting fluctuations in autonomic control (temperature dependent) during the day.

The integration of these signals and the tracking of their non-stationary statistics provided an outcome measure of performance that quantified the noise-to-signal transitions as the nervous system of the dancer actively controlled its self-generated motions and as it spontaneously moved during the night sleep. They revealed periods during rehearsal when the signals had high statistical regularities and distinguished those from highly random and noisy periods. Likewise, the methods were able to show the physical bounds corresponding to these noise-to-signal regimes. For each body part the dancer could know exactly within which temperature bounds and motion ranges her body was for each noise-to-signal state. This information could help her improve performance during the training, but also know how much resting she was getting at night during her sleep.

5.2 Conclusions

The study presented in this chapter opens up new horizons on integrating bodily signals. The new data type and research done in the present and previous chapter could be used for combining other signals such as heart rate with movement (Chapter 7) or audio and heart-rate (Chapter 10). Other possible directions are to integrate movement with heart-rate or brain-waves [76]. Moreover, this study revealed the need for real-time visualization of the extracted information so that to be comprehensive by the participant in a vision-driven co-adaptive set-up. Therefore, in the next chapter, we present the step-by-step development of an avatar aiming to demonstrate the real-time "mirrored" image of the participant endowed with color coded information extracted in the present and previous chapter. This way, in

our future work we will be able to close the loop in the co-adaptive interface by augmenting visual information and substituting other sensory modalities.

5.3 Appendix

1. Temperature dynamics during the dance routine of a ballet student versus her sleep following her practice: `https://youtu.be/WHpjJ0Fn5qE`

Chapter 6

Avatar: a Real-Time Visualization Tool of the Full Body

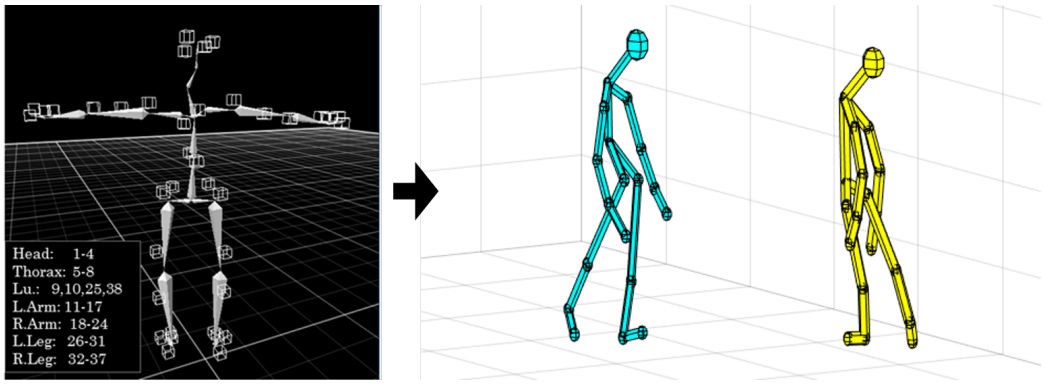

Figure 6.1: **Schematic Avatar Development: Shifting the position data extracted from Recap Software of PhaseSpace system to an in-Matlab developed avatar.**

The continuous tracking and analysis of the bodily signals acquired from the full-body generated the need for visualization tools. Specifically, we were in need of creating ways to illustrate the moment-to-moment estimated parameters coming from various sources across the body in a creative but also meaningful way that could be easily decoded by the participant to have an understanding of the physical conditions detected on their body.

In this chapter, I present the development steps of an in-Matlab build avatar which allows the coloring of its body-parts for visualization purposes. I describe possible uses of this idea such as vision-based co-adaptive interfaces, clinical applications, and visualization of an a posteriori analysis, and I discuss limitations that vision-based interfaces may put over other sensory-modality-driven systems[42].

6.1 Building an in-Matlab Avatar

Utilizing the proper visualization tool on a vision-driven interface is critical. To find a way to augment or substitute lost sensations in our research visually, I created an artificial human that will represent the participant's motion in real-time similarly to a mirror. This visualization will be the 3D-representation of the participant's existence (mirror is 2D) augmenting his corporeal sensation. By building this avatar in Matlab utilizing functions such as $cylinder(x, y)$ and $spere(x)$ I could additionally access the color parameter of the object and map it on color as it was done in the cell of the matrix in Figure 5.4. This way I could expand the concentrated information shown in Figure 5.5 to a real-time unfolding visualization as shown in the video in the Appendix of Chapter 5, but instead of the elliptical schema I could color the exact body part.

To develop the avatar, I used the forward kinematic map modeled on the arm and presented in work [105] and expanded it in full body. The equation of the recursive kinematic map is:

$$Bd_n = Bd_{n-1} + \Pi_{m=1}^{m=n} R^m * [0, 0, L_n] \tag{6.1}$$

where Bd_n is the position vector, R_n the rotation matrix, and L_n the length of the body-part n. The kinematic chain starts from the hips, body-part number 0, and unfolds to the rest of the body as shown in Figure 6.2. The code of the kinematic map was developed in Matlab.

From the motion capture equipment, I registered the position data of the (Fig. 6.6 and 6.4) or the skeleton (Fig. 6.3). In the case where I only had access to sensor position data, I had to estimate the positions of the bones approximately. Indeed, the use of skeleton data streamed out directly from the software of the corresponding equipment gave more realistic results. The approximate estimation of the skeleton from the sensors in our interface was done by averaging the positions of the sensors (ex. Use the 4 sensors of the head to estimate

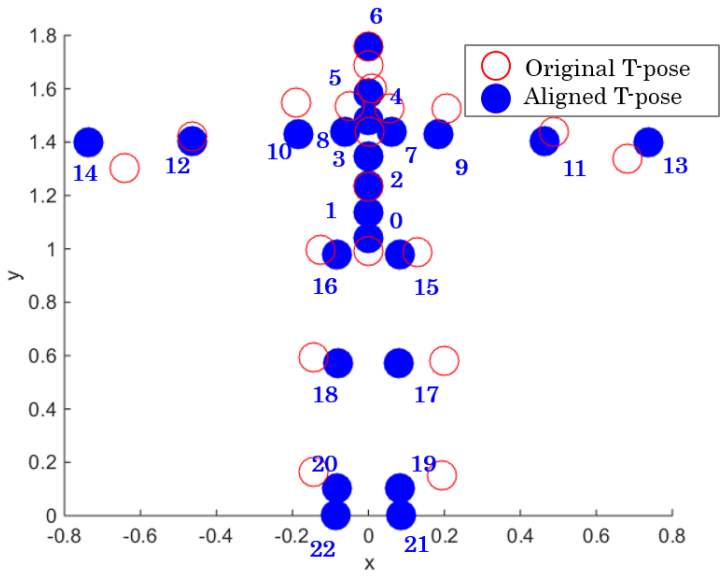

Figure 6.2: **Visualization of the original (red points) and re-aligned (blue points) body-part positions which match the initial orientation of the avatar. The numbers next to the points correspond to the sequence of the kinematic chain.**

the center of the scalp) (Fig. 1.1 left), placing sensors directly on the joints (shoulder, elbow, knees, e.c.t.) and assuming that body limbs have the same length. This way I could build realistic-looking virtual humans, Fig 6.5.

To align the initial avatar orientation with the orientation of the participant, I asked our participant to take T-pose, Figure 6.2. This was also the posed used from PhaseSpace equipment to build the Skeleton of the subject. Once the participant's body and the avatar's orientation were aligned, and the offset-orientation for each pair of body-parts was estimated. Then, the real-time visualization could unfold.

6.2 Uses of the Color-coded Avatar

6.2.1 Vision-driven Real-time Co-Adaptive Interface

The initial idea for the utilization of this tool came from the need to build a vision-driven co-adaptive interface Fig. 6.3).

This set-up used the PhaseSpace equipment which was able to estimate the skeleton

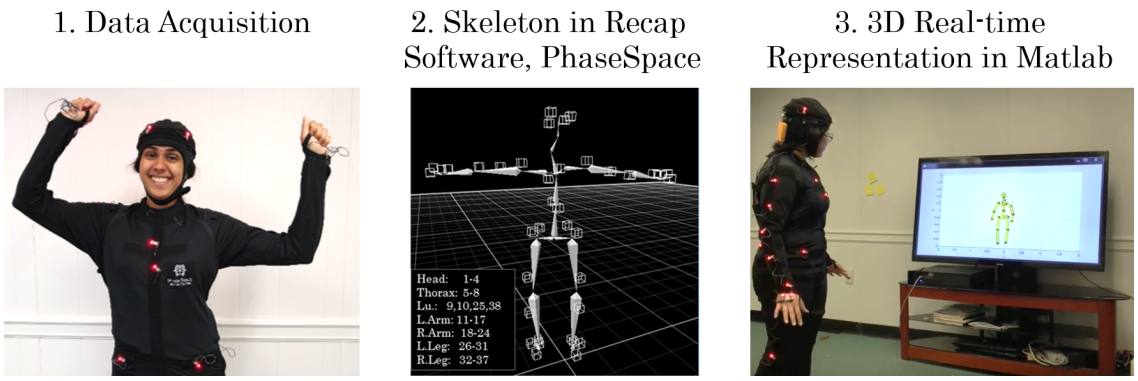

Figure 6.3: **The steps for the avatar development when using PhaseSpace system. First, the participant wears the LED-costume (step 1). Then, I activate the connection of the server with the wireless control to stream data to Recap software. In the Recap, I build the skeleton of the participants by asking them to take T-pose (step 2). Next, I stream the skeleton data to Matlab where I build the 3D avatar. A sample video of the interface can be found in Appendix video 2.**

data and streamed them in real-time to the Matlab developed interface. This application was used for the study presented in Chapter 7. Although in this work, the avatar was not used for representing color-coded information but only for augmenting the 3D corporeal sensation of the subject. Therefore, the impact of the visual body augmentation was not examined. Nonetheless, conducting research that involves the color-coded version of the avatar is within the lines and priorities of our future experimentation.

6.2.2 Clinical Applications

In a longitudinal study conducted in SMILab (part of the findings are presented in Chapter 1.4) I used the avatar in the a posteriori analysis to visualize moment-to-moment variabilities of parameters such as mean, variance, skewness, and kurtosis extracted from the positional data and its higher order derivatives in scalar form (linear speed, acceleration, etc) and the orientation data (angular speed, acceleration, etc). I examined the fluctuations in amplitude and timing of the peaks of these time series and estimated the distributions that best fit the continuous data expressed as a random (point) process (Appendix video 1).

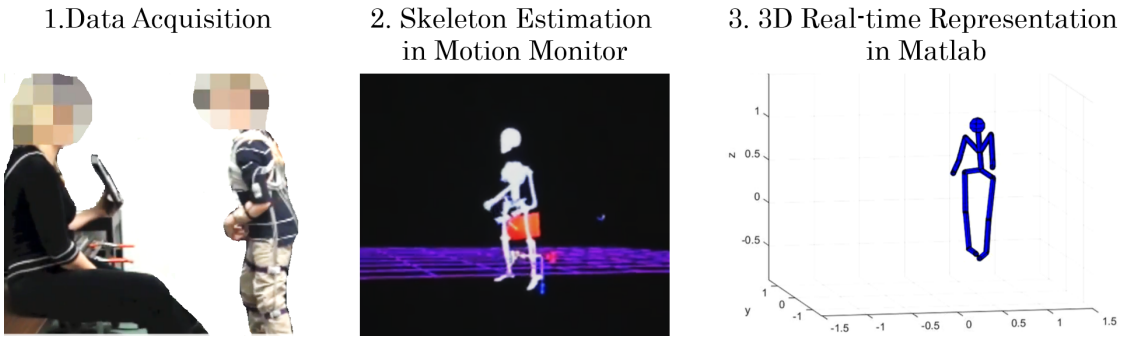

Figure 6.4: **The steps for the avatar development when using Polhemus and Motion Caption system. Step 1: Place the Polhemus wired sensors (** *polhemus.com* **) on the participants and collect walking data. Step 2: Use the Motion Monitor software (** *www.innsport.com* **) to build the real-time skeleton. Step 3: Apply the forward kinematic map to build the avatar in an off-line analysis. The video can be found in Appendix video 1.**

The study was investigating the impact of a drug in an impaired motor-control system of children with Phelan McDermid Syndrome. Each participant made a total of 5 visits. I examined baseline, and drug or placebo visits, and post-visit (wash-out phase). In the a posteriori analysis of the data (It could have been done in real-time given the technology we have built today), I visualized the variabilities of the four-moments (mean, variance, skewness, and kurtosis) in a moment-by-moment manner and for each visit separately. Such video could be used by a clinician who needs to access the actually performed motions as well as the underlining parameters and compare the results across visits (Appendix video 1)

6.2.3 Other Uses

Another a posteriori use of this tool is demonstrated in the video of the Appendix in Chapter 9. In this study, I used the avatar to visualize the synergies across the dancers bodies as they unfolded during the complex dance and the non-dance portions (while they waited, performed T-pose or plan their next routine). These patterns for each body and the coupled network were self-emerging sub-networks from the modularity analyses of the

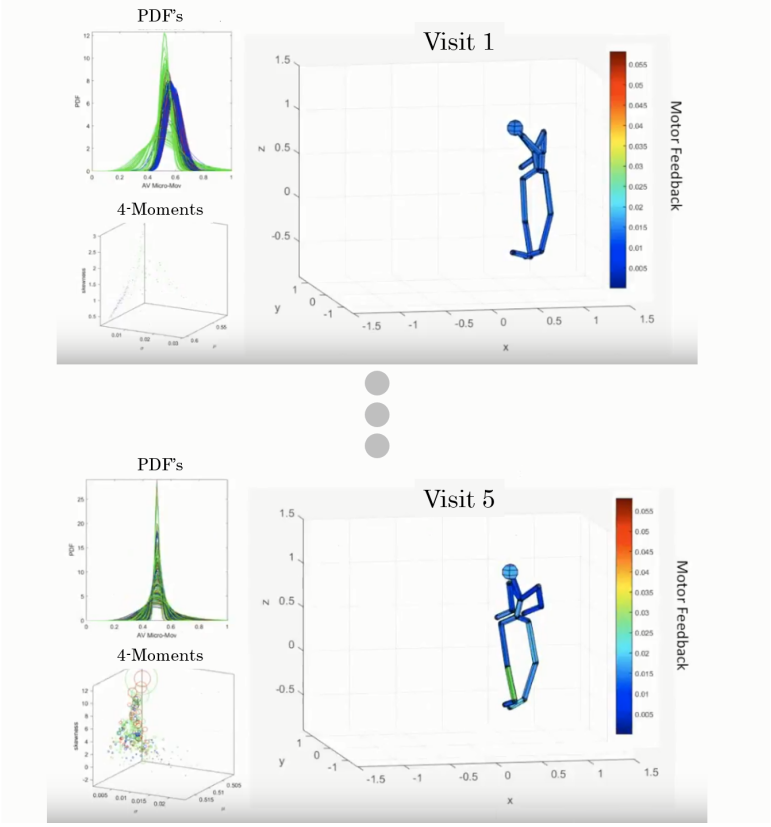

Figure 6.5: **A sample of the visualization of visit 1 and 5 from the clinical application of the avatar. The video of the unfolding variability can be seen in Appendix video 1.**

weighted directed graphs used to derive the adjacency matrices representing the network and its connections. Each joint is a node and each interconnecting piece an edge of the graph (see Fig. 9.7 for full description). I used the noise-to-signal (Gamma distribution dispersion) values empirically estimated for the conditions dancing and non-dancing to color code the modules that the network connectivity analyses uncovered.

6.3 Conclusions

In this chapter, I presented the steps for developing an in-Matlab virtual human that allows us to color-code its body parts based on the corresponding variability of the studied parameter.

1. Real Performance

2. 3D Real-time Representation in Matlab

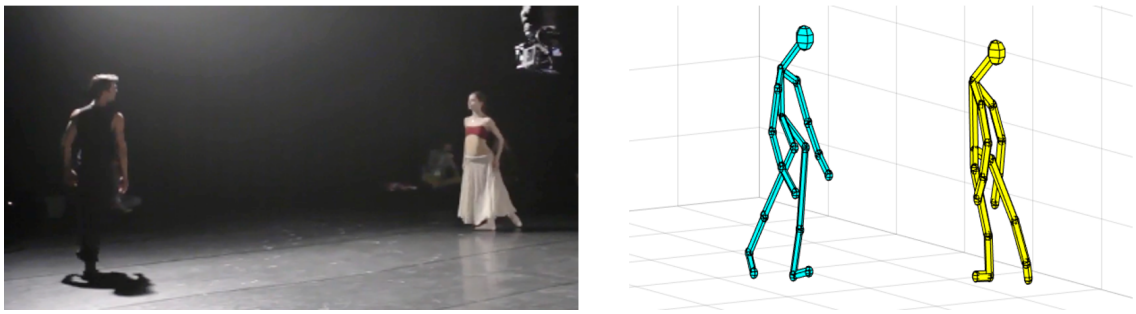

Figure 6.6: **The development of the avatars for the purpose of body network representation during ballet partnering, which is going to be elaborately presented in Chapter 9. The corresponding videos can be seen in the Appendix of Chapter 9**

I built this visualization tool to track the bodily motions as they unfold in vision-driven co-adaptive interfaces. I extended its use to various other concepts underscoring the need of visualization tools when complex motions are involved in the research. These ranged from the clinical domain to artistic training (ballet). Moreover, I was able to map variability across the body in a single session as well as longitudinally. Indeed, there will be even more studies that could make use of this tool, given the nature of our scientific approach which examines full body information from moment-to-moment.

Despite the advantages of this tool and the many possibilities it has open for further research, I discovered some interesting caveats with the use of an avatar as a way to substitute lost sensation with vision. The set-up of such interface creates spatial restrictions, which emerge from the use of the monitor. Specifically, the participants will have to stay within proper distance from the monitor to be able to see and extract the information needed. Also, they will have to maintain their orientation towards the monitor in order not to lose contact. These are all limitations that an individual would not experience if we were using another sensory modality to send feedback, for example, the auditory. Moreover, processing the position data to estimate the forward kinematic map adds delays to the rendering of the graphics, which, even though, are not significant, can reach a level of awareness and

be detected by the participant. In the future I plan to explore different avenues of visual perception to quantify several aspects of the influences of such delays on the perception of the self and one's own actions. These will be relevant to the neuro-scientific aspects of autism and social interaction problems the children have. The lab has found that many of those issues can be traced back to disruption with temporal dynamics of the 'social dance' between the person (agent) and others. My tools can be used to address those issues in a formal quantitative manner.

In the research I will present in the following chapters I broaden our interest towards co-adaptive interfaces that rely on the audio channel with the plan to augment to audio-visual domains in my postdoctoral work.

6.4 Appendix

1. Clinical application of the avatar visualization tools: `youtu.be/kZnKD5w2BmQ`

2. Vision-driven co-adaptive interface: `youtu.be/IVf-BPaODM4`

Chapter 7

Extracting Sensory and Contextual preferences

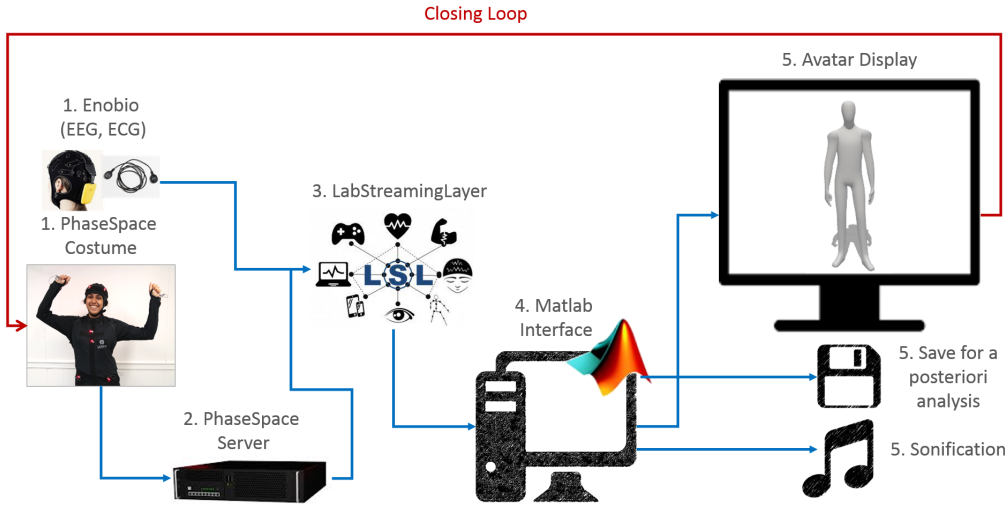

Figure 7.1: **Loop of co-adaptive/interactive audio-visual-kinesthetic interface and visualization tools (avatar-based).**

One of the challenges of movement Neuroscience has been to design methods that allow the extraction of sensory or contextual information from the continuous motor stream. The efferent motor stream is not only an output signal, but also serves as kinesthetic afferent input to the brain, helping in the control of ongoing motions. As such, sensory-motor flow is experienced together, integrated with every behavior we perform. How could we detect sensory differences and separate sensory from motor components in ongoing motions? This paper introduces methods and experiments that enable the automatic selection of preferred sources of sensory guidance extracted from the ongoing motor output stream during walking. Extracting such information from a participant's system could critically contribute to close the co-adaptation loop and steer the individual's systems towards desired

regimes. I illustrate the methods and results with two participants, one neurotypical and one with Asperger's syndrome [44].

7.1 Extracting Sensory and Contextual Information from the Motor Stream

The principle of reafference by Von Holst and Mittlestaedt [31] states that *"Voluntary movements show themselves to be dependent on the returning stream of afference which they themselves cause"*. Empirical evidence concerning the influences of past voluntary motions on future intended actions has given rise to the notion of internal models for action (IMA) [56][111][46]. Along those lines, it has been theorized that the brain creates internal models of its own self-generated dynamics and adapts them, generalizing from one situation to another. Indeed, this branch of computational motor control has been very fruitful to design questions about motor learning and generalization across different contexts. One aspect that remains challenging in this field of research is how to automatically separate from the reafferent stream, the sensory from the motor components. Anatomically, motor afferent and motor efferent signals travel through different fibers [8], yet functionally, they are integrated and dynamically changing from moment to moment and from context to context.

Part of the challenge (Fig.2.15) has been in the analyses of biophysical rhythms harnessed with instrumentation to capture motor dynamics and kinematics in natural behaviors. Most methods apply a grand averaging technique to the waveforms extracted from movement trajectories (e.g. continuous streams of speed temporal profiles or acceleration data, electromyographic data, etc.) The averaging of parameters from epochs of behavior tend to smooth out as noise the minute fluctuations in the sensory-motor stream. Yet, we submit that these fluctuations reflect changes in context, sources of sensory guidance, novelty of the situation, among other aspects of the sensory-motor signals. We posit here that these fluctuations could in fact be a very useful source of information to automatically extract sensory and

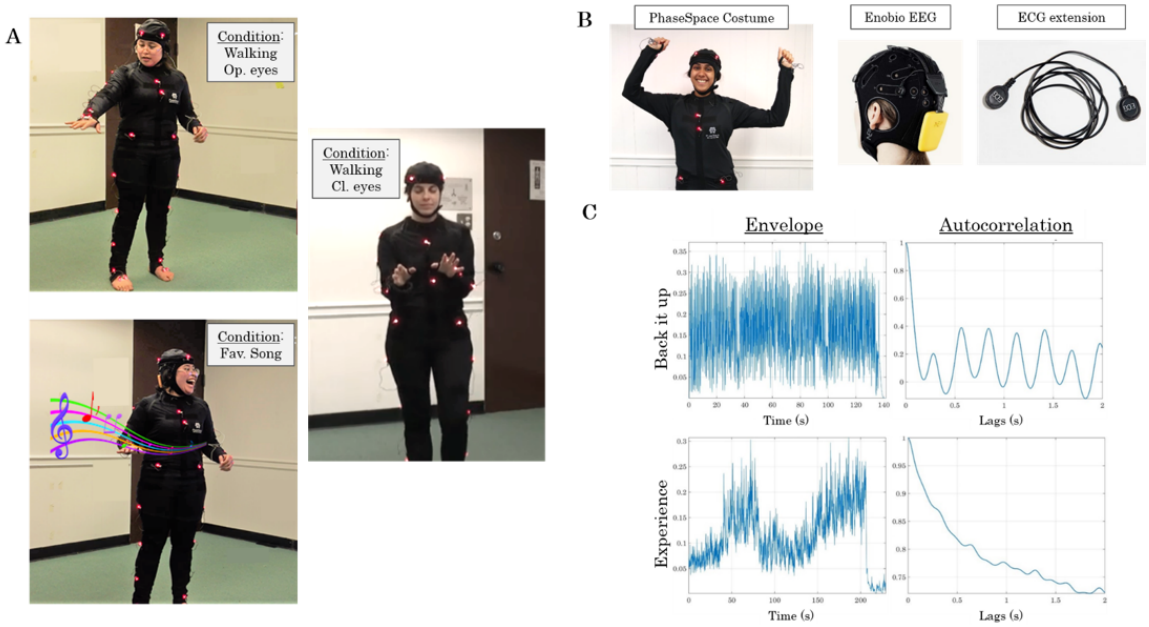

Figure 7.2: **Experimental Setup and Instrumentation. (A) Sample conditions: walking with open eyes, closed eyes, and music. (B) Phase Space active LEDs suit and Enobio wireless wearable head cap to extract ECG signals. (C) Signal processing of audio signals to reveal structure and sound characteristics.**

contextual information from the ongoing sensory-motor stream, and to further confirm the system's preference along a given sensory channel. To address these questions, we use a rather automated task involving walking within different contexts and using different types of music as auditory guidance.

7.2 Experimental and Computational Details

7.2.1 Experimental Design and Interface

Participants

Two young male adults participated in this experiment, one neurotypical and one with a clinical diagnosis of Asperger's syndrome (24 and 19 years old) respectively. Both signed the consent form approved by the IRB of Rutgers University, in compliance with the Helsinki act.

Experimental Tasks

A natural, automated walking routine was used as the underlying activity performed under different contexts, designed to manipulate the stream of sensory input: walking with eyes closed (to enhance proprioception); walking with eyes closed and music (to further enhance auditory input in the absence of vision and the presence of kinesthetic reafference); walking with eyes open (audio-visual and motor kinesthetic streams naturally coexist); walking with eyes open and music whereby the participants were exposed to audio but could also see an avatar moving endowed with their own real-time motions (audio-visual and motor reafferent streams are naturally enhanced)(Appendix video 1). Fig.7.2.A shows examples of the set up.

Instrumentation

The PhaseSpace Impulse (480Hz San Leandro, CA) was used to record bodily positions using 20 active LEDs on a wearable body and head suit. The Enobio EEG wireless wearable system (500Hz, Barcelona, Spain) was used to record the heart signal extracted from the EEG waveforms (Fig. 7.2.B),Appendix video 1. More specification about PhaseSpace and Enobio EEG can be found in Section 2.2. The music was played back through the Matlab interface (Matlab version 2016b, The MathWorks, Inc., Natick MA, USA.) and the musical feature extraction was done using the MIRtoolbox 1.7 (https://www.mathworks.com/matlabcentral/fileexchange/24583-mirtoolbox)

Sensory Stimuli

Several music types were used to enhance audio experiences. Two were pre-selected and played to both participants. The other was the favorite song of each participant. The songs common to both participants had different features: One was a pop song (`https://youtu.be/MYZ45VDNIrI`) with rhythmicity. The other was contemporary classical (`https://youtu.be/MYZ45VDNIrI?t=2m28s`), emotionally engaging and with escalating structure.

The favorite song provided a check on the methods, as it was used to confirm audio preference extracted from the sensory-motor stream. (We reserve the analyses of visual stream with the avatar use for other publication). Audio feature extraction and autocorrelation analyses were performed to characterize the auditory sensory stimuli and parameterize their stochastic signatures Fig.7.2.C (see explanation in next session.

Co-adaptive Interface and Visualization Tools

An interface was designed to create the sensory-motor loops and provide our control over the stimuli as we parameterized it. Figure 7.1 shows the schematics. Enobio and Phase Space streams were mediated by the Phase Space Sever as inputs to the Lab Stream Layer interface (https://github.com/sccn/labstreaminglayer) to synchronize all sources and input them to a Matlab interface performing the stochastic analyses for empirically-driven parameterization of the stream signals and play back to the user the avatar endowed with the real time motions and audio. These forms of audio-visual and kinesthetic sensory feedback present in the continuously outgoing motor stream were systematically parameterized, tracked and manipulated in the motor output stream self-generated by the end-user (Fig. 7.1 red arrow).

7.2.2 Standardized Data Type

Modeling Micro-movement as Spikes Trains

The motion trajectories of the body were converted to time-series of kinematic parameters (we focus on the speed temporal profiles here Fig. 2.5A, as the heart and EEG signals will be presented in other publications) and their overall mean empirically determined using maximum likelihood estimation (MLE) to select the best continuous family of probability distribution functions (PDF) that fit the frequency histograms of their peaks (more detail Chapter 2).

7.2.3 Micro-movement Spike Trains Represented by Continuous Gamma Process

Here we adopted a continuous Gamma process to represent continuously processed blocks of these fluctuations using a relaxed independent identically distributed (IID) assumption, whereby overlapping running windows of micro-movements were taken with a block size of 5seconds with overlapping sliding window equal to a random Gamma value (generated by the shape and scale values describing the distribution of the data) times the sampling rate of the data (500Hz). This block size ensured enough peaks to perform MLE with tight confidence regions (95%) for each estimated distribution parameter.

The continuous Gamma family fits the data well and was used to estimate the shape and scale parameters and build stochastic trajectories represented on the Gamma parameter plane (Fig. 2.11.E) with inset showing the estimated PDFs color codes by quadrants in this case. This trajectory included all 20 bodily sensors.

Tracking NSR and the Rate of Change of Stochastic Transitions

Then, we tracked the NSR and examined the rate of change in stochastic transitions as described in Chapter 2.

Cumulative information

The Gamma is an exponential family representing an additive random process. As such, here we accumulate the values of the log-shape and log-scale parameters across the blocks (continuously overlapping sliding widowed data) data and automatically extract body parts and conditions as their clusters in the scatter self-emerge on the Gamma log-log plane.

7.2.4 Visualization Tools

Synthesized Parameter Spaces

The representation of the empirically estimated scatter of Gamma shape and scale parameters (with their Gamma Parameter Plane Quadrants) and the fitting-line information along with the cumulative values of the empirically estimated parameters are summarized into two parameter spaces: (1) The plane spanned by the LUQ-RLQ ratio vs. Gamma Slope and (2) The plane spanned by the cumulative slope p vs. the Mean fitting (δ) residual error. Further, non-parametric analyses of these statistical indexes were performed using the Kruskal-Wallis non-parametric ANOVA to confirm the significance of the results from the stochastic analyses.

7.3 Results and Discussion

7.3.1 Statistically Significant Separation of Body Parts and Condition Preferences

The Gamma process analyses revealed an exponential trend in the data from all 20 body parts and across all 7 experimental conditions. Fig. 7.3 shows the exponential trend for the hip (torso area in the avatar inset) across all 128 blocks of data spanning 2.5 minutes in a full session. Here the reader can appreciate the tendency of an increase in the estimated Gamma shape value (towards symmetric distributions) accompanied by the decrease in the NSR. The log-log plot of the cumulative sums across blocks of overlapping windowed data is shown in the insets for all 20 body parts and each condition. Each color represents a body part, with arms (magenta) and legs (yellow) as the most predictive and lowest NSR signatures. The stochastic shifts were quantified in each condition according to the line-fitting slope and LUQ/RLQ ratio. Fig.7.3 shows the (color-coded) division between LUQ and RLQ for the hip marker.

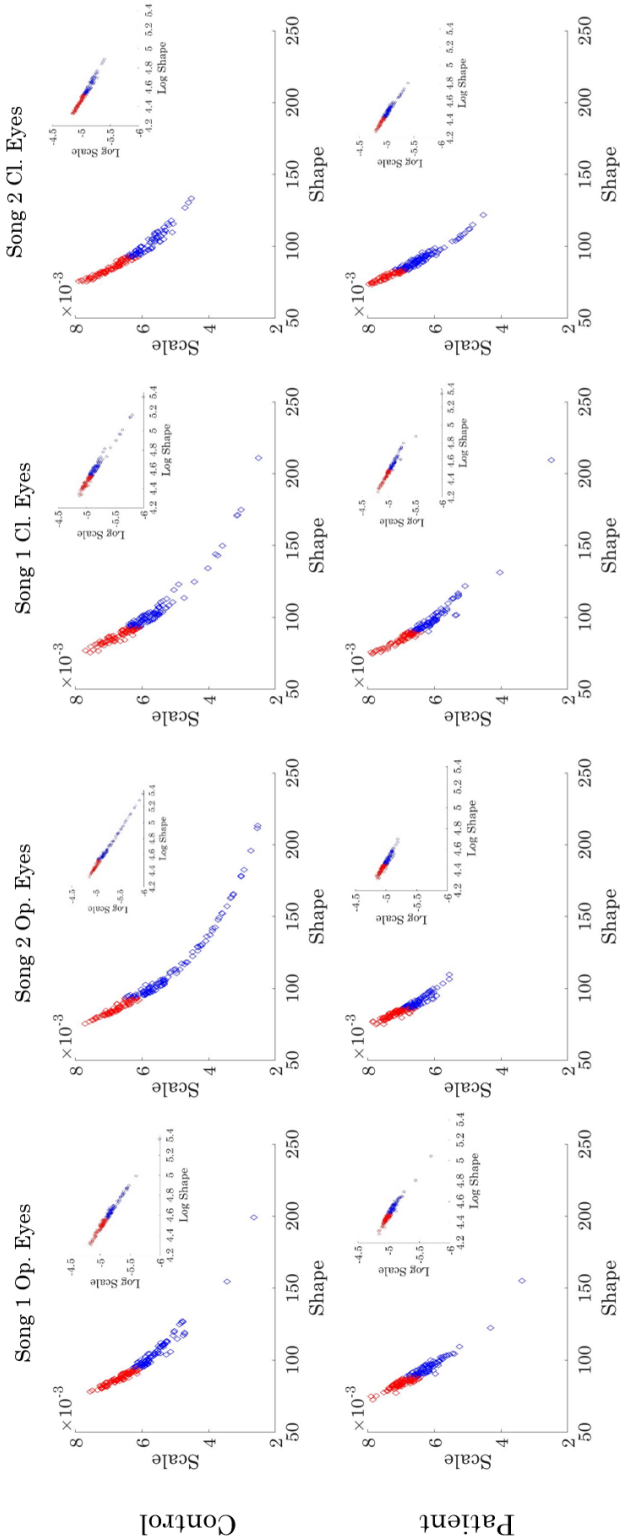

Figure 7.3: **The stochastic map on the Gamma parameter plane of the evolution of the signatures across the experimental session. The hip joint is used here for visualization. Insets highlight the cumulative metric involving the slope of the linear fit to the log-log of the scatter across all body parts.**

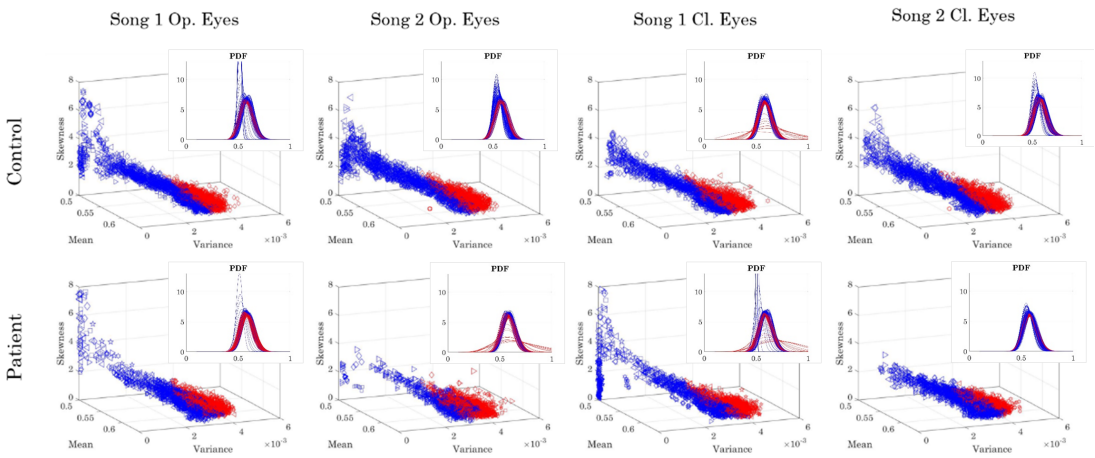

Figure 7.4: **Estimated Gamma moments and PDFs (insets) for all body parts. Colors highlight the LUQ (red) and RLQ (blue) automatic divisions based on the median statistic. The LUQ corresponds to higher variance along the y-axis.**

Across all body parts and conditions statistically significant differences for each estimated Gamma moment highlight the most predictive regimes with the lowest NSR Fig. 7.4

This information was then used to ascertain the LUQ/RLQ ratio and perform statistical analyses comparing the two participants; the various conditions and the different body parts. Exhaustive testing then pointed us to the body part that best performed in the precise sense of having the lowest NSR and the highest symmetry in the distribution (most uniformly distributed parameter values). Further, other indexes and parameter spaces revealed details on how to separate contextual information (e.g. walking with eyes closed vs. walking with eyes open) from auditory sensory preferences (listening with the eyes closed vs. listening with eyes open while walking.) For the same bio-mechanical task (walking) the patterns of fluctuations from moment to moment pointed to fundamental differences in sensory processing and integration within the motor output stream.

Table 1 reports the output of statistical analyses of variance on the motor fluctuations of the walking task across all conditions and body parts for each participant. Note here that this is a personalized assessment, such that each participant is profiled separately testing

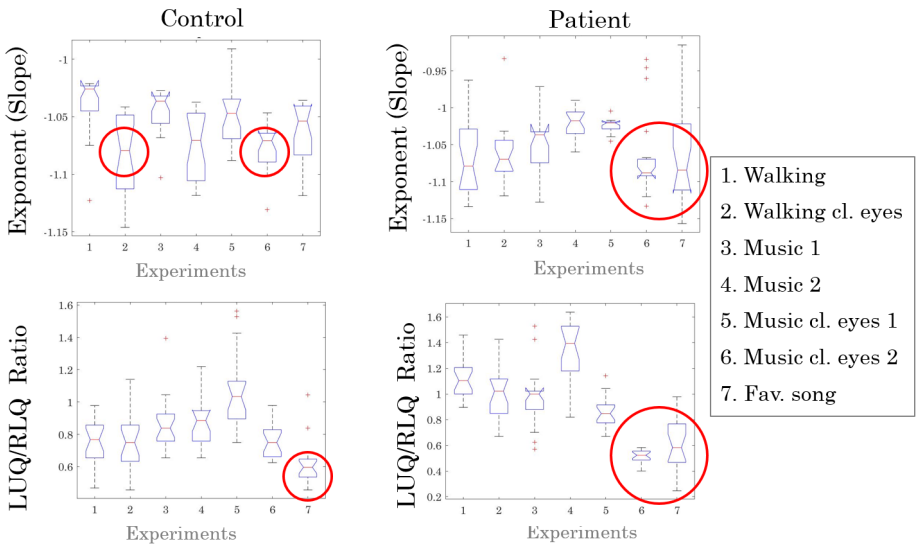

Figure 7.5: **Kruskal-Wallis Test. (A) The exponent (slope) of the linear fit to the log-log Gamma scatter. (B) The LUQ-RLQ ratio. Circles represent the highest rate of change towards the RLQ (low NSR and towards Gaussian predictive regime) in A and the highest frequency of points in the RLQ. These features define the preferred sensory context as the enhanced proprioception and favorite song for the control and patient.**

Table 7.1: **Statistical Significance of comparing four moments across all body parts to differentiate general effects of experimental conditions (columns) over body parts (rows) between the two participants.The non-parametric one-way ANOVA-Kruskal Wallis test.**

		Control		Patient	
		Chi-sq	Probability¿Chi-sq	Chi-sq	Probability¿Chi-sq
Compare Across Body Parts	Mean	78.58	$3.25 * 10^{-9}$	34.79	0.014
	Variance	62.74	$1.41 * 10^{-6}$	52.51	$5.45 * 10^{-5}$
	Skewness	81.93	$8.62 * 10^{-10}$	43.11	0.001
	Kurtosis	80.95	$1.28 * 10^{-9}$	76.42	$7.64 * 10^{-9}$
Compare Across Conditions	Mean	18.48	0.005	41.77	$2.04 * 10^{-7}$
	Variance	43.87	$7.87 * 10^{-8}$	60.85	$3.02 * 10^{-11}$
	Skewness	17.44	0.007	37.19	$1.62 * 10^{-6}$
	Kurtosis	15.09	0.019	21.98	0.001

Table 7.2: **Statistical Significance of Comparing Best Sensory Context using Kruskal Wallis Non-Parametric ANOVA. Columns are conditions and rows are the participants' 20 body parts with corresponding signatures.**

Case	Participant	Chi-sq	Probability¿Chi-sq
Exponent	Control	45.72	$3.4 * 10^{-8}$
Exponent	Patient	37.87	$1.2 * 10^{-6}$
Ratio	Control	58.87	$7.6 * 10^{-11}$
Ratio	Patient	98.42	$5.4 * 10^{-19}$

the column effects of sensory and contextual conditions. Effects on the body parts were also significant and further explored (see reports in Table 2 and Fig.7.5).

The visualization of the cumulative results can be appreciated in Fig.7.6 for all body parts. The resulting scatter self-clusters the shape and scale parameters across the blocks of data constructed from the continuous stream of motion in blocks of 5seconds. The size of the overlapping sliding window was a random Gamma value (generated by the shape and scale values that characterizes the data set) multiplied by the sampling rate of the data. This trend whereby as the shape increases in value (i.e. the distribution is more symmetric), the NSR decreases in value, helps us interpret the quadrant ratios below. For each body part along this line-fit of the accumulated log-log parameters, we obtain the slope and intercept and compute the LUQ/RLQ ratio to localize the frequency of the points in the scatter of each body part per each condition.

The results concerning the parameter spaces representing the LUQ/RLQ ratio vs. the Gamma slope fitting each log-log Gamma parameters' scatter across all 20 body parts and across all windowed data is displayed in Fig.7.7. There we can appreciate for each experimental condition involving auditory stimuli, that the ratio values below 1 expressing the highest predictability and lowest NSR regimes give out sensory preferences. Notice here that the favorite song condition was precisely incorporated in this paradigm as a "sanity check" to confirm our statistical analyses. Indeed, in both participants the favorite song and the enhanced music experience with eyes closed automatically emerge as the preferred

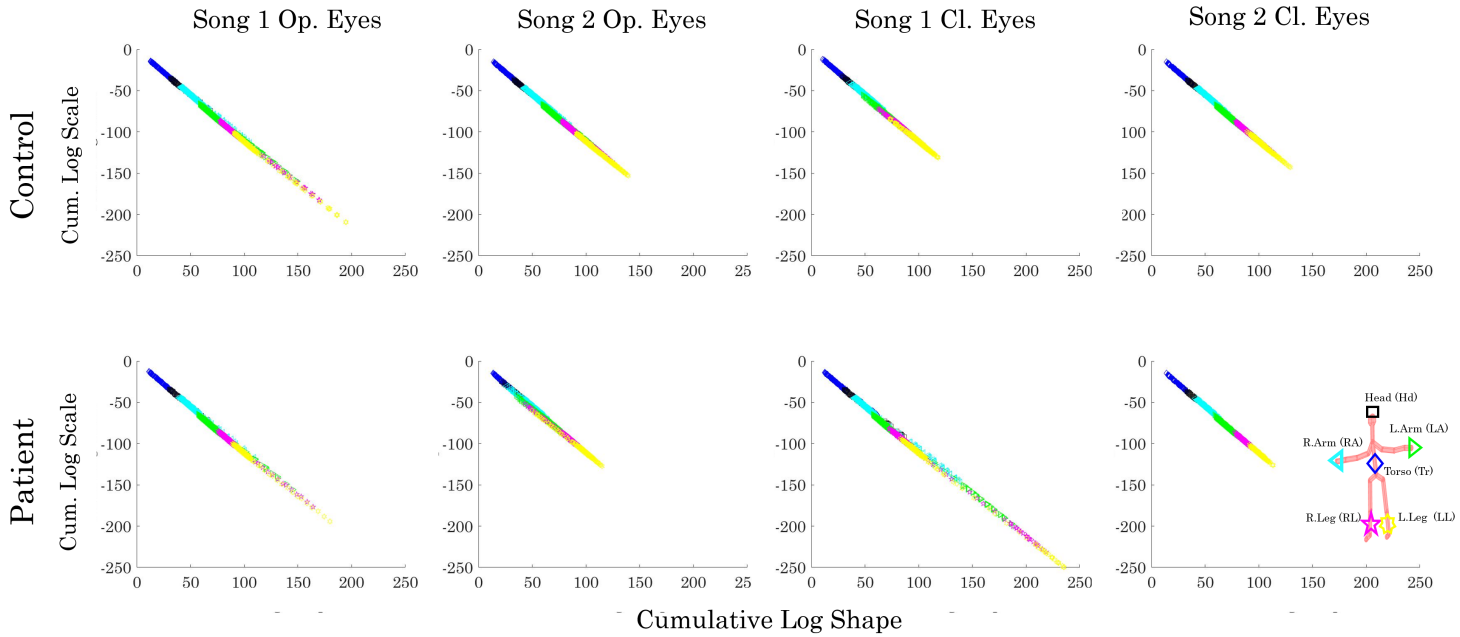

Figure 7.6: **Cumulative log-shape and log-scale automatically self-clusters body parts and reveals differences across task contexts and auditory sensory inputs.**

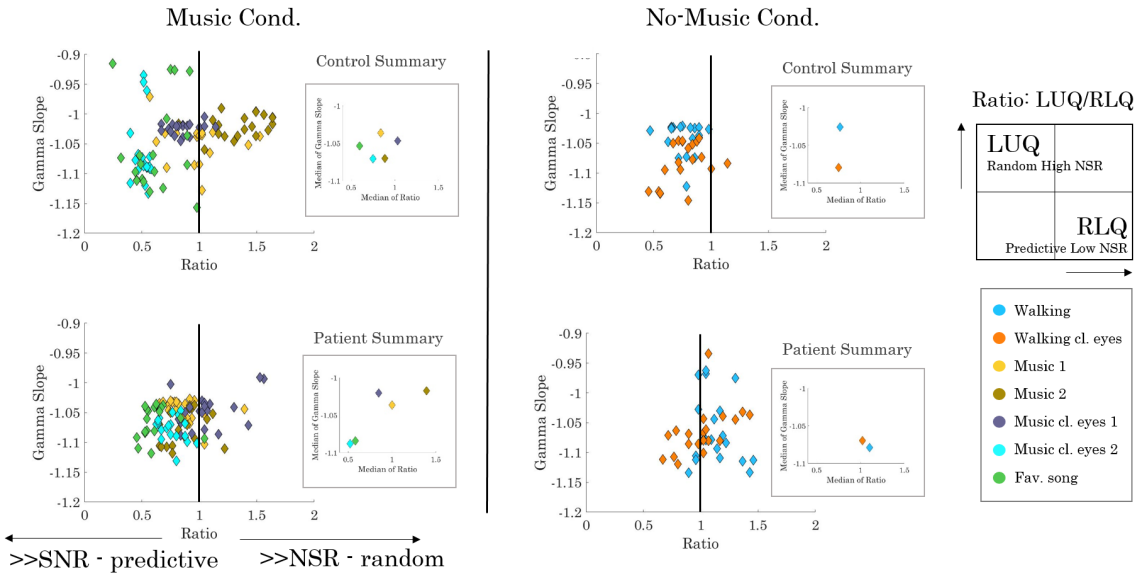

Figure 7.7: **Parameter space from indexes reflecting the Gamma scatter slope of the log-log shape and scale parameters vs. the LUQ/RLQ ratio. Insets reflect summary median values for each condition taken across all 20 body parts.**

sensory contexts.

In both cases, we can automatically extract this information from the motor output stream, as the participant senses its own kinesthetic reafference and audio input (Fig. 7.7.A). Along the vertical axis, the parameter space reflects the highest rate of change towards the RLQ (absolute value of the slope above 1) and along the horizontal axis, the highest frequency of points in the RLQ (LUQ/RLQ ratio below 1). Recall here that each estimated point encompasses hundreds of measurements of fluctuations in linear speed peaks' amplitude and spans an empirically estimated Gamma PDF family (the scatter from the overlapping windowed data). Insets in Fig.7.7 show the summary median values across the 20 body parts for each of the 5 audio-present conditions.

Likewise, for the conditions where no music was present, the bodily biorhythms from the control participant reveal a preference for enhanced proprioceptive experience. This is evident in the prevalence of the scatter below the LUQ/RLQ ratio value of 1, while having a median slope value with absolute value above 1. The patient's median signatures

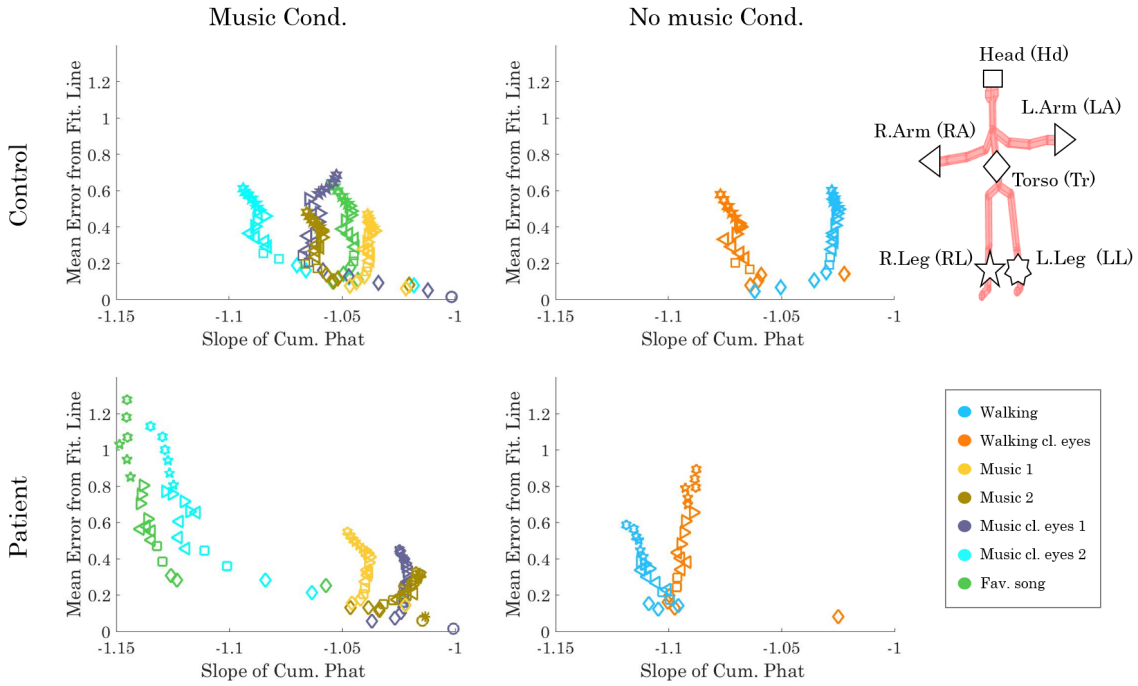

Figure 7.8: **Parameter space from indexes reflecting the slope of the cumulative log-shape and log-scale linear fit for each body part and condition vs. the mean residual error for the fitting line. Conditions and body parts separate automatically into clusters that reveal contextual preferences and sensory enhancement of the motor streaming signal.**

(inset in Fig.7.7.B) without music reveal higher prevalence in the random-noisy regimes (i.e. LUQ/RLQ ratio above 1) and faster convergence to this regime on average, for the natural walking condition with eyes open. Zooming out for individual body parts in Fig.7.7.B informs us of several markers' signatures in the walking with eyes closed condition (enhanced proprioception) that parts of his body do better when the eyes are closed.

7.3.2 Extracting Preferred Sensory Input from the Motor Stream

Inspection of the parameter plane spanned by the slope of the cumulative values of the linear fits the log-log shape and scale scatters along the horizontal axis and the mean error fit from the line reveal a separation of body parts and condition that once again confirms prior results in Fig.7.8.

Each experimental sensory context is separable and provides information about preferences. The condition where proprioception is enhanced (walking with eyes closed) reveals for the neurotypical control a preference with and without music. Under enhanced proprioception, this participant's nervous system's stochastic signatures reveal the highest absolute value of the slope indicating the fastest rate of change towards predictive and high NSR regimes.

The patient shows this is the case for the favorite song condition and the condition of the emotional song (music 2). Nevertheless, the higher fitting error makes this result more uncertain at the extremities than the torso area. This contrasts with the control, who had a tighter fit with lower residual error for all body parts.

7.4 Conclusions

In summary, we have presented new data type and methods of analyses that permit the tracking of the evolution of stochastic signatures derived from sensory-motor signals of the nervous system as the person naturally walks and receives audio signals with and without vision.

Because we derived these spike trains from the fluctuation in the biophysical motion parameters rather than applying grand averaging techniques -so prevalent in movement and behavioral neuroscience, we were able to preserve the information content of these fluctuations and use them to examine how they are modulated across conditions. In this sense, the same walking task, performed in the same room and within the same session (all experiments were done in the same session) funneled out fundamental differences between naturally walking with eyes open vs. walking with eyes closed - a condition where we enhanced the participant's kinesthetic sense of proprioception.

These methods automatically highlight the preferred contexts under different sound manipulations. Across the body, we were able to objectively quantify the preference for the favorite song and compare that to other conditions where audio and visual input also entered in the motor stream. This integrated flow of sensory and motor information had never been separated in the context of a human-avatar interface. As a result, this work is a proof that this can be done and although, in this chapter we do the analyses a-posteriori, it will be possible to build these stochastic trajectories in real time and track the changes in sensory and contextual preferences using the present methods of analyses. In this sense, our work provides methods to allow for the study of sensory-motor processes as they evolve in time, even within the time course of an experimental session in order to close the loop on a co-adaptive interface as it will be explained in the next chapter.

7.5 Appendix

1. Experimental set-up for measuring sound influence on natural movement through bodily physiological signals: `youtu.be/Nx-_Ib-8bFk`

2. Pop and contemporary classical song:

   `https://www.youtube.com/watch?v=MYZ45VDNIrI&feature=youtu.be`

Chapter 8

The Co-Adaptation Loop

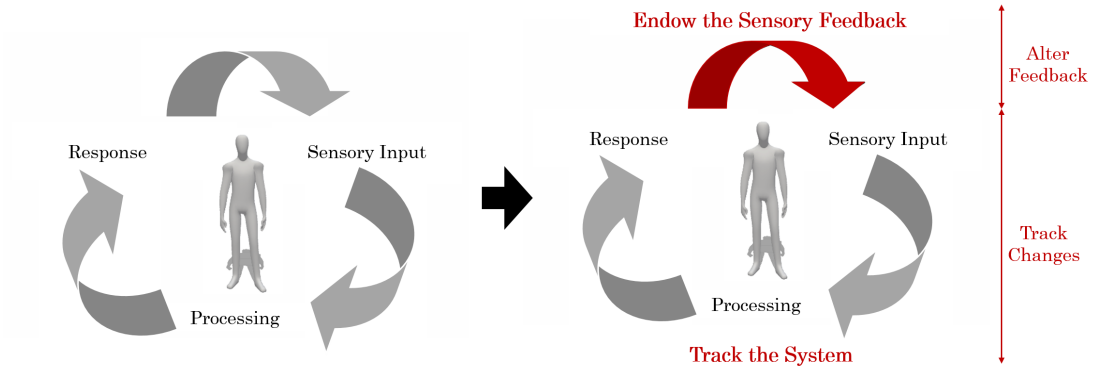

Figure 8.1: **Schematic of the shift from studying the natural co-adaptation loop to studying the steered co-adaption loop generated by an intelligent interface.**

In this chapter,I present the transition from the traditional open-loop to the continuous closed-loop study of the sensory-motor system (Fig. 8.1).I present the core elements that allowed us to close the loop and how I can create interfaces that have the intelligence to lead the participant's system to the desired regimes and which are going to be presented in the following chapters.

8.1 Open-Loop Approach

From Chapter 3 to 7, I presented studies where I investigated the behavior and patterns of human movement under various conditions. These studies were conducted under what I call traditional approach or what I most properly name in Sensory Motor Integration lab, as an open-loop approach.

In the open-loop approach, a study is conducted by setting up various conditions, expose

the participant to them and collect the data. The analysis and processes of the data take place later, where researchers compare the results between the conditions. This is the traditional concept of conducting research, where I ask our participants to perform a specific task under a particular condition, and then an offline analysis is applied to evaluate each condition and task. I named this approached as open-loop analysis (Fig. 8.2).

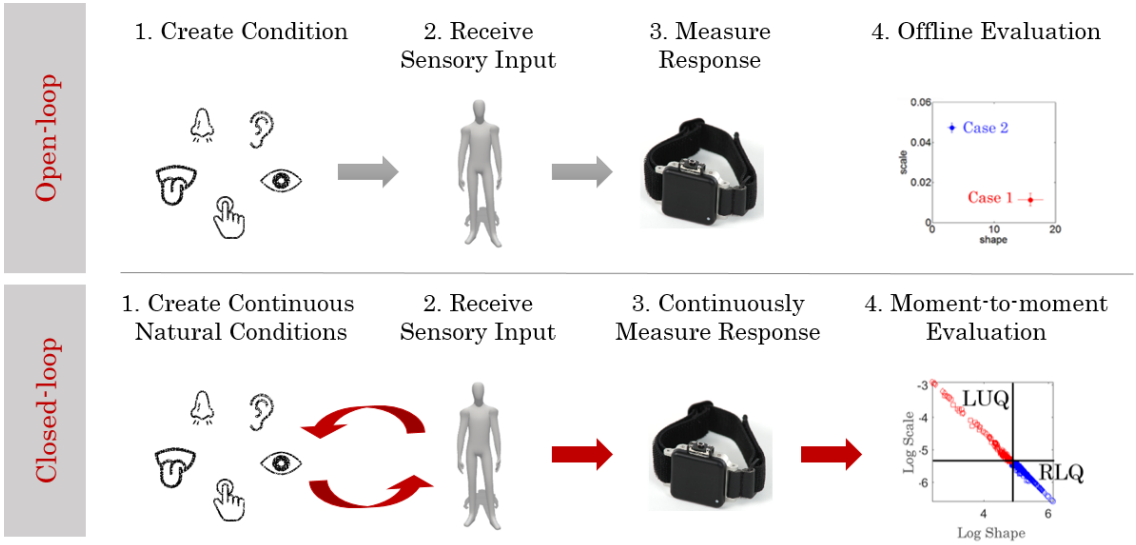

Figure 8.2: **Schematic of the shift from studying the natural co-adaptation loop to studying the steered co-adaption loop generated by an intelligent interface.**

8.2 The Missing Piece of the Open-Loop Approach

The open loop approach is widely used by the scientific community. In fact, this is the way we learn to conduct research. However, there is a missing piece in this approach.

It is broadly accepted that a successful study should be realistic. In other words, researchers should create as natural conditions as possible for the participants, because the closer to the real life a study is the most reliable the outcome will be. Indeed, modern technology has helped us in overcoming spatial restrictions and other limitation that older equipment might put (Chapter 2). But apart from this, as it has already been explained

our sensory-motor system works in a continuous loop with the environment. It continually receives various sensory inputs and generates outputs through the afferent and efferent channels, as explained in Chapter 2. This process is parallel and ongoing. Moment-to-moment variabilities of the incoming stream of the sensory input cause variabilities to the out-coming response (Chapter 1). In the real world, a small variation in one of the incoming streams might create a different reaction from our system. Wouldn't it be more appropriate to study the sensory-motor system as a closed-loop? It is part of its essence anyways.

8.3 The Closed-Loop Approach

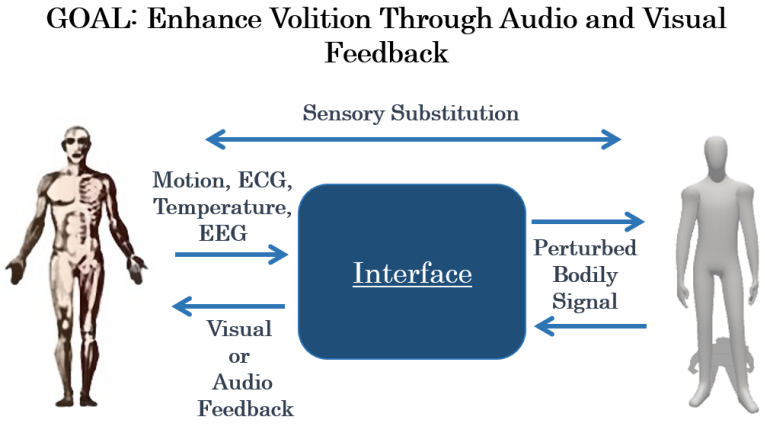

Figure 8.3: **Schematic of the closed-loop co-adaptive interface**

I define the closed-loop approach in the scientific research as a way to examine both the input and the output streams synchronously, analyze the data, evaluate the progress of the co-adaptation and feedback the sensory input in real-time to steer the system towards preferred regimes, Figure 8.3.

The findings presented from Chapter 2 to 5 and particularly the interpretation of the LUQ and RLQ (Section 2.5) have paved the way to develop criteria for judging whether improvement or worsening of the performance can be noted in the unfolding interaction between the participant and the interface[42]. What was missing from our research was to identify how we could select and alter the sensory input so that to steer the system towards

progression. In other words, we had to develop ways to decide which sensory modality is the most motivational and what are the preferences upon this modality that will please the system to perform at its best. These findings came from the work presented in Chapter 7 and these two criteria are named in this chapter as Selectivity and Preferability, respectively.

8.4 Extracting the Preferability and Selectivity of the Sensory-Motor System

We all have preferences, for instance favorite music or favorite colors among other. Our favorite song may lift our spirit and its tempo makes us clean faster our house or our drive to home more joyful. Our favorite color may make us feel nicer in our clothes - more sexy or professional- and this might play a significant role in our psychology in our first date or our job meeting. Indeed, our senses have preferences and they differ from individual to individual. In addition, we all have realized at some point in our life that in some tasks we more visual learners and in some other more auditory. This means that under some specific conditions some sensory modalities work better or faster and we like rely on them more because adaptation gets easier and faster. These are things that we take for granted in our daily life but what if an interface knew these preferences of our system and was immediately adapting to what makes us perform the best.

In Chapter 7, I managed to extract from the analysis of the motor stream the sensory modality that is preferable for the system of an individual, **Selectivity**, and what are the conditions that motivate this modality to perform to its bests, **Preferability**.

Selectivity: Extract from a motor stream the preferred sensory input.

Preferability: The individuals' sensory preferences that motivate their system towards the desired regimes.

Selectivity and preferability are two criteria that could lead our co-adaptive interface to intelligently adjust to the participant's personalized penchant, without going through a questionnaire or discussion in an off-line manner. The interface will be able to detect these likes, adapt to them, monitor the ongoing progress, and even readjust on any new favorites that may reveal during the on-going interaction. Overall the criteria of selectivity and preferability are the key parameters that can convert the co-adaptive interface to an intelligent system that is able to self-adapt.

8.5 Conclusions

Having developed all these methods and tools I was finally able to develop a closed-loop co-adaptive interface which is going to be presented in Chapter 10.

In Chapter 9, I study a natural closed-loop interaction. More particularly, I study the unfolding adaptation of a dancing dyad, two professional ballet dancers, while they perform their partnering choreography. In this study, although the analysis of the data take place a posteriori. The continuous interaction between the dancers: the touches, pushes, and pulls are somato-sensory feedback that is unfolding during the interaction and aim on leading the system (both bodies) towards balanced weight transfers, supports,and good synchronization. This closed-loop system was the perfect paradigm to study the co-adaptation loop, before moving towards the development of our interface.

Chapter 9

Ballet partnering: A Natural Closed-Loop Co-adaptation

Figure 9.1: **Image from the performance of the dancers.**

Partnering in dance is a natural closed co-adaptive loop where each dancer contentiously gives feedback to each other through touches, friction, pushes, pulls, and others to "communicate" about the stability of their unfolding performance. This is the way they develop body connections and they learn to rely on each other their bodies in motion. On these small interactions, invisible to the naked eye dancers can be lifted by or balance on each other creating impressive performances of harmony and flow.

In the work presented in this chapter, I use complex ballet partnering routines to develop new visual tools and analytics that quantify spontaneously emerging coordination patterns in complex naturalistic dyadic exchange. I capture the motions of professional dancers

performing their partnering routines (dancing condition) and contrast the results with their resting-calibration times, or their planning of subsequent routine segments (non-dancing condition). Here I introduce a new parameterization of the bodily movements' trajectories by coherence, phase and frequency and use weighted directed graphs to represent the dancers as dynamically coupled networks unfolding in time. Integrating connectivity metrics with stochastic analyses automatically captures coordination patterns and self-emerging cohesive coupling. Potential applications of this new analytical platform are discussed in the context of personalized medicine, education, basic research and the performing arts,as well as the development of the artificial co-adaptive interface that is going to be presented in the next chapter [40].

9.1 Methods to Track Dynamically Coupled Coordinated Bodies in Ballet Partnering

Successful human social exchange relies on properly coupling the dynamics of biorhythms embedded in speech, facial expressions, gaze, gestures, and body postures. While research involving speech and face-processing techniques in the context of dyadic exchange has been fruitful [113] [114]; there is a paucity of models that tap into the coupled full-body dynamics of dyadic social exchange. Some studies in ecological psychology have empirically addressed inter- and intra-personal interactions [24]. However, the scope of such research has been limited to the study of physical entrainment between the person and the rhythms of external objects [48] [47]. The empirical study of entrainment and bodily synergies coordinating behaviors between two interactive actors in the social realm has been particularly challenging [14] [24] [108]. As such, very few analytical methods exist to automatically assess and visualize the (invisible) coupled dynamics of complex dyadic exchange as they cohesively self-emerge, unfold and dissolve in real time.

The invisible cohesiveness of human bodily interactions synthetizes from the physical exchange between two or more bodies in coupled motion. Yet, such signatures are not

directly measurable by instrumentation attached to either one moving body alone. This is because the biorhythmic activities they give rise to when moving in tandem, tends to create rapport as a derivative of the multi-modal inter-bodily synergistic activity. The spontaneously self-emerging rapport evolves dynamically as the interaction unfolds. To quantify these hidden rhythms, or to characterize them in some way, we would need to explore unconstrained coupled motions in actors as they unfold in real time. This approach would allow us to tap into spontaneous minute fluctuations of movement parameters that are largely unknown to current motor-control physiology research focusing on planar goal-directed motions [88].

Movement parameters from motions involving activities of daily living, finger tapping and drumming for example are reportedly generating activities in low frequency ranges ([26] [53]), up to 20-30Hz range. But because of grand-averages that impose a theoretical mean from a priori assumed symmetric distributions, this blind averaging acts as a sort of strainer that filters out small and highly frequent variations that are inherently present in naturalistic movements of various classes (e.g. deliberately or spontaneously performed motions) [88] and see Appendix Figure A1.

The grand-averaging approach to motion analyses in motor physiology has not been empirically informed. It has tended to smooth out as noise the minute fluctuations in the amplitude and timing of the motor signals and discarded as nuisance the spontaneous segments of natural behaviors. However, when employing other statistical approaches to examine motor variability in its full richness and harnessing such highly frequently encountered fluctuations in spontaneous aspects of our behaviors, the so-called noise, becomes valuable signal to classify, treat and track outcomes of nervous systems disorders [93] [95] [112].

The new findings from examining motor variability and highly frequent minute fluctuations in motor performance have contributed to the contemporary personalized platform of Precision Psychiatry [100] and helped us expand our knowledge on social human (dyadic)

exchange in the context of autism spectrum disorders (ASD) [76] [103] [110] . Yet, other areas of human interactions that could enhance our understanding of cohesion remain largely under explored.

Social dyadic exchange has applications in Human Computer Interaction (HCI) and Artificial Intelligence (AI.) These fields may be more familiar with these issues than researchers in motor-control physiology because to them it is critical to uncover the mechanisms behind spontaneous aspects of social dyadic exchange. In AI researchers aim at recreating the type of human social rapport that self emerges in conversation, to endow artificial agents with socially-valid interactions. As such they study possible differences between verbal and non-verbal actions that take place during conversations [28] [58] [67] [68] [78]. Such studies reveal differences between (verbally) active exchange and passive, subtle gesture-based exchange [65] supporting the notion that in a social interaction there is more than meets the eye.

Research in AI has also demonstrated the utility of endowing robots and avatars with aspects of gaze and human facial micro-expressions that would escape conscious description by a human observer [13] [27] [29]. Such additions have enhanced the quality of the dyadic interaction between the human and the artificial agent by creating more realistic exchanges between the two agents. Moreover, attributes from natural behaviors inclusive of spontaneously emerging synergies are now routinely incorporated into computer programs driving robots and avatars in Virtual Reality (VR)-based interfaces [6] [15] [35] [114]. Nonetheless, because we cannot directly quantify the synthesis of this self-emergent wholesome coupling, we do not understand or know how to mechanistically explain it or model it. Indeed, most aspects of what makes an interaction look natural are explicitly extracted from the human motions and endowed to the artificial agent using long, cumbersome heuristics that cannot possibly cover all cases that transpire beneath human awareness.

What are the empirical ranges of parameters characterizing self-emergent social cohesiveness leading to rapport dynamics? Can we measure them as patterns of bodily coordination-dynamics spontaneously form and dissolve? If we were to study such patterns in naturalistic, unconstrained contexts like those in complex ballet partnering, we may at the very least empirically inform new models of AI and robotics about non-voluntary, spontaneous aspects of our actions that nevertheless significantly contribute to the development of agency and volitional control [103] [102] [90]. The type of empirical work that we bring to the reader's consideration, is important to complement and combine in artificial agents, the explicit programming of deliberate, goal-directed movements with the ability to develop spontaneously self-emerging cohesive patterns found in real human dyadic exchanges. In this paper, we introduce new methods for the general study of complex coupled dynamics from physical dyadic exchange. We cast the problem in the context of ballet partnering and physically measure individual patterns of synergistic activity from each dancer. We uncover patterns from the synthesized cohesiveness that their partnering spontaneously gives rise to and use their routines as our testbed to develop new biometrics of rapport dynamics self-emerging from coupled dyadic exchanges.

9.2 Methods and Motivation

Owing to the complexity of the human body, its abundant degrees of freedom (DoF) [7] and the multiple ways in which the same action can be accomplished [86] [105], it is difficult to computationally model synergistic behaviors in one body, let alone automatically computerize them within the context of partnering dance. To address such complexity and facilitate the empirical study of natural actions with abundant DoF, we offer a new parameterization of continuous biophysical signals from the nervous systems; new statistical techniques for personalized behavioral analyses and new representations to visualize in real time synergistic activities that spontaneously self-emerge and self-dissolve in coupled behaviors.

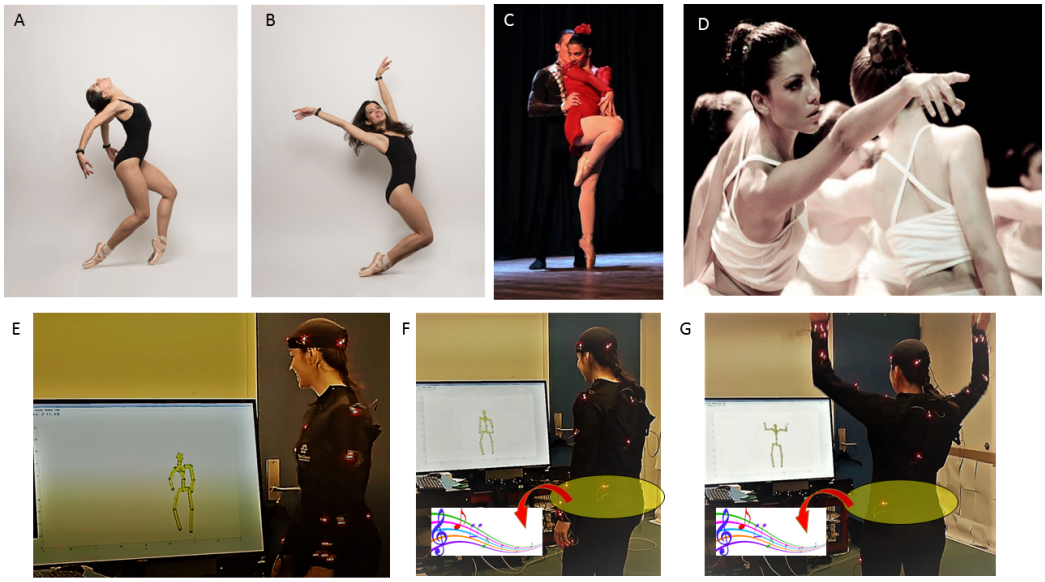

Figure 9.2: **Coordination of complex patterns of behavior in multiple settings. (A-B) Maintaining and controlling difficult postures. (C) Building synchronous synergies in dyadic exchange. (D) Maintaining a harmonious flow in a crowd of dancers performing a choreography. (E-G) Hybrid co-adaptive interfaces integrating artificial agents (avatar) and human using audio-visual means to guide the interaction. In this setting the person's task is to find a region of space that plays music when the hip enters the volume we program to that end (marked with the ellipsoid.)**

In the context of synergistic bodily modules, we see them emerge in ballet as the individual's body sustains complex postures up against gravity (Fig. 9.2A and B), as a dyadic exchange occurs with a partner (Fig. 9.2C), as a group of actors interacts to form fluid choreographic patterns, some of which are physical and some of which are derivatives of the physical exchange (Fig. 9.2D). Self-emergent coupled behavior leading to cohesiveness is also important when end-users interact with avatars in artificially created multi-modal co-adaptive environments. Such environments can be used to evoke social exchange mediated by audio-visual-kinesthetic feedback (Fig. 9.2E-G) [41] [42]. These subtle spontaneous behaviors that we can probe in artificial contexts also manifest during actual social dyadic interactions [99] [110] and could provide the bases of new tools for diagnoses of mental illness.

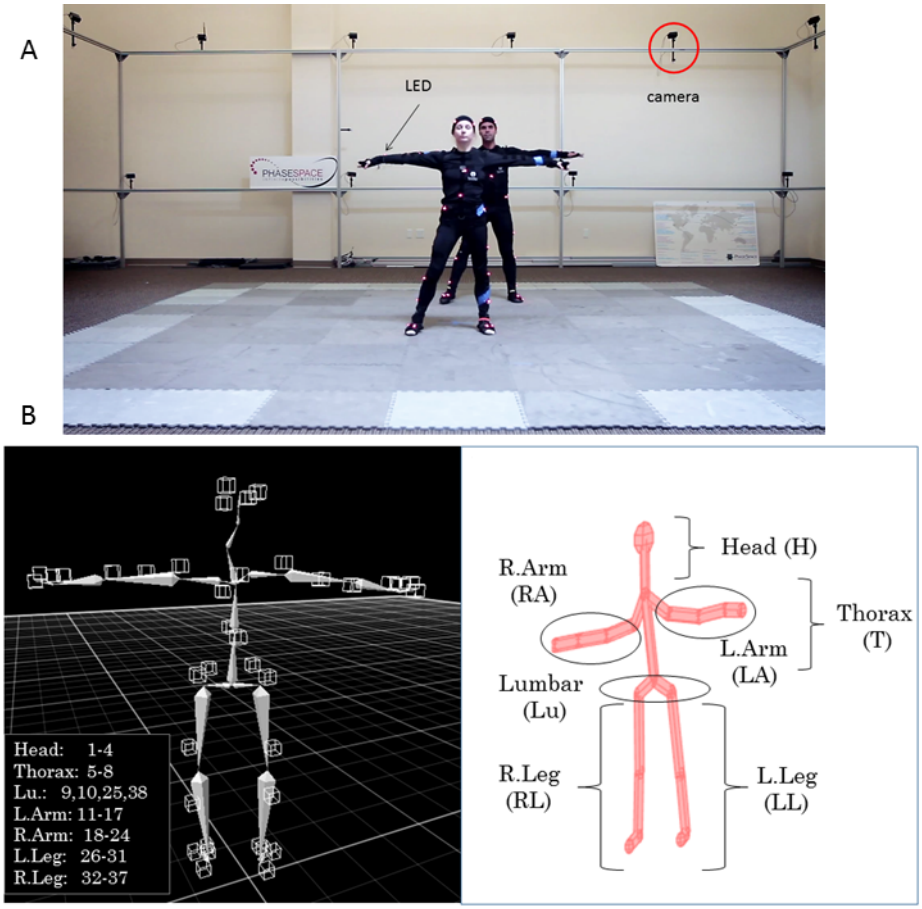

Figure 9.3: **The data collection and representation tools. (A) Two professional dancers in T-pose while being calibrated within the Phase Space. Cameras capturing the motion are marked and suits contain 38 LEDs in each dancer's body. Data is sampled at 960Hz. (B) Left panel: Skeleton showing the distribution of LEDs from 1-38 across the body segments. Right panel: Avatar designed using a forward kinematics model to track the various parameters of interest (see the movie from the Phase Space and Bot and Dolly in Link 1 of the Appendix.)**

The dance pieces that we present include segments of independent dancing (dance different choreographies without making any physical contact), synchronized dancing (dance same choreography without making any physical contact), and interactive dancing (dance affecting each other, e.g. get or give support to the other person, push, pull, and lift each other, among others). We pool these segments and coin them the dancing condition. They require timely and deliberate coordination and synchronous (synergistic) activities between the two dancers. They have been rehearsed many times. They are staged, and their staging is continuous from beginning to end. Appendix Table 9.2 lists all the subroutines that we use with the frames of interest for the dances and the main ranges of the parameters of interest. The last column provides links to videos of the dancers in Figure 9.3A represented by their skeletal models in Figure 9.3B.

In addition to the actual choreography, the recordings also contain movements of taking the T-pose to set up and calibrate the motion capture system. These also included walking to the initial pose and reviewing/planning the choreography through improvisation. These sections were named the non-dancing condition because although they contain social-motor behaviors of the two dancers socially interacting and other types of movements for calibration of the MOCAP system, these movements were not aimed at deliberately completing a routine from beginning to end. Their staging and realizations are intermittent and spontaneous (improvised) in nature.

Each recorded segment piece lasted between 0.5 to 2.1 minutes. Pooling across subroutines gave us 23 minutes of continuous kinematics data for each condition recorded at 960Hz split into 480Hz per dancer (see below).

9.2.1 Data Acquisition and Signal Processing

The data for this project was kindly donated to our lab by the Phase Space team. The work was part of an effort to merge aspects of the performing arts and robotics technology by Tarik Abdel-Gawad of Bot & Dolly and Kan Anant of the Phase Space. Full project can

be found at http://phasespace.com/portfolio-item/bot-and-dolly/. The Appendix contains snippets of the performance in tandem with our biometrics. These snippets are the actual videos from the frames in Appendix Table 9.2 and merely serve to illustrate the outcome of the methods and their correspondence with the actual activities of the dancers' full routine.

Instrumentation Specs

Movements were recorded using a 24 camera Impulse X2 Phase Space Motion Capture system (960 Hz, San Leandro, CA) (Fig. 9.3A). A total of 76 active Light Emitting Diodes (LED) sensors were utilized mounted on a suit across the body (Fig. 9.3B). Each dancer had 38 sensors spread across the body: 4 on the head, 12 on the legs (2x6, on each leg), 14 on the arms (2x7, in each arm), 4 around the pelvis (lumbar and hip areas), and 4 around the thorax. Figure 9.3B left panel shows the sensor location on the skeletal representation, while Figure 9.3B right panel shows the avatar representation we designed using forward kinematics to capture our movies and represent our data types.

Pre-Processing

Positional data from each of the 76 sensors were examined to automatically detect data loss due to occlusions. Figure 9.4A shows sample trajectories of the two dancers for a snippet of a routine in two rotated views (this one corresponds to Piece 3 in Appendix Table 9.2 and was chosen at random from all 17 snippets to provide an example of the complex curves the body parts of both dancers generate during their pirouettes). These positional movement trajectories in three dimensions and their corresponding speed profiles were then used to reveal spatial gaps and the timing of such gaps. For example, Figure 9.4B top left panel shows a raw movement trajectory from one LED (located on the female's right arm) that incurred in some data loss from occlusion by the other dancer. However, other LEDs on the arm captured the motion (see Figure 9.3B where the redundant locations of LEDs on both arms are shown, left arm LEDS 11-17 and right arm LEDSs 18-24). The data from

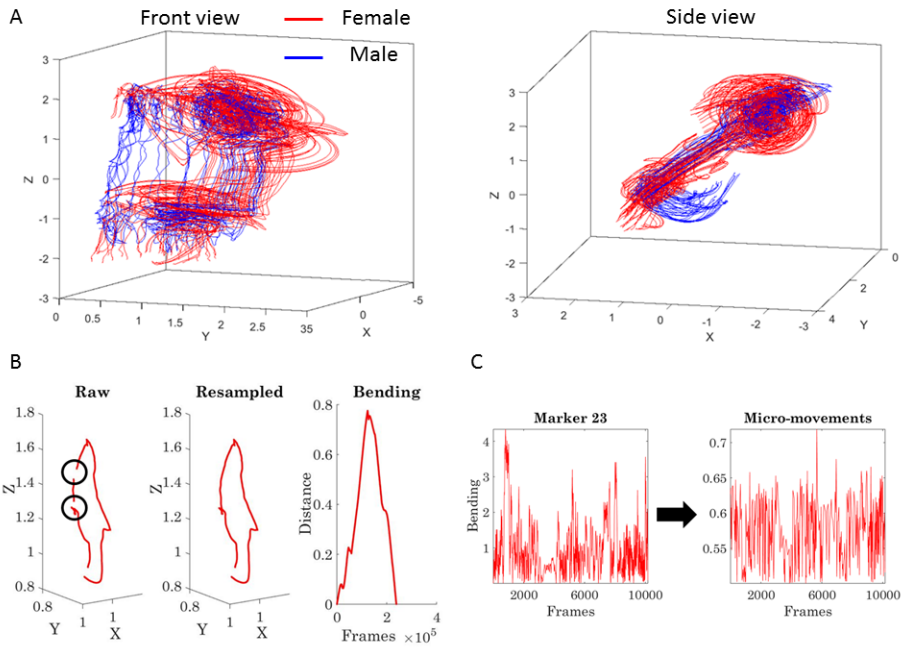

Figure 9.4: **Building our new micro-movements data type from kinematic parameters extractable from positional movement trajectories. (A) Two views of the movement trajectories from the two dancers (red female and blue male) while performing one segment of a dance routine. (B) Sample trajectory from a sensor showing discontinuities due to occlusion is reconstructed using in-house means built with resampling and spline interpolation. Local bending profile of the curved trajectory for the segment. (C) Bending profile across many frames of a routine converted to MM (see text for explanation) a unitless normalized waveform to represent real-valued spike trains of the peaks as continuous random process.**

the LED with occlusion-loss was subject to spline interpolation and the re-sampling of the trajectories to fill in the gaps without distortion. Figure 9.4B top-right panel shows the resulting resampled path conserving the original shape.

The resampling provides a new unit speed path devoid of the original temporal information. As such, we used a geometric index to build a data type of interest generating one of our waveform for analyses. To that end, we obtained a bending metric (related to local curvature) previously used in kinematics analyses [86] [87] of motor control research (see Appendix Figure 9.3A for further explanation) . This metric serves to profile the amount of epsilon-local bending of the curve (with no self-interceptions [1]) relative to the straight-line segment connecting two sampled points. It does so by measuring the distance from the point on the curve to the point on the local line at a right angle. This point-by-point deviation of the movement path from the local Euclidean straight line produces the bending profile for the segment. It is shown in Figure 9.4B (as Bending, expressed in cm), next to the other waveform of interest, the Linear Speed (expressed in m/s and derived from the positional data of one of the 76 LED marker trajectories in Figure 9.4A)

9.2.2 First Parameterization: The Micro-movements

The bending (and the speed) profiles provide a continuous waveform with peaks and valleys. We use the amplitude fluctuations of this waveform and re-parameterize such fluctuations (deviations from the overall empirically estimated mean amplitude) as micro-movement spikes, Section 2.4. Yet, unlike cortical spikes, which are binary, ours range between 0 and 1 in the real domain. The motivation to use fluctuations in bending (in addition to the fluctuations in linear speed) was twofold. One aspect is that we wanted to try a new parameter which is often mentioned by the dancers -the curvature of certain body parts.) Second, we wanted to take advantage of this camera-system data without concerning

[1] Self-intersections can be dealt with torsion (twisting of the curve) but their profiling is beyond the scope of the biometrics we present here, as we focus on the planar aspects of the curves through the bending metric.

ourselves with possible occlusions and data loss from some markers routines. Data loss is common to camera systems, so we thought it would be useful to others using cameras in motion capture to examine a geometric parameter related to the unit speed path we generate to fill in occlusions.

Lastly, we did not have access to a lot of data (23 minutes of dancing) so we wanted to maximize the amount of dancing data we could examine. In the case of small routine segments with occlusions, we can recover the geometric path without distorting the original path (Fig. 9.4B) and fine-sample the complex curves that these ballet routines generate. In so doing we sacrifice the temporal component of the speed (distance traveled in time) along the complex curve, but maintain the geometric component yielding the path local curvature. Curvature can be approximated by this bending metric, which is computationally cheaper to implement than the actual measure of curvature [18] in the types of real-time settings we use in the lab.

To convert the bending (and the speed) profiles to analog spike trains we use our data type coined micro-movements (MM). The MM track the fluctuations in the amplitude of the original waveform (e.g. bending or speed) and scale them to account for allometric effects, such that anatomical differences between the dancers, which affect speed and curvature of the trajectory, do not interfere with our statistical estimation (Fig. 9.4C) (Section 2.5).

Where the peaks and the local average values computed between the local minima surrounding the peaks are Gamma distributed (e.g. the frequency histogram of the average bending (cm) from the male (Figure 9.5A) and female (Figure 9.5B) movement trajectories are plotted and fit with Gamma PDF with insets showing the Gamma CDF fit. Appendix Figure A2 shows the version for the speed peak fluctuations. The unitless MM representing the real-numbered spike trains spanning between 0 and 1 thus provide a standardized waveform that we adopt as our data type (Figure 9.5C shows the MM waveform of one LED for a routine). Figure 9.5D shows all frames for the entire routine with a slice of 400 frames as inset showing the MM peaks of one subroutine. As explained, this data type accounts for

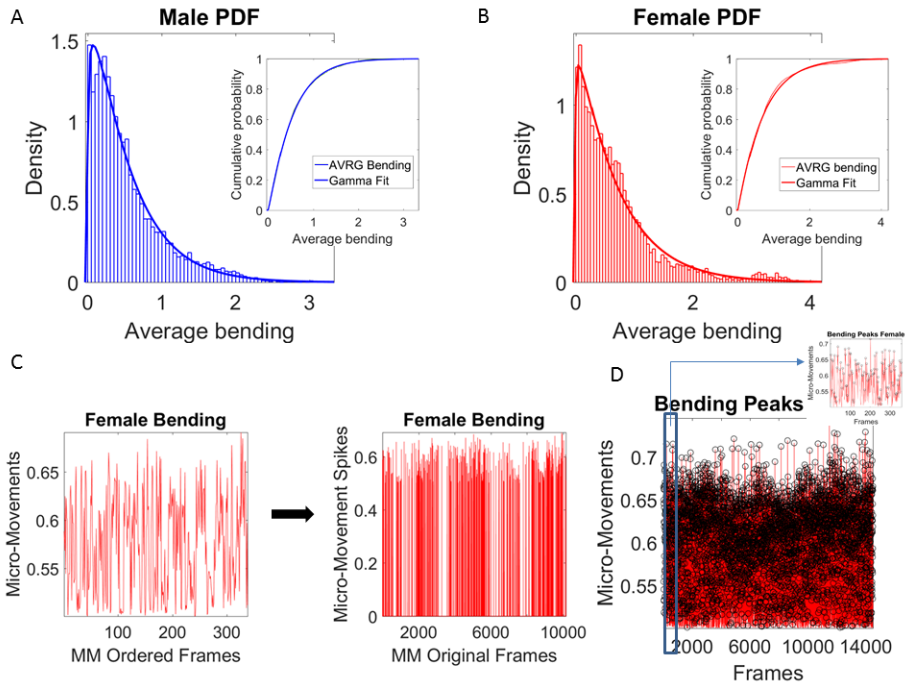

Figure 9.5: **The micro-movements representation and the Gamma process. (A-B) Average bending of the peaks (for male dancer A and female dancer B) obtained from equation (2) of the main text are Gamma distributed and so are the peaks of the bending profiles. As such, the MM derived from the normalization of equation (2) are also Gamma distributed and can be modeled by a Gamma process. (C) The MM of one block provide 400 peaks plotted in the order in which they occurred; but are zero-padded to recover the original number of frames to build metrics of pairwise cross-coherence across body parts of the two dancers (see next). (D) All MM (and a snippet of 400 peaks shown as inset) from gluing several routines together.**

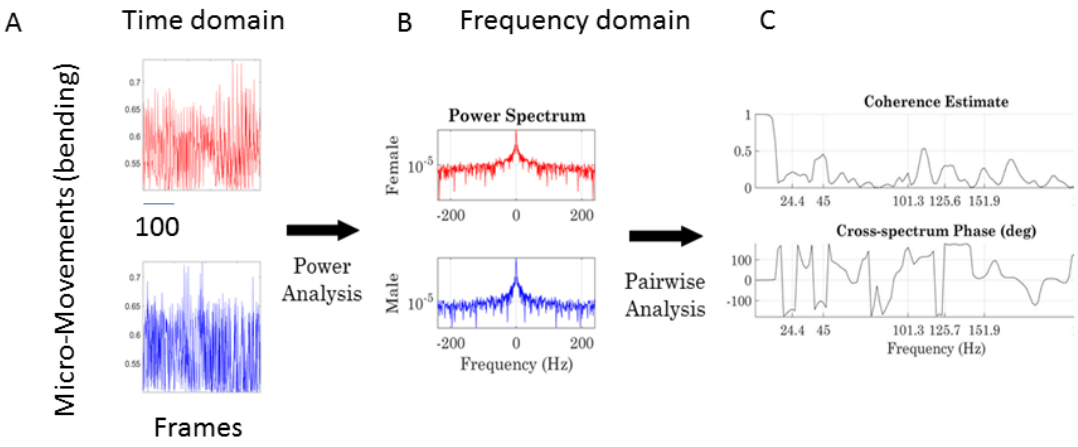

Figure 9.6: **From time to frequency domain. (A) The MM frames from different body nodes (within a dancer and across dancers) are FFT to perform power spectral analyses (B) and then pairwise cross-coherence analyses yield the frequency of the peaks (x-axis) and the phase shift (y-axis).**

possible allometric effects given by the different anatomical features of the participants [51] so we can compare individualized movement-related variations across different participants.

9.2.3 Second Parameterization: Coherence-Phase-Frequency (CPF)

The spike trains of MM reflect the normalized peaks in the order in which they were acquired. In this sense, the trajectories of some body parts may generate more curvature (or more fluctuations in speed) than those of other body parts. As such, they would give rise to fewer peaks in bending (or in speed) such that the signal would be misaligned across different body parts. To keep all body parts with the original number of frames, and align the two dancers' body nodes pairwise, we pad with zeros those frames with no fluctuations in bending peaks (i.e. where the bending is at the Gamma mean bending value; or likewise for the speed case). We remind the reader that the values are centered at the Gamma mean, such that zero correspond to the mean value of bending or speed peaks. An example is shown in Figure 9.5C right panel. On the left panel of 9.5C, the MM are plotted in the order in which they occurred, with 400 peaks detected as fluctuations away from the mean bending peak. On the right panel, these are then plotted using the original full number of

frames, zero-padded as explained above. This produces equal number of frames for each of the 38 body nodes of each dancer [2]. These data in the temporal domain (480Hz sampling frequency) is then used to convert to the frequency domain and perform pair-wise cross-coherence analyses using spectral power density analyses (i.e. between two given body parts of one dancer, and between the body parts across the two dancers.) Figure 9.6A shows two sample MM trains for a body part of the female and one of the male. These are used across seconds with an overlapping sliding window of up to .5 seconds to perform power spectrum analyses on their FFT signal. The number of overlapping frames is randomly chosen using the continuous Gamma family of probability distributions, generated with the MATLAB function gamrand, according the empirically estimated Gamma-mean and Gamma-variance, using the MLE approach, as explained above (fitting the Gamma shape and scale parameters obtainable from the whole data set to attain the mean and variance). These continuous blocks of MM signals are used to perform pairwise cross-coherence analyses (schematics in Figure 9.6 for the pair of nodes in Figure 9.6A, taken from two body parts of the female and male dancer -recall each has 38 body parts, so this is just one such comparison out of 76x76 to be performed).

The output of the cross-coherence in Figure 9.6C yields three pieces of information that we use in our statistical inference: (1) the maximum cross-coherence value for which we retain (2) the frequency value (top graph in Figure 9.6C) and (3) the phase value (bottom graph in Figure9.6C). In this way, we can examine the data within the known frequency ranges of human activities highlighted by the rectangle; but we can also examine patterns emerging within ranges beyond those. i.e. for the micro-movements (in the amplitude of motion path's bending peaks or the speed peaks) representing motor-output dependent vibrations. These forms of vibrations which can be input to visual, vestibular and kinesthetic

[2]Fluctuations below the mean can be informative in patient populations, but are more prone to be contaminated by instrumentation noise, thus requiring more signal processing to separate physiological signal from noise. In the bending parameter such small fluctuations are uninteresting but in other parameters like speed or acceleration they may add other sources of information with potential classification power for pathologies of the nervous systems.

channels are unexplored in complex partnering motions giving rise to cohesive behaviors not present in the types of stand-along tasks involving one actor that are so common in the field. Figure 9.6D shows the known human vibration sensitivity ranges [30]. These ranges reach far beyond those explored in motor control-physiology where simpler stand-alone motions (e.g. finger tapping) are studied using methods that rely on grand averages of parameters changing values at lower frequencies. Appendix Figure A3 provides an example of high frequency vs. low frequency peaks in commonly studied pointing behavior whereby retaining the high frequency peaks (so called noise) provides more information than exclusively using the peaks occurring with lower frequency. Considering all peaks and scaling them provides the normalized spike train data that we previously introduced to the field of autism [84] [93].

We take these abovementioned three pieces of information and use them to construct three matrices with 76 x 76 entries, 38 for the female's and 38 for the male's body nodes (shown in Figure 9.7). The first matrix contains along the rows and columns, all the female nodes followed by all the male nodes. There are 4 quadrants: top left representing the female-female pairwise relations, i.e. providing information about the pairwise cross-coherence of bodily biorhythms in the female. This sample sub-matrix gives information useful to discover the female bodily synergies for each frame. For example, within this upper-left quadrant, the entry (1, 35) of the matrix given by the head (row 1) and the left foot (column 35) marked by a square, gives the value of the peak cross-coherence (0.55) shown by the color bar. These two body parts are not as coherent as those matrix entries with cross-coherence values above .8. Also, matrix entries at 0 have 0 cross-coherence. The corresponding (1, 35) entry in the second matrix of phase lead values of Figure 9.7B provides information about the phase (head shifted ahead of the left foot 80 degrees in this case). The corresponding (1, 35) entry in the third matrix of Figure 9.7C provides the value of the frequency at which this occurs (in the range of 120 Hz) in this case. Of course, the next frame will have different configurations for the female body in motion.

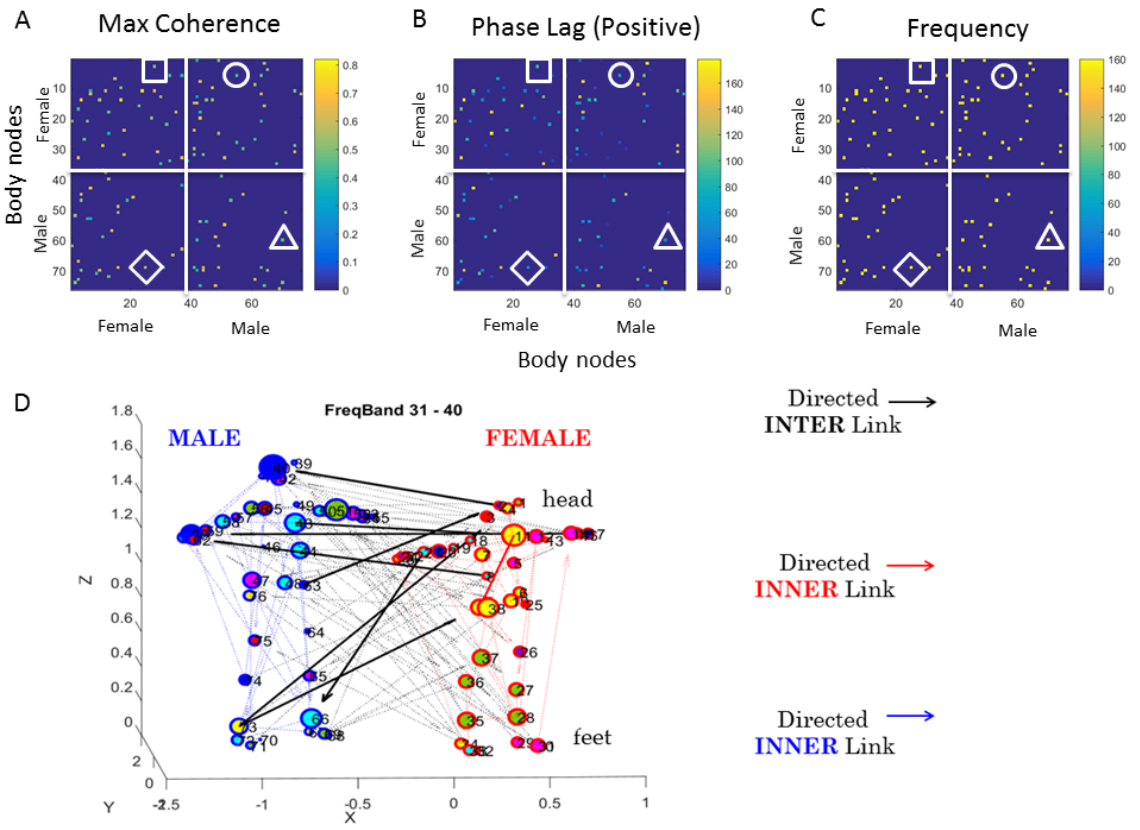

Figure 9.7: **The coherence, phase, frequency (CPF) parameterization and the weighted directed graph representation of the data as dynamically changing networks. (A) The adjacency matrix of 76x76 entries (38 for each dancer) representing the state of the two dancers in one block of MM data. Each dot represents a maximal value (a peak) of the cross-coherence with the range of coherence values represented in the color bar. Entries with 0-values have 0 cross-coherence. Four quadrants provide the pairwise values for the female body parts (38 LEDs on the top left quadrant); the female $->$ male (top right quadrant); the male $->$ female (bottom left quadrant) and the male body parts (bottom right quadrant.) Square, circle, diamond and triangle in each quadrant have the corresponding values of phase lead-in (B) and frequency in (C) (D) Network representation for a frequency band and block of MM data (see text) highlighting the interconnectivity of each body (blue weighted directed arrows male and red weighted directed arrows female.) Black weighted directed arrows are the coupled activities across the dyad (thicker arrows are higher weight given by the phase lead values). Circle size is the strength of the connectivity (in degree and out degree counting number of edges entering and leaving the node) and color is the module representing highly interconnected sub-nets that are sparsely connected to other clusters.**

The upper-right quadrant of the matrix on Figure 9.7A. On the other hand, provides information about the cross-coherence of the female and male body parts. There, a circle marks one example whereby entry (5, 57) (female thorax male right arm) and gives the information (as above) about the pairwise cross-coherence, phase and frequency for a block of data comprising this one snippet of the behavior. In this way, we can dynamically sample this information across the 23 minutes of dancing or non-dancing conditions. Notice here that we examine the information across different 10-based frequency bands to learn about these signatures in frequency ranges beyond those reported in the motor control physiology literature. That prior work concerns stand-alone simpler motions (e.g. finger tapping, gait, pointing, etc.) which do not engage a partner and as such, do not generate cohesiveness of motions with an external agent.

Recall here that the number of elements conforming a block of spikes entering in the probability density estimation procedure (along with the sliding window up to the block size) depends on the sampling resolution of the sensors and the number of peaks we attain for the given trajectory parameter (fluctuations in bending amplitude in this case) to empirically estimate the parameters of the underlying probability distribution function describing the block variability with tight 95% confidence intervals. Further, keep in mind the overlapping sliding window up to the block size, which we obtain at random drawing from the continuous family of Gamma probability distributions, using the estimated Gamma mean and Gamma variance from the entire data set. This use of the continuous Gamma family of probability distributions is not an arbitrary choice, but rather an empirically informed one, derived from studies involving thousands of human participants for whom we have extracted the stochastic signatures of naturally occurring behaviors at voluntary (Torres et al. 2016a) and involuntary [99] levels of control.

The other quadrants offer information about the female-male pairwise coherence (lower left) and the male-male bodily coherence (lower right) for this block of data which represents a snipped of the unfolding behavior.

This parameterization of the bending (or speed) data by coherence, phase and frequency (CPF) offers a new way to represent the bodily behavioral data as adjacency matrices of weighted directed graphs. The directionality in this case is provided by the presence of an entry value of the second matrix under the convention that in entry (i, j) the node i leads the node j: i j. The weight of the link between node i and node j is given by how much the phase leads, given by our convention using the positive phase shift range. In this method section, we focus primarily on the bending-related data to illustrate the network connectivity analyses, but all the same methods apply to the case where speed related parameters are used instead. We will present results based on both types of parameters.

Connectivity Analyses for Peripheral Bodily Networks Represented by Weighted Directed Graphs

A grid of interconnected nodes (connected by links) across the body can be used to represent, using a level of abstraction, some pattern of activity from the peripheral network of nerves in the human nervous systems. To that end, use the nodes and links in a weighted directed graph. Nodes in this case are body joints and links are active connections between pairs of nodes. The patterns they give rise to changes from moment to moment as a function of the variability inherent in the micro-movements of the parameter(s) we use to track motor related activity (in this case, the fluctuations in the amplitude of the bending or the speed, expressed as spike trains.)

Network representations have been used to characterize snapshots of Central Nervous Systems' activity in e.g. resting state fMRI activations or EEG biorhythms [82]; but never used to represent motor output activity across the Peripheral Nervous System comprising peripheral nerves of various kinds (i.e. conducting kinesthetic information from mechanoreceptors coding touch, pressure and movements; thermoreceptors coding temperature and nociceptors coding pain.) Here we adopt the brain connectivity toolbox [74] and adapt it to model full intra- and inter-body motions to uncover self-emerging patterns of cohesiveness

captured by our proposed metrics of entrainment and by connectivity metrics commonly used in network analyses. These include:

Degree distribution: The degree of a node in a network is the number of connections (edges or links) it has to other nodes. Since our network representation is a weighted-directed graph, we examine the incoming degree, the outgoing degree and the sum of the two. The degree distribution is the probability distribution P(k) of the degrees over the whole network. It is defined as the fraction of nodes with degree k, such that if there are n nodes in total, and nk of them have degree k, we have that . The shape of the distribution provides information about its connectivity. For example, in a network with right-skewed degree distribution, most nodes have low degree (i.e. fewer links to other nodes) and those in the tail are called the hubs of the network -as they have high degree of connectivity.

Strength: The strength of the node is similarly computed based on the number of edges connecting a node to other neighboring nodes but including the weights of the edges as well. Since the graphs we are using are directed, we obtain in-strength, out-strength and total strength.

Modularity: This is a measure of the network structure, designed to capture the division or the strength of the network into modules (sometimes called subnetworks, clusters or communities) that are maximally interconnected among its internal nodes and minimally connected with the other nodes outside the cluster. In this work we run the modularity algorithm multiple times to define a stable set of modules for each frequency band. Further, for each time block of activity we also obtain the steady modularity state and track the nodes that participate in each self-emerging module, to define dynamically changing synergies across the body of each dancer and between the two bodies together. The modules act as subnetworks that can transmit information from one to another along faster routes (see below shortest distance paths). Importantly they self-emerge from the network activity (i.e. the underlying cross-coherence of the micro-movements extracted from the changing curvature of the bodily nodes' motion trajectories; defining its connectivity pattern at a

given moment by maximal coherence (node), phase lead (weight) and direction (from node i to node j in our convention.)

Shortest distance path: A path in the network is sequence of edges (one edge is the link between two nodes) which connects a sequence of nodes (vertices in the graph). In the directed graph, the directed path is similarly defined but with the restriction that the direction must be similar for all edges in the sequence. In the weighted graph case (as ours) the weight of a path is the sum of the weights associated to the edges entering the sequence. The length (or cost) of the path is also used to define distance related connectivity metrics, such as the shortest path between two nodes (if one exists.)

Characteristic pathlength: This is the average path length (as defined above) of the network, i.e. the average number of steps along the shortest distance paths connecting two nodes, defined for all possible pairs of network nodes. It measures the efficiency of information transfer (of transport) on a network. In our case, this refers to the amount of coherence between any pair of nodes along with their phase leading information. The cross-coherence in our case is based on the micro-movements of the movement path curvature (dynamically changing over the time of the routine).

For each of these metrics, we can use a given frequency range to cast the outcome from the connectivity analyses (see Figure 9.7 for a network configuration in the frequency band of 31-40Hz). We can build the representation of a network state within a time-period from this adjacency matrix constructed using the CPF parameterization, whereby the nodes capture the amount of pairwise cross-coherence of the micro-movements (e.g. the edge of the circle representing the body part can be colored based on the coherence level); the size of the node represents a quantity associated with the degree of the connectivity between nodes (represented by incoming links, outgoing links, strength given by the net sum of incoming and outgoing links, or any connectivity-based ratio we can build therein, etc.). The directionality is as explained above by adopting the ij convention and the weight of the link can be expressed as the amount by which the node i leads the node j, expressed by the

thickness of the line or the type of line (dashed vs. continuous, etc.)

This network representation for one frame (block as defined above) in a frequency band is shown in Figure 9.7D based on the adjacency matrix of Figure 9.7A (restricted to the positive phase values in 6B). Note here that although this figure focuses on the frequency band of 31-40, it is only used as an example to illustrate the methods. We examined all frequency bands to compare low ranges (known in the physiological experiments of the motor neuroscience literature and high ranges unknown to physiologists but known to the community of structure and material engineers who study vibrations and their harmful or annoying levels to the sensitivity of human nervous systems). Figure 9.7D shows the female and male in T-pose to illustrate the configuration of the block of data we are using to describe the methods, but keep in mind that the dancers are moving (see links 5 and 6 showing the dancers moving in the dancing and in the non-dancing conditions.)

We underscore that there is nothing special about this frequency band in Figure 9.7D or even about the choice of connectivity parameters to visualize the unfolding dynamics of the connectivity patterns of the network. We just chose these connectivity metrics (out of many others) to help explain our new methods. For example, we use the metric of modularity, providing self-emerging community structure, to color the nodes; yet, we could have used other coloring schemas based on clustering coefficients or shortest-distance based metrics, etc. The choice of parameters to track and visualize will very much depend on the application the user has for the methods. The goals of a choreographer and dancer may be different than those of a school teacher and student, a caregiver and patient or a clinician and client.

The important point is that we have extended the use of networks and connectivity analyses from the brain [82] to the body [100]. As such, we have now developed a new way to visualize peripheral activity and self-emergent coordination patterns between two (or more) bodies in motion, as they perform natural activities. We can clearly also visualize individual patterns of coordination within each dancer's body. Further, this network idea

can be used to profile an entire crowd. For example, using wearables we can profile the network conformed by the audience and the dancers and track the self-emerging synergies during the performance based on the bodily reactions of the audience to the choreography and its execution by the artists. Likewise, we can assess the influences of the public on the artists' performance because we now have a closed feedback loop unfolding in time and showing self-emergent cohesive behaviors that we can translate to tangible coordination patterns.

Figure 9.7D showing the example of the network state for a given frequency band helps us appreciate the inner links of the male (blue colored); the inner links of the female (red colored) and the black links inter-connecting the dyad in both directions, the male and the female. They help us quantify who leads who when (i.e. at any given block of data). And within each dancer's body, these graphs inform which body parts of the dancer lead other body parts. Further, the modularity analyses reveal self-emerging sub-networks of joint activity (perhaps call them inter-bodily synergies). Here the magenta colored module spans the left foot of the female, her left arm and several of the male body parts (head, right shoulder, both forearms, right hip, right knee and left shank). The arrow direction tells us which body part leads and the thickness tells us by how much.

We can quantify the number of modules per frequency band (for example) and within each module, we can quantify the participation of each body part (node) in each self-emerging module. Examples are shown in Figure 9.8A, where we see for each dancer the profile of modules per 10-based frequency band and Figure 9.8B, where we count for each module the number of times a node (body part) participates in a module. Because modules may shift from block to block (i.e. as synergies would recruit and release different joints and the body would self-organize recruiting and releasing different synergies) we perform this count for each block separately and can query how much the two bodies entrain.

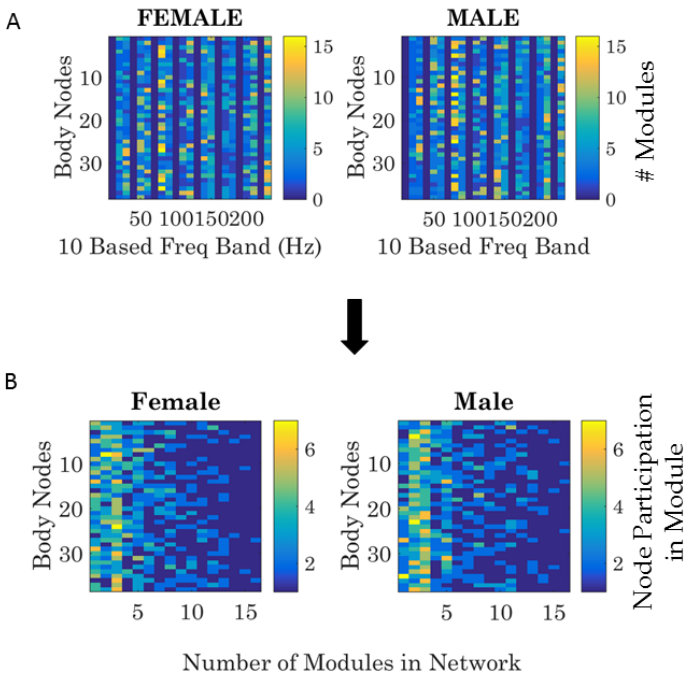

Figure 9.8: **Sample use of modularity metric across different 10-based frequency bands. (A) Different modules (16) self-emerge for each data block of the dynamically evolving network, as the routine unfolds for the female and male. (B) Counting the participation of each body node in each of the modules. The entry of the matrix (color map) gives the number of times a node participates in a module (horizontal range from 1 to 16 from (A)) for the female and male dancer e.g. during the dancing condition in this case.**

9.2.4 A Measure of Entrainment to Capture Togetherness

We can for example, divide the body into head (H), trunk (T) lumbar (Lu), left arm (LA), right arm (RA), left leg (LL) and right leg (RL) as in Figure 9.3B. Then, we can query for each module that we uncover, the node participation for the two dancers. In Figure 9.9, we present an example of such types of queries to see which body parts are participating together (maximally) within the same module. As such, Figure 9.9A shows the count in module 1 for each body part (comprising several LEDs, i.e. several nodes of the network). We count the number of times the nodes in H-male and H-female participate together by thresholding above the minimum number of the maximal number of times nodes participate in this module (6 in the female and 7 in the male, so we threshold above 3). Any body part

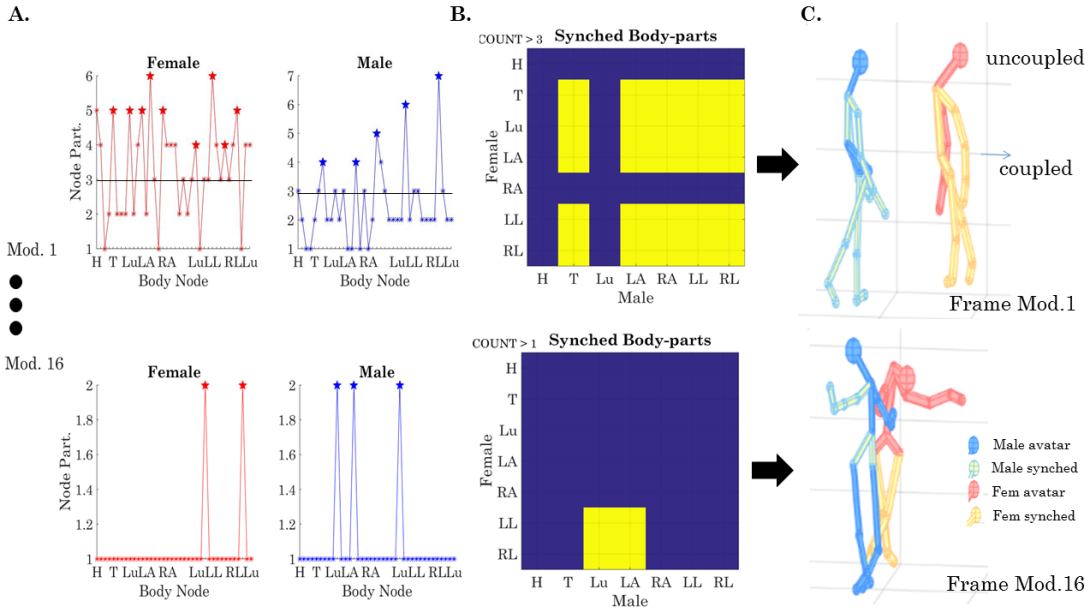

Figure 9.9: **Automatically detecting self-emerging coupling behavior between the two dancers. (A) For a given module of the network state, track the number of times a body segment in the female participates (e.g. the left arm LA comprised of LEDs 11-17 in Figure 2B left panel or the right arm RA comprised of LEDs 18-24) together with the corresponding body segment of the male. Obtain the minimum value of the maxima across both and threshold by half to set the criterion of togetherness. (B) Build binary matrix whereby values of 1 are colored in yellow to represent coupled behavior (i.e. together the nodes participate in the module for the number of times exceeding the threshold value.) (C) Avatar representation of the dancers' poses using the actual kinematic pose and color-coded by the coupled body parts of this block of MM data. Module 16 is also represented on the bottom panel (see links 2-4 in Appendix containing the movies.)**

above 3 (6/2, which is the minimum of the two maxima) falls in this set and is marked with stars as those nodes that peak (i.e. there is a change in the sign of their slope). Then, we color-code the 7 x 7 matrix by setting to 1 the entries that are above the threshold of 3 (in this module) and setting to 0 those equal or below this (self-evolving) threshold. In module one, we see that the trunk (T) and both arms and legs of the male (LA, RA, LL, RL) are entrained with the T and Lu and LA and both legs (LL and RL) of the female; yet, the H and Lu of the male are not entrained with any nodes of the female and the H and RA of the female are not entrained with any of the nodes of the male. Figure 9.9C top panel presents this configuration in avatar form, whereby the coupled nodes are plotted in yellow and the uncoupled nodes are plotted in red (female) or blue (male). Likewise, module 16 shown in the bottom panel shows the coupling of the male Lu and LA with the female LL and RL for another frame. The full movie showing the unfolding of the routine using these avatar representations of the modularity activity can be seen in the Appendix link 2 for Dancing and link3 for Non-Dancing conditions.

9.2.5 Statistical Platform for Individualized Behavioral Analyses (SPIBA): Using a Gamma Process to Characterize Stochastic Behavior

Underlying the macro-level representation of the network analyses are the stochastic patterns of nodes' activity variability at a micro-level. We invite the reader to think about micro-movements as vibrations that the person experiences through various sensory receptors in the visual, vestibular and kinesthetic domains.

Each body part captured by the LEDs displays a motion trajectory of the bending parameter. The spike trains of the MM derived from the bending metric are treated as random events representing a continuous random process under the general rubric of a Poisson Random Process, where events in the past may (or may not) accumulate evidence towards the prediction of future events. In the original stages of this work, we had assumed independent, identically distributed (I.I.D.) random process [96] [93] [95]. But in this paper,

we relax this assumption using an overlapping sliding window to define our data block for stochastic estimation (in contrast to previously using independent blocks); we sample the overlapping number of frames for the sliding window from a family of distributions (in contrast to randomly drawing the number of frames from one single distribution)(Section 2.5). Further, we consider stochastic trajectories and measure the stochastic shifts over time, thus not assuming a stationary random process.

These unitless normalized spike trains are used as input to a Gamma process to empirically estimate the Gamma parameters (e.g. using MLE with 95% confidence intervals) [93] [84]. The estimated shape and scale parameters are tracked on the Gamma parameter plane (where the vertical axis represents distribution-dispersion (scale) parameter values, and the horizontal axis represents the distribution-shape parameter values). These are used to estimate the Gamma PDFs, and moments to profile noise-to-signal transitions inherent in the multilayered, dynamically evolving biophysical data (Section 2.5).

9.2.6 Summary Statistics Profile

The estimation of the Gamma shape and scale parameters is used to estimate the Gamma moments: the mean, the variance, the skewness and the kurtosis (Section 2.5) (e.g. Figure 9.10F plots the moments corresponding to the estimated Gamma shape and scale parameters of Figure 9.10E, divided into quadrants using the median values; while Figure 9.10G shows their estimated Gamma PDFs). The mean values of the MM (i.e. the unitless normalized bending metric) indicate that larger values have lower curvature on average (because the average local bending term in the denominator is smaller and results in larger ratio with larger value of the MM fluctuation.) The color code of the PDF curves in Figure 9.10G correspond to different temperature ranges we collect with other sensors and display to visualize different classes of motions. Further, we use the avatar representation to color code the dancers by the level of noise provided by the scale b-parameter of the Gamma process estimation. The links 5 (dancing condition) and 6 (non-dancing condition) in the

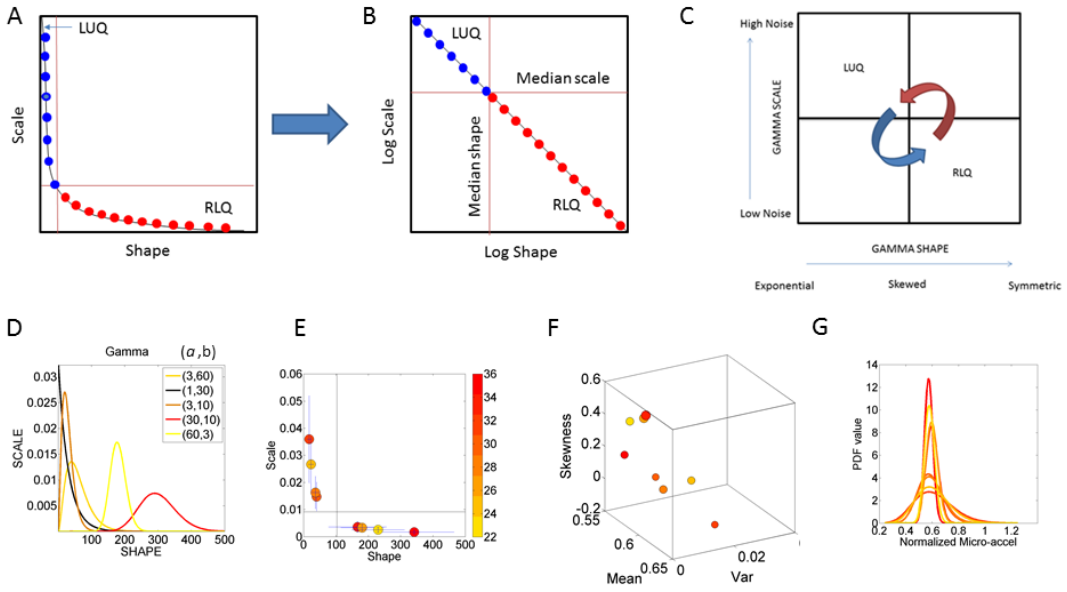

Figure 9.10: (A-B) Quadrants are obtained from the median values of the shape and scale parameters empirically estimated as a stochastic trajectory over time (e.g. for the entire 23 minutes of the dancing routine) In schematic form, the log-log representation of the scatter yields a tight linear fit hinting at a power law for human behavioral data where the random process divided by the quadrants can be empirically informed by human behavioral data. (C) The shape axis denotes the type of distribution shape from exponential at a=1 to skewed to symmetric. The scale axis representing the noise to signal ratio NSR (see text) with low to high values in the range indicated by the arrow. The LUQ is characterized by higher noise and more skewed shapes while the RLQ if characterized by lower noise and more symmetric shapes of the PDFs. The inner arrows indicate the shifts in the variability of the empirically estimated parameters whereby the distributions sometimes fall on the LUQ and others on the RLQ. The amplitude of the shift, its rate and the frequency of the change across quadrants provide information about the random process under examination. Empirical studies we pioneered in human behavioral data indicate the RLQ are prevalent for well matured neurotypical systems, while the LUQ prevalence is associated with pathological conditions. (D) Human behavioral (e.g. raw acceleration) data yields a Gamma family of PDFs. (E) Learning and adaptation produce scatters spanning both quadrants in humans. (F) Gamma moments represented in a multi-dimensional map with the x-axis representing the mean, the y-axis representing the variance, the z-axis representing the skewness and the size of the marker representing the kurtosis. Other features can be used to color code the map (e.g. skin temperature) and further help visualize, make statistical inferences and interpret the human behavioral data. (G) PDFs from MM of accelerometry data used to estimate Gamma moments and shape-scale parameters in panels E-F (taken from (Torres et al. 2016d) to explain the visualization methods).

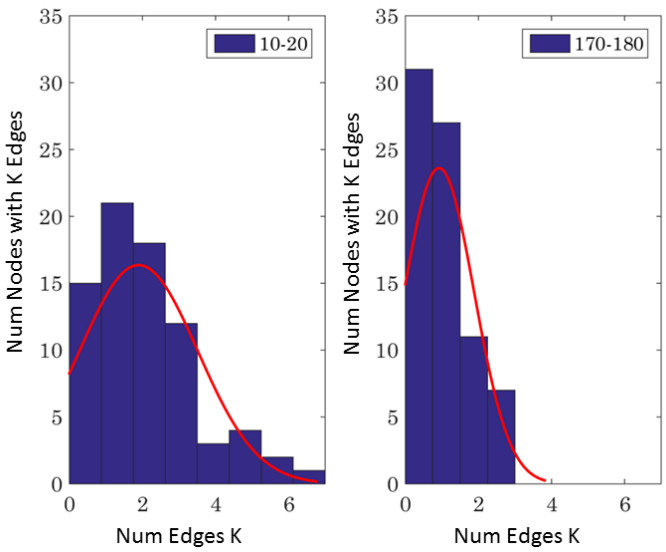

Figure 9.11: **Sample degree distributions for different frequency bands in one snippet of data reflecting the state of the network differently for lower vs. higher frequencies. At higher frequency, most nodes have up to three edges while at lower frequency there are nodes with up to 6 edges for this one block of MM data.**

Appendix provides sample videos conveying this information.

9.3 Results

9.3.1 Connectivity Metrics

Body-Body Networks Degree Distributions

The degree distributions of each network state were obtained by counting the number (K) of links in the network and quantifying the number of nodes with K edges at each stage. We examined the 10-based Frequency range (from 0-240Hz, 1/2 of the 480Hz sampling rate range distributed between the two dancers at 960Hz) for 23 cases. Figure 9.11 shows the degree distribution across the network for two different frequency bands. Figure 9.11A-B refer to the bending parameter while Figure 9.11C-D refer to the speed parameter.

The degree distributions illustrate the changes in network structure in different frequency ranges. In the case of bending, for lower frequencies, the number of nodes with low number

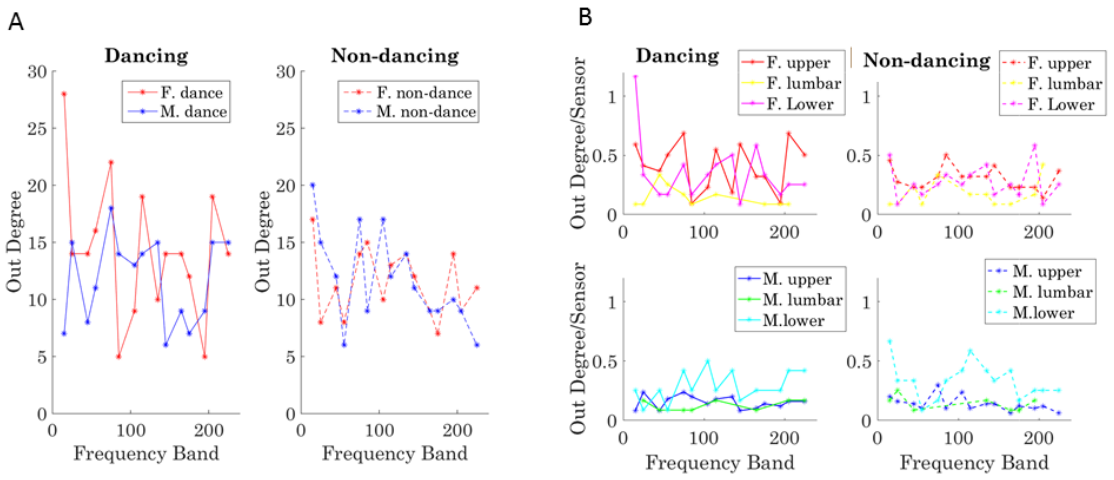

Figure 9.12: **Quantification of leading behavior across dancers and body parts. (A) Dancers summary of leading activity depicts the female as leading across most frequency bands, while non-dancing shows the male as the leading body figure. (B) Body areas of interest can be used to query leading behavior for the female and male individually. In the female the lower body leads for low-frequency bands but as the frequency increased the upper body leads; with the lumbar area beneath upper and lower extremities. In the non-dancing condition, the lower body leads (during calibration and T-pose and planning.) The male's lower extremities lead in both dancing and non-dancing cases.**

of links (edges) is lower than for higher frequencies, and at higher frequencies there are no nodes with more than 3 edges. As such, we learned that the degree distributions of the network, reflecting the overall connectivity of the network, change with the frequency range.

Body-Body Networks Leading Profiles

We examined the degree to which each body part of interest (shown in Figure 9.3B) was leading for a given frequency band and which dancer was leading in general for each condition. To that end, the number of links leaving the node (out-degree) was obtained, considering the weight of the edge as well to denote the leading profile. This weighted sum accumulated over a session (per each frequency band) provided a metric of the strength of the body part leading another body part (where all nodes point in one direction according to our i j convention. The leading profile can be studied for each dancer across the dancing and

non-dancing conditions by taking the overall sum. We plot the summary for each frequency band in Figure 9.12A. Further, the break down per body segment (upper body, body-core denoting lumbar and trunk, and lower body) is shown in normalized form in Figure 9.12B, where the dancing (left) and non-dancing (right) conditions are shown separately for the female (top) and the male (bottom). This normalized version expands on the results in Figure 9.12A, where the periodic patterns of this measure show the female leading in the dancing condition for most frequency bands and the male body leading in the non-dancing condition. Figure 9.12B informs us that the core region (lumbar plus trunk) of the male leads in both conditions, while the upper body (arms and head) of the female lead in the dancing condition; but the lower body (legs and feet) lead in the non-dancing condition (i.e. while T-posing, calibrating and planning.)

9.3.2 Dynamically Coupled Body-Body Networks

The analyses concerning the togetherness metric provides a frame by frame characterization of the dancers' entrainment and serves to aid visualization of a very complex routine into simpler modules. Here we underscore that the patterns emerged automatically for body parts we searched for, as the dancing or no-dancing conditions unfolded. If the end-user (e.g. researcher or choreographer) would like feedback on other body parts, it is possible as well to redefine the areas of interest across both bodies and profile those instead. In this sense, the method allows ample flexibility without sacrificing the automated aspects of self-emergent cohesiveness captured in the modularity metric of the network. Figure 9.9 used to explain these methods, shows this metric for a couple of selected frames. For the complete movies, please visit the links 2-3 listed in the Appendix.

9.3.3 Automatic Identification of Coordination Patterns

Across the different 10-based frequency bands, we computed the shortest distance paths (between nodes) as the network dynamically unfolded during the dancing condition. The

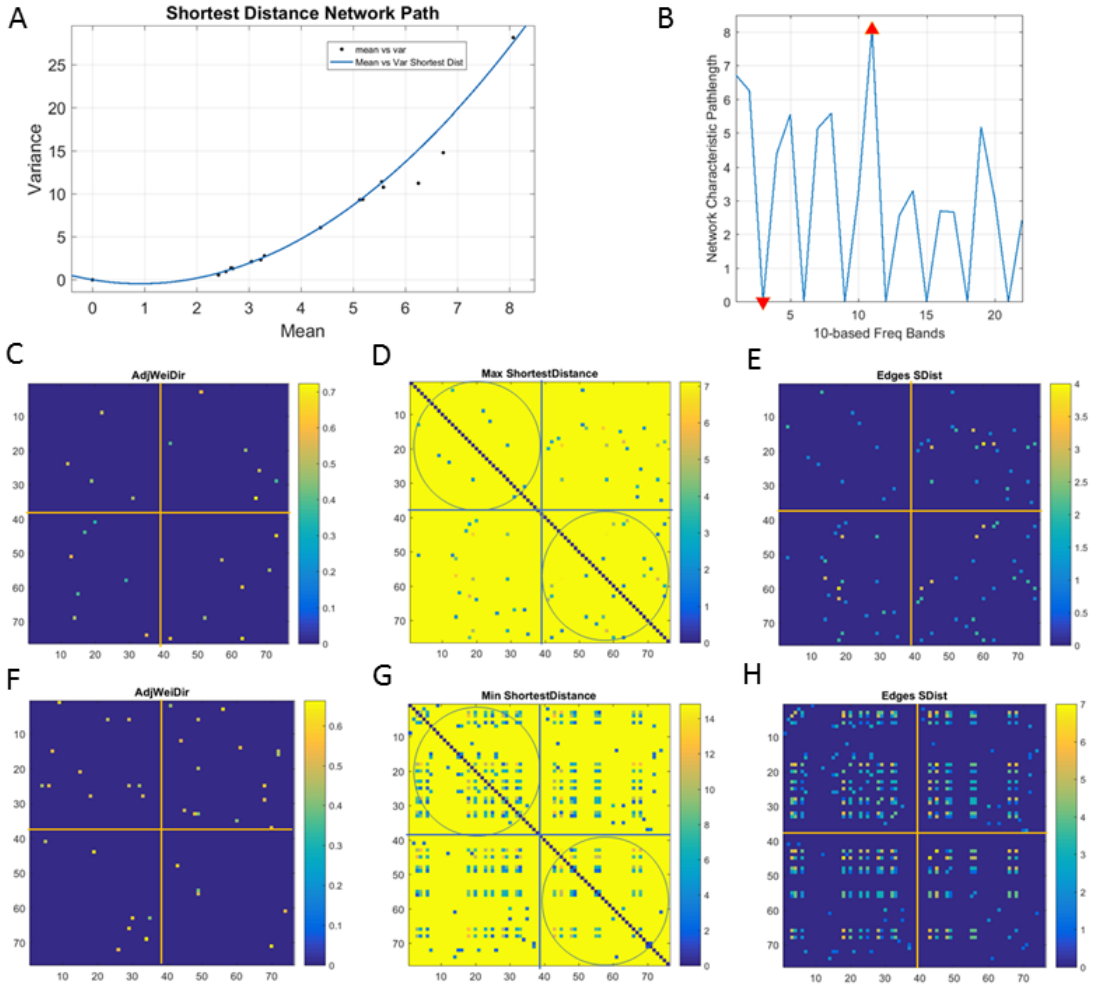

Figure 9.13: **Automatically detecting different patterns of coordination in the network using connectivity metrics. (A) The shortest distance path is obtained (pairwise) across all nodes of the network for different frequency bands and the mean and variance are estimated (using a Gamma process) revealing the non-linear relationship between the estimated moments. (B) Periodic behavior of this metric for the 10-based frequency band reveal a minimum and maximum values of the average shortest distance path (the characteristic path length.) (C) Adjacency metrics corresponding to the maximum (C) and minimum (F) with entries denoting the pairwise cross-coherence peak values. (D) Coordination patterns for the maximum and minimum (G) characteristic pathlength, along with corresponding matrices for the edges distance.**

distance matrix obtained using the connectivity toolbox of MATLAB (Rubinov and Sporns 2010) contains in its (i, j) entries the shortest paths between all pairs of (i, j) nodes. This information was used to estimate the mean and variance across all nodes' shortest distance path quantity, thus revealing a non-linear pattern between the estimated mean and estimated variance. This pattern is shown in Figure 9.13A: as the mean shortest distance network path increases the variance of this parameter grows exponentially. The network characteristic pathlength (the average shortest distance path) periodically changes across the 23 10-based frequency bands that we explored. Here, the minimal value and the maximal values denoting critical transition points between frequency bands reveal different states of the network in Figures 9.13C-E for the maximal characteristic pathlength and the minimal case in Figures 9.13F-H. The matrix in panels 12E and 12H correspond to the number of edges contained in the shortest weighted path, also obtained pairwise between nodes. Here the weights denote the positive phase shift of node i over node j, which we use by convention to denote that the body part represented by that node i leads the body part represented by that node j. As such, the maximal coherence at entry (i, j) with shortest weighted edge path is also maximally synchronous and reveals patterns of synergies across the dancers and / or within the body of each dancer. These can be appreciated (minimal shortest distance) for the female in Figure 9.13G top circled left panel; for the male on the circled bottom right panel and for female male and male female on the top right and bottom left panels respectively. They can also be appreciated for the corresponding edge (weighted) distance matrix in Figure 9.13H obtained for the lowest network characteristic pathlength in the range of 20-30Hz of Figure 9.13B. The maximal network characteristic pathlength occurred at the 110Hz while the minimum occurred at 20Hz in Figure 9.13B. These analyses reveal different coordination patterns for each dance and across the dancers' body for different frequency bands (within the 240Hz range that the camera-sensors revealed out of the 480Hz per dancer).

9.3.4 Individualized NSR-Body-Map Profiles for a Given Frequency Band

The node's activity in micro-movements underpinning the network connectivity patterns also contributes to our understanding of the dancer's coordination patterns. For any of the frequency bands under examination we can provide the statistical quantification of the emerging probability distributions that we empirically estimate. The evolution of the NSR across frames can also be captured and mapped throughout the dancer's performance organized by frequency bands (e.g. those revealed by the analyses in Figure 9.13 corresponding to the 20Hz range for minimal distance path are examined in Figure 9.14 and shown in movies of links 5 and 6 of the Appendix).

In the dancing condition of Figure 9.14A, we can appreciate a larger spread across the bodily nodes with differences across all moments, mean, variance, skewness and kurtosis. The insets show the empirically estimated PDFs with a tendency of higher skewness in the distributions of the male dancer and higher symmetry in the distributions of the female dancer. Further, the NSR profiles across the body nodes reveal higher variability in the legs patterns as the bending parameter changes along the movements' trajectories. The non-dancing condition contrasts with the alignment of the scatter and a prevalence of female symmetric PDFs across bodily nodes. This indicates a more predictable curvature profile than those of the male (with higher skewness in the estimated PDFs). Further the larger mean values of the female indicate lower curvature in the non-dancing condition (as the MM of the bending profile contain smaller bending values on average in the denominator of the normalization ratio). Here, the color bar also indicates NSR ratio values with higher noise in the trunk of each dancer for the non-dancing condition.

Table 9.1 shows the statistically significant differences of the empirically estimated shape and scale parameters of the Gamma distribution for the two conditions shown in Figure 9.14. Equivalent plots referring to the speed parameter are shown in the Appendix Figure A4.

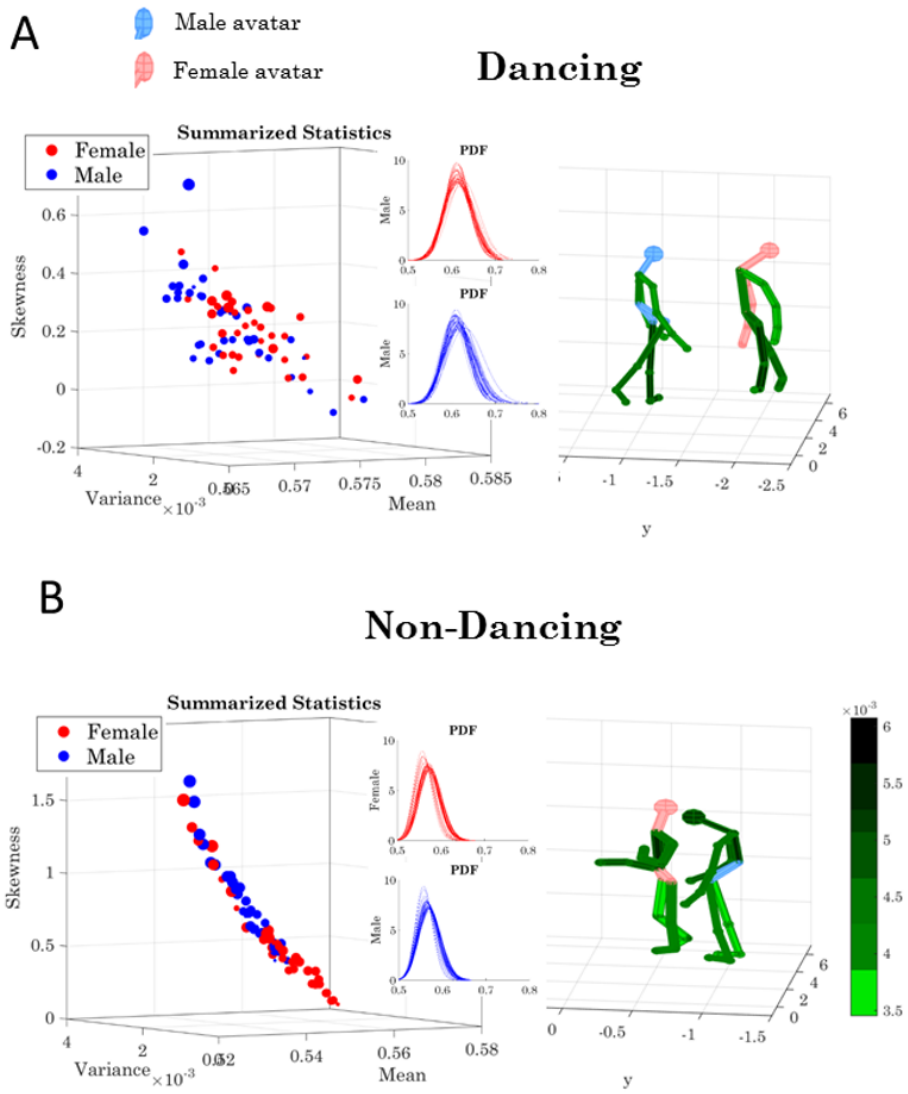

Figure 9.14: **Profiling the stochastic activity at the micro-level of MM underlying each node of the network. (A) Gamma moments space with insets of empirically estimated Gamma PDFs from the MM and color maps of the NSR depicted in a frame of the avatar representation of the dancers for the dancing condition. A higher level of NSR in this frame is located at the legs. (B) Same representation for the non-dancing condition with the color bar gradient denoting the level of NSR (higher noise at the trunk area in this frame.)**

Table 9.1: **Statistical comparison between the shape and scale parameters of the dancing and non-dancing conditions denoting different probability distributions across the dancers' body parts.**

Parameter	Condition	p-value
Shape(a)	dancing vs non-dancing	$1.3027e-21$
Scale(b)	dancing vs non-dancing	$2.4329e-18$

9.4 Discussion

This methods-paper integrates a new statistical platform with a new data parameterizations and new visualization tools developed for the study of complex coupled dynamical systems. We used partnering-dancers of classical ballet to provide an example of the use of these tools, but they can also be used in other (clinical) settings [110] and extended to brain-body coupled networks to study naturalistic behaviors and EEG-ECG signals in tandem [76]. We here reduced the enormous complexity of interactive bodies with abundant DoF that emerge during classical ballet routines and rehearsing intervals. These analyses informed us in a fast and simplified manner about the automatically entrained or de-entrained body parts in each dancer. More important yet, they revealed the dynamically evolving coupled cohesiveness of the two bodies in motion, a type of information invisible to the naked eye of a person coding videos, or an observer describing behavioral exchange (social or otherwise) between two people (or two animals in an animal model of behavior). This type of cohesiveness that self emerges from the coupled activity of two bodies in synchronous motions cannot be directly physically quantified with sensors on the body. This is so because the cohesiveness is a synthesis of new rhythms extractable from the body-body coupled interactions. This measure of togetherness does not exist in one physical body of one dancer or the other dancer alone. It rather exists in the dynamically changing coherent rhythms of the entrained bodies in motion that our methods revealed in both the bending and the speed cases. This is a case whereby the gestalt of the partnering dancers (in this case, the organized whole of the two bodies in motion) gives rise to information that is more than the sum of the many

contributing parts. It is a type of data that will inform AI models how to quantify this qualitative aspect of social dyadic exchange (the rapport dynamics evolving moment by moment.)

The methods also enable quantification of leading profiles based on network evolution in the connectivity patterns and underlying profiles of NSR. The dynamic nature of these data is amenable to provide movies (1) of the network performance across different frequency bands, (2) of the automatically identified togetherness that the end-user can query across body segments of interest, and (3) of the NSR stochastic evolution distributed across the grid of nodes of both dancers. These movies can also provide the temporal evolution of the personalized inner-networks' synergies of each dancer; or of those of the coupled mode from the coupled network modularity analyses.

These variable coordination patterns of inner-body and inter-body synergistic coupling are automatically extracted from the inherent variability in the micro-movements of the trajectory parameter under consideration (the bending of the curve describing the motion path). Here, this bending metric was our parameter of interest because it reflects high level planning that dancers can relate to. Different body parts generate different curvatures on demand. Dancers controlling the motions of their own body and leading the motions of the partner's body can bring up to conscious planning the prospective movements of body parts they rely on for a given sub-routine of the choreography. Other kinematic parameters (e.g. speed and acceleration, etc. in the linear and angular domains) can also be used (see e.g. see the use of linear acceleration and angular speed in other network analyses considering dynamics of brain-EEG with body-IMU dynamics and also the angular accelerations of nodes along a grid of body joints [76] [100] [110]). Because the use of these analytics is completely automated, and the cohesiveness of the activity spontaneously self-emerges from the coupled behavior, these tools may pave the way to study coupled dynamics in a broader sense, including patterns of coupled interactions in social bodies such as those of a theater involving the audience and the performers; or social crowds in naturalistic settings.

The type of empirical data one could gather using the present approach can inform models of artificial agents about spontaneously self-emergent behaviors conducive of autonomy / agency of the brain over one's own body or over the bodies of others, when leading a social exchange. Indeed, leading profiles are automatically extracted with the weighted directed network approach that we introduced here as a new tool extending previous work in brain network analyses to analyses of closed-feedback-loops of bodies in motion.

One could conceive the micro-movement parameterization that we introduce here as a representation of a form of oscillatory vibrations (putatively) experienced by the nervous systems of the dancers through different sensory channels. These would include processing of their motion-dependent biorhythms along vision, vestibular (balance) and tactile receptors. It is known that humans are sensitive to mechanical oscillations ranging in frequency from well below 1Hz up to at least 100KHz -a much broader range than the range of human hearing [77] as explained by Guignard in Chapter 29 of the book (focusing on Vibrations) and Chapter 30 (focusing on Noise). Surprisingly, motor physiologists have only registered frequencies of motions for stand alone tasks where the person performs motions that range from finger tapping [ref] to gait [ref] to musical instrument playing [ref]. Yet physiologists have not measured the frequency bands in which features of complex dyadic motions are registered. Perhaps part of this void is accounted for by the paucity of studies that tackle coupled motions that emerge from the biorhythms generated by two or more bodies in motion. Perhaps contributing to lack of information along those lines are the current statistical methods that average out the minute fluctuations that we harness by parameterizing movement parameters via our micro-movements and examine only a highly smoothed version of the original signal. By using this parameterization of the trajectory bending parameter we capture oscillations across a broad range of frequencies that are known to be sensed by humans in the context of vibrations of the types we are modeling with the micro-movements spike trains and the Gamma process SPIBA offers.

While the field that studies the neurophysiology of human movements has not tapped

into these higher frequencies (they report frequencies below 20Hz), the research literature of structural engineering has done ample research on aspects of sound, vibration and noise that are relevant to humans. They must do this type of research to determine the types of materials and structures that are adequate to dampen humans' sensitivities to materials' vibrations that may reach human detection and perception in the auditory domain and in the touch domain and become annoying or even harmful to humans. The need for such research arises, for example, in airplanes where humans travel for several hours. The vibrations from the airplane engines must be dampened by proper materials to avoid levels of noise that could be harmful to humans -as their nervous systems detect those levels. Likewise, vibrations conducted by materials from buildings could be harmful or annoying to humans because their nervous systems sense them.

Material and structural engineers have great knowledge about the frequencies accessible to the human nervous systems, not just in the auditory domain but also in the tactile domain (as the feet and skin receptors sense such vibrations.) For example, it is reported that the range from 0.1-3Hz are characteristic of large artificial structures that may transmit vibrations to humans (e.g. building materials and transportation systems); 3-30Hz exist in the every-day vibrations transmitted by vehicles and machinery, building walls, house frames, wind loads, seismic activities, vibrating forces from industrial operations, trains passing by, road traffic, among others. Above 30Hz, humans sense vibrations through windows, small panels and audible noise from shaking or rambling sounds. However, higher frequencies (such as those we uncover here in the cohesive motion patterns of the partnering dancers) are generally not associated with danger and as such, humans do not react to them with fear (as measured in the context of materials and structural engineering) [30]. In this sense, it is interesting to think of this form of high-frequency vibration in the context of the type of ballet partnering that we studied as sensory feedback that can safely re-enter the nervous system along more than one sensory channel.

The LEDs on the dances' suits transmit visual input from the dancers' bodies in motion

(i.e. from those parts of the body that are visible to each dancer); from the partner's body in motion and from the coupled synergies of the two bodies in motion that each dancer's nervous system may detect and perceive in dance-forms or patterns. Further, along the tactile / touch sense, the dancers can experience the vibrations of their own bodies in entrained motion as they pull-push and twirl together. In this sense, the type of data that we examined here (the moment-by-moment amplitude micro-movements of the bending signal) can be understood as a form of vibration experienced as sensory reafference from one dancer to the other.

This type of reafferent peripheral activity emerging from coordinated bodies in motion, express self-emergence of coupled behaviors during dyadic exchange. To capture it here, we used purely data-driven statistical (distribution free) methods and network connectivity analyses. These approaches to study dyadic interactions are new to behavioral neuroscience. Yet, their use could be easily adapted to other laboratory, school, home and clinical settings. In laboratory settings, they could be used to assess the exchange between the experimenter and the participant. In the clinical settings, they could assess clinician and patient interactions -thus changing the way diagnoses are conferred today (i.e. purely relying on accredited/certified clinicians who are paid to perform such assessments [103]). In the classroom settings, they could evaluate the teacher and pupil interactions, and in the home environments they could assess the caregiver and patient using mobile health approaches.

These methods can also be extended to animal models whereby the interactions across animals in a colony can be monitored using camera-based systems (as those used here) or wearable sensors (as in [76] [110]). Indeed, the dyadic exchange is ubiquitous to many settings and can serve as a basic unit of other more complex non-linear dynamical systems modeling social interactions in general. Because we explore these biometrics at a macro-level of behaviors and at the stochastic micro-level of variability underpinning these higher-level behavioral patterns, we provide new means to connect multiple layers of complexity through

a common analytical and visualization platform e.g. amenable to use with new wearable biosensors.

The advent of wearable biosensors and off-the shelf camera systems are among the many tools from which MM and CPF parameterizations can be derived. Then, the statistical platform for individualized behavioral analysis (SPIBA) can be applied and our weighted directed graph networks used to visualize self-emerging connectivity patterns in very complex and large networks.

These new methods and paradigms may serve to unify and advance more than one field and area of enquiry in the performing arts. We hope that more generally, our new tools can be used to study interacting bodies in motion. These may include gaming, VR, humans in social contexts and hybrid interactive-co-adaptive interfaces of human-avatar and human-robot environments.

Finally, for the purpose of this thesis, the work present in this chapter has contributed on developing methods to study the connectivity network of the bodies in motion and potentially used it in an avatar-participant dyad in a vision-driven co-adaptive interface.

9.5 Appendix

Links of movies in YouTube:

1. Dancers during T-pose and calibration `youtu.be/L9UhfpmWFV0`
2. Modules and coupling behavior with avatar representation for Dancing condition `www.youtube.com/watch?v=XbPbUmu8ZZ0`
3. Modules and coupling behavior with avatar representation for Non-Dancing condition `www.youtube.com/watch?v=8p-vcuRkCp8`
4. Dancers and avatar during a routine `www.youtube.com/watch?v=pHJ8qYgCg0k` (part of the video demonstrates *vimeo.com*/96030980 from Bod and Dolly project by Tarik Abdel-Gawad, dancers: Maria Kochetkova and Jaon Boada)

5. Avatars' representation of the NSR bodily maps Dancing condition. www.youtube.com/watch?v=FY98PxsDIdQ

6. Avatars' representation of the NSR bodily maps Non-Dancing condition. www.youtube.com/watch?v=2qXg8bRQZ8c

Table 9.2: **Lists of all subroutines that were used as dancing segments.**

Name	Segment (Fr)	Length (Fr)	Length (sec)	Link
Piece 1	16000 – 19300	6710	13.33	youtu.be/KHp5uyawm4Y
Piece 2	-	-	0	
Piece 3	12890 – 19600	6710	13.96	youtu.be/_zbKB_vYOTc
Piece 4	6600 – 10800	4200	8.75	youtu.be/pK8tTc76lr4
Piece 5	5500 – 17900	12400	25.83	youtu.be/73DsonVp5BU
Piece 6	8000 – 48400	40400	84.16	youtu.be/yC0nTQBrfQ4
Piece 7	7400 – 22800	15400	32.08	youtu.be/wNYZrzy26yU
Piece 8	25000 – 52500	27500	57.29	youtu.be/yKREUOi_mWs
Piece 9	5200 – 10500	5300	11.04	youtu.be/9RVJQYO4nWE
Piece 10	-	-	0	
Piece 11	1200 – 19500	7500	15.62	youtu.be/b8kFFscZsaY
Piece 12	9000 – 28000	19000	39.58	youtu.be/vFCFyKGlAsQ
Piece 13	19000 – 55000	36000	75.00	youtu.be/Kpp33rjC7L0
Piece 14	7500 – 29800	22300	46.46	youtu.be/5RhaSvwQL6c
Piece 15	6800 – 56600	49800	103.75	youtu.be/QtC-EdXwDQ4
Piece 16	5700 – 24660	18960	39.50	youtu.be/YBIFk1me3hs
Piece 17	16100 – 50500	34400	71.66	youtu.be/kPlLd-m8xHg
Piece 18	11500 – 45400	33900	70.62	youtu.be/M-UVxZMgsZI

Chapter 10

Real-Time Closed-Loop Co-adaptation: Steering the System

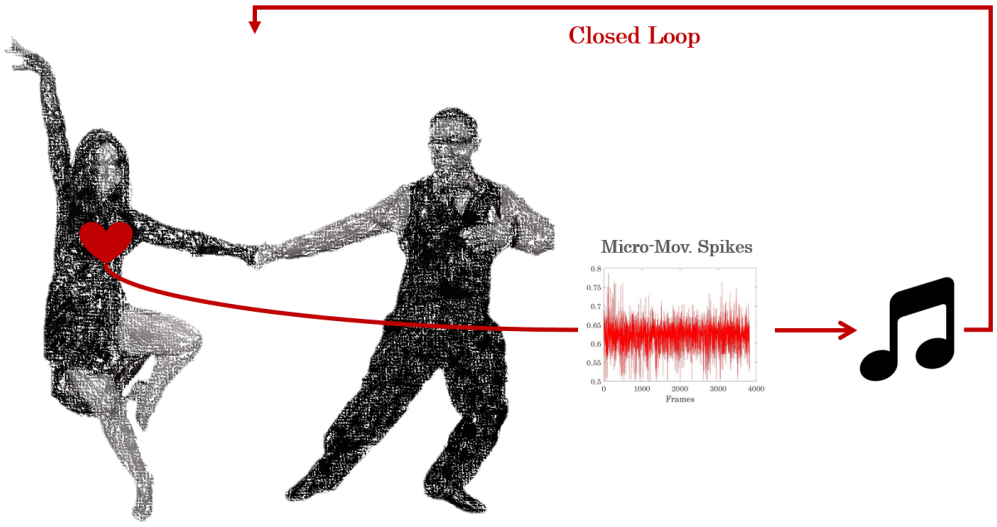

Figure 10.1: **The closed-loop heart-audio co-adaptive interface studied on Salsa dancers.**

In this chapter we present our last study where we introduce the artificial closed-loop co-adaptive interface driven by the stochastic feedback from biophysical rhythms of two partnering dancers. As they exchange information hidden to the naked eye of an observer, we show how to externally steer the autonomic signals of the heart through adaptive music. Our closed-loop set up provides a new platform to help dancers causally modulate deliberate control of their bodies in motion while using spontaneous fluctuations to help synthesize new autonomic dynamics [43].

10.1 A Study of Physiological Signal Entrainment Through the Real-Time Sonification of Heart Rate Data

The stability of autonomic activity is vital for the survival of the organism. This activity seems impervious to environmental influences, such that deliberately controlling it from the outside poses a great challenge. In neurotypical systems, steering autonomic signals externally (e.g. attempting to shift the heart rhythms) may seem superfluous, or maybe mainly linked to regulating stress and its consequences. Even though yoga, or other meditative techniques, it has been challenging to teach people how to self-regulate their heart rhythms [9][22]. Could we do so causally while interfacing the person's heart with a computer? The question is very challenging, but it could help many people with arrhythmias or compromised hearts. Examples abound and range from premature babies in the neonatal intensive care unit, to young children in the spectrum of autism [102][76]. Part of the challenge seems to rest in our pervasive reliance on open-loop recording systems to carry on such research. In the open loop settings, we collect biophysical data and analyze it a-posteriori to then provide feedback to the person at a time when the context in which such data was harnessed has already changed. Closed loop settings such as those used in brain-computer interfaces have not been useful either, as they seem to rely on assumptions of stationarity [57][80]. Such assumptions do not necessarily hold when we examine fluctuations in the system rather than grand-averaged states of behavior harnessed in quasi-static and artificial environments.

Motions and their sensations are dynamic. They ought to be studied in naturalistic environments, where dynamical changes that occur from moment to moment can be readily captured and fed back to the nervous systems in empirically-informed parametric ways. Such methods would enable causal control of the internally self-generated rhythms from the outside.

Causal control cannot be dictated to the nervous system in a top-down fashion because

this would interfere with the systems' own autonomy. In this sense, it would be great to have the ability to provide the desired feedback in real time and to do so while relying on subtle signals that do not pose additional resistance from the person's autonomous nervous systems: i.e. the systems that operate largely beneath the person's deliberate awareness. In this sense, it would be ideal to interface directly with the person's heart rhythms, spontaneously entrain them with the rhythms of music and in this way steer the autonomic systems' states towards systematically desirable regimes of high predictability.

One such a setting could be through partnering dancers, where the person is busy interacting with the partner and the music may serve as a natural way to entrain external sensory inputs (such as audio signals) with the person's self-generated internal rhythms (such as those from the heartbeats).

Music is known to be processed through fast auditory channels where receptors are well-equipped to process vibrations [19] and respond to music emission even at the fetal stages, before birth [52]. Likewise, kinesthetic receptors can process vibrations along a broad range of frequencies and help the person feel its surroundings [71][70]. Perhaps if we were to sonify internally self-generated (kinesthetic) bodily biorhythms, including those of the heart, we could parameterize them as vibrations and easily blend them with sound (Fig.2.7 and 2.8).

Indeed, we could (1) build a closed loop interface to co-adapt the person's internally self-generated vibrations with the external ones from musical (sound) streams; (2) build appropriate data types to enable the process of blending external and internally self-generated rhythms; (3) provide proper analytics to track real-time co-adaptation of these biorhythms and (4) provide a proper experimental setting to induce causal change and precisely quantify its immediate effects in real time.

In the case of the kinematics and the heart signals, we know that both have peaks and are highly sensitive to changes in cognitive demands (Fig.10.3) within the open loop context [75]. Yet, we do not know how the amplitude and timings of kinematic signals from the motions of the body and heart may change in the context of a closed loop co-adaptive

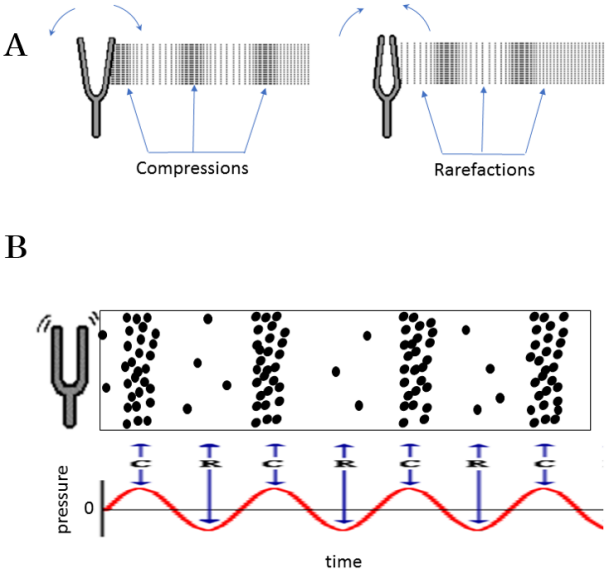

Figure 10.2: **Converting sounds to spike representations. Analogy of waveforms from biorhythms and waveforms from sound representation to use the spikes extracted from biorhythms as sound. (A) Tuning fork motions evoking compressions and rarefactions in alternating patterns. (B) Particle representation and sinusoidal waveform representing the sound traveling in a medium.**

interface.

This paper describes steps 1-4 above and provides evidence that we can parameterize and steer someone's autonomic signals using music as an external controller.

10.2 Experimental and Computational Details

10.2.1 Partnering Dance Co-adaptation

Participants

Two experienced salsa dancers (a male and female, 30 years old) participated in the experiment. They signed the consent forms approved by the Rutgers University Institutional Review Board in accordance with the Helsinki Act.

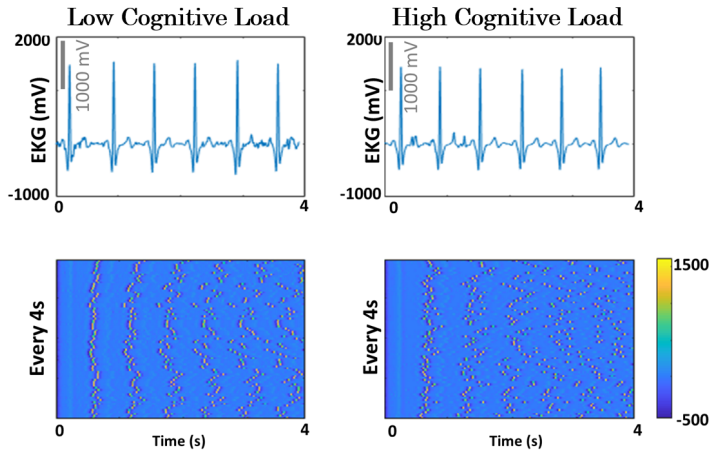

Figure 10.3: **Prior research has shown that in open loop settings the heart signals are affected by changes in cognitive loads, but this merely opens the question of correlation between changes in cognitive load and changes in heart rhythms (also shown as spike trains). Could we establish causation and systematically steer these autonomic rhythms in closed loop settings?**

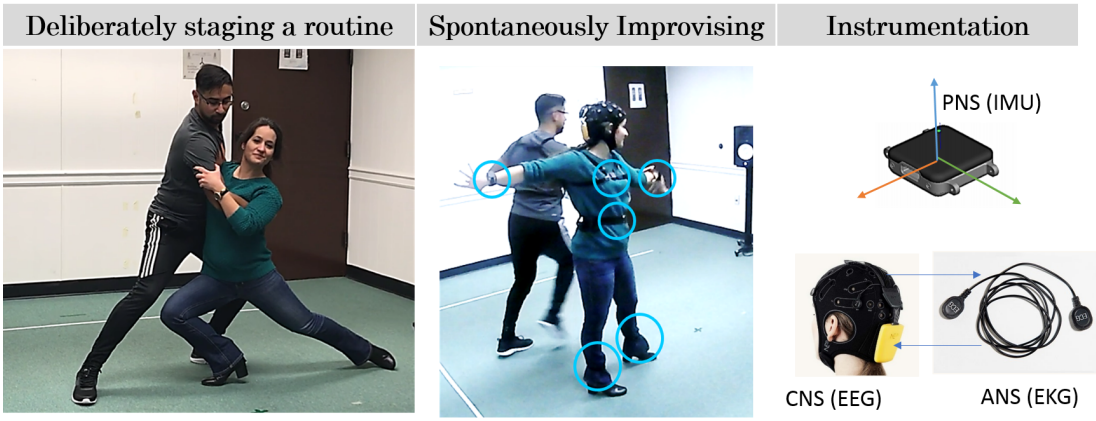

Figure 10.4: **Experimental design and instrumentation (A) Deliberate staging a routine vs. spontaneously improvising it. (B) Wearable biosensors to harness biorhythms from the central and peripheral nervous systems and to extract autonomic (heart) signals.**

Experimental Design

The task consisted of two parts. Part 1 was to perform a well-rehearsed routine staging a choreography and using deliberate poses, Fig 10.4A-left panel. Part 2 was to spontaneously improvise, Fig 10.4A-right panel (Appendix video 1).

Instrumentation

CNS and ANS biorhythms: A 32-channel EEG system, Enobio NeuroElectrics (500Hz, Barcelona, Spain), was used to record brain activity as well as HR (Fig 10.4). For more specification of the equipment that was use see Chapter 2. We focus on the analysis of the HR data for the present paper.

PNS biorhythms: Twelve inertial measurement units (IMU in Fig 10.4B) were used to record bodily activity in the form of linear acceleration, angular speed and temperature (opals APDM, 128Hz, Portland, OR.) These sensors were placed on the thorax, lumbar, wrists and ankles of both participants and recorded activity synchronously across all 12 IMUs.

10.2.2 Co-adaptive Closed Loop Interface

Enabling Synchronized Streaming.

We used the Lab Streaming Layer (LSL) platform to synchronize all streams of activity from the various instruments (https://github.com/sccn/labstreaminglayer /wiki) to send data from Enobio to the Python interface.

Closing the Loop

The autonomic heart activity was harnessed, converted to spike trains and sonified, along with the music (methods explained next). The spike trains derived from the peaks were

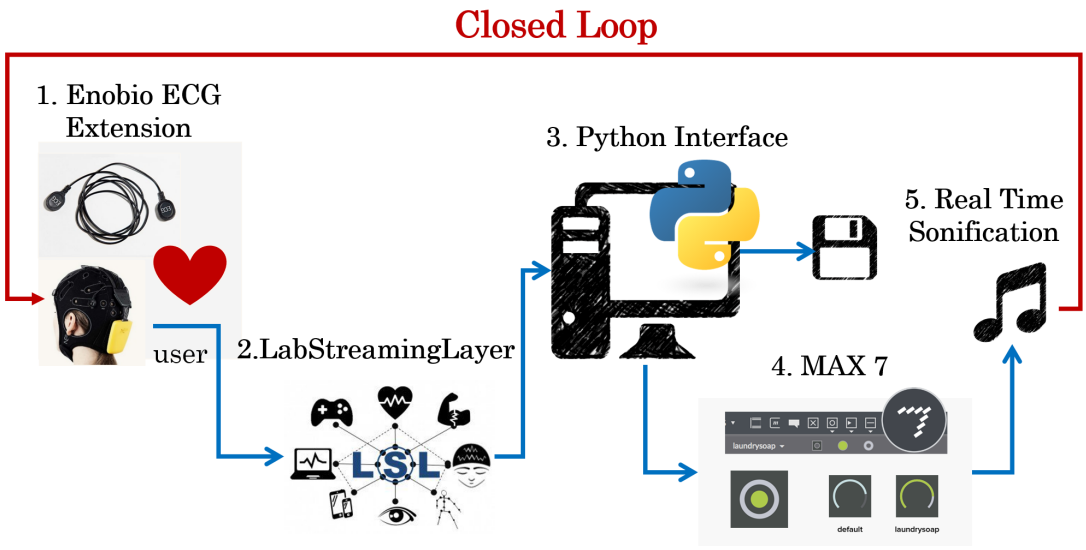

Figure 10.5: **The closed-loop co-adaptive interface to modulate the internally self-generated heartbeat signals using external music's audio features.**

processed, sonified and played back using music composition (see next). The python interface extracted the times of the heartbeats R-peaks and streamed those "pocks" to Max 7, where these "pocks" were collected to reset the tempo of the original song according to the ongoing frequency of peaks the heart streamed in real time. The self-generated output became re-entrant input to the nervous system and was re-parameterized in real time. The schematic of the interface is shown in Fig. 4.

The Python interface is designed to continuously receive chunks of data streamed by the LSL at a frequency of 500Hz. At the beginning of the recording, it buffers 4sec-long data (2000 frames), which utilizes as an assistive vector to process the data. Once it collects those 2000 frames, it sends a signal to start the Max interface and it begins streaming 0 or 1 values for each new frame of data it receives. When 1, it means a peak value was detected. When 0, it means no peak has been detected. After 4 seconds, the system updates the buffer by adding the new value to the end of the buffer and dismissing the oldest value for every frame of data it receives. On each update, the buffer with the ECG data was filtered using the Butterworth IIR band pass filter for 5-30Hz at 2nd order. The range of

the band pass filter was selected based on the finding that a QRS complex is present in the frequency range of 5-30Hz. Then, we used a find-peaks function to detect the R peaks and their location.

To achieve the closest to real-time streaming, we designed our algorithm to stream 1 when detecting a peak at the most recently added frame, the last one, while accounting for the time it takes to filter and process these values. Such time periods are uncertain because they require forecasting the future trend of the signal. As a result, we had to detect peaks at a consistent earlier frame and estimate forward. To that end, we empirically examined different values of n number of earlier frames and investigated the limiting cases, so that n had the smallest possible value (be as recent as possible) and the corresponding ECG value had enough neighbor values to be filtered and be processed properly for reliable forward estimation. Initial stages to build the interface took extensive experimentation, upon which we settled on n=10. This value provides good buffering while delaying 1/50 sec. The interface is also capable of saving the raw data collected during a session for a-posteriori analysis. These data were used to calibrate the buffering time.

Heart-Rate-Controlled Playback Interface.

The playback interface consists of software designed using the musical programming language Max (cycling74.com). Filtered heart R peaks are transmitted in real time to Max from the Python script via Open Sound Control (OSC) (http://opensoundcontrol.org/). Additionally, signals to start and stop playback, as well as an index value of peak numbers used for testing the system are also transmitted to Max via OSC. Within the playback interface, the interpeak intervals are measured and converted to beats per minute. This data is scaled to create a playback speed scaling factor, where 1 equals "normal" playback speed, 0.5 equals half speed, and 2 equals double playback speed. There are two modes for data scaling, a linear scale, where an increase in the dancers' heart rate will produce faster playback, and an inverted scale, where an increase in the dancers' heart rate will produce slower

playback. Using Max's sfplay~ object, any audio file may be loaded into the software, and playback is controlled in one of two modes: playback speed, where slower playback speed produces a lower pitch, as in the playback of analog recordings, or time-stretch mode, where playback speed and pitch are decoupled. The interface was also capable of recording the audio. A link to the recorded audio files can be found in Table 1 (links will be added after acceptance (if), see supplemental material).

10.2.3 Micro-Movements Spike Trains to Parameterize Motions as Self- Generated Vibrations

The heart R-peaks were converted to spikes which we standardized to lie in the [0,1], as already explained in Chapter 2. Figures 2.7 and 2.8 illustrates the Micro-movement spikes of the heart rate and audio data, respectively.

We use the Music Information Retrieval -MIR toolbox of Matlab to extract the envelope of these spike trains and examine the auto-correlation signatures expressing periodicity and structure in each piece. Fig.10.6 shows the original waveforms of the music and the altered waveform after applying the heart R-peak transformation extracted in near real time.

10.3 Results and Discussion

10.3.1 Detecting Different Types of Autonomy

The main question we had in this paper was whether we could causally alter the heart rate signal by blending it in near real time with music, as the dancers performed the routine in two fundamentally different modes. One mode involved spontaneous improvisation while the other mode involved the staging of a well-rehearsed routine in a quite deliberate way. The latter becomes automatic as the dancers have rehearsed it often enough to have it flowing quite well. Yet the dyadic body-posing and the various form-components of the routine maintain a top-down level of goal-directness that makes the overall performance

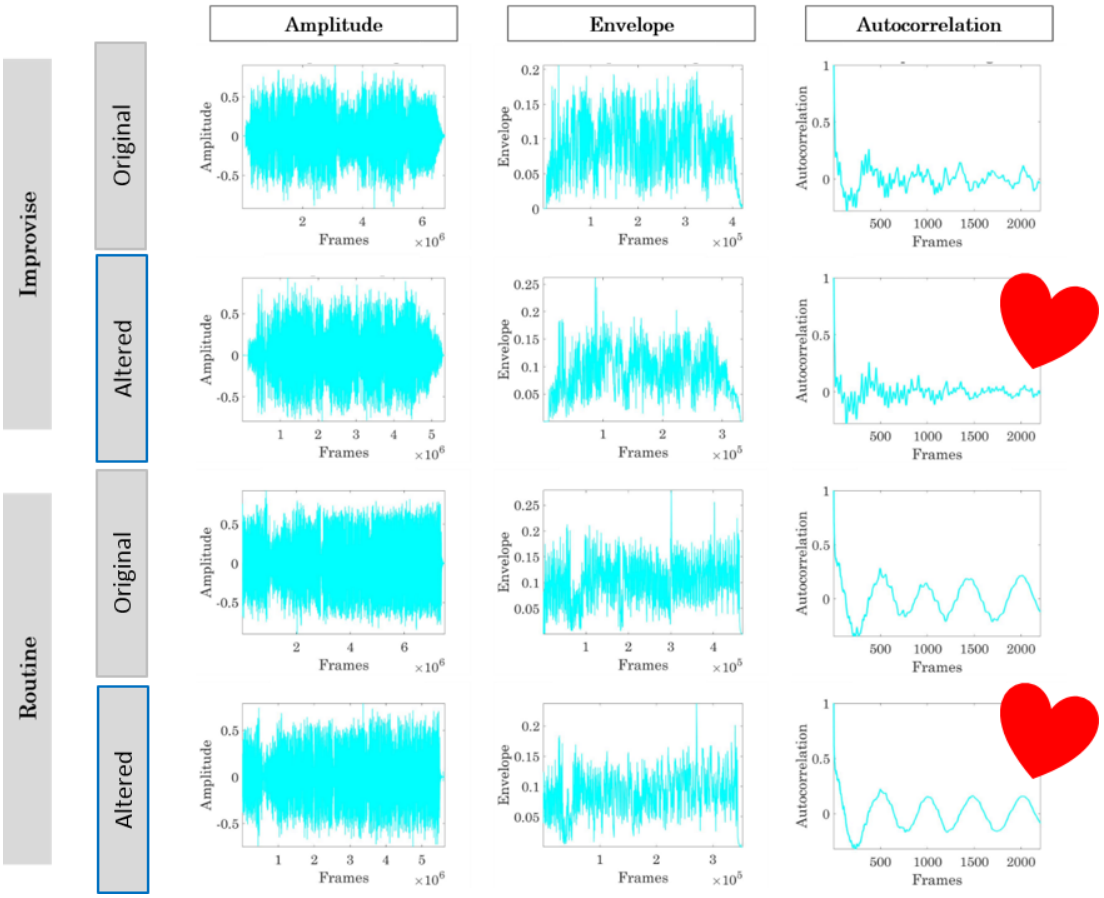

Figure 10.6: **Original vs. altered music using near real-time Max transformation and playing it back to the dancers using the closed-loop interface. You can listen samples of these songs in Appendix video 1.**

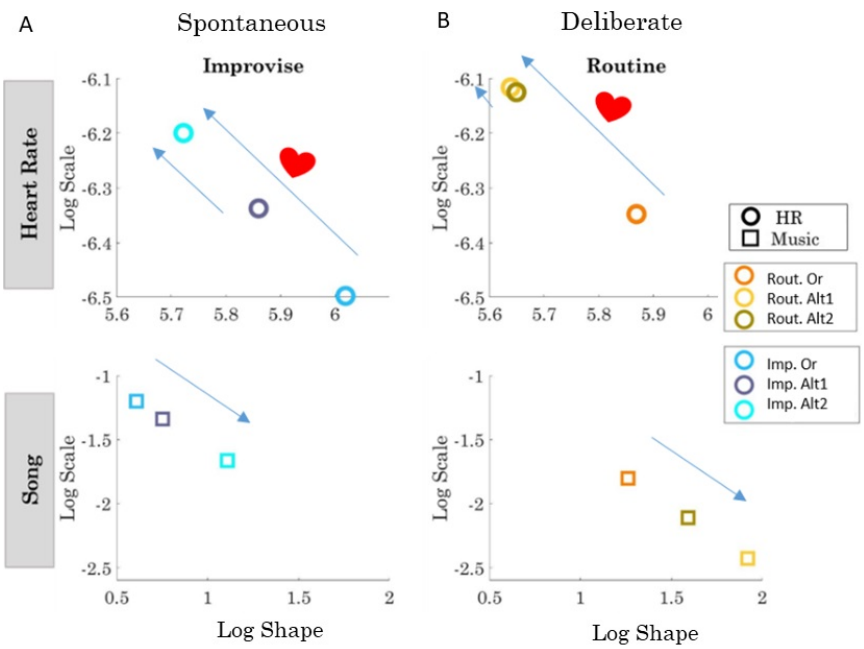

Figure 10.7: **The Gamma signatures of the heartbeat (top row) and the songs (bottom row) for the two conditions, as well as their corresponding Probability Density Functions.**

quite deliberate.

In contrast to this intentionally staged condition, the spontaneous improvisation would necessarily lead to self-emerging bottom-up components that we expected would have a different signature in their rates of change as the measurements were being taken in near-real time.

Indeed, upon continuous buffering of data for the spontaneous improvisation condition, we quantified a stochastic shift away from the signatures of heart playing to the music in its original form. Systematic shifts of the heart signals with the near real time heart-R-peak alterations to the music causally led the heart to changes away from its original state. This can be observed in Fig 10.7A where the arrows indicate the systematic shifts from responses to regular music as the dancers adapt to it in real time. We coined this spontaneous autonomy because the heart responds to spontaneous performance based on its own self-generated biorhythms in this condition.

The condition where the dancers performed the staged routine did show an initial shift away from the response to the original music. However, in contrast to the spontaneous improvisation case, here the heart-R-peak alterations to the music did not lead to a systematic shift in heart rhythms when the altered music was played over and over as it changed less with the heart changes. The participants adapted rather rapidly under this deliberate autonomy condition, There the change remained in a robust location of the Gamma parameter plane and even though there was an initial transition in stochastic regime, the fluctuations in self-generated heart signals found a steady state thereafter. Corresponding PDFs estimated from the Gamma parameters are shown in Fig.10.8.

10.3.2 Steering the Autonomic Signals in a Closed Stochastic Feedback Loop

The Gamma signatures of the heart are shown in Fig. 10.7-10.8. The arrows in Fig.10.7 were used to emphasize the trend of the signatures to move toward the LUQ after repetition of the condition. The differences between the datasets that generated these signatures is also illustrated with their corresponding PDF. The same analysis is applied on the music.

Finally, we estimated the four moments for the heartbeat and the songs, Fig. 10.9. To better understand the relationships between those four parameters, we also plotted pairwise the mean and the variance, the skewness and the kurtosis. The shift of the signatures on the latter figures demonstrates the adaptation of the heart on the alteration of the song.

10.3.3 Visualizing the Results in other Statistical Dimensions

The Gamma parameter plane and PDFs provide a tool to visualize our results in a new way. In addition to that, we also estimated the Gamma moments and plotted them along different dimensions (Fig. 10.9). The Gamma mean was plotted along the x-axis; the Gamma variance was plotted along the y-axis; the skewness was plotted along the z-axis and the size of the marker was used to represent the kurtosis. This data representation

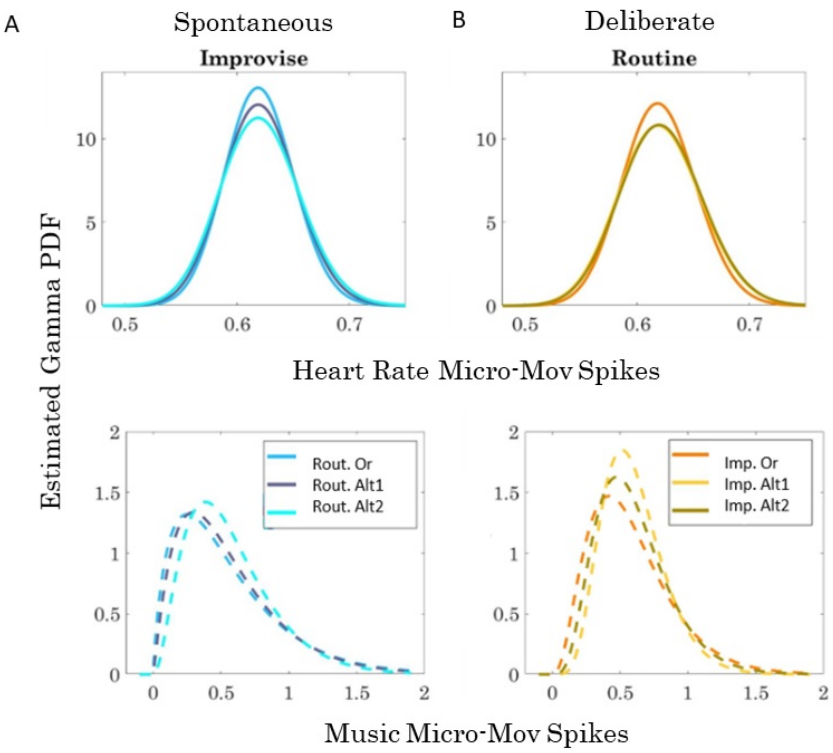

Figure 10.8: **The Gamma PDFs estimated from the empirical values of the shape and scale. (A) The spontaneous autonomy case which involves improvisation (top for the heart and bottom for the music spikes) Note the original has more symmetric shape and lower dispersion (lower NSR) than the altered versions using the real-time heartbeats. (B) The deliberate autonomy case whereby the altered music initially drove the responses away from the original music, but then remained steady despite systematic changes in music (bottom panel).**

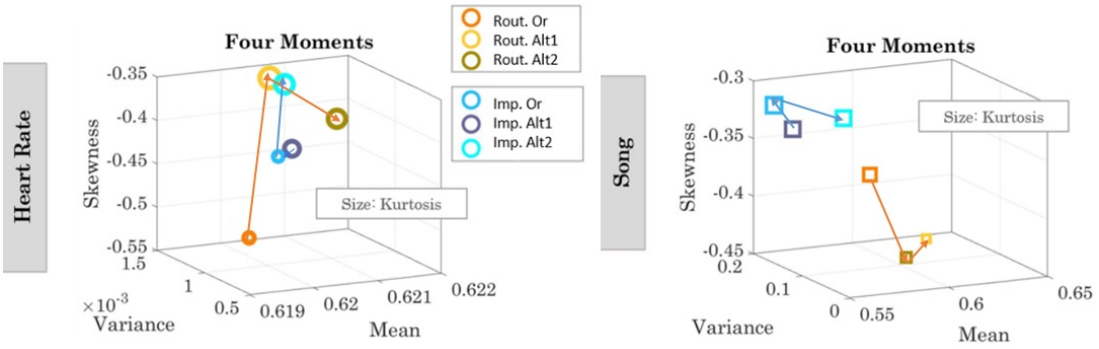

Figure 10.9: **The Gamma Moments in the order in which they changed for each of the spontaneous and deliberate autonomies. Arrows mark the trajectory of the Gamma process for both the heart (left) and music (right) signals.**

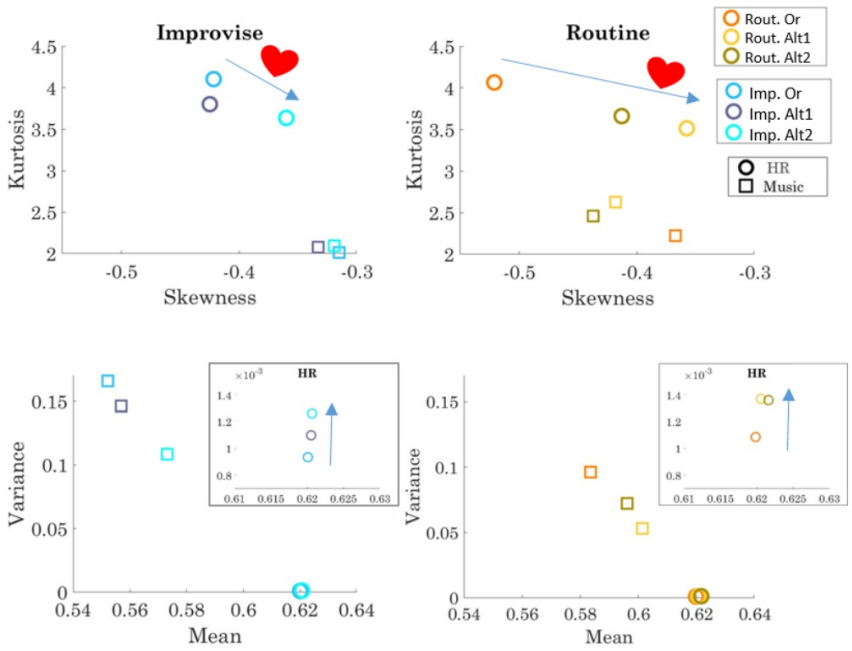

Figure 10.10: **Patterns along various Gamma-moment planes also reveal fundamental differences between modes of autonomy.**

helped us further uncover self-emerging patterns in the fluctuations that the projection on the Gamma plane could mask (Fig.10.10).

Lastly, we performed several non-parametric statistical tests (ranksum, Kruskal-Wallis one-way analyses of variance) and confirmed the significance of these differences along the spikes concerning the fluctuations in timing (InterBeat Interval times).

10.4 CONCLUSIONS

In this work we aimed at diaeveloping an interface to close the feedback loops between externally generated sensory inputs and internally self-generated biorhythms. Our goal was to establish cause-and-effect loops whereby the ongoing autonomic activity could be separated into fundamentally different stochastic regimes. These regimes would serve to characterize spontaneous vs. deliberate autonomy: two modes that we have been exploring in our research involving autistic individuals [91], dancers [41][42] and skilled athletes [88] [90]. This prior work had identified fundamental differences on the influences that changes

Table 10.1: **Songs of the conditions**

Conditions	Song	Artist	Link
Improvise	Alza La Pata Y Vete Flaca	Orchestra Suprema	youtu.be/dWuC5sfr7WI
Improvise Alt.1	-	-	youtu.be/dWuC5sfr7WI?t=3m14s
Improvise Alt.2	-	-	youtu.be/dWuC5sfr7WI?t=5m12s
Routine	Machu Pichu	Alfredito Linares	youtu.be/dWuC5sfr7WI?t=7m42s
Routine Alt.1	-	-	youtu.be/dWuC5sfr7WI?t=10m29s
Routine Alt.2	-	-	youtu.be/dWuC5sfr7WI?t=12m36s

Table 10.2: **Comparison between Modes of Autonomy (Wilcoxon rank-sum test)**

Data	Improvise vs Routine	Original vs Altered Song
MM Heartbeat Amplitude	0.137	0.009
Interbeat Interval (IBI)	9.3610^{-24}	1.9310^{-80}

in dynamics have on intentional vs. spontaneous (uninstructed) movements. While several trajectory features remain invariant to changes in dynamics in the former; the latter are highly dependent on changes in dynamics [88], context [66] [85] [87] and source of sensory guidance [101][96]. Here we find consistency with this dichotomy in a more general context of partnering dancers. This is a situation whereby coupled dynamics give rise to additional (social) dyadic influences on these two classes of movements. We were able to provide a new paradigm to explore these different modalities of neuromotor control with a closed loop co-adaptive interface that altered the heart rhythms using auditory (musical) input re-parameterized by the female's heart rhythms in real time.

More specifically, we managed to extract the time of heartbeats of the dancer and use them to alter the speed of the song they were dancing to in real time. While the alterations in the musical features seemed subtle, Fig. 10.6., they did have a significant impact on the audio -as modulated by the heart in real time, Table 1 provides the links to the original and altered music (links will be added (if) after acceptance, see supplemental material).

Most surprising was the change that the song alteration caused on the stochastic signatures of the fluctuations of the heart. The heart is an autonomic organ hard for an individual to control with intent. Yet, we managed to shift its signatures over the Gamma plane, Fig. 10.7, and based on the Wilcoxon rank sum test, Table 2, we shifted the amplitude of the

MM spikes and their corresponding timing in the altered vs. original conditions.

Their differences in temporal fluctuations were rather significant when dancing to the original version of the song as compared to dancing to the real-time heart-R-peaks' altered version. It is also noteworthy that the closed loop nature of this experiment produces responses that return as re-parameterized re-entrant input: while the heart adapts to the changes of the music that the person self-generates; the music also inherits features of the heart. More specifically, the stochastic signatures of the songs shifted towards the RLQ, Fig. 10.7, which indicates that the audio signal converted to more symmetric expected values with lower dispersion -i.e. easier to anticipate with high certainty.

Although this work involved salsa dancing, the same type of analyses could be carried on with other dyadic interactions in the context of social exchange, whereby the sound input could be extracted from speech. The ability to parameterize as fluctuation-spikes multiple forms of sensory inputs from the external environment and blend them with those self-generated from the internal environment of the nervous systems, gives us great power to separate deliberate from spontaneous autonomy and use the latter to steer the person's signatures in real time. Since we know which regimes are desirable on the Gamma parameter plane, and since the spontaneous mode transpires largely beneath the person's awareness, here we have a tool with the potential to steer autonomous control with minimal resistance.

This paradigm has great use to help boost autonomy in early neurodevelopmental stages of systems for which this important aspect of brain development is compromised. It is also of potential use for systems with neurodegenerative conditions where loss of autonomy compromises the person's self-agency.

Because our methods are personalized, we can adapt them to the individual interfacing with our system and tailor the adaptive process specially to the person's needs and autonomic system's preferences. All and all, we here provide a platform to assess levels of autonomous control and steer them in real time.

10.5 Appendix

1. The routines and the sonification of the heart: `youtu.be/7XmhxEu8Fug`

2. The original and heart-beat altered songs: `youtu.be/dWuC5sfr7WI`

Chapter 11

Conclusions

In this thesis, I presented new data-types and analytics for building co-adaptive multimodal interfaces guided by real-time stochastic feedback. The work is divided into two main sections, the open-loop, Chapter 3-7, and closed-loop, Chapter 9 and 10. The open-loop section includes four preliminary studies conducted to develop tools and methods that allowed us to explore sensory preferences and adaptive behavior so I could use that information later within the close the loop context, when I built an intelligent co-adaptive interface. The closed-loop was a critical part of the work presented in this thesis where novel technology was developed.

In the first study, Chapter 3, I investigated motor learning and adaptation. I exposed the participants to 3 different pointing tasks (varying in a number of dots patterns, increasing in complexity), where they had to discover and learn the hidden pattern of the regular points as well as familiarize themselves with a sudden event, aiming to distract the learning process. In this study, I tracked the impact of repetition in the development of habitual behaviors, and the effects of sudden surprises on the sensory-motor adaptation process. I also managed to characterize motor fatigue in the progress of co-adaptation.

In the next study, presented in Chapter 4, I wanted to examine relations between different bodily signals. Particularly, I inspected the impact of body temperature range in the quality of movements performed. I employed 40 individuals, 20 Schizophrenia patients and 20 controls, to perform a single-target pointing task. The study revealed differences in the temperature level and ranges between the patients and control during rather automated pointing behavior, with a presence of excess noise and random involuntary micro-motions

in the patients reaches.

To have a closer look at the bodily signal integration and possible information I can extract from such signals, I presented a study, where I adopt a data type that enables sensory fusion, Chapter 5. This data-type expresses motion-dependent temperature and temperature-dependent motions. I collected data of 6h of intense rehearsals of pre-professional ballet student followed by her sleep. I applied the Gamma analysis in the full body (arms, legs, torso, and lumbar) and in a continuous format examined variabilities in the stochastic signatures every 20 min. I contrasted and compared the intended movements performed during the rehearsal with the spontaneous ones generated during sleep, and discussed the impact of temperature fluctuations on the movement fluctuations. This study opened new horizons to study bodily signal integration as well as offered new visualization tools amenable to illustrate the evolution of the noise-to-signal mapped across the body. I provided such maps for the experimental set-up, the ballet class, and the rehearsal times, thus developing a mobile tool to study ballet routines on the go using wearables.

I then worked on developing an avatar in the Matlab-graphics environment where I could control it and color-code it according to many different data types. This allowed me to bypass the 'black-box' nature of most plug-in rendering software and deal with the visualization of changes in biorhythmic activity in real-time, creating as well a mirror-like representation of the individual. By coloring body parts according to various parameters I could gain a fast sense of the evolution of the stochastic process I was studying within a given sensory context. I was then able to augment or substitute sensory information from audio-visual signals by using the motor output variability and documenting the rates of change of their signatures in real time, Chapter 6. This set-up could be used in interfaces driven by audio-visual channels. However, at this point, I identified the limitation that the visual representation of sensory information might work slower comparing to the audio mapping that tends to have a more immediate effect. Further, I explored different scenarios of temporal dynamics of the rendering and introduced delays to probe the person's reaction

to the co-adapting avatar. I concluded that visual information brings awareness to the participant and that awareness could be reactive -thus interfering with my goals of adapting the signals beneath the person's awareness. Hence, I turned to investigate the role of audio signal and probed the sensory-motor systems using sound and manipulating this channel.

In the study of Chapter 7, I exposed two college-age individuals (Asperger Spectrum Syndrome student and control) into various sensory modalities while performing natural movements. Specifically, they had to walk with open and closed-eyes while listening to different songs, including their favorite one. From the stochastic analyses, I extracted the dominant sensory modality (or sensory channel) from the motor output stream and build indexes of **selectivity**. This was a contributing criteria to detect preferred sensory context (highlighted sensory input). This uncovered **preferability** an index signaling the preferred mode of sensor input that turned the motor output variability towards higher signal-to-noise ratio and shifted the distribution shape from skewed to symmetric. I point out here that these shape-dispersion criteria is empirically informed and emerged from the lab's research across years of characterization of the sensory motor systems variability in athletes, dancers, neonates, young children and adults of all ages, as well as pathologies of the nervous systems. My research contributed to this body of empirical knowledge. These two critical parameters (selectivity and preferability) enabled us to finally close the loop by building an interface that can intelligently (automatically without human heuristics) select from the continuous motor stream of the natural motions of the person, the preferred conditions (sensory modality and sensory input) and steer the co-adaptation process towards desired regimes (less noisy (dampened dispersion) and more symmetric distribution shape).

These four studies informed our closed loop interface phase. They provided bounds in stochastic parameters describing the distributions of human sensory-motor behaviors in naturalistic settings.

The first closed loop study, Chapter 9, scrutinizes a natural co-adaptive loop, a dancing dyad composed by a female and a male professional ballet dancer. I grouped the data into

dancing and non-dancing segments, and I applied network connectivity analysis invented in the lab across the body-parts of the dyad and detected self-emergent cohesive patterns in the synergies the two dancers formed. The results uncovered a new language to build a vocabulary and syntax amenable to describe complex choreographic routines. The methods developed in this study could be used as well to provide visualization tools allowing the study of avatar-participant dyadic network.

Finally, I built an artificial audio-driven co-adaptive interface, Chapter 10, for complex partnering dances of contemporary pop music. This interface converts heart rate spikes to sound and uses signatures of heartrate variability extracted in real time from the female salsa dancer to control the tempo of the performed song in two fundamentally different modes: spontaneous improvisation and deliberate choreographic (staged) routines. The experiment showed that I could steer the stochastic signatures of the heart an autonomic signal- towards targeted stochastic regimes in two fundamentally different ways with two distinct types of rate of change: deliberate whereby the signatures change and remained robust thereafter (impervious to continues music manipulations) and spontaneous, whereby the signatures change and continue shifting with the real time music manipulations. This part of the thesis confirmed that these two classes of motions have distinct signatures. More importantly my work is the first to unambiguously establish that these two modalities (previously detected at the kinematics level of bodily motions) does exist in the autonomic level. We indeed have deliberate and spontaneous autonomy characterized by distinct stochastic regimes of change.

11.1 Discussion and Innovation

In the presented work, I studied movement as a mean of expressing natural behavior. To that end, I significantly emphasized the studies of unconstrained motions of the full body in a naturalistic manner. I employed research grade motion capture technology and translated our results to mobile computing with wearable biosensors, minimally intrusive and amenable

to study activities of daily living, complex dancing choreographed routines and dyadic partnership. I provided proof of concept that all these methods can be deployed at home, at the gym, dance studios, or anywhere outside the lab for a true mobile sensing platform. I did studies within the confines of the lab and an experimental session but also outdoors and tracking the person longitudinally across days, weeks and months.

I studied a wide range of population from professional ballet dancers to children with Autism with problematic motor control, without focusing just on a particular category. I took the approach to sample broadly in cross sections of the population, to build a better understanding of all possible preferences, differences, and expectations I might need to address in the closed-loop interfaces.

Along with movement, I recorded other bodily signals, since they too contribute to natural behavior. Specifically, I presented the investigation of temperature and heart rate (Chapter 4, 5, and 10). For the analysis I probed all the bodily signals as moment-to-moment variabilities normalized as a deviation from the mean, creating a standardized, unitless scale accounting for allometric effects across the population. This allowed me to explore cross-sections of the population. I then parameterized them to examine their Gamma signatures -shape and scale (noise) parameters-, Gamma mean, variance, skewness, and kurtosis among other parameters. I studied the rate of change of these parameters continuously and examined how changes in the natural behavior throughout a task affect those parameters. Moreover, I integrated signals to focus on possible relations and patterns that might emerge. In chapters 4 and 5, I demonstrated an example of temperature and movement integration. However, this analysis could be applied to any pair of bodily signals. Additionally, I build visualization tools that can illustrate the color-coded variability of the parameters studied (ex. mean, variance, kurtosis) in real-time. This thesis provides various tools to facilitate the real time tracking of biophysical signals harnessed during natural and complex motions: 3D plots, color maps, matrices to name a few. To add anthropomorphic sense to our stochastic analyses and map the person's signatures across the moving body, I

created a virtual human, Chapter 6, that affords different representations and can be used in tandem with other animation and 3D-rendering engines in future work.

Among the deliverables of the thesis, I characterized the individualized process of learning, including fatigue. I also uncovered differences in the stochastic patterns across diverse populations: professional ballet dancers, advanced level dance students (ballet and salsa), regular non-athletic individuals, children with Autism, Asperger Syndrome and Schizophrenia patient. Moreover, I identified the classification of motions that are statistically significant. Such cases are:

1. 1. The independent movement rehearsed during ballet training versus the spontaneous motions generated during sleep (Chapter 5)
2. 2. The professionally-rehearsed movements of a ballet choreography versus regular walking (Chapter 9)
3. 3. The stochastic shifts during improvised salsa dancing versus well-practices choreography

These examples along with previous work [88] provide further support to the proposed map between sensory-motor levels of functionality and probability families Chapter 1.

Most important, I extracted from the continuous motor stream the dominant sensory modality (preferred sensory channel) for each participant and obtained the personalized rate of change of adaptation via the power-law-like linear fit to the log-log Gamma parameter plane and the LUQ/RLQ ratio.

I used a weighted-directed graph representation of dyadic exchange using network connectivity analyses on two dancing bodies and extracted information for the degree of distribution of the body-network, the leading profiles, coupled body parts, and coordination of each body separately and synergistically as one cohesive, self-emergent unit. Moreover, I expanded the range of analyses of human motion to a broader frequency band than traditional physiology (i.e. usually constrained to 30-40Hz).

Finally, I converted biophysical spikes to sound and used those from the heartbeat to blend with several musical pieces, using audio features to modulate volume and speed. These manipulations caused adjustments of the motion's tempo via the modified song using the speed of the heart. Through this implementation I accomplished three primary outcomes:

1. 1. Conversion of continuous analog signals from motion to spike trains ranging in the real domain [0,1]; from spikes to sound and from sound to audio play-back

2. 2. Enhancement of biophysical rhythmic variability and causal change (in closed biofeedback loop) of the stochastic signatures in both deliberate and spontaneous modes of autonomy.

3. 3. Proof of concept that we can steer the nervous systems signatures with less resistance in the spontaneous improvisation mode than in the deliberate staged choreographic mode.

11.2 Future Work

Three main directions can be distinguished in our future research line: the sonification of various parameters of several bodily signals, the development of vision-driven co-adaptive interfaces, and the use of co-adaptive interfaces for therapeutic purposes.

For the first case, I plan on creating sonification methods for movement, temperature, and brain waves, in addition to those of the heart rate. I am interested in augmenting or altering existing song, as I did in the presented example, Chapter 10, as well as creating (composing) new pieces of sound by mapping different parameters of the bodily signals onto audio features.

An example will be to map temperature on the volume of the sound, NSR to some background noise, and set the heart rate as the beat of the song. Although this would be a project at the junction of the arts and computing, it has the potential to help populations

that do not adequately sense their body. Indeed I can substitute or augment their lost sensations with sound-based modalities. Also, it can be used as a training tool, by augmenting our sensations and bringing into awareness motions that we are unaware of.

In the domain of vision-based co-adaptive interfaces, although I recognize the limitation that these interfaces may have in that they bring awareness to the participant and as such preclude us from controlling the motor signatures beneath awareness, I am keen on investigating possible benefits for basic science questions. For example, I could further explore limiting times in visual attention during natural motions introducing various perturbations via the spatio-temporal features of the avatar motions (as shown in the video 2 Appendix Chapter 6). An example is the study presented in Chapter 1, where the children had a more limited space (sitting in front of the monitor to watch the media when activated via their own self-generated motions) and yet this study had a significant impact on the children's sense of agency. I plan to expand that setup to contexts where the children move around in the room. Moreover, for autistic individuals with high visual intelligence (ex. photographic memory) this setup may help us sensory substitute their noisy and random kinesthetic patterns.

Finally, I can target neuroplasticity while using sensory substitution, as in work related to prosthetic arms that feel, brain to brain communication among other [12] [62] [50]. Previous research conducted in the SMILab has utilized an version of the co-adaptive interface to evoke volitional control and the sense of agency in children with Autism [93]. As already explained in Chapter 1 where part of the results alluded to the study, the closed feedback loop paradigm had a significant effect on steering the system of the autistic children towards regimes similar to those of healthy children. This provided proof of concept to build the full body co-adaptive interface aimed at improving other aspects of natural and social behaviors in children with neurodevelopmental disabilities. As such, for my postdoctoral work I am keen on expanding my research to the autistic population to examine the preferences and needs and help them gain autonomous control over their bodies.

Bibliography

[1] Astonishing sophia live interaction at web summit — humanoid robot.

[2] Craig AD. Cooling, pain, and other feelings from the body in relation to the autonomic nervous system. *Handb Clin Neurol*, 117:103–9, 2013.

[3] SV Adamovich, K August, A Merians, and E Tunik. A virtual reality-based system integrated with fmri to study neural mechanisms of action observation-execution: a proof of concept study. *Restorative neurology and neuroscience*, 27(3):209, 2009.

[4] Amazon. Alexa voice service overview, February 2016.

[5] Peterson Becky. I met sophia, the world's first robot citizen, and the way it said goodbye nearly broke my heart, October 2017.

[6] Guillermo Bernal and Pattie Maes. Emotional beasts: Visually expressing emotions through avatars in vr. In *Proceedings of the 2017 CHI Conference Extended Abstracts on Human Factors in Computing Systems*, pages 2395–2402. ACM, 2017.

[7] Nikolai Bernstein. The co-ordination and regulation of movements. *The co-ordination and regulation of movements*, 1966.

[8] Gary G Berntson and John T Cacioppo. *Handbook of neuroscience for the behavioral sciences*, volume 2. John Wiley & Sons, 2009.

[9] Edward B Blanchard and Larry D Young. Self-control of cardiac functioning: A promise as yet unfulfilled. *Psychological Bulletin*, 79(3):145, 1973.

[10] Dieter Bohn. Google is introducing a new smart display platform, Jan. 2018.

[11] Marius Brazaitis, Albertas Skurvydas, Kazimieras Pukėnas, Laura Daniuseviciūtė, Dalia Mickevicienė, and Rima Solianik. The effect of temperature on amount and structure of motor variability during 2-minute maximum voluntary contraction. *Muscle & nerve*, 46(5):799–809, 2012.

[12] Maura Casadio, Rajiv Ranganathan, and Ferdinando A Mussa-Ivaldi. The body-machine interface: a new perspective on an old theme. *Journal of Motor behavior*, 44(6):419–433, 2012.

[13] Mina Choi, Rachel Kornfield, Leila Takayama, and Bilge Mutlu. Movement matters: Effects of motion and mimicry on perception of similarity and closeness in robot-mediated communication. In *Proceedings of the 2017 CHI Conference on Human Factors in Computing Systems*, pages 325–335. ACM, 2017.

[14] Charles A Coey, Manuel Varlet, and Michael J Richardson. Coordination dynamics in a socially situated nervous system. *Frontiers in human neuroscience*, 6:164, 2012.

[15] Jeffrey F Cohn. Foundations of human computing: facial expression and emotion. In *Proceedings of the 8th international conference on Multimodal interfaces*, pages 233–238. ACM, 2006.

[16] Jonathan Cole and Jonathan O Cole. *Pride and a daily marathon*. MIT Press, 1995.

[17] Christian De Looper. Google wants to make its next personal assistant more personable by giving it a childhood, May 2016.

[18] Manfredo P Do Carmo. *Differential Geometry of Curves and Surfaces: Revised and Updated Second Edition*. Courier Dover Publications, 2016.

[19] Giorgos Dritsakis, Rachel M Van Besouw, Pádraig Kitterick, and Carl A Verschuur. A music-related quality of life measure to guide music rehabilitation for adult cochlear implant users. *American journal of audiology*, 26(3):268–282, 2017.

[20] Darell Etherington. Connected speaker packing an always-on siri-style assistant, Nov. 2014.

[21] Ugo Fano. Ionization yield of radiations. ii. the fluctuations of the number of ions. *Physical Review*, 72(1):26, 1947.

[22] Walter D Fenz and Jon M Plapp. Voluntary control of heart rate in a practitioner of yoga: negative findings. *Perceptual and motor skills*, 30(2):493–494, 1970.

[23] Ingo Fietze, Jutta Strauch, Martin Holzhausen, Martin Glos, Christiane Theobald, Hanna Lehnkering, and Thomas Penzel. Sleep quality in professional ballet dancers. *Chronobiology international*, 26(6):1249–1262, 2009.

[24] Paula Fitzpatrick, Veronica Romero, Joseph L Amaral, Amie Duncan, Holly Barnard, Michael J Richardson, and RC Schmidt. Social motor synchronization: Insights for understanding social behavior in autism. *Journal of autism and developmental disorders*, 47(7):2092–2107, 2017.

[25] Stacy L Fritz, Denise M Peters, Angela M Merlo, and Jonathan Donley. Active video-gaming effects on balance and mobility in individuals with chronic stroke: a randomized controlled trial. *Topics in stroke rehabilitation*, 20(3):218–225, 2013.

[26] Shinya Fujii, Kazutoshi Kudo, Tatsuyuki Ohtsuki, and Shingo Oda. Tapping performance and underlying wrist muscle activity of non-drummers, drummers, and the world's fastest drummer. *Neuroscience letters*, 459(2):69–73, 2009.

[27] Maia Garau, Mel Slater, Simon Bee, and Martina Angela Sasse. The impact of eye gaze on communication using humanoid avatars. In *Proceedings of the SIGCHI conference on Human factors in computing systems*, pages 309–316. ACM, 2001.

[28] Darren Gergle and Alan T Clark. See what i'm saying?: using dyadic mobile eye tracking to study collaborative reference. In *Proceedings of the ACM 2011 conference on Computer supported cooperative work*, pages 435–444. ACM, 2011.

[29] Guillaume Gibert, Florian Lance, Maxime Petit, Gregoire Pointeau, and Peter Ford Dominey. Damping robot's head movements affects human-robot interaction. In *Proceedings of the 2014 ACM/IEEE international conference on Human-robot interaction*, pages 162–163. ACM, 2014.

[30] JC Guignard. Human sensitivity to vibration. *Journal of sound and vibration*, 15(1):11–16, 1971.

[31] E von Hoist and H Mittelstaedt. The principle of reafference: interactions between the central nervous system and the peripheral organs. *PC Dodwell (Ed. and trans.), Perceptual processing: Stimulus equivalence and pattern recognition. New York: Appleton*, 1971.

[32] E von Holst and H Mittelstaedt. The principle of reafference: Interactions between the central nervous system and the peripheral organs. *PC Dodwell (Ed. and Trans.), Perceptual processing: Stimulusequivalence and pattern recognition*, pages 41–71, 1971.

[33] Hossein Mousavi Hondori, Maryam Khademi, Lucy Dodakian, Alison McKenzie, Cristina V Lopes, and Steven C Cramer. Choice of human–computer interaction mode in stroke rehabilitation. *Neurorehabilitation and neural repair*, page 1545968315593805, 2015.

[34] Ingrid Maria Hopkins, Michael W Gower, Trista A Perez, Dana S Smith, Franklin R Amthor, F Casey Wimsatt, and Fred J Biasini. Avatar assistant: improving social skills in students with an asd through a computer-based intervention. *Journal of autism and developmental disorders*, 41(11):1543–1555, 2011.

[35] Gudberg K Jonsson and Kristinn R Thorisson. Evaluating multimodal human-robot interaction: A case study of an early humanoid prototype. In *Proceedings of the 7th international conference on methods and techniques in behavioral research*, page 9. ACM, 2010.

[36] Pieter Jorissen, Maarten Wijnants, and Wim Lamotte. Dynamic interactions in physically realistic collaborative virtual environments. *Visualization and Computer Graphics, IEEE Transactions on*, 11(6):649–660, 2005.

[37] E Jovanov, N Hanish, V Courson, J Stidham, H Stinson, C Webb, and K Denny. Avatara multi-sensory system for real time body position monitoring. In *Engineering in Medicine and Biology Society, 2009. EMBC 2009. Annual International Conference of the IEEE*, pages 2462–2465. IEEE, 2009.

[38] Vilelmini Kalabratsidou and Elizabeth B Torres. Invariant and variable relations emerge with degrees of difficulty within habitual and surprise touch-pointing motions. *Journal of Vision*, 14(10):418–418, 2014.

[39] Vilelmini Kalampratsidou and Elizabeth Torres. Exploring new wearable sensing technology in perceptual experiments. *Journal of vision*, 15(12):979–979, 2015.

[40] Vilelmini Kalampratsidou and Elizabeth B Torres. Methods to track dynamically coupled coordinated bodies in ballet partnering. In *Journal of Neurophysiology (under review)*. APS.

[41] Vilelmini Kalampratsidou and Elizabeth B Torres. Outcome measures of deliberate and spontaneous motions. In *Proceedings of the 3rd International Symposium on Movement and Computing*, page 9. ACM, 2016.

[42] Vilelmini Kalampratsidou and Elizabeth B Torres. Body-brain-avatar interface: a tool to study sensory-motor integration and neuroplasticity. In *Fourth International Symposium on Movement and Computing, MOCO*, volume 17, 2017.

[43] Vilelmini Kalampratsidou and Elizabeth B Torres. Dancing to ones heart-beat: A study of physiological signal entrainment through the real-time sonification of heart rate data. In *Proceedings of the 5th International Symposium on Movement and Computing (under review)*, page 9. ACM, 2018.

[44] Vilelmini Kalampratsidou and Elizabeth B Torres. Extracting sensory and contextual information from the motor stream. In *Proceedings of the 5th International Symposium on Movement and Computing (under review)*, page 9. ACM, 2018.

[45] Fakhreddine Karray, Milad Alemzadeh, Jamil Abou Saleh, and Mo Nours Arab. Human-computer interaction: Overview on state of the art. 2008.

[46] Mitsuo Kawato and Daniel Wolpert. Internal models for motor control. *Sensory Guidance of Movement*, 218:291–307, 1998.

[47] JA Scott Kelso and Jane E Clark. *The development of movement control and coordination*. John Wiley & Sons, 1982.

[48] JAS Kelso and VK Jirsa. Coordination dynamics: issues and trends. *BerlinHeidelberg: Springer-Verlag*, 2004.

[49] Jerillyn S Kent, S Lee Hong, Amanda R Bolbecker, Mallory J Klaunig, Jennifer K Forsyth, Brian F O'Donnell, and William P Hetrick. Motor deficits in schizophrenia quantified by nonlinear analysis of postural sway. *PloS one*, 7(8):e41808, 2012.

[50] T Kuiken. The prosthetic arm that feels. *TED. Lecture*, October 2011.

[51] Jordi Lleonart, Jordi Salat, and Gabriel J Torres. Removing allometric effects of body size in morphological analysis. *Journal of Theoretical Biology*, 205(1):85–93, 2000.

[52] Marisa López-Teijón, Álex García-Faura, and Alberto Prats-Galino. Fetal facial expression in response to intravaginal music emission. *Ultrasound*, 23(4):216–223, 2015.

[53] Kenneth A Mann, Frederick W Wernere, and Andrew K Palmer. Frequency spectrum analysis of wrist motion for activities of daily living. *Journal of Orthopaedic research*, 7(2):304–306, 1989.

[54] William D McArdle, Frank I Katch, and Victor L Katch. *Exercise physiology: nutrition, energy, and human performance*. Lippincott Williams & Wilkins, 2010.

[55] Brit McCandles. Charlie rose interviewsa robot?, June 2017.

[56] R Christopher Miall and Daniel M Wolpert. Forward models for physiological motor control. *Neural networks*, 9(8):1265–1279, 1996.

[57] Giovanni Mirabella and Mikhail Lebedev. Interfacing to the brains motor decisions. *Journal of neurophysiology*, 117(3):1305–1319, 2017.

[58] Louis-Philippe Morency, Iwan de Kok, and Jonathan Gratch. Context-based recognition during human interactions: Automatic feature selection and encoding dictionary. In *Proceedings of the 10th international conference on Multimodal interfaces*, pages 181–188. ACM, 2008.

[59] Ferdinando A Mussa-Ivaldi, Maura Casadio, Zachary C Danziger, Kristine M Mosier, and Robert A Scheidt. Sensory motor remapping of space in human–machine interfaces. *Progress in brain research*, 191:45, 2011.

[60] Jillian Nguyen, Ushma Majmudar, Thomas V Papathomas, Steven M Silverstein, and Elizabeth B Torres. Schizophrenia: The micro-movements perspective. *Neuropsychologia*, 85:310–326, 2016.

[61] Femke Nijboer, Adrian Furdea, Ingo Gunst, Jürgen Mellinger, Dennis J McFarland, Niels Birbaumer, and Andrea Kübler. An auditory brain–computer interface (bci). *Journal of neuroscience methods*, 167(1):43–50, 2008.

[62] M Nikolelis. Brain-to-brain communication has arrived. how we did it. *TED. Lecture*, October 2014.

[63] Marianna Obrist, Rob Comber, Sriram Subramanian, Betina Piqueras-Fiszman, Carlos Velasco, and Charles Spence. Temporal, affective, and embodied characteristics of taste experiences: A framework for design. In *Proceedings of the 32nd annual ACM conference on Human factors in computing systems*, pages 2853–2862. ACM, 2014.

[64] Marianna Obrist, Alexandre N Tuch, and Kasper Hornbæk. Opportunities for odor: experiences with smell and implications for technology. In *Proceedings of the 32nd annual ACM conference on Human factors in computing systems*, pages 2843–2852. ACM, 2014.

[65] Catharine Oertel, Kenneth A Funes Mora, Joakim Gustafson, and Jean-Marc Odobez. Deciphering the silent participant: On the use of audio-visual cues for the classification of listener categories in group discussions. In *Proceedings of the 2015 ACM on International Conference on Multimodal Interaction*, pages 107–114. ACM, 2015.

[66] Elizabeth B orres and David Zipser. Simultaneous control of hand displacements and rotations in orientation-matching experiments. *Journal of Applied Physiology*, 96(5):1978–1987, 2004.

[67] Sunghyun Park, Jonathan Gratch, and Louis-Philippe Morency. I already know your answer: Using nonverbal behaviors to predict immediate outcomes in a dyadic negotiation. In *Proceedings of the 14th ACM international conference on Multimodal interaction*, pages 19–22. ACM, 2012.

[68] Pedro Passos, Keith Davids, and Jia Yi Chow. *Interpersonal Coordination and Performance in Social Systems*. Routledge, 2016.

[69] D Purves, GJ Augustine, D Fitzpatrick, WC Hall, AS LaMantia, and LE White. Neuroscience, 5th edn, 2012.

[70] D Purves, E Brannon, R Cabeza, SA Huettel, K LaBar, M Platt, and M Woldorff. Principles of cognitive neuroscience. 2008. *Sunderland, Mass.: Sinauer Associates. xv*.

[71] Dale Purves. *Brains: how they seem to work*. Ft Press, 2010.

[72] Thomas Reilly and Ben Edwards. Altered sleep–wake cycles and physical performance in athletes. *Physiology & behavior*, 90(2):274–284, 2007.

[73] Sheldon M Ross. *Introduction to probability and statistics for engineers and scientists*. Academic Press, 2014.

[74] Mikail Rubinov and Olaf Sporns. Complex network measures of brain connectivity: uses and interpretations. *Neuroimage*, 52(3):1059–1069, 2010.

[75] Jihye Ryu and Elizabeth B Torres. Characterization of sensory-motor behavior under different mindsets. *The Annual Meeting of the Society for Neuroscience*, 2015.

[76] Jihye Ryu, Joseph Vero, and Elizabeth B Torres. Methods for tracking dynamically coupled brain-body activities during natural movement. In *Proceedings of the 4th International Conference on Movement Computing*, page 2. ACM, 2017.

[77] A SCANO. Gillies ja-a textbook of aviation physiology, 1966.

[78] Daniel Schulman and Timothy Bickmore. Changes in verbal and nonverbal conversational behavior in long-term interaction. In *Proceedings of the 14th ACM international conference on Multimodal interaction*, pages 11–18. ACM, 2012.

[79] Sue Ann Seah, Diego Martinez Plasencia, Peter D Bennett, Abhijit Karnik, Vlad Stefan Otrocol, Jarrod Knibbe, Andy Cockburn, and Sriram Subramanian. Sensabubble: a chrono-sensory mid-air display of sight and smell. In *Proceedings of the 32nd annual ACM conference on Human factors in computing systems*, pages 2863–2872. ACM, 2014.

[80] Maryam M Shanechi, Amy L Orsborn, and Jose M Carmena. Robust brain-machine interface design using optimal feedback control modeling and adaptive point process filtering. *PLoS computational biology*, 12(4):e1004730, 2016.

[81] Roni Shiloh, Abraham Weizman, Rafael Stryjer, Natan Kahan, and Dan-Andrei Waitman. Altered thermoregulation in ambulatory schizophrenia patients: a naturalistic study. *The World Journal of Biological Psychiatry*, 10(2):163–170, 2009.

[82] Olaf Sporns. *Discovering the human connectome*. MIT press, 2012.

[83] Harriet Taylor. Could you fall in love with this robot?, March 2016.

[84] EB Torres and JV Jose. Novel diagnostic tool to quantify signatures of movement in subjects with neurobiological disorders, autism and autism spectrum disorders. *US patent application. New Brunswick, NJ: Office of Technology Commercialization, Rutgers, The State University of New Jersey*, 2012.

[85] Elizabeth Torres and Richard Andersen. Space–time separation during obstacle-avoidance learning in monkeys. *Journal of neurophysiology*, 96(5):2613–2632, 2006.

[86] Elizabeth B Torres. *Theoretical framework for the study of sensory-motor integration*. PhD thesis, 2001.

[87] Elizabeth B Torres. New symmetry of intended curved reaches. *Behavioral and Brain Functions*, 6(1):21, 2010.

[88] Elizabeth B Torres. Two classes of movements in motor control. *Experimental brain research*, 215(3-4):269–283, 2011.

[89] Elizabeth B Torres. The rates of change of the stochastic trajectories of acceleration variability are a good predictor of normal aging and of the stage of parkinson's disease. *Frontiers in integrative neuroscience*, 7, 2013.

[90] Elizabeth B Torres. Signatures of movement variability anticipate hand speed according to levels of intent. *Behavioral and Brain Functions*, 9(1):10, 2013.

[91] Elizabeth B Torres. Rethinking the study of volition for clinical use. In *Progress in Motor Control*, pages 229–254. Springer, 2016.

[92] Elizabeth B Torres. *Objective Biometric Methods for the Diagnosis and Treatment of Nervous System Disorders*. June 2018.

[93] Elizabeth B Torres, Maria Brincker, Robert W Isenhower, Polina Yanovich, Kimberly A Stigler, John I Nurnberger, Dimitris N Metaxas, and Jorge V José. Autism: the micro-movement perspective. *Frontiers in integrative neuroscience*, 7, 2013.

[94] Elizabeth B Torres, Jonathan Cole, and Howard Poizner. Motor output variability, deafferentation, and putative deficits in kinesthetic reafference in parkinsons disease. *Frontiers in human neuroscience*, 8:823, 2014.

[95] Elizabeth B Torres and Kristina Denisova. Motor noise is rich signal in autism research and pharmacological treatments. *Scientific reports*, 6:37422, 2016.

[96] Elizabeth B Torres, Kenneth M Heilman, and Howard Poizner. Impaired endogenously evoked automated reaching in parkinson's disease. *Journal of Neuroscience*, 31(49):17848–17863, 2011.

[97] Elizabeth B Torres, Robert W Isenhower, Jillian Nguyen, Caroline Whyatt, John I Nurnberger, Jorge V Jose, Steven M Silverstein, Thomas V Papathomas, Jacob Sage, and Jonathan Cole. Toward precision psychiatry: statistical platform for the personalized characterization of natural behaviors. *Frontiers in neurology*, 7, 2016.

[98] Elizabeth B Torres and Brian Lande. Objective and personalized longitudinal assessment of a pregnant patient with post severe brain trauma. *Frontiers in human neuroscience*, 9, 2015.

[99] Elizabeth B Torres, Sejal Mistry, Carla Caballero, and Caroline P Whyatt. Stochastic signatures of involuntary head micro-movements can be used to classify females of abide into different subtypes of neurodevelopmental disorders. *Frontiers in integrative neuroscience*, 11, 2017.

[100] Elizabeth B Torres, Jillian Nguyen, Sejal Mistry, Caroline Whyatt, Vilelmini Kalampratsidou, and Alexander Kolevzon. Characterization of the statistical signatures of micro-movements underlying natural gait patterns in children with phelan mcdermid syndrome: towards precision-phenotyping of behavior in asd. *Frontiers in integrative neuroscience*, 10, 2016.

[101] Elizabeth B Torres, Anastasia Raymer, Leslie J Gonzalez Rothi, Kenneth M Heilman, and Howard Poizner. Sensory-spatial transformations in the left posterior parietal cortex may contribute to reach timing. *Journal of neurophysiology*, 104(5):2375–2388, 2010.

[102] Elizabeth B Torres, Beth Smith, Sejal Mistry, Maria Brincker, and Caroline Whyatt. neonatal diagnostics: Toward dynamic growth charts of neuromotor control. *Frontiers in pediatrics*, 4, 2016.

[103] Elizabeth B Torres and Caroline Whyatt. *Autism: The Movement Sensing Perspective*. CRC Press, 2017.

[104] Elizabeth B Torres, Polina Yanovich, and Dimitri N Metaxas. Give spontaneity and self-discovery a chance in asd: spontaneous peripheral limb variability as a proxy to evoke centrally driven intentional acts. *Frontiers in integrative neuroscience*, 7:46, 2013.

[105] Elizabeth B Torres and David Zipser. Reaching to grasp with a multi-jointed arm. i. computational model. *Journal of neurophysiology*, 88(5):2355–2367, 2002.

[106] Elizabeth Barbara Torres. Atypical signatures of motor variability found in an individual with asd. *Neurocase*, 19(2):150–165, 2013.

[107] Ksenia I Ustinova, Wesley A Leonard, Nicholas D Cassavaugh, and Christopher D Ingersoll. Development of a 3d immersive videogame to improve arm-postural coordination in patients with tbi. *J Neuroeng Rehabil*, 8:61, 2011.

[108] Cordula Vesper and Michael J Richardson. Strategic communication and behavioral coupling in asymmetric joint action. *Experimental brain research*, 232(9):2945–2956, 2014.

[109] Ulrich W Weger and Stephen Loughnan. Virtually numbed: Immersive video gaming alters real-life experience. *Psychonomic bulletin & review*, 21(2):562–565, 2014.

[110] Caroline P Whyatt and Elizabeth B Torres. The social-dance: decomposing naturalistic dyadic interaction dynamics to the'micro-level'. In *Proceedings of the 4th International Conference on Movement Computing*, page 24. ACM, 2017.

[111] Daniel M Wolpert, R Chris Miall, and Mitsuo Kawato. Internal models in the cerebellum. *Trends in cognitive sciences*, 2(9):338–347, 1998.

[112] D Wu, E Torres, J Nguyen, S Mistry, C Whyatt, V Kalampratsidou, A Kolevzon, and Jose. How doing a dynamical analysis of gait movement may provide information about autism. *Bulletin of the American Physical Society*, 62, 2017.

[113] Xiang Yu, Junzhou Huang, Shaoting Zhang, and Dimitris N Metaxas. Face landmark fitting via optimized part mixtures and cascaded deformable model. *IEEE transactions on pattern analysis and machine intelligence*, 38(11):2212–2226, 2016.

[114] Lin Zhong, Qingshan Liu, Peng Yang, Junzhou Huang, and Dimitris N Metaxas. Learning multiscale active facial patches for expression analysis. *IEEE transactions on cybernetics*, 45(8):1499–1510, 2015.